Development of New Diesel Oxidation and NH_3 Slip Catalysts

Hansen, Thomas Klint

Publication date:
2017

Document Version
Publisher's PDF, also known as Version of record

Ph.D. Thesis

Development of New Diesel Oxidation and NH_3 Slip Catalysts

Thomas Klint Hansen

Kongens Lyngby
June 2017

DTU Chemical Engineering
Department of Chemical and Biochemical Engineering

Technical University of Denmark
Anker Engelunds Vej 1
Building 101A
2800 Kgs. Lyngby
Denmark

Phone: (+45) 45 25 25 25
Email: dtu@dtu.dk
www.dtu.dk

Printed by GraphicCo

Dedicated to Julie

'Tis a lesson you should heed:
Try, try, try again.
If at first you don't succeed,
Try, try, try again.

Thomas H. Palmer

Preface

This thesis entitled "Development of New Diesel Oxidation and NH_3 Slip Catalysts" is submitted in partial fulfillment of the requirements for the Doctor of Philosophy degree (Ph.D.) at the Technical University of Denmark (DTU). It accounts for the most significant results achieved from the independent scientific research that I, Thomas Klint Hansen, have conducted as part of the Ph.D. program. The work was completed at the Combustion and Harmful Emission Control (CHEC) Research Centre at the Department of Chemical and Biochemical Engineering (KT) in close collaboration with Haldor Topsoe A/S (HTAS), from April 2013 to May 2017. The research project was supervised by Professor Anker Degn Jensen (DTU), Dr. Ir. Ton V. W. Janssens (HTAS), and Senior Researcher Brian Brun Hansen (DTU). The requirements for completion of the Ph.D. program also include the completion of courses, teaching, dissemination, and the public defense of this thesis.

This Ph.D. project was part of the larger research project entitled *Next Generation Exhaust Gas Cleaning Technologies for Diesel Vehicles (NEXT)* that focused on developing new and improved technologies for catalytic exhaust gas aftertreatment from heavy duty diesel vehicles. The NEXT project is a collaboration between KT at DTU and HTAS. The financial support from Innovation Fund Denmark under grant number 103-2012-3 is gratefully acknowledged.

Undertaking and completing a Ph.D. program is not an easy task, as any former or current Ph.D. student knows well. It is in many aspects similar to riding a roller coaster for the first time. When you climb aboard, you do not actually realize what you have gotten yourself into. As the roller coaster begins to climb the first hill and the rest of the track comes into view, you become overwhelmed by the magnitude of what lies ahead. At this point, there is only one thing to do; hang on tight and power through as you are thrown through highs and lows, and unexpected twists and turns. Before you know it, you are in the final stretch and the end station becomes clearly visible. You pull into the station, climb off the roller coaster, and appreciate how great an experience it actually was. You also realize that the next time you ride a roller coaster, you will have an idea of what to expect and how to handle the unexpected.

Similarly to riding a roller coaster, completing the Ph.D. program is more manageable and enjoyable when undertaken together with others. I would therefore like to express my sincere gratitude to my supervisors, Anker Degn Jensen, Ton V. W. Janssens, and Brian Brun Hansen. Their supervision and input throughout the project has been very valuable. We have had many good discussions within a very broad range of topics, and I hope that we can continue the collaboration for some time to come. I am also very grateful to the rest of the NEXT project participants from Haldor Topsoe A/S and DTU for their input at our quarterly project meetings.

A special thanks is extended to Kasper Linde, Andreas Åberg, and Ian Allen. I have greatly appreciated the professional and social aspects of the collaboration

between our Ph.D. projects within the NEXT project. It has helped me on more than one occasion to overcome challenges in the project. I am also grateful that Kasper and I could continue our five years of close collaboration from the bachelor's and master's programs throughout the Ph.D. program. I hope to remain in contact with the NEXT Ph.D. students and work with them again in the future.

Throughout the Ph.D. project, I have also had the pleasure of supervising Martin Hansen, Rune Damborg, Rikke Bjerregaard, Henrik Teglborg, and Thomas Andersen in their student projects. Thank you for your hard work and contribution to the Ph.D. project. I have also enjoyed my collaboration with Assistant Professor Martin Høj and Assistant Professor Jakob Munkholt Christensen in the supervision of these projects.

I am also extremely grateful to the CHEC technicians, Anders Tiedje, Nikolaj Nissen, Rasmus Christensen, and Anders Kjersgaard, who's advice and assistance in building, modifying, and automating the fixed bed reactor setups were invaluable.

I would also like to thank all my fellow Ph.D. students at KT who are or have been on a similar journey as the one I have been on. You have all contributed to a very pleasant working environment, both professionally and socially. In this context, I would also like to especially thank my officemates throughout the years: Marimar, Mohammad, Siqiang, Trine, and Steen. I have enjoyed sharing an office with all of you, and I am grateful for our social and professional interactions.

Last but definitely not least, I would like to thank my family and friends for their support throughout the entire Ph.D. program. I owe the biggest thanks to my fiancée, Julie, for her unwavering support and patience during the last and longest months of the Ph.D. project.

Thomas Klint Hansen
Kongens Lyngby
June 7th, 2017

Summary

Diesel engines used in the transport sector and for other heavy machinery form pollutants during the combustion process. Emission of these pollutants into the atmosphere has harmful consequences on human health and the environment. In order to mitigate these harmful effects, regulations have been imposed by environmental protection agencies on the most significant pollutants, including CO, hydrocarbons, NO_x, and particulate matter. To reduce emissions to the levels specified by the recent Euro VI regulations, it is necessary to apply catalytic exhaust gas aftertreatment systems.

A modern diesel exhaust aftertreatment system commonly consists of a Pt-based diesel oxidation catalyst (DOC) to oxidize CO and unburnt hydrocarbons to CO_2 and H_2O, and oxidize NO to NO_2. This is followed by the diesel particulate filter (DPF), which entraps particulate matter from the exhaust gas. A solution of urea is injected after the DPF to supply NH_3 for the selective catalytic reduction (SCR) of NO_x over an NH_3-SCR catalyst. A mixture of NO and some NO_2 evokes the fast SCR reaction, which increases NO_x reduction. Emissions of NO_x can be further decreased by dosing a stoichiometric excess of NH_3. However, NH_3 is also a regulated pollutant and it is therefore necessary to include an ammonia slip catalyst (ASC) for the selective catalytic oxidation of excess NH_3 to N_2 and H_2O.

The purpose of this research project has been to develop an optimized diesel oxidation catalyst with a low noble metal content and a highly active ammonia slip catalyst with an improved N_2 selectivity.

The Pt-based DOC constitutes a significant part of system costs. To effectively utilize the platinum and reduce cost, the influence of Pt particle size on catalytic activity for CO, hydrocarbon, and NO oxidation was studied using 1 wt.% Pt/Al_2O_3 catalysts with Pt particles diameters between 1.3 and 18.7 nm. The mass based oxidation activity of CO, C_3H_6, and NO showed an optimal Pt particle size between 2–4 nm for all three reactions. Based on the turnover frequencies and the distribution of surface atoms of Pt particles, the reactions appear to be mainly catalyzed by terrace atoms, which are most abundant between 2–4 nm. The decrease in catalytic activity for large Pt particles can be explained by the diminishing Pt surface area, while the decrease in activity for small particles is due to the lack of terrace atoms required for catalyzing the oxidation of CO, hydrocarbons, and NO.

The modern ASC is a multi-functional catalyst that combines the high ammonia oxidation (AMOX) activity of a Pt-based catalyst with the capability of an SCR catalyst to reduce formed NO_x to N_2 using NH_3. The high selectivity of the AMOX catalyst towards N_2O and NO_x at temperatures above 225–250°C, corresponding to a poor N_2 selectivity, is counterproductive for the aftertreatment system. By including an SCR catalyst, the N_2 selectivity is greatly improved. The AMOX component of the ASC was considered by investigating the catalytic oxidation of NH_3 over a series of noble metal catalysts (1 wt.% Pt/Al_2O_3, 5 wt.% Pt/Al_2O_3, 5

wt.% Rh/Al_2O_3, and 5 wt.% Pd/Al_2O_3). The Pt catalysts were the most active and a series of 1 wt.% Pt/Al_2O_3 catalysts with varying Pt particles sizes of 1.3–18.7 nm and of ∼200 nm was subsequently tested. Large Pt particles of 7.7 nm, 18.7 nm, and ∼200 nm were the most active, and Pt particles of ∼200 nm also achieved lower yields of N_2O and NO_2, but with an increase in the total NO_x formed. Furthermore, Pt particles of 2–4 nm achieved the greatest NO_2/NO_x ratios, in line with observations for NO oxidation over 1 wt.% Pt/Al_2O_3.

A single channel 1D-1D steady state mathematical model of the ammonia slip catalyst was further developed and validated in order to improve system understanding and reduce experimental efforts. The model includes film diffusion from the gas channel to the washcoat surface, and the diffusion and reaction throughout the washcoat layers of one monolith channel. The kinetic models applied were derived based on activity measurements for 1 wt.% Pt/TiO_2-SiO_2 (AMOX) and 3.5 wt.% Cu-BEA (SCR). The monolith model was validated against experimental data for NH_3 oxidation over four monolithic catalysts: single layer AMOX, single layer SCR, single mixed layer, and dual layer configurations. The model description agrees well with experimental data for NH_3 conversion and selectivities to NO_x, N_2O, and N_2.

The validated model was used to analyze the performance of the single layer and dual layer ammonia slip catalysts with respect to variations in the following parameters: the intrinsic activity of the AMOX catalyst, the loadings of the AMOX and SCR catalysts, the effective diffusivity of the catalyst layers, the NO oxidation activity of the AMOX catalyst, and the ability of each catalyst to form N_2O. For all ASC catalysts, an adequate Pt loading is necessary since it determines the ammonia oxidation activity available. If the Pt loading is sufficient, then the catalyst loadings and effective diffusivity become the key design parameters since these factors determine the effectiveness factor of the catalyst and the magnitude of SCR activity available for NO_x reduction. By varying the NO oxidation activity of the AMOX catalyst it is possible to alter the NO_2/NO_x ratio and evoke the fast SCR reaction, thereby improving NO_x reduction, but also increasing N_2O selectivity. Additionally, excluding N_2O formation from either the AMOX or SCR catalyst identified the AMOX catalyst as the main source of N_2O formation. Thus, development of an ASC with low N_2O yield should focus on the AMOX component. The multi-objective optimization of ten ASC configurations for NH_3 oxidation at 300°C was used to study the sensitivity towards the catalyst architecture of the ASC. The resulting Pareto fronts indicate that the optimal catalyst systems with the most potential are those involving mixed layers of AMOX and SCR catalysts, rather than pure layers of AMOX or a top layer of SCR. This is mainly due to the ability of the mixed layers to circumvent N_2O formation with the more immediate reduction of NO_x with NH_3.

Resumé

Dieselmotorer anvendt i transportsektoren og til andet tungt maskineri danner forurenede stoffer under forbrændingsprocessen. Udledning af disse forurenede stoffer til atmosfæren har skadelige konsekvenser for menneskers helbred og miljøet. For at begrænse disse skadelige effekter er der blevet indført lovgivning af miljøbeskyttelsesmyndigheder for de mest betydelige forurenende stoffer, inklusiv CO, kulbrinter, NO_x og partikler. For at reducere emissioner til niveauer specificeret af Euro VI lovgivningen, er det nødvendigt at anvende katalytiske rensnings systemer.

Et moderne katalysatorsystem på et deisel køretøj består af en Pt-baseret diesel oxidations katalysator (DOC) til at oxidere CO og uforbrændte kulbrinter til CO_2 og H_2O, samt at oxidere NO til NO_2. Denne proces efterfølges af et partikel filter (DPF). En opløsning af urea indsprøjtes efter DPF for at forsyne med NH_3 til den selektive katalytiske reduktion (SCR) af NO_x over en NH_3-SCR katalysator. En blanding af NO med noget NO_2 fremkalder den "hurtige" SCR reaktion, som markant øger NO_x reduktion. Emissioner af NO_x kan blive yderligere nedbragt ved dosering af et støkiometrisk overskud af NH_3. Da NH_3 også er et reguleret forurenende stof, er det derfor også nødvendigt at inkludere en ammoniak slip katalysator (ASC) til den selektive katalytiske oxidation af overskydende NH_3 til N_2 og H_2O.

Formålet med dette forskningsprojekt har været at udvikle en optimeret diesel oxidations katalysator med et lavt indhold af ædelmetal og en højaktiv ammoniak slip katalysator med forbedret N_2 selektivitet.

Den Pt-baserede DOC udgør en betydelig del af systemets pris. For at anvende Pt effektivt og reducere omkostningerne blev påvirkningen af Pt partikelstørrelsen på den katalytiske aktivitet for CO, kulbrinte, og NO oxidation undersøgt ved brug af 1 vægt % Pt/Al_2O_3 katalysatorer med Pt partikeldiametre imellem 1.3 og 18.7 nm. Den massebaserede oxidationsaktivitet for CO, C_3H_6, og NO viste en optimal Pt partikelstørrelse imellem 2–4 nm for alle tre reaktioner. Baseret på den målte omsætningsfrekvens og fordelingen af overfladeatomer af Pt partiklerne, tyder det på at reaktionerne hovedsagligt bliver katalyseret af terrasse atomer, som der findes flest af imellem 2–4 nm. Den reducerede katalytiske aktivitet for store Pt partikler skyldes det formindskede Pt overflade areal, mens faldet i katalytisk aktivitet for de små partikler skyldes mangel på terrasse atomer, som er nødvendige for at katalysere oxidationen af CO, kulbrinter, og NO.

Den moderne ASC er en multifunktionel katalysator der, kombinerer den høje ammoniak oxidations (AMOX) aktivitet af en Pt-baseret katalysator med SCR katalysatorens evne til at reducere NO_x til N_2 ved brug af NH_3. Den høje selektivitet af AMOX katalysatoren mod N_2O og NO_x ved temperaturer over 225–250°C, svarende til en dårlig N_2 selektivitet er kontraproduktiv. Ved at inkludere en SCR katalysator forbedres N_2 selektiviteten i høj grad. AMOX komponenten i ASC blev studeret ved at undersøge den katalytiske oxidation af NH_3 for en række ædelmetal katalysatorer (1 vægt % Pt/Al_2O_3, 5 vægt % Pt/Al_2O_3, 5 vægt % Rh/Al_2O_3, og

5 vægt % Pd/Al_2O_3). Pt katalysatorerne var de mest aktive og en serie af 1 vægt % Pt/Al_2O_3 katalysatorer med Pt partikel størrelser fra 1.3 til 18.7 nm og ∼200 nm blev efterfølgende testet. Store Pt partikler dvs. 7.7 nm, 18.7 nm, og ∼200 nm var de mest aktive, og Pt partikler af ∼200 nm opnåede også de laveste udbytter af N_2O og NO_2, men medførte også en stigning i den totale mængde af dannet NO_x. Yderligere blev det klarlagt, at Pt partikler af 2–4 nm opnåede de største NO_2/NO_x forhold, hvilket stemmer overens med resultater for NO oxidation over 1 vægt % Pt/Al_2O_3.

En enkelt-kanals 1D-1D steady-state matematisk model for en ammoniak slip katalysator blev yderligere udviklet og valideret for at forbedre forståelsen af systemet og mindske eksperimentelt arbejde. Modellen betragter film diffusion fra gassen i kanalen til overfladen af katalysatorlaget, og diffusion og reaktion gennem katalysatorlaget for en enkelt monolit kanal. De anvendte kinetiske modeller blev udledt baseret på aktivitetsmålinger af 1 vægt % Pt/TiO_2-SiO_2 (AMOX) og 3.5 vægt % Cu-BEA (SCR). Monolit modellen blev valideret mod eksperimentelle data for NH_3 oxidation over fire monolit katalysatorer: enkelt-lag AMOX, enkelt-lag SCR, enkelt blandet lag, og to lags konfigurationer. Modelbeskrivelsen stemmer godt overens med eksperimentel data for NH_3 omsætning og selektivitet af NO_x, N_2O, og N_2.

Den validerede model blev brugt til at analysere ydeevnen af enkelt og to-lags ammoniak slip katalysatorerne over for ændringer i følgende parametre: den intrinsiske aktivitet af AMOX katalysatoren, mængden af AMOX og SCR katalysatorer, den effektive diffusivitet af katalysator lagene, NO oxidations aktiviteten af AMOX katalysatoren, og evnen af hver katalysator til at danne N_2O. For alle katalysatorer, var en tilstrækkelig mængde Pt vigtig, da den bestemmer den tilgængelige ammoniak oxidation aktivitet. Hvis mængden af Pt er tilstrækkelig, bliver mængden at katalysator og den effektive diffusivitet de vigtigste design parametre, da disse bestemmer effektivitetsfaktoren for katalysatoren og størrelsen af SCR-aktivitet til rådighed for NO_x reduktion. Ved at variere AMOX katalysatorens NO oxidationsaktivitet er det muligt at ændre på NO_2/NO_x forholdet og fremkalde den "hurtige" SCR reaktion, og dermed forbedre NO_x reduktion, men også øge N_2O selektivitet. Derudover, ved at skiftevis eksludere dannelsen af N_2O fra AMOX og SCR katalysatoren blev AMOX katalysatoren identificeret som hovedkilden til N_2O dannelse. Som følge heraf skal udvikling af en ASC med lav N_2O udbytte fokusere på AMOX katalysatoren. Multi-mål-optimering af ti ASC konfigurationer for NH_3 oxidation ved 300°C blev brugt til at undersøge følsomheden overfor katalysatorkonstruktionen af ASC. De resulterende Pareto fronter indikerede at katalysatorsystemer med størst potentiale er dem, der involverer blandede lag af AMOX og SCR katalysatorer fremfor dem med rene lag af AMOX eller dem med et SCR toplag. Dette skyldes i høj grad det blandede lags evne til at undgå N_2O dannelse ved den mere tilgængelig reduktion af NO_x med NH_3.

Contents

CHAPTER 1

Introduction to the Thesis

Chapter 1 Introduction to the Thesis presents the background and motivation for the Ph.D. project, including the diesel engine cycle, the formation and consequences of pollutants, the emission regulations, and the emission reduction strategies with an emphasis on catalytic exhaust gas aftertreatment. Based on this, the project objectives are defined and the structure of the Ph.D. thesis is presented. This chapter also includes an overview of publications, conference contributions, and student projects supervised.

1.1 Background and Motivation

1.1.1 The Diesel Engine

The diesel engine, first developed in the 1890's by Rudolf Diesel [1], has become a staple technology of society. It converts the chemical energy stored in diesel fuel to mechanical energy, which is used to drive small utility applications, cars, trucks, trains, and marine vessels [2]. Compared to its counterpart, the gasoline engine, the diesel engine generally operates with a higher compression ratio, which results in a higher thermal efficiency, thereby achieving a superior fuel economy and producing lower emissions (g/km) of carbon dioxide (CO_2), a major greenhouse gas (GHG) [3, 4]. This is a significant benefit of the diesel engine with regard to slowing global warming [4]. The diesel engine can either be a two-stroke or a four-stroke engine, with the four-stroke diesel engine being the predominant type, while mainly marine vessels are equipped with the more compact and powerful two-stroke engine [3, 5]. Figure 1.1 shows the four-stroke engine cycle and details its working principles.

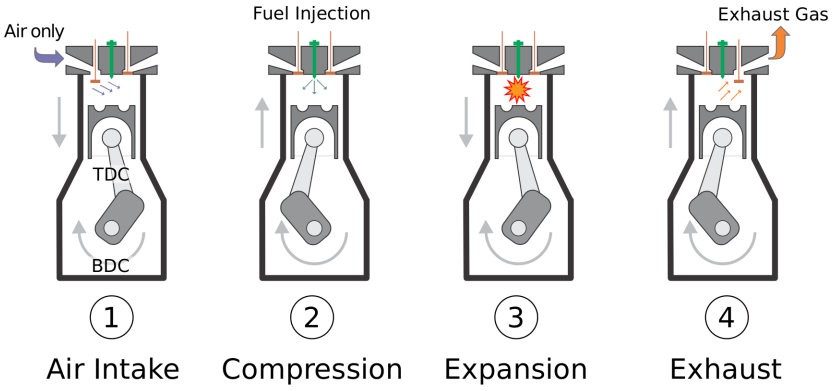

Figure 1.1: *The four-stroke cycle for the four-stroke diesel engine [2].*

① Air Intake - Air is taken into the cylinder as the piston moves from the top-dead-center (TDC) downwards to the bottom-dead-center (BDC) [2].

② Compression - The air is compressed by the movement of the piston upwards, back to the TDC position. The compression causes the air in the cylinder to heat up to a temperature above the auto-ignition temperature of diesel fuel. As the piston nears the TDC, the diesel fuel is injected into the hot air as highly dispersed droplets. Upon mixing with air and being heated to the auto-ignition temperature, the fuel begins to combust [2, 3].

③ Expansion - As the diesel fuel combusts in the presence of excess air, energy is released in the form of heat and the pressure is greatly increased. The pressure increase in the cylinder forces the piston downwards to the BDC position [2].

④ Exhaust - The products of the combustion process are released into the exhaust system, and are eventually released into the atmosphere [2].

As the diesel engine repeats the four-stroke cycle, the piston moves back and forth. By using a crankshaft connected to the piston, the linear motion of the piston is transformed to the rotary motion that is used to drive machinery [2].

1.1.2 Exhaust Gas Properties and Emission Formation

As the diesel engine operates, the exhaust gas is released into the exhaust system. The properties of the exhaust gas from the diesel engine depend on the engine load and can therefore vary considerably, with common volumetric gas flows between 500–1500 m^3/h and exhaust gas temperatures generally in the range of 200–500°C [6–8]. The exhaust gas consists of the remnants, products, and by-products of the combustion mixture. Since the combustion mixture consists of the injected diesel fuel and an abundant amount of air (79% N_2 and 21 vol.% O_2), typically in excess by a factor of 1.8 relative to the stoichiometric air-to-fuel ratio [5], the majority of the exhaust gas is unreacted N_2 and O_2. Ideally, the diesel fuel mixture combusts completely in air, releasing heat and forming only CO_2 and H_2O, according to the general reaction R 1.1. The general reaction is used since diesel fuel is a mixture of many hydrocarbons, mainly alkanes and cycloalkanes with carbon numbers between 10 to 22, that is produced from the distillation of crude oil [9].

$$C_xH_y + (x + \frac{1}{4}\,y)\,O_2 \longrightarrow x\,CO_2 + \frac{1}{2}\,y\,H_2O \qquad \text{(R 1.1)}$$

It then follows that diesel exhaust gas consists primarily of 2–12 vol.% CO_2, 2–12 vol.% H_2O, 3–17 vol.% O_2, and a balance of N_2 [5, 10]. The composition is given as intervals, since the exact exhaust composition depends on operating conditions and design of the diesel engine [10].

However, the combustion of diesel fuel is more complicated than indicated by reaction R 1.1 and harmful by-products are formed, which are released into the atmosphere as part of the exhaust gas [11]. The most significant harmful emissions are unburnt hydrocarbons (HC), carbon monoxide (CO), nitrogen oxides (NO_x), nitrous oxide (N_2O), particulate matter (PM), and a small amount of sulfur oxides (SO_x) [11]. Figure 1.2 illustrates the relative contribution of the major constituents (N_2, O_2, CO_2, H_2O) and the primary pollutants (HC, CO, NO_x, PM) to the composition of a typical diesel exhaust gas in terms of weight percentage [12]. The typical concentration of the harmful by-products is around 0.1 wt.% (see Figure 1.2), and such concentrations are sufficient to have a significant impact on human health and the environment.

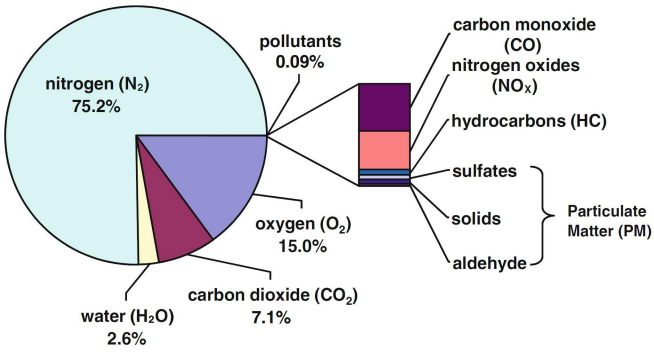

Figure 1.2: *The relative contribution of the major constituents and the primary pollutants to the composition of a typical diesel exhaust gas in terms of weight percentage [12].*

The incomplete combustion of fuel is a main source of harmful compounds and it is caused by poor mixing of fuel and air in the combustion chamber, which results in regions of fuel-rich mixtures [11]. The lack of oxygen in these regions leads to hydrocarbons that are unburnt, partially decomposed, or partially oxidized, such as formaldehyde [11, 13]. It also results in the formation CO, which is an intermediate in HC combustion [11]. Lubrication oil is an additional source of hydrocarbon emissions [11]. Consequently, a typical diesel exhaust contains 20–330 ppm-C of HC compounds and 10–1200 ppm CO, with peak values of up to 5000 ppm CO during acceleration [5, 13]. Hydrocarbons and their derivatives are sometimes lumped together and considered jointly as volatile organic compounds (VOC) or as non-methane volatile organic compounds (NMVOC) when excluding methane (CH_4) [14].

Nitrogen oxides form during the combustion process as a result of reactions at high pressures (up to 230 bar [12]) and high temperatures (above 1400–1700°C) between N_2 and O_2, and the resulting intermediates formed [11, 13]. Typical emissions of NO_x are between 50–1000 ppm [5, 13]. Of the NO_x exiting the diesel engine, 70-90% is nitric oxide (NO), while the remainder is nitrogen dioxide (NO_2) formed from the oxidation of NO [11, 13].

Nitrous oxide can form as an intermediate in NO formation during combustion [11, 13]. It is emitted in the exhaust gas in very small quantities of 3 ppm and is excluded from the NO_x grouping [13].

Particulate matter in the hot engine exhaust gas consists mainly of carbon particles (soot) resulting from incomplete combustion and metallic ash originating from engine wear and inorganic materials in the fuel, fuel additives, or lubrication oil [11, 15]. PM emissions are expressed on a mass basis (g/kWh, g/km, mg/m^3), with typical emission levels of about 65 mg/m^3 [5], 0.1–0.39 g/kWh for all PM, and 0.02–0.04 g/kWh for soot [10].

Sulfur oxides are formed from the combustion of sulfur compounds in the fuel or lubrication oil [11, 13]. The SO_x concentration in diesel exhaust is therefore dependent on the sulfur level of the diesel fuel [13]. For example, a low sulfur diesel fuel with 500 ppm-S leads to an exhaust gas with about 20 ppm SO_2 [5, 13]. In recent years, ultra low sulfur diesel (10–50 ppm-S) and sulfur-free diesel ($\leq$10 ppm-S) have been introduced to avoid environmental consequences and poisoning of catalytic components of the aftertreatment system [9]. The majority of SO_x in the engine exhaust consists of SO_2, with only 2–5% SO_3 formed from oxidation of SO_2 [13].

Table 1.1 summarizes the typical levels of the different major constituents and pollutants in the diesel engine exhaust gas. Although the presented emissions are formed in small quantities relative to the major constituents of the exhaust gas, the cumulative effect of pollutants from many different sources leads to detrimental consequences for human health and the environment [4, 16, 17]. This is especially the case for densely populated cities worldwide (e.g. Los Angeles, Mexico City, and Beijing), where diesel exhaust contributes to the formation of a brown-grayish fog of smoke (smog) consisting of a mixture of NO_x, SO_x, PM, CO, HC and its derivatives [4]. Smog causes irritation to the human respiratory system, including coughing, choking, and stinging eyes, and may also have mutagenic and carcinogenic effects [4, 16, 17]. Additionally, NO_x and SO_x emissions result in acid rain which can lead to acidification of waters and destruction of forests [4, 16]. The reduction of emissions

from diesel engines can therefore lead to an improvement in the living environment in densely populated areas, and this has been the motivation for introducing emission regulations.

Table 1.1: *Typical levels of major constituents and pollutants composing the diesel engine exhaust gas [5, 10, 13].*

Major Constituents		**Pollutants**		
Specie	**Vol.%**	**Specie**	**ppm**	**g/kWh**[a]
CO_2	2 – 12	HC	20 – 330	0.08 – 0.75
H_2O	2 – 12	CO	10 – 500	0.89 – 3.28
O_2	3 – 17	NO_x	50 – 1000	3.21 – 3.73
N_2	balance	PM_{Total}	–[b]	0.10 – 0.39
		PM_{Soot}	–	0.02 – 0.04
		SO_x	$\leq$20[c]	
		N_2O	$\sim$3	

[a] Based on diesel engine emissions from 1990's [10].
[b] $\sim$65 mg/m^3 for PM_{Total}.
[c] Directly proportional with sulfur level of fuel [5, 13].

1.1.3 Emission Inventories and Regulations

The emissions discussed in Section 1.1.2 are produced and released from many different sources. National agencies, such as the Environmental Protection Agency (EPA) of the USA and the European Environment Agency (EEA) of the European Union, prepare detailed yearly estimates of the emissions based on consumption data and emission factors from the different sector groups in order to maintain an overview of emissions and to identify the most significant sources [14]. Figure 1.3 presents the EU emission inventories for HC (part of NMVOC), CO, NO_x, and PM for 2014.

As indicated by Figure 1.3, the transport sector consisting of on-road and non-road applications, of which diesel engines are a significant part, is responsible for contributing 12% of NMVOC, 23% of CO, 46% of NO_x, and 15% of PM to the European emissions [18]. Similar numbers are valid for the American emissions inventory, where the transport sector is accountable for 7% of VOC, 50% of CO, 55% of NO_x, and 6% of PM [19]. The EEA does not differentiate between gasoline and diesel sources, instead a division of contributions from gasoline and diesel engines in the Danish transport sector is presented in Figure 1.4.

The Danish emission inventory for the transport sector indicates a clear and significant contribution of emissions from diesel engines applied to on-road and non-road transport, with a combined contribution of 21% of NMVOC, 10% of CO, 55% of NO_x, and 67% of PM. Again, similar trends are observed for the American transport sector where 9% of VOC, 5% of CO, 62% of NO_x, and 64% of PM come from diesel engines [19]. This further consolidates the importance of controlling emissions from diesel engines, especially NO_x and PM. Therefore, environmental regulations on emissions from non-road diesel vehicles (marine vessels, locomotives, aircrafts) and on-road diesel vehicles (passenger cars, light-duty, heavy-duty) have been introduced in a large number of countries worldwide and are periodically revised to impose stricter regulations in the future.

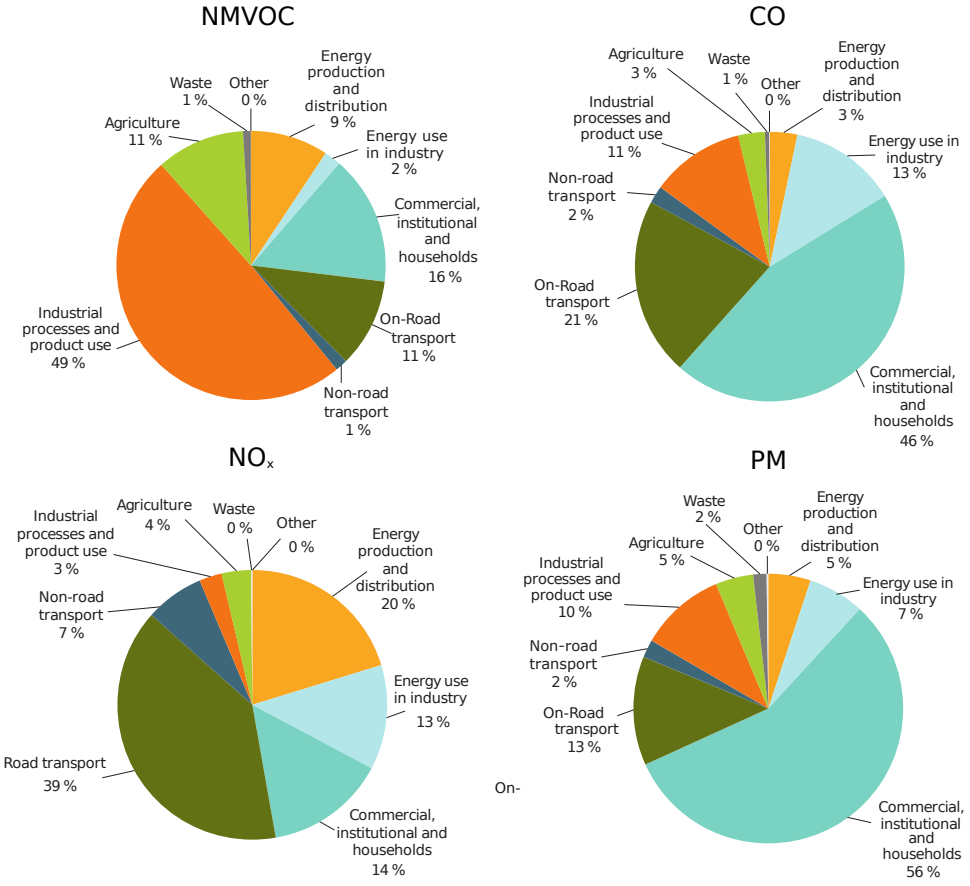

Figure 1.3: *European emission inventory for 2014 for NMVOC (includes HC), CO, NO_x, and PM. The data is collected and reported by the European Environment Agency [18].*

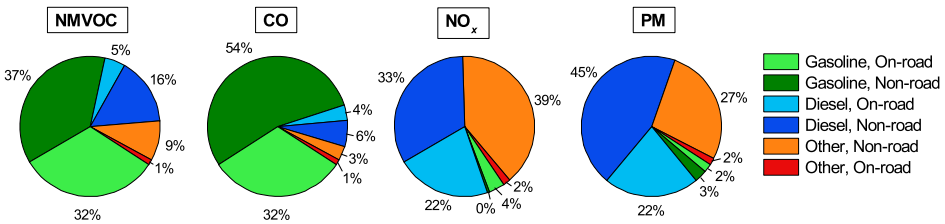

Figure 1.4: *Danish national emission inventory for the transport sector for 2014 [20].*

Focusing on emissions from heavy-duty diesel (HDD) vehicles, covering trucks ($>$ 3500 kg) and buses, the EU introduced the Euro I–VI regulations on emissions of CO, HC, NO_x, and PM [21–23]. Generally, regulations are specified as mass based emissions relative to the distance driven (g/km) or to the mechanical work done by the engine (g/kWh) [10]. Additionally, the newer regulations also impose restrictions on NH_3 emissions and the number of PM particles (PN) released, in terms of number of particles emitted per mechanical work done by the engine (1/kWh). Table 1.2

presents the Euro I–VI regulations for HDD vehicles with a technically permissible maximum laden mass over 3500 kg [21, 23]. Note that Euro I and II regulations only considered steady-state testing, while Euro III–VI introduced transient driving cycles.

Table 1.2: *EU emission standards for heavy-duty diesel engines for stationary and transient cycles (Stationary/Transient) [21, 23].*

Stage	**Year**	**Test**	**CO (g/kWh)**	**HC (g/kWh)**	**NO_x (g/kWh)**	**PM (g/kWh)**	**PN (1/kWh)**
Euro I[a]	1992	ECE R–49	4.5	1.1	8.0	0.612	–
Euro I[b]	1992	ECE R–49	4.5	1.1	8.0	0.36	–
Euro II	1996	ECE R–49	4.0	1.1	7.0	0.25	–
Euro II	1998	ECE R–49	4.0	1.1	7.0	0.15	–
Euro III	2000	ESC/ETC/ELR	2.1/5.45	0.66[c]/0.78[c]	5/5	0.1/0.16	–
Euro IV	2005	ESC/ETC/ELR	1.5/4	0.46[c]/0.55[c]	3.5/3.5	0.02/0.03	–
Euro V	2008	ESC/ETC/ELR	1.5/4	0.46[c]/0.55[c]	2/2	0.02/0.03	–
Euro VI[d]	2013	WHSC/WHTC	1.5/4	0.13/0.16	0.4/0.46	0.01/0.01	8[e]/6[e]

ECE R–49: Steady-state diesel engine test cycle introduced by ECE Regulation No. 49
ESC/ETC: European Stationary/Transient Cycle
ELR: European Load Response Engine Test - for smoke opacity measurement.
WHSC/WHTC: World Harmonized Stationary/Transient Cycle
[a] ≤85 kW
[b] >85 kW
[c] Non-Methane Hydrocarbons
[d] Concentration limit of 10 ppm NH_3 applies to WHSC/WHTC
[e] 1×10^{11}

1.1.4 Emission Reduction Strategies

In order to reduce emissions from diesel exhaust systems and meet emission regulations, vehicle manufacturers and collaborators have had to undertake an interdisciplinary task involving the advancement of combustion technology, engine design optimization, improvement of fuel and oil quality, and development of catalytic exhaust aftertreatment systems [22, 24, 25].

The formation of emissions is influenced by engine design and operating conditions, and initial emission reduction strategies were therefore focused on developing combustion technology and optimizing engine design. Using this strategy, vehicle manufacturers were able to meet early emission regulations (Euro I and II) through the development of advanced fuel injection systems, improvements in air intake, and modifications to the combustion chamber [25]. Additionally, the introduction of electronic control technologies and algorithms, such as those for injection control, have had a significant impact [25]. Furthermore, engine design tuning was necessary in order to balance the trade-off between NO_x and PM, and meet emission standards [25]. Figure 1.5 illustrates the NO_x-PM emission levels achieved with initial engine technologies together with the early EU and US emission regulations.

In the 2000's, the introduction of more stringent regulations, including the Euro IV, Euro V, and Euro VI, forced manufacturers to devise new strategies of how to meet regulations. Euro IV and V regulations were met by designing the engine to operate with low engine-out emissions of PM and introducing the deNOx unit to sufficiently reduce the high engine-out emissions of NO_x [25, 26]. However, to meet Euro VI regulations it has been necessary to implement exhaust gas recirculation

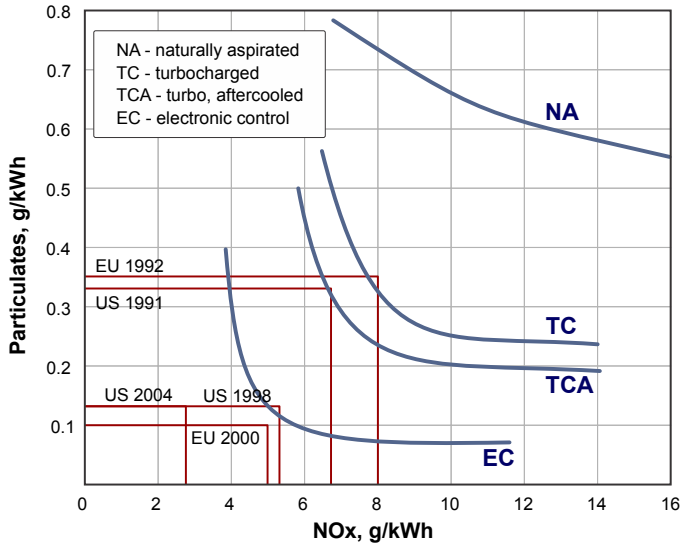

Figure 1.5: *Illustration of NO_x-PM trade-off for early diesel engine technologies introduced to meet initial emission regulations [25].*

(EGR) to reduce engine-out emissions of NO_x, followed by the application of particulate filters and deNOx units to further reduce emissions levels of the exhaust gas [25, 26]. These reduction strategies are qualitatively illustrated in Figure 1.6 using engine-out emissions corresponding to different Euro regulations with respective NO_x-PM trade-offs, and the general impact of introducing deNOx catalysts and particle filters.

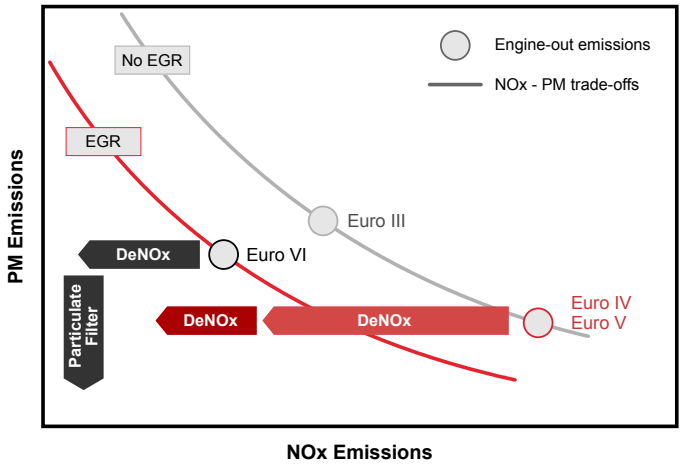

Figure 1.6: *Qualitative illustration of the general impact of exhaust gas recirculation (EGR), deNOx catalysts, and particulate filters on the diesel engine-out emissions corresponding to different Euro regulations [26].*

As evident from the evolution of emission reduction strategies, it has become necessary to employ and develop catalytic diesel exhaust aftertreatment systems to meet current and future regulations.

1.1.5 Catalytic Diesel Exhaust Gas Aftertreatment

Diesel exhaust afteratreatment is achieved by passing the hot exhaust gas through a train of catalyst units where the harmful emissions (HC, CO, NO_x, PM) are catalytically converted to harmless compounds (N_2, CO_2, H_2O). Monolithic catalysts are used to ensure low pressure drops across the catalyst units. They are prepared using monolith substrates made of either ceramic materials (cordierite; $2\,MgO{\cdot}2\,Al_2O_3{\cdot}5\,SiO_2$), metal foils (Fe-Cr-Al), or silicon carbide (SiC), and consist of many parallel channels, usually between 200–400 cpsi (cells per square inch) with 0.004–0.012 mil (100–300 µm) thick walls [27–29]. A catalyst coating is applied to the channel walls of the monolith substrate. Figure 1.7 illustrates the monolith substrate and an axial view of a coated monolith substrate.

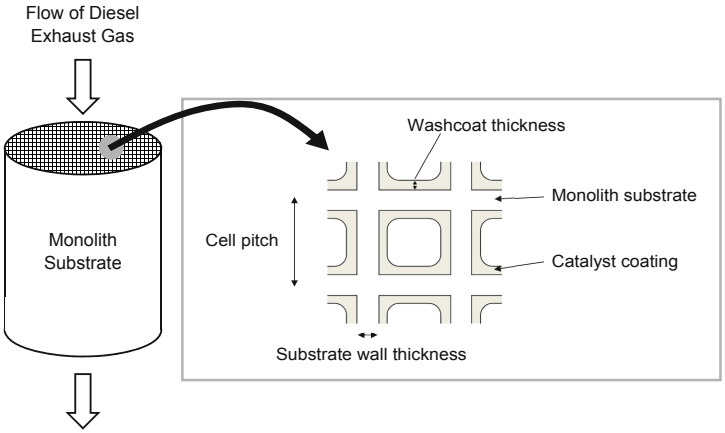

Figure 1.7: *Sketch of diesel exhaust gas flowing through a coated monolith substrate with illustration of catalyst coated monolith channels [30].*

A state-of-the-art diesel exhaust aftertreatment system contains at least four basic catalytic elements, namely, a diesel oxidation catalyst (DOC), a diesel particulate filter (DPF), a catalyst for the selective catalytic reduction of NO_x with ammonia (NH_3-SCR), and an ammonia slip catalyst (ASC). Furthermore, the ammonia is supplied as an aqueous solution of urea, which is injected in the exhaust gas stream in controlled amounts by a control unit. The arrangement of these elements can be different, but a common arrangement is shown in Figure 1.8A. A brief description of the catalytic elements is given below.

Diesel Oxidation Catalyst (DOC): The function of the DOC is to oxidize all unburnt fuel and CO to H_2O and CO_2. It also oxidizes NO to NO_2, which is beneficial to the oxidation of soot needed for regeneration of the DPF, and for the reduction of NO_x. This catalyst consists mainly of supported particles of Pt and Pd, and is close-coupled to the engine exhaust [6, 8, 31].

Diesel Particulate Filter (DPF): The particulate matter is filtered out of the exhaust gas using a wall-flow filter. The wall-flow filter is a monolith substrate where adjacent channels are alternately plugged at each end, which forces the exhaust gas through the porous monolith walls, as illustrated in Figure 1.8B [5, 32]. During operation, the particles accumulate in the walls of the filter. This causes

an increase in the pressure drop across the DPF, and consequently, the filter must be regenerated [6, 32]. The DPF regeneration is done by burning off the accumulated soot particles. Filter regeneration can either be done actively (periodically) or passively (continuously) [6, 32, 33]. Active regeneration is done by injecting extra fuel to increase the exhaust gas temperature to above 600°C, at which point soot is rapidly oxidized by O_2 [6, 33]. Passive regeneration relies on the ability of NO_2 to oxidize soot at normal operating conditions and temperatures (300–400°C) of the exhaust system [6, 33, 34]. If sufficient NO_2 is produced, the accumulation of soot in the filter can be balanced continuously by the rate of soot oxidation with NO_2, without a net accumulation of soot over time [6]. The NO_2 needed for passive regeneration can be generated in the DOC. Alternatively, a catalyzed diesel particulate filter (cDPF), in which the filter walls are impregnated with a catalyst (e.g. Pt), can be used to generate the necessary NO_2 for soot oxidation [6, 33, 35].

Control Unit for Urea Dosage: The control unit applies principals of process regulation and tailpipe measurements of NH_3 and/or NO_x concentrations to dose an aqueous solution of urea ($CO(NH_2)_2$) into the hot exhaust gas [36]. The water evaporates and urea thermally decomposes, via the formation and subsequent hydrolysis of isocyanic acid, to two molecules of NH_3. The resulting NH_3 is used as the reducing agent in the selective catalytic reduction of NO_x to N_2 and H_2O [36, 37].

Selective Catalytic Reduction (SCR) of NO_x: The selective catalytic reduction of NO_x with NH_3 and O_2 (NH_3-SCR) to N_2 and H_2O is used to remove NO_x from the exhaust gas. The SCR reactions are commonly catalyzed by V_2O_5-WO_3/TiO_2, Cu-zeolites, or Fe-zeolites [6, 38, 39]. Usually, a slight stoichiometric excess of NH_3 between 10–20% is used, since the SCR reaction becomes more efficient under these conditions, but this also results in an NH_3 slip from the SCR catalyst [36, 38]. A mixture of NO with some NO_2, generated upstream in the DOC or cDPF, also increases the rate of the NH_3-SCR reactions [6, 38, 39].

Ammonia Slip Catalyst (ASC): The excess NH_3 in the exhaust gas is removed by selective catalytic oxidation (SCO) with oxygen to N_2 and H_2O. The ASC commonly uses a Pt-based catalyst to provide the ammonia oxidation (AMOX) activity, combined with an NH_3-SCR catalyst to increase N_2 selectivity [6, 38, 40].

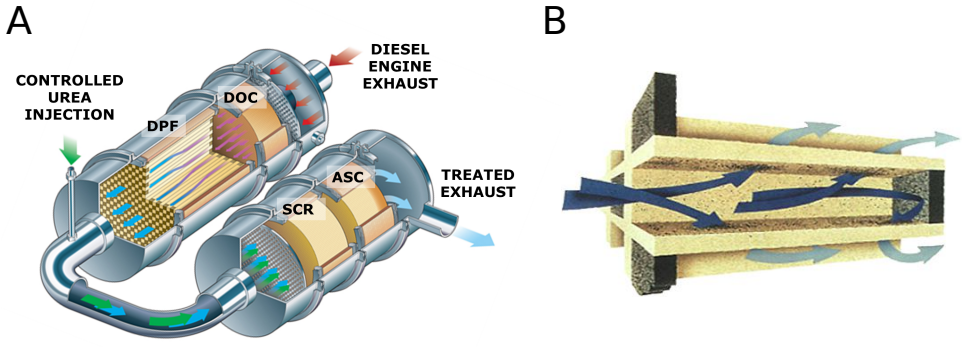

Figure 1.8: *A) A state-of-the-art diesel exhaust aftertreament system [6]. B) Illustration of the wall-flow filter used for the Diesel Particulate Filter [29].*

A summary of the units of the diesel exhaust aftertreatment system is presented in Figure 1.9, together with histograms illustrating the relative concentrations of regulated emissions at the points indicated by arrows, as the exhaust gas passes through the aftertreatment system.

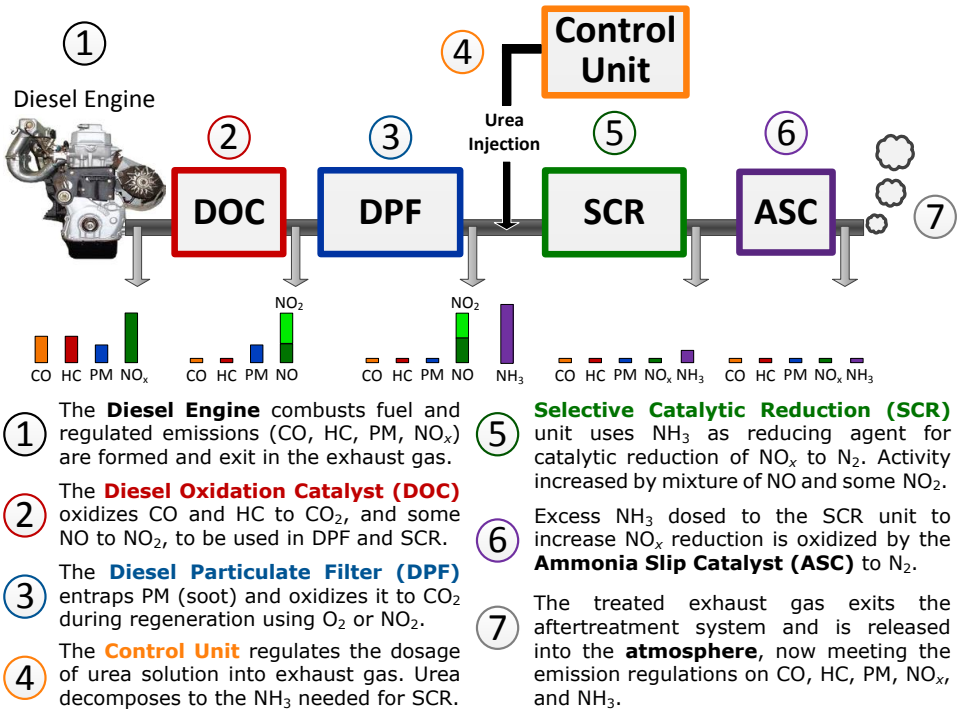

Figure 1.9: *Summary of a typical state-of-the-art diesel exhaust aftertreatment system [41]. The histograms illustrate the relative concentrations of the regulated emissions at the points indicated by the arrows, as the exhaust gas passes through the aftertreatment system.*

The continued development of the diesel exhaust aftertreatment system is focused on challenges related to meeting future emission regulations while also maintaining or reducing costs [42, 43].

In order to meet emission regulations, the developed catalyst systems must be effective at treating harmful emissions under a broad range of conditions corresponding to different driving conditions, such as cold-start situations where the aftertreatment system is initially cold, stop-and-go driving associated with city driving, and more stationary conditions resembling highway cruising [6, 44–46]. The exhaust gas properties are dependent on the engine load and will vary with respect to concentrations of pollutants and main constituents, volumetric gas flows, and exhaust gas temperatures [7, 13]. The temperature is an important parameter since the exhaust gas is used to heat up the catalysts to the temperatures necessary to obtain sufficient catalyst activity (>200°C) [42]. The exhaust gas temperature generally lies in the range of 200–500°C for normal operation, but is lower during the first few minutes after a cold start and can increase to 600–800°C under conditions associated with active regeneration of the DPF [6–8, 33]. However, future improvements

in fuel economy will likely entail a decrease in exhaust gas temperature and require development of catalysts that are sufficiently active already at 150°C [6, 42].

In addition to meeting emission regulations, vehicle manufacturers are also interested reducing system and operating costs, for example by lowering the loading of noble metals in the catalyst or application of zeolite SCR catalysts [31, 43, 47]. Furthermore, a low system mass can facilitate a swifter heat-up and help avoid penalties in the fuel economy, while compact systems are needed to meet volume restrictions on the truck [6, 7, 26, 42, 47, 48]. The catalyst systems must also be durable and stable, withstanding thermal deactivation and possible catalyst poisoning, in particular poisoning by SO_2 [43].

1.2 Project Objectives

This Ph.D. project was part of the project entitled *Next Generation Exhaust Gas Cleaning Technologies for Diesel Vehicles (NEXT)*. It has been the focus of the *NEXT* project to develop new and improved technologies for catalytic exhaust gas cleaning from heavy duty diesel vehicles, with the overall goals of reducing emissions, cost, and space requirements.

The focus of this Ph.D. project has been the development of the diesel oxidation catalyst and the ammonia slip catalyst for the diesel exhaust aftertreatment system. The *NEXT* project objectives translate to the development objectives specified in the following sections for the diesel oxidation catalyst and the ammonia slip catalyst.

1.2.1 Development Objectives for the Diesel Oxidation Catalyst

Current diesel oxidation catalysts used for the oxidation of CO, hydrocarbons, and NO are based on expensive noble metals such as Pt and Pd, resulting in a high unit price of the catalytic unit. It was therefore a general project objective to develop a diesel oxidation catalyst with a reduced dependence on noble metals while retaining a low temperature activity for oxidation of CO, hydrocarbons, and NO. This was to be achieved through the following objectives:

- Maximize noble metal utilization by identifying the optimal particle size for CO, HC and NO oxidation.
- Improve fundamental knowledge of mechanisms behind the optimal noble metal particle size.

1.2.2 Development Objectives for the Ammonia Slip Catalyst

Current ammonia slip catalysts used for the oxidation of NH_3 to N_2 and H_2O rely on a combination of an NH_3 oxidation catalyst and an SCR catalyst. The NH_3 oxidation catalyst is usually based on Pt, which oxidizes NH_3 to N_2, NO_x, and N_2O. The SCR catalyst then reduces the NO_x formed to N_2 and H_2O through the SCR reactions with leftover NH_3. It was therefore a general project objective to develop ammonia slip catalysts for efficient removal of excess NH_3 with a focus on new catalyst formulations (ideally less dependent on noble metals) and reactor configurations. This was to be achieved through the following objectives:

- Develop a mathematical model for the ammonia slip catalyst, including the kinetic models for the ammonia oxidation catalyst and the selective catalytic reduction catalyst, including obtaining the necessary kinetic data.
- Investigate the concept of using dual layer ASC catalysts, with different configurations of oxidation and SCR catalysts.
- Improve understanding of the key design parameters of the ASC for obtaining a high conversion of NH_3 combined with a high N_2 selectivity.

1.3 Structure of Ph.D. Thesis

This Ph.D. thesis reports the research conducted to develop the diesel oxidation catalyst and the ammonia slip catalyst, with each chapter written in a manner that it can be read by itself. There is therefore some inevitable overlap of information. The final chapter of the thesis reflects on the research conducted and presents considerations for further work. A short description of the contents of each chapter is given hereafter:

Chapter 2 - The Effect of the Pt Particle Size on the Oxidation of CO, C_3H_6, and NO over Pt/Al_2O_3:

The significance of controlling the Pt particle size was investigated for the 1 wt.% Pt/Al_2O_3 catalyst. This was done with the aim of identifying the Pt particle size corresponding to the highest mass based rate of reaction, in order to decrease the necessary Pt loading. Catalysts were prepared by wetness impregnation and characterized using CO chemisorption and transmission electron microscopy. The catalyst performance was evaluated using fixed bed reactors.

Chapter 3 - NH_3 Oxidation over Pt, Rh, and Pd Supported on Al_2O_3 and the Effect of the Pt Particle Size:

The oxidation of NH_3 over Pt, Pd, and Rh supported on Al_2O_3 is investigated using commercial catalysts. The effect of Pt particle size on the activity and product selectivity for NH_3 oxidation over 1 wt.% Pt/Al_2O_3 catalysts was investigated using the catalysts prepared and characterized in Chapter 2, along with a Pt/Al_2O_3 catalyst prepared by mechanical mixing. The catalyst performance was evaluated using fixed bed reactors.

Chapter 4 - Monolith Model for the Ammonia Slip Catalyst:

The model developed for the monolithic ammonia slip catalyst is presented, including the kinetic models for the ammonia oxidation catalyst and the selective catalytic reduction catalyst. The model is validated against experimental data for small monolithic catalysts of different ASC configurations.

Chapter 5 - Model Analysis of the Ammonia Slip Catalyst:

The validated model for the monolithic ammonia slip catalyst (from Chapter 4) is used to analyze the performance sensitivity of the ammonia slip catalyst to variations in design parameters. Pareto fronts generated from

multi-objective optimization of ten possible catalyst configurations for dual mixed layer system are used to evaluate the performance sensitivity to the ASC configuration.

Chapter 6 - Further Work:

Based on the research conducted and results achieved, research questions which merit further work are presented. Topics concern the diesel oxidation catalyst, the ammonia oxidation catalyst, and the ammonia slip catalyst.

1.4 Publications and Conference Contributions

International Peer-Reviewed Journals

Thomas Klint Hansen, Brian Brun Hansen, Peter N.R. Vennestrøm, Ton V.W. Janssens, and Anker Degn Jensen: "Modelling and Optimization of Multi-functional Ammonia Slip Catalysts for Diesel Exhaust Aftertreatment". *In preparation to be submitted.*

Thomas Klint Hansen, Martin Høj, Brian Brun Hansen, Ton V.W. Janssens, and Anker Degn Jensen: "The Effect of Pt Particle Size on the Oxidation of CO, C_3H_6, and NO over Pt/Al_2O_3 for Diesel Exhaust Aftertreatment", *Accepted for publication in Topics in Catalysis.*

Oral Conference Contributions

Thomas Klint Hansen, Thomas Guldbrand Andersen, Martin Høj, Brian Brun Hansen, Ton V.W. Janssens, Jakob Munkholt Christensen, and **Anker Degn Jensen**: "The Effect of Pt Particle Size on the Oxidation of NH_3 over Pt/Al_2O_3 for Diesel Exhaust Aftertreatment". Presented at: The 13th European Congress on Catalysis (EUROPACAT), 2017, Florence, Italy.

Thomas Klint Hansen, Brian Brun Hansen, Peter N.R. Vennestrøm, Ton V.W. Janssens, and **Anker Degn Jensen**: "Modeling and Optimization of a Dual Layer Ammonia Slip Catalyst for Diesel Exhaust Aftertreatment". Presented at: The 2nd International Symposium on Catalytic Science and Technology in Sustainable Energy and Environment (EECAT), 2016, Tianjin, China.

Thomas Klint Hansen, Brian Brun Hansen, Ton V.W. Janssens, and Anker Degn Jensen: "Modeling and Optimization of a Dual Layer Ammonia Slip Catalyst for Diesel Exhaust Aftertreatment". Presented at: The 16th International Congress on Catalysis (ICC), 2016, Beijing, China.

Thomas Klint Hansen, Brian Brun Hansen, Ton V.W. Janssens, and Anker Degn Jensen: "Modeling and Optimization of a Dual Layer Ammonia Slip Catalyst for Diesel Exhaust Aftertreatment". Presented at: The 17th Nordic Symposium on Catalysis (NSC), 2016, Lund, Sweden.

Thomas Klint Hansen, Martin Høj, Brian Brun Hansen, Ton V.W. Janssens, and Anker Degn Jensen: "Influence of Pt Particle Size on CO, C_3H_6, and NO Oxidation over Pt/Al_2O_3". Presented at: The 17th Nordic Symposium on Catalysis (NSC), 2016, Lund, Sweden.

Poster Conference Contributions

Thomas Klint Hansen, Brian Brun Hansen, Ton V.W. Janssens, and Anker Degn Jensen. "Modelling of Dual Layer Ammonia Slip Catalyst for Diesel Exhaust Aftertreatment" Presented at: 4th International Symposium on Modeling of Exhaust-Gas After-Treatment (MODEGAT), 2015, Karlsruhe, Germany.

Thomas Klint Hansen, Brian Brun Hansen, Ton V.W. Janssens, and Anker Degn Jensen. "Correlation between NO Reduction and N_2O Formation during Standard SCR over Cu-BEA". Presented at: 24th North American Catalysis Meeting (NAM), 2015 , Pittsburgh, United States of America.

Thomas Klint Hansen, Brian Brun Hansen, Ton V.W. Janssens, and Anker Degn Jensen. "Dual Layer Ammonia Slip Catalyst for Diesel Exhaust Aftertreatment". Presented at: 1st EFCATS-CNRS European Summer School on Catalyst Preparation, 2014, Vogüé, France.

1.5 Supervision of Student Projects

Thomas Guldbrand Andersen, Bachelor's thesis: "Study of Noble Metal Based NH_3 Oxidation Catalysts for Diesel Exhaust Aftertreatment", February, 2017.

Henrik Teglborg, Master's thesis: "Development of Alternative Diesel Oxidation Catalyst Formulations", January, 2016.

Rikke Bjerregaard, Master's thesis: "Synthesis and Testing of Alternative Diesel Oxidation Catalyst Formulations", February, 2015.

Rune Falck Damborg, Master's thesis: "Catalytic Oxidation of CO and C_3H_6 under Diesel Exhaust Conditions", September, 2014.

Martin Møller Hansen, Bachelor's thesis: "Kinetic Modeling of the SCR Component of a Dual Layer Ammonia Slip Catalyst", March, 2014.

1.6 References

[1] H. Jääskeläinen. Early History of the Diesel Engine. In *DieselNet Technology Guide*. Ecopoint Inc., 2013. Online. `https://dieselnet.com/tech/diesel_history.php` Accessed: February 27th, 2017.

[2] H. Jääskeläinen and M.K. Khair. Engine Fundamentals. In *DieselNet Technology Guide*. Ecopoint Inc., 2014. Online. `https://dieselnet.com/tech/diesel_fundamentals.php` Accessed: February 27th, 2017.

[3] H. Jääskeläinen and M. K. Khair. Diesel Engines. In *DieselNet Technology Guide*. Ecopoint Inc., 2013. Online. `https://dieselnet.com/tech/diesel_engines.php` Accessed: February 27th, 2017.

[4] W.A. Majewski and H. Jääskeläinen. Environmental Effects of Emissions. In *DieselNet Technology Guide*. Ecopoint Inc., 2004. Online. `https://dieselnet.com/tech/env_effect.php` Accessed: March 1st, 2017.

[5] J. Kašpar, P. Fornasiero, and N. Hickey. Automotive Catalytic Converters: Current Status and Some Perspectives. *Catalysis Today*, 77:419–449, 2003.

[6] A. Walker. Future Challenges and Incoming Solutions in Emission Control for Heavy Duty Diesel Vehicles. *Topics in Catalysis*, 59:695–707, 2016.

[7] H. Jääskeläinen. Diesel Exhaust Gas. In *DieselNet Technology Guide*. Ecopoint Inc., 2011. Online. `https://www.dieselnet.com/tech/diesel_exh.php` Accessed: August 9th, 2016.

[8] A. Russell and W.S. Epling. Diesel Oxidation Catalysts. *Catalysis Reviews: Science and Engineering*, 53(4):337–423, 2011.

[9] W.A. Majewski and H. Jääskeläinen. What is Diesel Fuel. In *DieselNet Technology Guide*. Ecopoint Inc., 2016. Online. `https://dieselnet.com/tech/fuel_diesel.php` Accessed: February 28th, 2017.

[10] W.A. Majewski. What Are Diesel Emissions. In *DieselNet Technology Guide*. Ecopoint Inc., 2012. Online. `https://dieselnet.com/tech/emi_intro.php` Accessed: February 28th, 2017.

[11] M.K. Khair and H. Jääskeläinen. Emission Formation in Diesel Engines. In *DieselNet Technology Guide*. Ecopoint Inc., 2015. Online. `https://dieselnet.com/tech/diesel_emiform.php` Accessed: February 28th, 2017.

[12] H. Tschoeke, A. Graf, J. Stein, M. Krüger, J. Schaller, N. Breuer, K. Engeljehringer, and W. Schindler. *Handbook of Diesel Engines, Diesel Engine Exhaust Emissions*, chapter 15. Springer, 2010.

[13] Gaseous Emissions. In *DieselNet Technology Guide*. Ecopoint Inc., 2010. Online. `https://dieselnet.com/tech/emi_gas.php` Accessed: March 1st, 2017.

[14] Diesel Emission Inventory. In *DieselNet Technology Guide*. Ecopoint Inc., 2001. Online. `https://dieselnet.com/tech/env_inv.php` Accessed: March 2nd, 2017.

[15] W.A. Majewski. Diesel Particulate Matter. In *DieselNet Technology Guide*. Ecopoint Inc., 2016. Online. `https://dieselnet.com/tech/dpm.php` Accessed: March 1st, 2017.

[16] Health and Environmental Effects. In *DieselNet Technology Guide*. Ecopoint Inc., 2012. Online. `https://dieselnet.com/tech/env_top.php` Accessed: February 28th, 2017.

[17] Health Effects of Gas Phase Components. In *DieselNet Technology Guide*. Ecopoint Inc., 1999. Online. https://dieselnet.com/tech/health_gas.php Accessed: March 1st, 2017.

[18] European Union Emission Inventory Report 1990–2014 under the UNECE Convention on Long-range Transboundary Air Pollution (LRTAP). Technical Report 16, European Environment Agency, 2016.

[19] United States Environmental Protection Agency. 2014 National Emissions Inventory (NEI) Data. Online. https://www.epa.gov/air-emissions-inventories/2014-national-emissions-inventory-nei-data Accessed: February 28th, 2017, February 2017.

[20] O. Nielsen, M.S. Plejdrup, M. Winther, M. Nielsen, S. Gyldenkærne, M.H. Mikkelsen, R. Albrektsen, M. Thomsen, K. Hjelgaard, P. Fauser, H.G. Bruun, V.K. Johannsen, T. Nord-Larsen, L. Vesterdal, I. Callesen, E. Schou, K. Suadicani, E. Rasmussen, S.B. Petersen, L. Baunbæk, and M.G. Hansen. Denmarks's National Inventory Report 2015 and 2016. Technical Report 189, Danish Centre for Environment and Energy, 2016.

[21] EU. Commision Regulation (EU) No 582/2011. *Official Journal of the European Union*, 25.6.(L 182):1–168, 2011.

[22] W.A. Majewski. Diesel Emission Control. In *DieselNet Technology Guide*. Ecopoint Inc., 2014. Online. https://dieselnet.com/tech/engine_control.php Accessed: February 28th, 2017.

[23] EU: Heavy-Duty Truck and Bus Engines. In *DieselNet Technology Guide*. Ecopoint Inc., 2015. Online. https://dieselnet.com/tech/engine_design.php Accessed: March 5th, 2017.

[24] H. Jääskeläinen and W.A. Majewski. Engine Technology Evolution: Heavy-Duty Diesels. In *DieselNet Technology Guide*. Ecopoint Inc., 2014. Online. https://dieselnet.com/tech/engine_heavy-duty.php Accessed: March 6th, 2017.

[25] W.A. Majewski and H. Jääskeläinen. Engine Design for Low Emissions. In *DieselNet Technology Guide*. Ecopoint Inc., 2015. Online. https://dieselnet.com/tech/engine_design.php Accessed: March 5th, 2017.

[26] H. Jääskeläinen and W.A. Majewski. Heavy-Duty Diesel Engines with Aftertreatment. In *DieselNet Technology Guide*. Ecopoint Inc., 2016. Online. https://dieselnet.com/tech/engine_heavy-duty_aftertreatment.php Accessed: March 6th, 2017.

[27] Ceramic Catalyst Substrates. In *DieselNet Technology Guide*. Ecopoint Inc., 2011. Online. https://www.dieselnet.com/tech/cat_subs_cer.php Accessed: March 7th, 2017.

[28] W.A. Majewski. Metallic Catalyst Substrates. In *DieselNet Technology Guide*. Ecopoint Inc., 2015. Online. https://www.dieselnet.com/tech/cat_subs_met.php Accessed: March 7th, 2017.

[29] W.A. Majewski. Wall-Flow Monoliths. In *DieselNet Technology Guide*. Ecopoint Inc., 2005. Online. `https://www.dieselnet.com/tech/dpf_wall-flow.php` Accessed: March 7th, 2017.

[30] J. Jansson. *Urea-SCR Technology for deNOx After Treatment of Diesel Exhausts*, chapter 3 Vandia-Based Catalysts for Mobile SCR. Springer Science+Business Media, 2014.

[31] W.A. Majewski. Diesel Oxidation Catalyst. In *DieselNet Technology Guide*. Ecopoint Inc., 2012. Online. `https://dieselnet.com/tech/cat_doc.php` Accessed: February 28th, 2017.

[32] W.A. Majewski. Diesel Particulate Filters. In *DieselNet Technology Guide*. Ecopoint Inc., 2011. Online. `https://dieselnet.com/tech/dpf.php` Accessed: March 8th, 2017.

[33] W.A. Majewski. Diesel Filter Regeneration. In *DieselNet Technology Guide*. Ecopoint Inc., 2005. Online. `https://dieselnet.com/tech/dpf_regen.php` Accessed: March 8th, 2017.

[34] Catalyzed Diesel Filters. In *DieselNet Technology Guide*. Ecopoint Inc., 2005. Online. `https://www.dieselnet.com/tech/dpf_cat.php` Accessed: June 1st, 2013.

[35] Diesel Filter Systems. In *DieselNet Technology Guide*. Ecopoint Inc., 2005. Online. `https://www.dieselnet.com/tech/dpf_sys.php` Accessed: June 1st, 2013.

[36] H. Jääskeläinen and W.A. Majewski. Urea Dosing Control. In *DieselNet Technology Guide*. Ecopoint Inc., 2015. Online. `https://dieselnet.com/tech/cat_scr_mobile_control.php` Accessed: March 8th, 2017.

[37] W.A. Majewski. Urea Dosing and Injection Systems. In *DieselNet Technology Guide*. Ecopoint Inc., 2015. Online. `https://dieselnet.com/tech/cat_scr_mobile_urea_dosing.php` Accessed: March 8th, 2017.

[38] W.A. Majewski. Selective Catalytic Reduction. In *DieselNet Technology Guide*. Ecopoint Inc., 2005. Online. `https://dieselnet.com/tech/cat_scr.php` Accessed: March 8th, 2017.

[39] T.V.W. Janssens, H. Falsig, L.F. Lundegaard, P.N.R. Vennestrøm, S.B. Rasmussen, P.G. Moses, F. Giordanino, E. Borfecchia, K.A. Lomachenko, C. Lamberti, S. Bordiga, A. Godiksen, S. Mossin, and P. Beato. A Consistent Reaction Scheme for the Selective Catalytic Reduction of Nitrogen Oxides with Ammonia. *ACS Catalysis Research*, 5:2832–2845, 2015.

[40] S. Shrestha, M.P. Harold, K. Kamasamudram, A. Kumar, L. Olsson, and K. Leistner. Selective Oxidation of Ammonia to Nitrogen on Bi-functional Cu–SSZ-13 and Pt/Al_2O_3 Monolith Csatalyst. *Catalysis Today*, 267:130–144, 2016.

[41] K. Johansen. Multi-Catalytic Soot Filtration in Automotive and Marine Applications. *Catalysis Today*, 258:2–10, 2015.

[42] M. Zammit, C. DiMaggio, C. Kim, C. Lambert, G. Muntean, C. Peden, J. Parks, and K. Howden. Future Automotive Aftertreatment Solutions: The 150°C Challenge Workshop Report. Technical report, Pacific Northwest National Laboratory, 2012.

[43] W.A. Majewski. Diesel Catalysts. In *DieselNet Technology Guide*. Ecopoint Inc., 2016. Online. `https://dieselnet.com/tech/cat_diesel.php` Accessed: March 8th, 2017.

[44] World Harmonized Vehicle Cycle (WHVC). In *DieselNet Technology Guide*. Ecopoint Inc., 2015. Online. `https://dieselnet.com/standards/cycles/whvc.php` Accessed: March 14th, 2017.

[45] World Harmonized Stationary Cycle (WHSC). In *DieselNet Technology Guide*. Ecopoint Inc., 2008. Online. `https://dieselnet.com/standards/cycles/whsc.php` Accessed: March 14th, 2017.

[46] World Harmonized Transient Cycle (WHTC). In *DieselNet Technology Guide*. Ecopoint Inc., 2007. Online. `https://dieselnet.com/standards/cycles/whtc.php` Accessed: March 14th, 2017.

[47] W.A. Majewski. Commercial DOC Technologies. In *DieselNet Technology Guide*. Ecopoint Inc., 2011. Online. `https://dieselnet.com/tech/cat_pm.php` Accessed: March 13th, 2017.

[48] W.A. Majewski. SCR Systems for Mobile Engines. In *DieselNet Technology Guide*. Ecopoint Inc., 2005. Online. `https://dieselnet.com/tech/cat_scr_mobile.php` Accessed: March 15th, 2017.

CHAPTER 2

The Effect of the Pt Particle Size on the Oxidation of CO, C_3H_6, and NO over Pt/Al_2O_3

Platinum-based oxidation catalysts applied for diesel exhaust aftertreatment constitute a significant part of system costs. Effective utilization of platinum is therefore relevant to reduce costs while retaining performance. To this end, the influence of Pt particle size on catalytic activity for CO, hydrocarbon, and NO oxidation was studied. 1 wt.% Pt/Al_2O_3 catalysts were prepared by wet impregnation, drying, and different calcination and thermal treatments, yielding Pt particles with diameters between 1.3 and 18.7 nm, as determined by CO pulse titration and transmission electron microscopy. Activity measurements for CO, C_3H_6 (hydrocarbon representative), and NO oxidation showed an optimal Pt particle size with respect to the mass based activity between 2–4 nm for all three reactions. From measured turnover frequencies and site statistics of Pt particles, the reactions appear to be mainly catalyzed by terrace atoms, which are most abundant between 2–4 nm. The decrease in catalytic activity for larger Pt particles is therefore due to the diminishing Pt surface area, while the decrease in activity for smaller Pt particles is due to the decline in number of available terrace atoms required for CO, HC, and NO oxidation.

2.1 Introduction

In order to comply with strict emission control regulations [1, 2], modern diesel-driven vehicles are equipped with a catalytic exhaust aftertreatment system to reduce the emission of harmful compounds [3]. The main harmful compounds in a diesel exhaust gas are particulate matter (soot particles), NO_x, CO, and unburnt hydrocarbons (HC), which are converted to CO_2, H_2O, and N_2 in the aftertreatment system [3]. To achieve this, a modern aftertreatment system typically consists of a diesel oxidation catalyst (DOC), a diesel particulate filter (DPF) and a catalytic NO_x abatement unit further downstream, which consists of a catalyst for the selective catalytic reduction with NH_3 (NH_3-SCR) combined with an ammonia slip catalyst (ASC) for oxidation for residual NH_3 (see Figure 2.1).

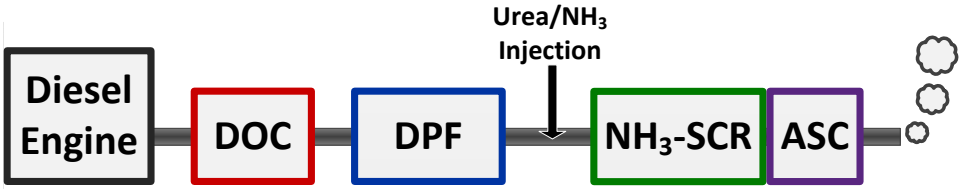

Figure 2.1: *Diagram of a typical diesel exhaust aftertreatment system consisting of a diesel oxidation catalyst (DOC), a diesel particulate filter (DPF), the injection of urea or NH3, a catalyst for the selective catalytic reduction of NO_x with NH_3 (NH_3-SCR), and an ammonia slip catalyst (ASC).*

The temperature in the exhaust gas varies, depending on the driving load, but generally lies in the range 200–500°C [3–5]. The combination of a high exhaust gas flow (500–1500 m^3/h) [4] and a limited space for catalysts requires a good catalyst performance at high space velocities while maintaining a low pressure drop at any operating temperature. This is achieved by using catalysts coated on monolith substrates [6]. Furthermore, diesel fuel contains sulfur compounds that when combusted lead to SO_x in the exhaust gas, which can poison and deactivate catalysts during operation [5, 7].

The main purpose of the DPF is to capture the soot particles produced in the engine. A common type of filter is the wall-flow filter, in which the exhaust gas is forced through the walls of a monolith, whereby the soot particles are retained [3, 5]. The amount of soot accumulated in the filter increases with time, which results in an undesired pressure drop. Therefore, some regeneration of the filter is required. One method to do this is active regeneration, which entails periodically raising the temperature to above 600°C by injection of post engine fuel, which causes the soot to burn in the oxygen of the exhaust gas [3, 5]. An alternative method is passive regeneration, in which the temperature for soot oxidation is lowered to the normal operating temperature range (350–500°C), which makes a continuous soot oxidation under normal operation possible. To this end, a catalyst for soot oxidation can be applied to the DPF, or NO_2 generated in the DOC can be used for the removal of soot [3, 5].

The NO_x abatement system consists of a catalyst for the selective catalytic reduction with NH_3 (NH_3-SCR) combined with an ammonia slip catalyst (ASC) [3]. In the SCR reactions, NO_x is converted by ammonia and oxygen to N_2 and

H_2O, with high selectivity [3, 5, 8]. The ammonia is usually provided by injection of urea at the inlet to the SCR unit. In practice, a 5–10% excess of ammonia is used in the NH_3-SCR to improve the performance [8], and the ASC removes the excess ammonia by selective oxidation of ammonia with oxygen to N_2 and water [9]. The presence of NO_2, up to a NO_2/NO_x ratio of 0.5, can also improve the SCR performance, as it allows for the fast-SCR reaction to occur [5, 8].

The DOC removes CO and unburnt hydrocarbons in the exhaust gas by oxidation to CO_2 and H_2O. Additionally, the DOC is used to oxidize NO to NO_2, which, as mentioned above, may improve SCR performance and enhance the regeneration of the DPF in systems using passive regeneration [3, 5, 7]. DOC formulations are usually based on Pt supported on metal oxides [5, 7]. Pt is also less sensitive to sulfur, compared to other noble metals and metal oxides [5, 7], making the catalysts robust in environments with small amounts of SO_2 and SO_3. To improve the thermal stability of the DOC and reduce cost, some of the Pt can be replaced by Pd, although Pd is significantly less tolerant to sulfur [5, 7].

The support materials used in a DOC are common metal oxides, such as Al_2O_3, SiO_2, CeO_2, TiO_2, ZrO_2, zeolites, or a combination of these [5]. A common support material is γ-Al_2O_3, due to its high surface area (100–200 m^2/g) and good thermal stability [5]. Therefore, Pt/Al_2O_3 is a good model catalyst for a DOC, and has been used in many studies on Pt catalysts [5, 10–45].

A focus area for DOC development is the improvement of low temperature catalytic activity [5, 10, 46]. This is relevant due to the development of more fuel-efficient engines, which result in lower exhaust gas temperatures. In addition, a good low temperature activity also helps reduce the emissions during cold start of the engine, which account for a significant part of the total emissions [3, 4].

Another development of the DOC is aimed at cost reduction, either by replacement of the noble metal with cheaper materials or by a more effective use of the noble metals, allowing for a significant reduction of the noble metal content [5, 11, 46]. High catalytic activity and cost-effective utilization of metals is generally associated with small particles (high dispersion) of the active phase [5, 12, 13]. However, small Pt particles show a low turnover frequency (TOF) for CO oxidation [12, 47, 48], HC oxidation [13–18], and NO oxidation [12, 19, 20] in studies with a large excess of oxygen relative to reactants, similar to conditions in diesel exhaust aftertreatment, e.g. 10 vol.% O_2, 5 vol.% H_2O, 1000 ppm NO_x, 300 ppm HC, 1000 ppm CO [49]. As a result, an optimum in Pt particle size exists, with a corresponding maximum in catalytic activity.

To our knowledge, no studies investigate the influence of Pt particle size on the oxidation of CO, HC, and NO, relevant for the diesel oxidation catalyst, over the same catalysts. Furthermore, few studies include H_2O in the feed gas, which is present in diesel exhaust gas (2–12 vol.% H_2O) and promotes CO oxidation while inhibiting both HC and NO oxidation [7, 21–23]. It was therefore the purpose of this work to investigate the effect of Pt particle size for all three oxidation reactions relevant for the DOC (CO, HC, and NO) under diesel exhaust gas conditions, and identify the respective optimal Pt particle sizes over broad range of average Pt particle diameters (between 1.3–18.7 nm). The feed gas for activity measurements contained either 2.8 or 7.8 vol.% water vapor and about 10 vol.% O_2 in order to better emulate the catalytic activity under diesel exhaust gas conditions. We show that the oxidation of CO, C_3H_6, and NO all exhibit the same optimum Pt particle

size range and that the high mass based catalytic activity does not necessarily coincide with the maximum TOF. We relate these observations to the change in abundance of corner, edge, and terrace atoms.

2.2 Experimental

2.2.1 Catalyst Preparation

To prepare Pt/Al_2O_3 catalysts with different Pt particle sizes, two batches of alumina were impregnated with 1 wt.% Pt and dried. The batches were then split into smaller portions before being calcined and thermally treated with different temperatures, gas atmospheres, and durations (see Table 2.1) in order to obtain a series of nine catalysts with different Pt particle sizes in the range 1.3 to 18.7 nm.

For the impregnations, 3 g or 10 g of γ-Al_2O_3 support material (Puralox NWa-155; Sasol; surface area 153.7 m^2/g) was suspended in an aqueous solution (20 mL solution/g γ-Al_2O_3) of 2.59 mM $H_2PtCl_6{\cdot}6\,H_2O$ (ACS reagent; Sigma-Aldrich) under stirring at 50°C in an open beaker [48]. The water evaporated overnight and a dry solid sample remained. The samples were dried further in a horizontal tube furnace (ETF 30-50/15-S; Entech) in 3 NL N_2/min at 80°C for 4 hrs. Subsequent calcination and thermal treatments were done in the same horizontal tube furnace. From the first batch of 3 g, two portions of 1 g each were given the oxidative calcination treatments (O_2/N_2 or $H_2O/O_2/N_2$) presented in Table 2.1, yielding samples A and B. The entire second batch of 10 g was calcined in a 3 NL/min flow of N_2 at 550°C for 8 hrs and a 1 g portion was taken as sample C. Six 1 g portions of the remaining batch were then exposed to the different thermal treatments presented in Table 2.1, yielding samples D to I. The use of a chlorine Pt precursor can lead to residual chlorine after calcination that can inhibit catalytic activity [50, 51], but the calcination and thermal treatments applied in this study, together with the presence of H_2O in the reactor feed (Section 2.2.2.2), will effectively remove chlorine [50, 51]. Additionally, a commercial 1 wt.% Pt/Al_2O_3 powder catalyst (205966; Sigma-Aldrich) was used as a benchmark in both fresh, SA1, and thermally treated states, SA2. The properties and thermal treatment of the benchmark catalysts are also presented in Table 2.1. Table 2.1 presents an overview of the eleven catalysts studied, indicating their calcination and thermal treatments, as well as the resulting Pt dispersion and average Pt particle diameter calculated from the CO adsorption capacity and verified by TEM (Section 2.2.2.1).

The Pt contents of samples A, D, and SA1 were determined by inductively coupled plasma optical emissions spectrometry (ICP-OES), and were assumed to be representative of each respective batch. The Pt contents of the three batches were very similar with 0.94 wt.% Pt for the first batch (samples A and B), 0.98 wt.% Pt for the second batch (samples C to I), and 0.92 wt.% Pt for the commercial catalyst (samples SA1 and SA2). These Pt contents were used for subsequent calculations. The eleven catalyst samples were tableted, crushed, and sieved to a fraction of 150–300 µm before further characterization and testing.

Table 2.1: *Overview of catalysts prepared. Catalysts from the first batch (A–B) were given oxidative calcinations at 550°C for 8 hours, and no further thermal treatment. Catalysts from the second batch (C–I) were all initially calcined in a flow of N_2 at 550°C for 8 hours, and most samples (D–I) were subsequently given thermal treatments with different temperatures, atmospheres, and durations. 1 wt.% Pt/Al_2O_3 catalysts from Sigma-Aldrich, fresh (SA1) or thermally treated (SA2), were also considered. The atmospheres for calcination and thermal treatments were pure N_2, 10 vol.% O_2 in N_2, or 3 vol.% H_2O and 10 vol.% O_2 in N_2. The CO adsorption capacity, Pt dispersion, and average Pt particle size were determined by CO pulse titration. Average Pt particle diameters determined with TEM for samples C, D, and I are given in parentheses.*

Sample Name	**Calcination Atmosphere @550°C for 8 hrs**	**Thermal Treatment Temperature (°C)**	**Thermal Treatment Atmosphere ()**	**Thermal Treatment Duration (hrs)**	**CO Adsorption Capacity, $N_{CO\,ads}$ (mmol CO_{ads}/g_{Pt})**	**D_{Pt}, Pt Dispersion (%)**	**d_{Pt}, Average Pt Particle Diameter (nm)**
A	H_2O+O_2+N_2	–	–	–	4.12	80	1.3
B	O_2+N_2	–	–	–	3.53	69	1.6
C	N_2	–	–	–	2.67	52	2.1 (2.5 ± 1)
D	N_2	600	N_2	12	2.13	42	2.7 (2.8 ± 1)
E	N_2	650	N_2	12	1.88	37	3
F	N_2	750	N_2	12	1.81	35	3.2
G	N_2	750	N_2	48	1.34	26	4.3
H	N_2	650	H_2O+O_2+N_2	8	0.74	14	7.7
I	N_2	750	H_2O+O_2+N_2	8	0.31	6	18.7 (23 ± 14)
SA1	Sigma-Aldrich	–	–	–	2.55	50	2.1
SA2	Sigma-Aldrich	550	H_2O+O_2+N_2	8	1.18	23	4.5

2.2.2 Catalyst Characterization

2.2.2.1 Pt Particle Size

The catalysts were analyzed by CO pulse titration (Autosorb-iQ2; Quantachrome Instruments) to measure CO adsorption capacity, which was used to calculate the Pt dispersion and average Pt particle diameter. The procedure for pretreatment and CO pulse titration was as follows: First, a 0.5 g sample was heated to 100°C (10°C/min) and dried in a 30 NmL/min flow of air for 30 minutes. To remove impurities, the sample was then heated to 350°C (10°C/min) and oxidized in a 30 NmL/min flow of air for 30 minutes. Next, the system was evacuated and the sample cooled to 100°C under vacuum. A 30 NmL/min flow of pure H_2 was then introduced and the sample was heated to 350°C (10°C/min) and reduced for 120 minutes. The system was then evacuated and the sample was heated to 550°C (10°C/min) under vacuum and held at 550°C for 120 minutes to remove any adsorbed water formed from the oxidative and reductive treatments. After cooling to 35°C under vacuum, CO pulse titration was performed at 35°C using a 279 µL injection loop filled with pure CO and a 30 NmL/min flow of He carrier gas. A thermal conductivity detector (TCD) at the sample cell outlet measured the CO in the effluent gas and was used to determine the CO adsorption capacity ($N_{\mathrm{CO\,ads}}$; mmol CO_{ads}/g_{Pt}). After CO pulse titration, the sample was heated to 550°C (20°C/min) in a 30 NmL/min flow of He to desorb CO from the catalyst surface and then cooled to room temperature. For most samples, the characterization was repeated for a second portion of the catalyst sample and the average of the two measurements was used. Analyzed samples were subsequently stored at room temperature in ambient air.

Assuming that CO adsorbs as a monolayer on the Pt surface atoms, the CO adsorption capacity is directly proportional to the number of surface Pt atoms ($N_{\mathrm{Pt,S}}$; Pt_S atom/g_{Pt}). Using a stoichiometric factor of unity for the adsorption of CO on Pt [42, 52, 53], the Pt dispersion (D_{Pt}; %) is calculated as the ratio of surface Pt atoms to the total number of Pt atoms (N_{Pt}; Pt atom/g_{Pt}):

$$D_{\mathrm{Pt}} = \frac{N_{\mathrm{Pt,S}}}{N_{\mathrm{Pt}}} \cdot 100\% = \frac{N_{\mathrm{CO\,ads}}}{N_{\mathrm{Pt}}} \cdot 100\% \tag{2.1}$$

Note that for equation (2.1), the units of $N_{\mathrm{CO\,ads}}$ are simply number of CO molecules/g_{Pt}. The surface-averaged Pt particle diameter (d_{Pt}; nm) is calculated from the ratio of Pt volume (V_{Pt}; $Å^3$ Pt/g_{Pt}) to Pt surface area ($A_{\mathrm{Pt,S}}$; $Å^2$ Pt/g_{Pt}), assuming hemispherical Pt particles [52]. The Pt volume is calculated from the Pt density (ρ_{Pt}; $2.145 \cdot 10^{-23}$ $g_{Pt}/Å^3$ Pt [53]), while the Pt surface area is calculated from $N_{\mathrm{Pt,S}}$ and the cross-sectional area of one Pt atom ($A_{\mathrm{Pt,X}}$; 8.0 $Å^2$ Pt/Pt atom [53]). The equation for the average Pt particle diameter is therefore:

$$d_{\mathrm{Pt}} = 6 \cdot V_{\mathrm{Pt}} / A_{\mathrm{Pt,S}} = \frac{6}{\rho_{\mathrm{Pt}} \cdot N_{\mathrm{Pt,S}} \cdot A_{\mathrm{Pt,X}}} \tag{2.2}$$

Catalyst samples C, D, and I were analyzed using Transmission Electron Microscopy (TEM) to verify the average Pt particle diameters determined from CO pulse titration. A FEI Titan ETEM, running at a 300 kV acceleration voltage with spherical aberration corrector was used to characterize the samples in vacuum at

room temperature. The Pt particles observed had a close to circular shape and the Pt particle diameters were therefore measured for a circle that tightly outlined each particle.

2.2.2.2 Activity Measurements

The catalysts were tested for the oxidation of CO, HC, and NO. All samples used in the activity measurements were taken from the portion previously used in the CO pulse titration, and which had subsequently been stored at room temperature in ambient air (Section 2.2.2.1).

The CO oxidation activity was measured using a quartz U-tube reactor (D_i = 3 mm). The reactor was loaded with a mixture of 10 mg catalyst (150–300 µm) and 50 mg glass beads (212–300 µm), fixed between two plugs of quartz wool. The flow was directed upwards through the catalyst bed, and the temperature was measured with a thermocouple placed inside the reactor at the catalyst bed outlet.

To measure the CO oxidation activity, a flow of a 310 NmL/min was used with a feed gas consisting of 240 ppm CO, 2.8 vol. % H_2O, 9.7 vol. % O_2, and balance N_2, resulting in a space velocity of 0.021 mol/(g_{cat}·s). Water vapor was added to the gas mixture by bubbling it through a heated water flask at 30°C. The activity measurements were done by heating the catalyst from 40°C to 550°C at a rate of 5°C/min, holding at 550°C for 1 hour, followed by cooling to about 40°C. The cooling rate was set to 5°C/min, which could be followed until about 425°C where the cooling rate became limited to the natural cooling of the system. The concentrations of CO and CO_2 in the gas were measured using a continuous gas analyzer (Uras-26; ABB) and the concentration of water was determined using a humidity probe (HC2-IC102; Rotronic), which were both placed after the reactor. The heating and cooling procedures were repeated on the same reactor loading in most cases, to check repeatability of the results.

The catalysts were tested for hydrocarbon oxidation in the same manner as described above for CO oxidation, by replacing CO with 145 ppm of propene. Even though a typical diesel exhaust contains a variety of hydrocarbon components, propene (C_3H_6) was used as a model compound for hydrocarbon oxidation, following common practice [5, 10, 11, 23, 24, 46]. The propene conversion was determined based on the CO_2 concentrations measured in the product gas, using the same analyzer as for CO oxidation, and the stoichiometry of the reaction equation, forming three CO_2 molecules per C_3H_6 molecule. The CO_2 concentrations measured at 550°C corresponded to full conversion and these were used to determine the feed concentration of propene, which agreed well with that expected from the set gas flows.

For NO oxidation, a different flow reactor setup equipped with a NO_x analyzer was used. A quartz U-tube reactor (D_i = 6 mm) was loaded with a mixture of 20 mg catalyst sample (150–300 µm) and 100 mg glass beads (212–300 µm), fixed between two plugs of quartz wool. The gas flowed upwards through the catalyst bed and the temperature was measured with a thermocouple placed inside the reactor at the catalyst bed outlet. The feed gas was 485 ppm NO, 7.8 vol. % H_2O, 9.7 vol. % O_2, and balance N_2, with a total flow of 1030 NmL/min, resulting in a space velocity of SV = 0.035 mol/(g_{cat}·s). Water was added to the gas mixture by bubbling a separate flow of N_2 through water at 80°C. The concentrations of NO

and NO_2 were measured using a continuous gas analyzer (Limas11-HW; ABB) and the concentration of water was determined using a humidity probe (HC2-IC102; Rotronic). The procedure for the activity measurements were similar to those used in CO and C_3H_6 oxidation, with heating from 100°C to 550°C at a rate of 5°C/min, holding at 550°C for 1 hour, and cooling to 100°C. The cooling was done at an initial rate of 5°C/min until the heat loss became controlling at 450°C and the cooling rate became lower. For NO oxidation, heating and cooling procedures were repeated a second and third time for two different catalysts, and these showed no significant difference (see Figure A.4 in Appendix A.1). Therefore, the repeated cycles were omitted for all other samples in the measurement for NO oxidation.

2.3 Results

2.3.1 Determination of the Pt Particle Size

Table 2.1 presents the CO adsorption capacity measured by CO pulse titration for the different catalysts, as well as the calculated Pt dispersions and average Pt particle diameters. Since Pt dispersion and Pt particle diameter are inversely proportional, we choose to use the Pt particle diameter to describe the dispersion and to obtain a direct reference to the Pt particle size. The data in Table 2.1 shows that the calcination atmosphere and subsequent thermal treatments with various temperatures, gas atmospheres, and durations can be used to vary the average Pt particle diameter of the catalyst.

The smallest Pt particles were obtained for samples A, B, and C that were only calcined at 550°C for 8 hrs, with different gas atmospheres during calcination having a limited effect. Calcination in a wet oxidative atmosphere produced the smallest Pt particles of 1.3 nm (sample A) and the dry oxidative atmosphere yielded slightly larger Pt particles of 1.6 nm (sample B), while calcination in a dry inert atmosphere of N_2 resulted in a small additional increase to 2.1 nm (sample C). These results indicate that Pt particles of 1–2 nm are obtained from the initial calcination of $[PtCl_6]^{2-}$ adsorbed on the surface of γ-Al_2O_3 and can be controlled to some extent by varying the calcination atmosphere between pure N_2 and wet or dry oxidative atmospheres.

Pt particles larger than 2 nm were formed by thermally treating catalyst samples that had been prepared by calcination in a dry N_2 atmosphere at 550°C for 8 hrs, corresponding to sample C. The increase in Pt particle diameter was controlled by varying the temperatures, durations, and atmospheres of the thermal treatments. Thermally treating the catalysts in a flow of N_2 at 600°C, 650°C, or 750°C for 12 hrs gave limited increases in Pt particle diameter for samples D (2.7 nm), E (3.0 nm), and F (3.2 nm) in Table 2.1. Furthermore, increasing the duration of the thermal treatment in a flow of N_2 at 750°C from 12 hrs (sample F) to 48 hrs (sample G) led to a slight increase in Pt particle diameter from 3.0 nm to 4.3 nm. To form the large Pt particles of samples H (7.7 nm) and I (18.7 nm), the thermal treatments of catalysts were done in a flow of N_2, O_2, and water vapor at 650°C or 750°C for 8 hrs. Similarly, the fresh Sigma-Aldrich catalyst with 2.1 nm Pt particles (sample SA1) was thermally treated in a flow of N_2, O_2, and water vapor at 550°C for 8 hrs, yielding sample SA2 with relatively larger Pt particles of 4.5 nm. Overall, these

results indicate that the combination of oxygen, water vapor, and high temperature drives the sintering of Pt particles.

Figure 2.2 shows TEM images for catalyst samples C, D, and I, alongside the number based particle size distributions and the corresponding log-normal distributions. The Pt particles of sample C are mostly between 1–4 nm, with an average Pt particle diameter of 2.5 ± 1 nm, while most particles of sample D are between 1–4.5 nm with an average Pt particle diameter of 2.8 ± 1 nm. These Pt particle sizes match well with 2.1 and 2.7 nm found from CO pulse titration. For sample I, which has much larger particles, only 19 particles were identified by TEM. The sizes vary from 11–63 nm, but the majority of the particles are between 11 and 22 nm. This is also in good agreement with the results from CO pulse titration, with an estimated average particle size of 18.7 nm. These results indicate that the average Pt particle diameters obtained by CO pulse titration are a good estimate of the Pt particle size.

2.3.2 Effect of the Pt Particle Size on Activity

During the 1st heating cycle to 550°C, changes in the prepared catalysts occur leading to higher activity, while the data for the 1st cooling and 2nd heating/cooling cycles are comparable, indicating that the catalysts have reached a stable state after the initial heating to 550°C (see Figures A.1, A.2, A.3, and A.4 of the Appendix A.1). Sintering may occur during the 1st heating and cooling cycle, but the overlaying activity measurements of SA1 (2.1 nm) and SA2 (4.5 nm) for C_3H_6 oxidation (see Figure A.2a and A.2b), which unlike CO and NO oxidation does not exhibit hysteresis behavior [54], indicate that sintering is negligible for samples with Pt particles of 2.1 nm or larger. The samples with Pt particles smaller than 2.1 nm, such as A (1.3 nm) and B (1.6 nm), will still have the smallest Pt particles after the 1st heating and cooling cycle, and sintering will at most shift the particle sizes partly towards 2.1 nm. This gives a small margin of uncertainty in the exact Pt particle size of A and B used in the following presentation of results.

The activity measurements from the 1st cooling cycles for CO oxidation, C_3H_6 oxidation, and NO oxidation, are shown in Figure 2.3. All catalysts are active for each of the three oxidation reactions, but clear differences in the temperatures at which the rate of each reaction becomes appreciable are observed. For the most active catalysts, this occurs in the range of 45–65°C for CO oxidation, 100–130°C for C_3H_6 oxidation, and 150–250°C for NO oxidation.

Figure 2.3a shows the CO conversion during the 1st cooling cycle. Above 120°C, the catalysts all maintain complete oxidation of CO to CO_2. For the catalysts with average particle diameters of 1.6 (B), 2.1 (C), 2.1 (SA1), 2.7 (D), and 3.2 nm (F), the CO oxidation starts at the lowest temperature and these are therefore the most active. The catalysts with smaller and larger particles all require a higher temperature for CO oxidation and are therefore less active, pointing to an optimal Pt particle size for CO oxidation. The oscillatory behavior seen for sample C (2.1 nm) in Figure 2.3a and for sample F (3.0 nm) in Figure A.1c of the Appendix A.1, is known for CO oxidation over Pt and the phenomena associated with this have been thoroughly discussed elsewhere [25, 26, 55], and is beyond the scope of this article.

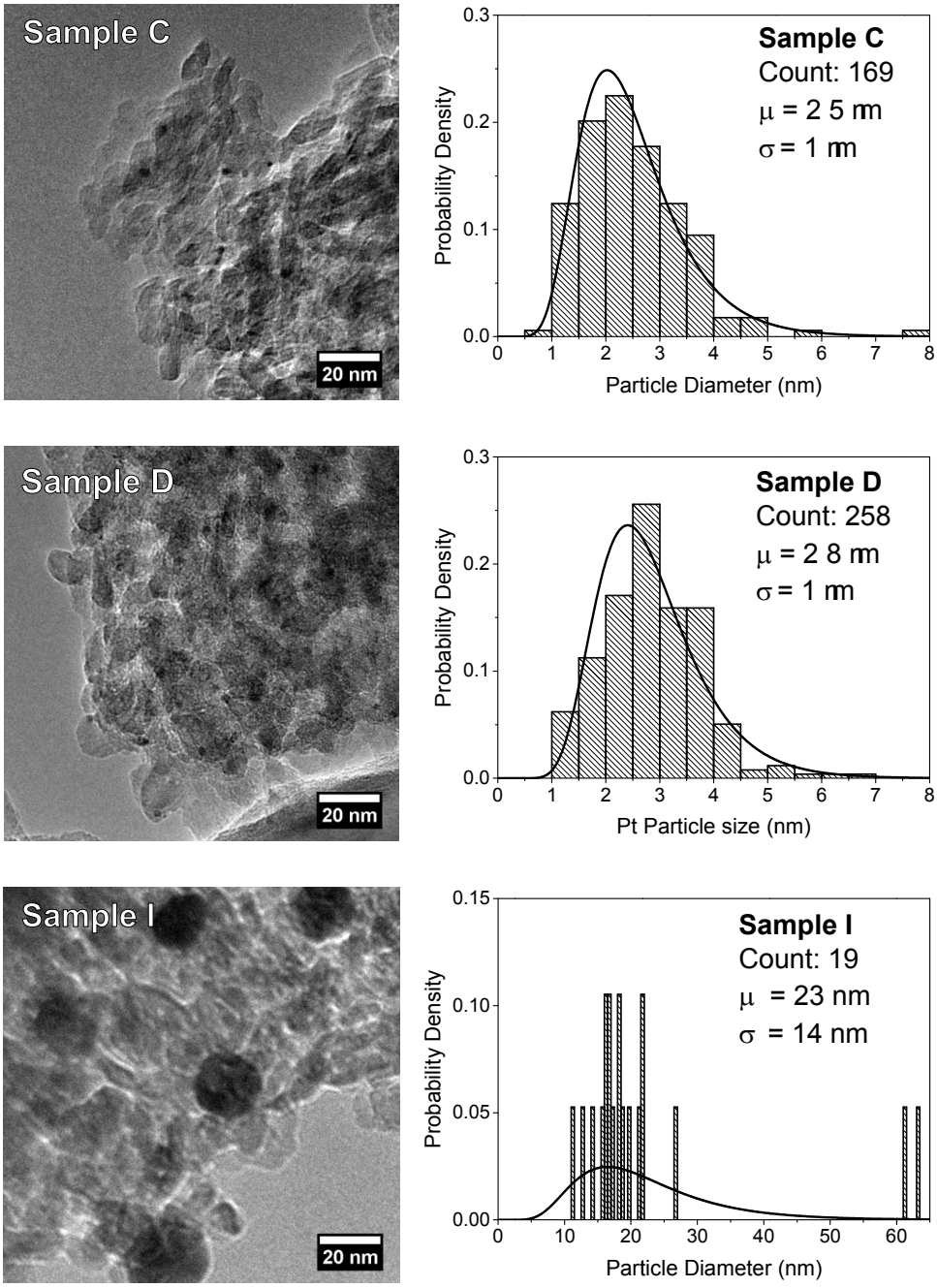

Figure 2.2: *Left column: TEM images for samples C, D, and I. Right column: Number based Pt particle size distributions based on TEM images and corresponding log-normal distributions for samples C, D and I. μ is the number average Pt particle diameter with a standard deviation of σ.*

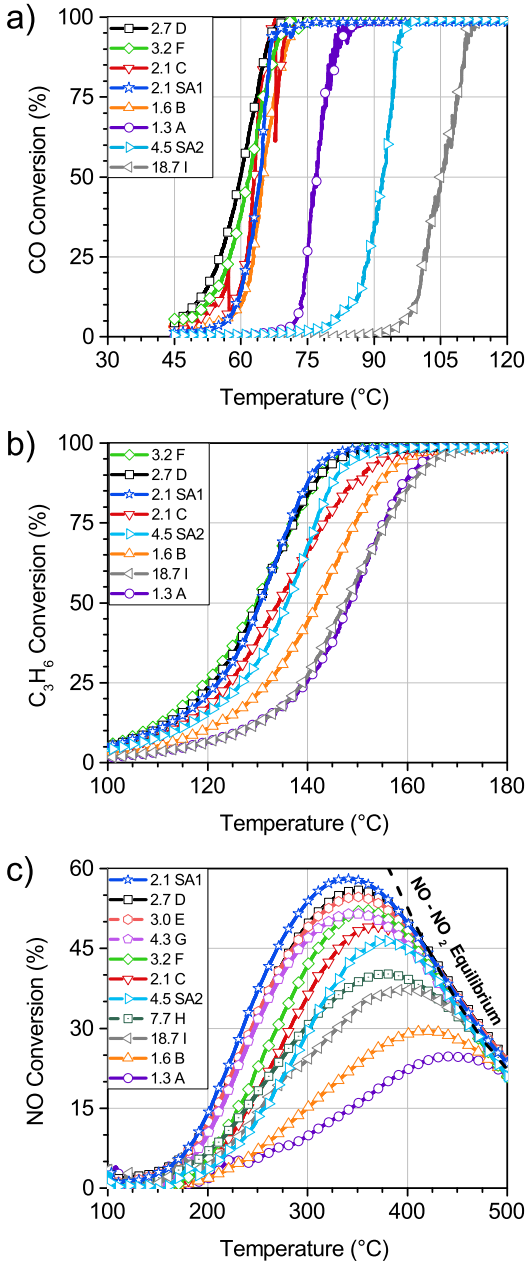

Figure 2.3: *Conversion curves for 1st cooling cycles. a) CO oxidation: 10 mg catalyst, 310 NmL/min gas flow, SV = 0.021 mol/(g_{cat}·s), 240 ppm CO, 2.8 vol.% H_2O, 9.7 vol.% O_2, and balance N_2. b) C_3H_6 oxidation: 10 mg catalyst, 310 NmL/min gas flow, SV = 0.021 mol/(g_{cat}·s), 145 ppm C_3H_6, 2.8 vol.% H_2O, 9.7 vol.% O_2, and balance N_2. c) NO oxidation: 20 mg catalyst, 1030 NmL/min gas flow, SV = 0.035 mol/(g_{cat}·s), 485 ppm NO, 7.8 vol.% H_2O, 9.7 vol.% O_2, and balance N_2. The dashed black line is the thermodynamic equilibrium for NO and NO_2.*

A similar trend is observed for C_3H_6 oxidation. In Figure 2.3b, the C_3H_6 conversion during the 1st cooling cycle shows that the onset temperature of the reaction is higher than for CO oxidation. Below 100°C, no significant C_3H_6 conversion is obtained for any catalyst and above 180°C full conversion of C_3H_6 is reached. The catalysts with Pt particles diameters of 2.1 (SA1), 2.7 (D), and 3.2 nm (F) were the most active, while smaller and larger Pt particles resulted in a lower catalytic activity, indicating an optimum in Pt particle size for C_3H_6 oxidation as well.

For NO oxidation, the data looks quite different compared to CO and C_3H_6 oxidation. Figure 2.3c shows the NO conversion during the 1st cooling cycle with a maximum in conversion between 325–450°C. This maximum is due to the NO_2 decomposition imposed by the thermodynamic equilibrium of the reaction $NO + \frac{1}{2} O_2 \rightleftharpoons NO_2$, which shifts toward $NO + O_2$ with increasing temperature, resulting in a lower NO conversion at higher temperatures. The equilibrium NO conversion is indicated by the dashed black line in Figure 2.3c. Below 300°C, where the contribution of the reverse reaction is limited, there are significant differences in catalytic activity observed. The most active catalysts have an average Pt particle diameter of 2.1 (SA1), 2.7 (D), 3.0 (E), and 4.3 nm (G). This indicates that there is an optimal particle size for NO oxidation, like for CO and C_3H_6 oxidation.

In order to better visualize the observed trends of activity with the Pt particle diameter, we used the temperature at which 50% conversion was measured (T_{50}) for CO oxidation and C_3H_6 oxidation. For NO oxidation, not all catalyst samples reached 50% conversion and therefore, the temperature for 20% conversion (T_{20}) was used instead. A lower T_{50} or T_{20} corresponds to a higher activity; the choice of conversion level is arbitrary and different choices did not lead to significantly different trends. Figure 2.4 shows the observed trends for the T_{50} and T_{20} with the Pt particle size, derived from 1st cooling and 2nd heating/cooling cycles for CO, C_3H_6, and NO oxidation. In Figure 2.4, for catalysts with repeated CO pulse titration measurements, the end points of the error bars indicate the individual Pt particle sizes calculated from the repetitions.

For CO oxidation, in Figure 2.4a, the catalysts with an average Pt particle diameter of 1.6 (B), 2.1 (C), 2.1 (SA1), 2.7 (D), and 3.2 nm (F) show the lowest T_{50} at around 60°C, and therefore are the most active catalysts for CO oxidation. The T_{50} for smaller particles is about 75°C for 1.3 nm (A) and about 110°C for very large particles of 18.7 nm (I), indicating a significantly lower activity for these catalysts. A similar trend is observed for C_3H_6 oxidation in Figure 2.4b; catalysts with an average Pt particle diameter of 2.1 (SA1), 2.7 (D), and 3.2 nm (F) achieve the lowest T_{50} of about 135°C. The T_{50} for both the smallest particles of 1.3 nm (A) and largest of 18.7 nm (I) are about 148°C. For NO oxidation, in Figure 2.4c, the T_{20} is lowest for samples with Pt particle diameters of 2.1 (SA1), 2.7 (D), 3.0 (E), and 4.3 nm (G) at about 220°C. The largest Pt particles of 18.7 nm (I) show an increase in T_{20} to 275°C, related to a decrease in activity. In contrast, decreasing the Pt particle diameter to 1.3 nm (A) results in a very significant increase of T_{20} to 380°C and therefore a significant decrease in the catalytic activity. These data show that the highest activity for all three reactions relevant for application of Pt as diesel oxidation catalyst is obtained for catalysts with an average Pt particle diameter in the range of 2–4 nm.

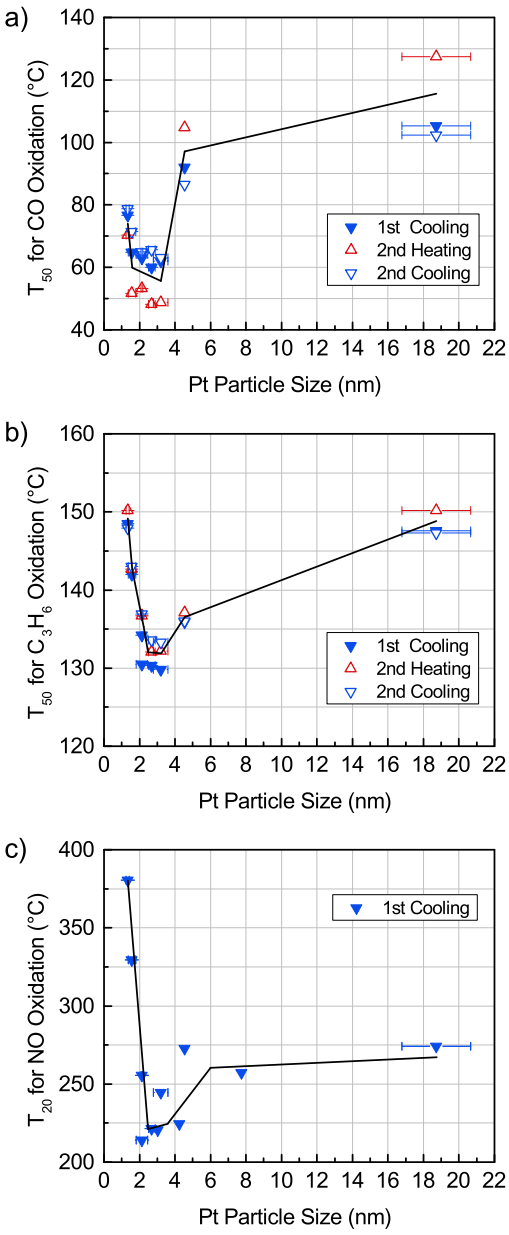

Figure 2.4: *Temperatures for 50% conversion (T_{50}) for 1 wt.% Pt/Al_2O_3 with varying Pt particle diameters during a) CO oxidation: 10 mg catalyst, 310 NmL/min gas flow, SV = 0.021 mol/(g_{cat}·s), 240 ppm CO, 2.8 vol.% H_2O, 9.7 vol.% O_2, and balance N_2, and b) C_3H_6 oxidation: 10 mg catalyst, 310 NmL/min gas flow, SV = 0.021 mol/(g_{cat}·s), 145 ppm C_3H_6, 2.8 vol.% H_2O, 9.7 vol.% O_2, and balance N_2. c) Temperatures for 20% conversion (T_{20}) for NO oxidation: 20 mg catalyst, 1030 NmL/min gas flow, SV = 0.035 mol/($_{cat}$·s), 485 ppm NO, 7.8 vol.% H_2O, 9.7 vol.% O_2, and balance N_2. The end points of the error bars indicate the individual Pt particle sizes for catalysts with repeated CO pulse titration measurements. For all three graphs, the black lines are to help guide the eye.*

To check whether the loss of activity for larger particles is due to the loss of Pt surface area, the turnover frequency (TOF = mol/(s·mmol Pt_S)) was determined for the CO, C_3H_6, and NO oxidation reactions. If the loss of surface area solely causes the loss of activity for larger Pt particles, then the TOF should remain constant. The TOF was calculated from the mass based rate of reaction (r'= mol/(s·g_{Pt})) and the number of surface Pt atoms, $N_{Pt,S}$ per gram platinum, as derived from the CO adsorption capacity, $N_{CO\,ads}$. The rate of reaction rate, r', was evaluated for each reaction at the temperature at which 10% conversion was reached for the most active catalyst, to ensure differential conditions. The TOF was therefore evaluated at 50°C for CO oxidation (10% CO conversion for sample D (2.7 nm)), at 105°C for C_3H_6 oxidation (10% conversion for sample F (3.2 nm)), and 190°C for NO oxidation (10% conversion for sample SA1 (2.1 nm)).

The TOFs for CO, C_3H_6, and NO as function of average Pt particle diameter are presented in Figure 2.5 along with the rates of reaction and CO adsorption capacities. From Figure 2.5a, the TOF for CO oxidation increases from 1.3 (A) to 2.7 nm (D), achieving the maximum TOF value for 2.7 nm (D). An increase in the Pt particle diameter to 4.5 (SA2) and 18.7 nm (I) causes a steep decrease in the TOF for CO oxidation. Furthermore, the maximum in rate of reaction for CO oxidation coincides with the maximum TOF at a Pt particle size of 2.7 nm (D). For the C_3H_6 oxidation TOF in Figure 2.5b, the TOF increases with the Pt particle diameter from 1.3 (A) to 3.2 nm (F). For larger Pt particles, the TOF continues to increase slightly, unlike the TOF for CO oxidation. Although the highest C_3H_6 TOF value is observed for 18.7 nm (I) Pt particles, the maximum mass based rate of reaction is measured for the samples with a Pt particle size between 2–4 nm. Similarly, the TOF for NO oxidation in Figure 2.5c increases with a change in the Pt particle diameter from 1.3 (A) to 2.1 (SA1) – 2.7 nm (D), and has significantly higher values for 7.7 nm (H) and 18.7 nm (I). For C_3H_6 and NO oxidation, the maximum TOF does therefore not correspond to the maximum in the mass based rate of reaction for 2–4 nm Pt particles. The fact that the TOF for C_3H_6 and NO oxidation does not decrease significantly for large particles is consistent with a loss of activity due to a decrease of Pt surface.

2.4 Discussion

An optimum in the rate of reaction for the oxidation of CO, C_3H_6, and NO was observed for Pt particle diameters of 2–4 nm for all three reactions. For application as a DOC, this means that tuning the Pt particle size to this range enhances the CO, HC (C_3H_6), and NO oxidation reactions. However, the TOF does not follow this trend. For CO oxidation, the maximum in TOF occurs for 2–3 nm Pt particles [12], while the TOF increases with Pt particle size for both HC oxidation [13–18] and NO oxidation [12, 19, 20]. The observation that the optimum particle diameter coincides with a maximum in TOF for CO oxidation but not for HC and NO oxidation indicates that the reasons for the maxima in rates of reaction are different.

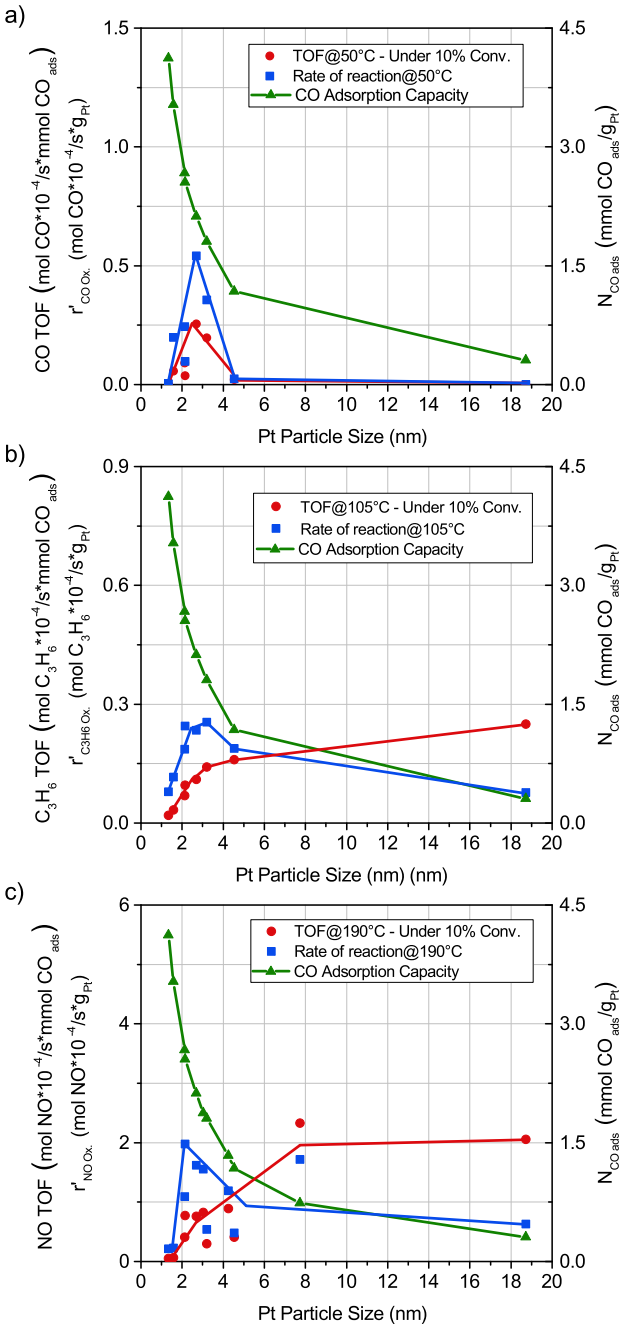

Figure 2.5: *The turnover frequency (TOF, red) for varying Pt particle diameters calculated for a) CO oxidation at 50°C, b) C_3H_6 oxidation at 105°C, and c) NO oxidation at 190°C from the rate of reaction (r', blue) and CO adsorption capacity ($N_{\mathrm{CO\,ads}}$, green), which is directly proportional to the number of available Pt atoms. The measurements are for the 1st cooling cycle. Solid lines for rate of reaction (r', blue) and turnover frequency (TOF, red) are to help guide the eye.*

A phenomenon occasionally used to explain particle size effects is the transition from a metallic to a non-metallic behavior that occurs when Pt particles become sufficiently small, since the band structure responsible for the metallic character of Pt cannot fully develop for very small particles [30, 31, 56, 57]. In general, this effect is most significant for clusters and particles below 1 nm in size for $Pt/\gamma\text{-}Al_2O_3$ [30, 57]. The smallest average Pt particle diameter considered in this work is 1.3 nm, and therefore we expect this effect to have a minor contribution to the lower TOF for the small Pt particles in this study. Instead we focus on the changes in the distribution of types of surface Pt atoms with variation in Pt particle sizes, and the resulting influence on catalyst behavior.

A change in Pt particle size affects the relative number of corner, edge, and terrace atoms, and since the contribution of these surface Pt atoms to the catalytic activity can be different, the catalytic activity becomes dependent on the Pt particle size. Figure 2.6 shows the calculated total and relative abundance of corner, edge, and terrace Pt atoms as a function of the Pt particle diameter for a 1 wt.% Pt loading, with the assumption that the Pt particles have a truncated octahedral shape and are supported on a (111)-plane. The calculations are done as outlined in the supplementary material of reference [58]. Figure 2.6a shows that Pt particles smaller than 4 nm have an appreciable number of edge and corner atoms, and that the number of terrace atoms starts to decrease, while the large Pt particles are dominated by terrace atoms. A comparison of Figure 2.6a with Figures 2.5b and 2.5c indicate that the TOFs for C_3H_6 and NO oxidation follow the relative amount of Pt terrace atoms, and the highest C_3H_6 and NO TOFs are obtained for large Pt particles, as previously reported [5, 12–20]. As a consequence, the maximum rates for HC and NO oxidation coincide with the maximum total number of terrace atoms, which occurs in the range of 2–4 nm. The decrease in reaction rate for large particles is then due to a lower number of Pt atoms in terraces.

In contrast to HC and NO oxidation, the oxidation of CO exhibits a maximum in TOF at 2.7 nm and very low TOF for large Pt particles. Particles of 2.7 nm in diameter have a high amount of edge atoms, but the maximum amount of edge atoms is found at about 1.5 nm. If CO oxidation were governed by edge sites alone, then we should have found the highest CO oxidation activity for catalyst B, with a particle size of 1.6 nm. This indicates that edges are not the only source of catalytic activity for CO oxidation, and the maximum in TOF occurring close to the maximum in terrace atoms points to a contribution of the terrace atoms as well. The reason for the lower CO-oxidation activity of large Pt atoms is then the lack of edge sites, rather than the loss of terrace sites as was the case for HC and NO oxidation.

From the discussion above, it follows that the role of the terrace sites in HC and NO oxidation is different compared to CO oxidation. The higher activity of the terraces for the oxidation of NO has been ascribed to a reaction of O_2 with vacancies on terraces nearly saturated with O* adatoms [19]. As terraces bind the oxygen atoms weaker, the vacancies are easier to create on terraces, thus favoring the NO oxidation. For hydrocarbon oxidation, the weakly bound O* species on terrace atoms are needed for the removal of H atoms in hydrocarbon oxidation [18]. For CO oxidation, the presence of edge sites is important, and the CO oxidation occurs preferentially between oxygen chemisorbed to step sites and CO adsorbed to

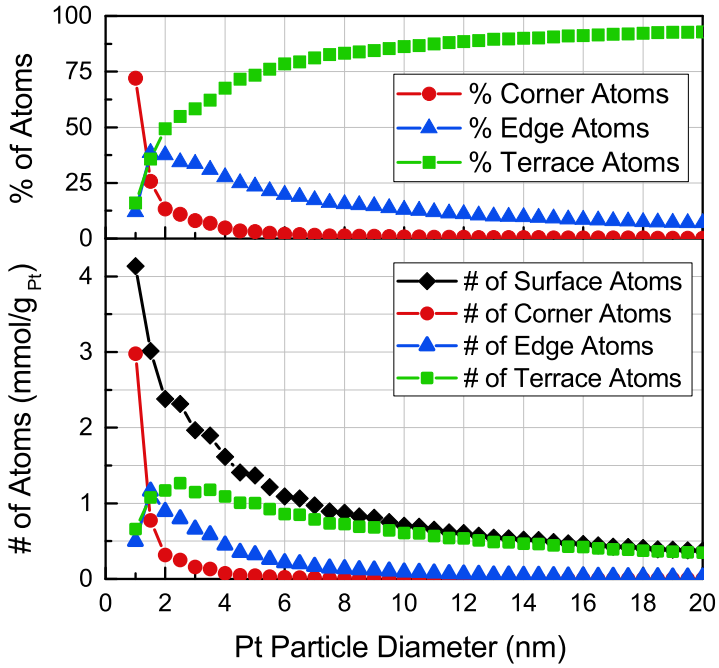

Figure 2.6: *Calculated total and relative number of corner, edge and terrace atoms for Pt particles of different sizes, assuming a truncated octahedron geometry and perfectly uniform particle size distributions. Bottom panel: The total number of different Pt atoms per gram Pt (mmol Pt atoms/g_{Pt}). Top panel: The relative number of corner, edge, and terrace Pt atoms per specific Pt particle size, given as a percentage.*

terrace atoms [59–62]. The CO oxidation reaction then becomes dependent on the presence of both terrace and edge sites.

An alternative explanation for the importance of edge sites in CO oxidation is the effect of water on the CO oxidation reaction. By using isotopically labeled oxygen, it was shown that water is actually the main source of the oxygen in CO_2 in the low temperature CO oxidation over Pd/Al_2O_3 in a wet feed gas [63]. This suggests that CO_2 is in fact formed from CO and water in a water gas shift reaction, rather than by an oxidation of CO with oxygen. Pt is also an efficient catalyst for water gas shift [64], and therefore the water gas shift reaction can also occur in CO oxidation under the wet conditions in a diesel exhaust gas. The water gas shift reaction requires dissociation of the water molecule to form adsorbed OH fragments, which then react with CO to form CO_2. DFT calculations indicate that this step is difficult on a Pt(111) surface and large particles, but becomes easier with decreasing Pt particle size due to an increase in edge and corner atoms [65, 66]. Furthermore, the enhanced O_2 dissociation on the edge sites may actually be beneficial for the dissociation of H_2O, since H_2O can readily react with O* in the presence of an extra H_2O to facilitate the formation of OH* ($H_2O^* + O^* + H_2O^* \rightarrow 2\ OH^* + H_2O^*$) [67–69]. The subsequent formation of COOH* from CO* and OH* occurs more easily on terrace atoms (0.56 eV activation energy on Pt(111)) compared to step atoms (1.4 eV activation energy on Pt(211)) [70], and the final step, in which CO_2 is

formed, occurs readily through the transfer of H from COOH* to a neighboring OH*, forming H_2O [69]. This means that the reaction pathway depends on both the edge atoms - for the dissociation of O_2 and H_2O - and on the terrace atoms for formation of COOH* [67, 68], in agreement with our observation that the maximum rate of CO oxidation is observed for a particle size that lies between the sizes corresponding to the maximum amount of edge and terrace atoms. In HC and NO oxidation, a similar reaction path with water does not exist, and consequently, water has an inhibitive effect on HC and NO oxidation [7, 21–23].

The lower activity for small Pt particles below 2 nm can also be understood from the site distribution shown in Figure 2.6. Small particles contain mostly edge and corner atoms, and the lack of terrace atoms, which are required for the CO, HC, and NO oxidation reactions, then results in the low activities. Figure 2.6 shows that particles smaller than 2 nm contain less terrace atoms, which is in good agreement with our observation that both the activity and TOF are lower for catalysts with Pt particle size below 2 nm. Furthermore, small Pt particles are also more easily oxidized than large particles [40, 41, 68, 71] and, consequently, the reduction of small Pt particles becomes harder. This is indicated by the 100–150°C higher reduction temperature of oxidized Pt particles of 1.5 nm in size compared to for Pt particles of 4 nm [40, 71]. However, as oxygen always is present under the typical conditions in a DOC, it is difficult to distinguish whether the lower activity is the result from a change in chemistry due to oxide formation, or due to the loss of active sites, as both effects always will occur simultaneously.

According to the discussion above, the optimal Pt particle size of 2–4 nm for the oxidation of CO, C_3H_6, and NO over Pt/Al_2O_3 catalysts in the presence of water is mainly determined by the number of terrace sites. For the oxidation of C_3H_6 and NO, Pt particles larger than approximately 4 nm are less active due to the loss in surface area, but the TOF remains more or less constant. For CO oxidation, edge sites also play a role, and therefore the larger particles are less active due to the loss of edge sites, resulting in a lower TOF for large particles. The lower activity and TOF for the oxidation of CO, C_3H_6, and NO for particles smaller than 2 nm can be understood by the lower amount of terrace sites in such particles, although the effects of a higher stability of Pt oxide in small particles are possible and indistinguishable.

2.5 Conclusion

The optimum Pt particle size for the oxidation of CO, C_3H_6, and NO was investigated through preparation, characterization, and activity measurements of a range of 1 wt.% Pt/Al_2O_3 catalysts. The catalysts were prepared by wet impregnation and different calcination and thermal treatments, in order to obtain a range of samples with Pt particles diameters of 1.3–18.7 nm, as determined from CO pulse titration and verified by TEM.

Comparison of catalytic activity as a function of temperature and Pt particle diameter showed that the greatest catalytic activities were achieved for Pt particle diameters between 2–4 nm for all three reactions. The results indicate that for C_3H_6 and NO oxidation, terrace surface atoms achieved the highest TOF values and were identified as the most active type of surface atoms, with the greatest abundance of

terrace atoms corresponding to the optimum Pt particle diameter between 2–4 nm. With increasing Pt particle size, the rate of reaction decreases due to the significant decrease in Pt surface area relative to the slight increase in TOF.

For CO oxidation, the particle size dependency is more complex and a maximum in TOF was observed for 2.7 nm, suggesting that CO oxidation under diesel exhaust conditions is dependent on both terrace and edge atoms. The dependence of CO oxidation on both terrace and edge atoms results in an optimum TOF between 2–4 nm, since the absence of terraces in small particles or edges in large particles effectively decreases the reaction rate of the individual reactions.

Based on the results in this study, a diesel oxidation catalyst based on Pt/Al_2O_3 with Pt particles between 2 and 4 nm in diameter is optimal for CO, hydrocarbon, and NO oxidation in the presence of water.

2.6 References

[1] EU. Commision Regulation (EU) No 582/2011. *Official Journal of the European Union*, 25.6.(L 182):1–168, 2011.

[2] Environmental Protection Agency. Control of Air Pollution From New Motor Vehicles: Heavy-Duty Engine and Vehicle Standards and Highway Diesel Fuel Sulfur Control Requirements. *Federal Register*, 66(12):5001–5193, 2001.

[3] A. Walker. Future Challenges and Incoming Solutions in Emission Control for Heavy Duty Diesel Vehicles. *Topics in Catalysis*, 59:695–707, 2016.

[4] H. Jääskeläinen. Diesel Exhaust Gas. In *DieselNet Technology Guide*. Ecopoint Inc., 2011. Online. `https://www.dieselnet.com/tech/diesel_exh.php` Accessed: August 9th, 2016.

[5] A. Russell and W.S. Epling. Diesel Oxidation Catalysts. *Catalysis Reviews: Science and Engineering*, 53(4):337–423, 2011.

[6] Cellular Monolith Substrates. In *DieselNet Technology Guide*. Ecopoint Inc., 1998. Online. `https://www.dieselnet.com//tech/cat_substrate.php` Accessed: August 20th, 2016.

[7] W.A. Majewski. Diesel Oxidation Catalyst. In *DieselNet Technology Guide*. Ecopoint Inc., 2012. Online. `https://dieselnet.com/tech/cat_doc.php` Accessed: February 28th, 2017.

[8] T.V.W. Janssens, H. Falsig, L.F. Lundegaard, P.N.R. Vennestrøm, S.B. Rasmussen, P.G. Moses, F. Giordanino, E. Borfecchia, K.A. Lomachenko, C. Lamberti, S. Bordiga, A. Godiksen, S. Mossin, and P. Beato. A Consistent Reaction Scheme for the Selective Catalytic Reduction of Nitrogen Oxides with Ammonia. *ACS Catalysis Research*, 5:2832–2845, 2015.

[9] S. Shrestha, M.P. Harold, K. Kamasamudram, A. Kumar, L. Olsson, and K. Leistner. Selective Oxidation of Ammonia to Nitrogen on Bi-functional Cu–SSZ-13 and Pt/Al_2O_3 Monolith Csatalyst. *Catalysis Today*, 267:130–144, 2016.

[10] M.J. Hazlett and W.S. Epling. Spatially Resolving CO and C_3H_6 Oxidation Reactions in a Pt/Al_2O_3 Model Oxidation Catalyst. *Catalysis Today*, 267:157–166, 2016.

[11] A.P. Wong, E.A. Kyriakidou, T.J. Toops, and J.R. Regalbuto. The Catalytic Behavior of Precisely Synthesized Pt–Pd Bimetallic Catalysts for Use as Diesel Oxidation Catalysts. *Catalysis Today*, 267:145–156, 2016.

[12] A. Boubnov, S. Dahl, E. Johnson, A.P. Molina, S.B. Simonsen, F.M. Cano, S. Helveg, L.J. Lemus-Yegres, and J. Grunwaldt. Structure–Activity Relationships of Pt/Al_2O_3 Catalysts for CO and NO Oxidation at Diesel Exhaust Conditions. *Applied Catalysis B: Environmental*, 126:315–325, 2012.

[13] A.M. Gololobov, I.E. Bekk, G.O. Bragina, V.I. Zaikovskii, A.B. Ayupov, N.S. Telegina, V.I. Bukhtiyarov, and A.Yu. Stakheev. Platinum Nanoparticle Size Effect on Specific Catalytic Activity in *n*-Alkane Deep Oxidation: Dependence on the Chain Length of the Paraffin. *Kinetics and Catalysis*, 50(6):830–836, 2009.

[14] T.F. Garetto and C.R. Apesteguía. Oxidative Catalytic Removal of Hydrocarbons over Pt/Al_2O_3 Catalysts. *Catalysis Today*, 62:189–199, 2000.

[15] K. Otto, J.M. Andino, and C.L. Parks. The Influence of Platinum Concentration and Particle Size on the Kinetics of Propane Oxidation over Pt/γ-Alumina. *Journal of Catalysis*, 131:243–251, 1991.

[16] L.M. Carballo and E.E. Wolf. Crystallite Size Effects during the Catalytic Oxidation of Propylene on Pt/γ-Al_2O_3. *Journal of Catalysis*, 53:366–373, 1978.

[17] N. Radic, B. Grbic, and A. Terlecki-Baricevic. Kinetics of Deep Oxidation of *n*-Hexane and Toluene over Pt/Al_2O_3 Catalysts Platinum Crystallite Size Effect. *Applied Catalysis B: Environmental*, 50:153–159, 2004.

[18] M. García-Diéguez, Y. Chin, and E. Iglesia. Catalytic Reactions of Dioxygen with Ethane and Methane on Platinum Clusters: Mechanistic Connections, Site Requirements, and Consequences of Chemisorbed Oxygen. *Journal of Catalysis*, 285:260–272, 2012.

[19] B.M. Weiss and E. Iglesia. NO Oxidation Catalysis on Pt Clusters: Elementary Steps, Structural Requirements, and Synergistic Effects of NO_2 Adsorption Sites. *Journal of Physical Chemistry C*, 113(30):13331–13340, 2009.

[20] A.D. Smeltz, W.N. Delgass, and F.H. Ribeiro. Oxidation of NO with O_2 on Pt(111) and Pt(321) Large Single Crystals. *Langmuir*, 26(21):16578–16588, 2010.

[21] O. Mihai, A. Fathali, X. Auvray, and L. Olsson. DME, Propane and CO: The Oxidation, Steam Reforming and WGS over Pt/Al_2O_3. The Effect of Aging and Presence of Water. *Applied Catalysis B: Environmental*, 160–161:480–491, 2014.

[22] W. Hauptmann, M. Votsmeier, J. Gieshoff, A. Drochner, and H. Vogel. Inverse Hysteresis during the NO Oxidation on Pt under Lean Conditions. *Applied Catalysis B: Environmental*, 93:22–29, 2009.

[23] X. Auvray and L. Olsson. Stability and Activity of Pd-, Pt- and Pd–Pt Catalysts Supported on Alumina for NO Oxidation. *Applied Catalysis B: Environmental*, 168:342–352, 2015.

[24] A. Abedi, J. Luo, and W.S. Epling. Improved CO, Hydrocarbon and NO Oxidation Performance using Zone-coated Pt-based Catalysts. *Applied Catalysis B: Environmental*, 207:220–226, 2013.

[25] A.M. Gänzler, M. Casapu, A. Boubnov, O. Müller, S. Conrad, H. Lichtenberg, R. Frahm, and J. Grunwaldt. Operando Spatially and Time-resolved X-ray Absorption Spectroscopy and Infrared Thermography during Oscillatory CO Oxidation. *Journal of Catalysis*, 328:216–224, 2015.

[26] J. Singh, M. Nachtegaal, E.M.C. Alayon, J. Stçtzel, and J.A. van Bokhoven. Dynamic Structure Changes of a Heterogeneous Catalyst within a Reactor: Oscillations in CO Oxidation over a Supported Platinum Catalyst. *ChemCatChem*, 2:653–657, 2010.

[27] Y. Chin, C. Buda, M. Neurock, and E. Iglesia. Selectivity of Chemisorbed Oxygen in C–H Bond Activation and CO Oxidation and Kinetic Consequences for CH_4–O_2 Catalysis on Pt and Rh Clusters. *Journal of Catalysis*, 283:10–24, 2011.

[28] L. Olsson and E. Fridell. The Influence of Pt Oxide Formation and Pt Dispersion on the Reactions $NO_2 \Leftrightarrow NO + \frac{1}{2} O_2$ over Pt/Al_2O_3 and $Pt/BaO/Al_2O_3$. *Journal of Catalysis*, 210:340–353, 2002.

[29] X. Auvray, T. Pingel, E. Olsson, and L. Olsson. The Effect of Gas Composition during Thermal Aging on the Dispersion and NO Oxidation Activity over Pt/Al_2O_3 Catalysts. *Applied Catalysis B: Environmental*, 129:517–527, 2013.

[30] F. Behafarid, L.K. Ono, S. Mostafa, J.R. Croy, G. Shafai, S. Hong, T.S. Rahman, S.R. Bare, and B. Roldan Cuenya. Electronic Properties and Charge Transfer Phenomena in Pt Nanoparticles on γ-Al_2O_3: Size, Shape, Support, and Adsorbate Effects. *Physical Chemistry Chemical Physics*, 14:11766–11779, 2012.

[31] I.E. Beck, V.I. Bukhtiyarov, I.Yu. Pakharukov, V.I. Zaikovsky, V.V. Kriventsov, and V.N. Parmon. Platinum Nanoparticles on Al_2O_3: Correlation between the Particle Size and Activity in Total Methane Oxidation. *Journal of Catalysis*, 268:60–67, 2009.

[32] E.S. Putna, J.M. Vohs, and R.J. Gorte. Oxygen Desorption from α-Al_2O_3 (0001) Supported Rh, Pt and Pd Particles. *Surface Science*, 391:L1178–L1182, 1997.

[33] M. García-Diéguez and E. Iglesia. Structure Sensitivity via Decoration of Low-coordination Exposed Metal Atoms: CO Oxidation Catalysis on Pt Clusters. *Journal of Catalysis*, 301:198–209, 2013.

[34] E.I. Altman and R.J. Gorte. The Desorption of CO from Small Pt Particles on Al_2O_3. *Surface Science*, 172:71–80, 1986.

[35] E.I. Altman and R.J. Gorte. A Comparison of the Desorption of CO from Pt and Rh Particles on α-$Al_2O_3\{0001\}$. *Surface Science*, 195:392–402, 1988.

[36] E.I. Altman and R.J. Gorte. Temperature-Programmed Desorption Study of NO on Pt Particles Supported on α-$Al_2O_3\{0001\}$. *Journal of Physical Chemistry*, 93:1993–1997, 1989.

[37] J. Singh and J.A. van Bokhoven. Structure of Alumina Supported Platinum Catalysts of different Particle Size during CO Oxidation using in situ IR and HERFD XAS. *Catalysis Today*, 155:199–205, 2010.

[38] E.M.C. Alayon, J. Singh, M. Nachtegaal, M. Harfouche, and J.A. van Bokhoven. On Highly Active Partially Oxidized Platinum in Carbon Monoxide Oxidation over Supported Platinum Catalysts. *Journal of Catalysis*, 263:228–238, 2009.

[39] A.Yu. Stakheev, A.M. Batkin, N.S. Teleguina, G.O. Bragina, V.I. Zaikovsky, I.P. Prosvirin, A.K. Khudorozhkov, and V.I. Bukhtiyarov. Particle Size Effect on CH_4 Oxidation Over Noble Metals: Comparison of Pt and Pd Catalysts. *Topics in Catalysis*, 56:306–310, 2013.

[40] R.W. McCabe, C. Wong, and H.S. Woo. The Passivating Oxidation of Platinum. *Journal of Catalysis*, 114:354–367, 1988.

[41] C. Wang and C. Yeh. Oxidation Behavior of Alumina-supported Platinum Metal Catalysts. *Applied Catalysis A: General*, 209:1–9, 2001.

[42] C. Karakaya and O. Deutschmann. A Simple Method for CO Chemisorption Studies under Continuous Flow: Adsorption and Desorption Behavior of Pt/Al_2O_3 Catalysts. *Applied Catalysis A: General*, 445-446:221–230, 2012.

[43] H. Matsuhashi, S. Nishiyama, H. Miura, K. Eguchi, K. Hasegawa, Y. Iizuka, A. Igarashi, N. Katada, J. Kobayashi, T. Kubota, T. Mori, K. Nakai, N. Okazakim, M. Sugioka, T. Umekio, Y. Yazawa, and D. Lu. Effect of Preparation Conditions on Platinum Metal Dispersion and Turnover Frequency of Several Reactions over Platinum-supported on Alumina Catalysts. *Applied Catalysis A: General*, 272:329–338, 2004.

[44] D. Chan, S. Tischer, J. Heck, C. Diehm, and O. Deutschmann. Correlation between Catalytic Activity and Catalytic Surface Area of a Pt/Al_2O_3 DOC: An Experimental and Microkinetic Modeling Study. *Applied Catalysis B: Environmental*, 156–157:153–165, 2014.

[45] A.D. Allian, K. Takanabe, K.L. Fujdala, X. Hao, T.J. Truex, J. Cai, C. Buda, M. Neurock, and E. Iglesia. Chemisorption of CO and Mechanism of CO Oxidation on Supported Platinum Nanoclusters. *Journal of the American Chemical Society*, 133:4498–4517, 2011.

[46] A.J. Binder, T.J. Toops, R.R. Unocic, J.E. Parks, and S. Dai. Low-Temperature CO Oxidation over a Ternary Oxide Catalyst with High Resistance to Hydrocarbon Inhibition. *Angewandte Chemie*, 127:13461–13465, 2015.

[47] F.J. Gracia, L. Bollmann, E.E. Wolf, J.T. Miller, and A.J. Kropf. In situ FTIR, EXAFS, and Activity Studies of the Effect of Crystallite Size on Silica-supported Pt Oxidation Catalysts. *Journal of Catalysis*, 220:382–391, 2003.

[48] G.R. Bamwenda, S. Tsubota, T. Nakamura, and M. Haruta. The Influence of the Preparation Methods on the Catalytic Activity of Platinum and Gold Supported on TiO_2 for CO Oxidation. *Catalysis Letters*, 44:83–87, 1997.

[49] Gaseous Emissions. In *DieselNet Technology Guide*. Ecopoint Inc., 2010. Online. `https://dieselnet.com/tech/emi_gas.php` Accessed: March 1st, 2017.

[50] E. Marceau, M. Che, J. Saint-Just, and J.M. Tatibouët. Influence of Chlorine Ions in Pt/Al_2O_3 Catalysts for Methane Total Oxidation. *Catalysis Today*, 29:415–419, 1996.

[51] E. Marceau, H. Lauron-Pernot, and M. Che. Influence of the Metallic Precursor and of the Catalytic Reaction on the Activity and Evolution of $Pt(Cl)/\delta$-Al_2O_3 Catalysts in the Total Oxidation of Methane. *Journal of Catalysis*, 197:394–405, 2001.

[52] S. Lowell, J. Shields, M. Thomas, and M. Thommes. *Characterization of Porous Solids and Powders: Surface Area, Pore Size, and Density*, chapter 12 Chemisorption: Site Specific Gas Adsorption. Academic Publishers, 2004.

[53] Quantachrome Instruments, Boynton Beach. *Autosorb iQ and ASiQwin Gas Sorption System Operating Manual*, 2015.

[54] A. Abedi, R. Hayes, M. Votsmeier, and W.S. Epling. Inverse Hysteresis Phenomena During CO and C_3H_6 Oxidation over a Pt/Al_2O_3 Catalyst. *Catalysis Letters*, 142:930–935, 2012.

[55] G. Ertl. *Reactions at Solid Surfaces*. John Wiley and Sons, Inc., 2010.

[56] A.K. Prashar, S. Mayadevi, P.R. Rajamohanan, and R.N. Devi. In situ Encapsulation of Pt Nanoparticles in Mesoporous Silica: Synthesis, Characterisation and Effect of Particle Size on CO Oxidation. *Applied Catalysis A: General*, 403:91–97, 2011.

[57] B. Roldan Cuenya and F. Behafarid. Nanocatalysis: Size- and Shape-dependent Chemisorption and Catalytic Reactivity. *Surface Science Reports*, 70:35–187, 2015.

[58] A. Carlsson, A. Puig-Molina, and T.V.W. Janssens. New Method for Analysis of Nanoparticle Geometry in Supported fcc Metal Catalysts with Scanning Transmission Electron Microscopy. *Journal of Physical Chemistry B*, 110:5286–5293, 2006.

[59] J. Xu, P. Henriksen, and J.T. Yates. Direct Spectroscopic Observation of the Reactive Catalytic Site for CO Oxidation on Pt(335). *The Journal of Chemical Physics*, 97:5250–5252, 1992.

[60] J.T. Yates. Surface Chemistry at Metallic Step Defect Sites. *Journal of Vacuum Science and Technology A*, 13:1359–1367, 1995.

[61] J.G. Wang, W. Li, M. Borg, J. Gustafson, A. Mikkelsen, T.M. Pedersen, E. Lundgren, J. Weissenrieder, J. Klikovits, M. Schmid, B. Hammer, and J.N. Andersen. One-Dimensional PtO_2 at Pt Steps: Formation and Reaction with CO. *Physical Review Letters*, 95(256102):1–4, 2005.

[62] W. Li. Oxidation of Platinum Surfaces and Reaction with Carbon Monoxide. *Journal of Physics: Condensed Matter*, 20(184022):1–7, 2008.

[63] R. Caporali, S. Chansai, R. Burch, J.J. Delgado, A. Goguet, C. Hardacre, L. Mantarosie, and D. Thompsett. Critical Role of Water in the Direct Oxidation of CO and Hydrocarbons in Diesel Exhaust After Treatment Catalysis. *Applied Catalysis B: Environmental*, 147:764–769, 2014.

[64] A. Boisen, T.V.W. Janssens, N. Schumacher, I. Chorkendorff, and S. Dahl. Support Effects and Catalytic Trends for Water Gas Shift Activity of Transition Metals. *Journal of Molecular Catalysis A: Chemical*, 315:163–170, 2010.

[65] A. Bruix, J.A. Rodriguez, P.J. Ramírez, S.D. Senanayake, J. Evans, J.B. Park, D. Stacchiola, P. Liu, J. Hrbek, and F. Illas. A New Type of Strong Metal-Support Interaction and the Production of H_2 through the Transformation of Water on $Pt/CeO_2(111)$ and $Pt/CeO_x/TiO_2(110)$ Catalysts. *Journal of the American Chemical Society*, 134:8968–8974, 2012.

[66] J.L.C. Fajín, M.N.D.S. Cordeiro, and J.R.B. Gomes. Density Functional Theory Study of the Water Dissociation on Platinum Surfaces: General Trends. *Journal of Physical Chemistry A*, 118(31):5832–5840, 2014.

[67] M.J.T.C. van der Niet, A. den Dunnen, L.B.F. Juurlink, and M.T.M. Koper. The Influence of Step Geometry on the Desorption Characteristics of O_2, D_2, and H_2O from Stepped Pt Surfaces. *The Journal of Chemical Physics*, 132(174705):1–8, 2010.

[68] L.K. Ono, J.R. Croy, H. Heinrich, and B. Roldan Cuenya. Oxygen Chemisorption, Formation, and Thermal Stability of Pt Oxides on Pt Nanoparticles Supported on $SiO_2/Si(001)$: Size Effects. *Journal of Physical Chemistry C*, 115:16856–16866, 2011.

[69] X. Gong, P. Hu, and R. Raval. The Catalytic Role of Water in CO Oxidation. *Journal of Chemical Physics*, 119(12):6324–6334, 2003.

[70] J.S. Yoo, F. Abild-Pedersen, J.K. Nørskov, and F. Studt. Theoretical Analysis of Transition-Metal Catalysts for Formic Acid Decomposition. *ACS Catalysis*, 4:1226–1233, 2014.

[71] M.Yu. Smirnova, A.V. Kalinkina, E.I. Vovka, and V.I. Bukhtiyarov. Size Effect in the Oxidation–Reduction Processes of Platinum Particles Supported onto Silicon Dioxide. *Kinetics and Catalysis*, 56(6):801–809, 2015.

CHAPTER 3

NH_3 Oxidation over Pt, Rh, and Pd Supported on Al_2O_3 and the Effect of the Pt Particle Size

The catalytic oxidation of NH_3 was investigated for a series of noble metal catalysts (1 wt.% Pt/Al_2O_3, 5 wt.% Pt/Al_2O_3, 5 wt.% Rh/Al_2O_3, and 5 wt.% Pd/Al_2O_3) and a series of 1 wt.% Pt/Al_2O_3 catalysts with varying Pt particles sizes (1.3–18.7 nm and ~200 nm), under conditions relevant for diesel exhaust aftertreatment (500 ppm NH_3, 2 vol.% H_2O, 10 vol.% O_2, balance N_2 for 150–550°C). The Pt catalysts are the most active of the noble metal catalysts studied, achieving 50% conversion between 198–226°C, compared to 264°C for Rh and 302°C for Pd. However, the Pt catalysts are also the most selective towards NO_x and N_2O, while Rh is the least selective towards N_2O and Pd is the most selective towards N_2. The effect of the Pt particle size on product selectivity and activity was studied using catalysts with Pt particle sizes of 1.3–18.7 nm and ~200 nm. The Pt particles of 7.7 nm, 18.7 nm, and ~200 nm are the most active, with Pt particles of ~200 nm also achieving lower yields of N_2O and NO_2, but with an increase in the total NO_x formed. Furthermore, Pt particles of 2–4 nm achieved the greatest NO_2/NO_x ratios, in line with the previously observed tendency for NO oxidation to NO_2 over 1 wt.% Pt/Al_2O_3 [1]. The potential benefits of controlling the Pt particle size to tailor the NO_2/NO_x from the AMOX catalyst to best suit the applied SCR catalyst are discussed.

3.1 Introduction

Nitrogen oxides (NO_x) formed during diesel combustion are significant pollutants that have harmful effects on human health and the environment, and NO_x emissions are therefore regulated by law [2–5]. Diesel exhaust aftertreatment systems use the selective catalytic reduction of NO_x with NH_3 (NH_3-SCR) to convert NO_x to N_2 and H_2O. By dosing urea to supply a small stoichiometric excess of NH_3, the SCR of NO_x becomes more efficient [6]. However, NH_3 emissions are also restricted by regulations [5, 7]. An ammonia slip catalyst (ASC) is therefore placed directly after the SCR unit to lower NH_3 emissions through the selective catalytic oxidation of ammonia (NH_3-SCO) with O_2 to N_2 and H_2O [7, 8].

Although SCR catalysts exhibit NH_3 oxidation activity with high N_2 selectivity, it is first significant at temperatures above 300–350°C [9–12]. An ASC therefore contains a dedicated ammonia oxidation (AMOX) catalyst to provide NH_3 oxidation activity at lower temperatures (<300°C) [8, 13]. Noble metals (Pt, Pd, and Rh) are highly active oxidation catalysts [14–21] and supported Pt particles are the best known AMOX catalysts for diesel exhaust systems, showing good activity above 200°C [12, 22, 23]. Nitrogen is the main reaction product at lower temperatures, but the selectivity towards N_2 decreases as the temperature increases above 225°C, offset by an increased selectivity to N_2O between 225–400°C and NO_x above 250°C [12, 14–23]. Due to the poor N_2 selectivity of Pt and the counterproductive formation of NO_x and N_2O, a modern state-of-the-art ASC consists of a combination of an AMOX catalyst and an NH_3-SCR catalyst in a layered or mixed configuration [8, 12, 13, 22, 24, 25]. The combination of AMOX and SCR catalysts enables the reduction of NO_x formed by the AMOX catalyst with available NH_3, thereby improving the N_2 selectivity through the NH_3-SCR reactions [8, 12, 13, 22, 24, 25]. Nitrous oxide formation is particularly unfavorable, since it is not readily reduced to N_2 through the SCR reactions [22, 24, 26]. In this manner, the performance of the ASC is dependent on the individual activities and product selectivities of the AMOX and SCR catalysts, but also on the interactions of the two catalyst systems, including their reactants and products [26, 27].

Previous studies of noble metal catalysts for ammonia oxidation, specifically of Pt, Pd, and Rh, indicate that Pt is the most active AMOX catalyst, but also the least selective towards N_2 [14–21, 28]. However, these studies have often been done under conditions not relevant for diesel exhaust aftertreatment systems by excluding H_2O, using low concentrations of O_2 (<4 vol.% O_2), considering high concentrations of NH_3 (>1000 ppm NH_3), limiting the temperature interval (<350°C or >700°C), or by not detecting the relevant products (N_2O or NO_2) in the exit gas [16]. Additionally, the Pt particle size has a significant effect on the oxidation activity of the Pt/Al_2O_3 catalyst (Chapter 2; [1]) and possibly the product selectivity from NH_3 oxidation [8]. However, to the author's knowledge, this has not yet been investigated and reported on in literature for NH_3 oxidation under conditions relevant for diesel exhaust aftertreatment.

Based on the considerations presented and the aim to further improve the ASC, it is the objective of this work to evaluate Pt, Pd, and Rh supported on Al_2O_3 as AMOX catalysts and to clarify the effect of the Pt particle size, under conditions relevant for diesel exhaust aftertreatment (500 ppm NH_3, 2 vol.% H_2O, 10 vol.% O_2, and balance N_2 for 150–550°C).

3.2 Experimental

3.2.1 Catalyst Preparation and Characterization

Noble metal catalysts supported on Al_2O_3 were acquired from Sigma-Aldrich (SA) and were 1 wt.% Pt/Al_2O_3 (Sigma-Aldrich; 205974), 5 wt.% Pt/Al_2O_3 (Sigma-Aldrich; 205966), 5 wt.% Rh/Al_2O_3 (Sigma-Aldrich; 83720), and 5 wt.% Pd/Al_2O_3 (Sigma-Aldrich; 205710). An overview of these catalysts is presented in Table 3.1.

A series of 1 wt.% Pt/γ-Al_2O_3 were prepared in a previous work [1] (Chapter 2, pg. 21) by a combination of wet impregnation of γ-Al_2O_3 with $H_2PtCl_6 \cdot H_2O$ and subsequent thermal treatments in a flow of N_2, N_2+O_2, or N_2+O_2+H_2O at temperatures between 550–750°C for durations of 8-48 hours [1]. Five samples covering the range of 1.3–18.7 nm were selected for this study: 1.3 nm, 2.7 nm, 4.3 nm, 7.7 nm, and 18.7 nm. To prepare a 1 wt% Pt/γ-Al_2O_3 catalyst with very large Pt particles, 20 mg of Pt nanopowder with a particle size of 200 nm (Sigma-Aldrich; 771937) was mechanically mixed with 1.98 g of γ-Al_2O_3 (Puralox NWa-155; Sasol; surface area 153.7 m^2/g). The mixture was thoroughly ground together in a mortar, assisted by a few drops of water. The sample was tableted, crushed, and sieved to 150–300 µm. The sample was then calcined in a flow of N_2 at 550°C for 8 hours. Table 3.1 presents an overview of the 1 wt.% Pt/γ-Al_2O_3 catalysts with varied Pt particle sizes.

Table 3.1: *Overview of the catalysts studied for NH_3 oxidation. Noble metal catalysts with Pt, Rh, or Pd supported on Al_2O_3 were acquired from Sigma-Aldrich. 1 wt.% Pt/Al_2O_3 catalysts with varying Pt particle sizes were prepared in-house by wet impregnation (WI) or mechanical mixing (MM). Average noble metal particle size was determined by CO pulse titration (Chapter 2, pg. 21) [1, 29].*

Catalyst	**Avg. Particle Diameter (nm)**	**Preparation Method and/or Source**
1 wt.% Pt/Al_2O_3	1.3	Sigma-Aldrich; 205974
5 wt.% Pt/Al_2O_3	–	Sigma-Aldrich; 205966
5 wt.% Rh/Al_2O_3	3.3	Sigma-Aldrich; 83720 [29]
5 wt.% Pd/Al_2O_3	6.2	Sigma-Aldrich; 205710 [29]
1 wt.% Pt/Al_2O_3	1.3	WI (Chapter 2) [1]
1 wt.% Pt/Al_2O_3	2.7	WI (Chapter 2) [1]
1 wt.% Pt/Al_2O_3	4.3	WI (Chapter 2) [1]
1 wt.% Pt/Al_2O_3	7.7	WI (Chapter 2) [1]
1 wt.% Pt/Al_2O_3	18.7	WI (Chapter 2) [1]
1 wt.% Pt/Al_2O_3	∼200	MM

All catalysts, except for 5 wt.% Pt/Al_2O_3 (SA) and 1 wt.% Pt/Al_2O_3 (∼200 nm), were characterized by CO pulse titration as described in Chapter 2, pg. 21 [1] for Pt catalysts and in [29] for the Rh and Pd catalysts. The CO adsorption capacity measured was used to calculate an average Pt particle size by assuming a stoichiometric factor of unity for the adsorption of CO on Pt (Chapter 2, pg. 21 [1]). Furthermore, the Pt particle sizes of samples 2.7 nm and 18.7 nm were affirmed using transmission electron microscopy (TEM) in Chapter 2, pg. 21 [1]. The noble metal particle sizes determined based on CO pulse titration are presented together

with the catalysts in Table 3.1. For the 1 wt.% Pt/Al_2O_3 sample prepared from Pt nanopowder with a specification of 200 nm, the final average Pt particle size of the catalyst is expected to be very similar to the starting material, and is therefore identified as ∼200 nm in Table 3.1 and the remainder of this chapter.

3.2.2 Catalyst Activity Measurements

The catalytic oxidation of NH_3 was evaluated using a fixed bed flow reactor setup operated at conditions relevant for diesel exhaust aftertreatment. Before catalyst testing, all catalyst samples were tableted, crushed, and sieved to 150–300 µm. A quartz U-tube reactor (D_i = 6 mm) was loaded with a mixture of 20 mg catalyst sample (150–300 µm) and 100 mg glass beads (212–300 µm; Sigma-Aldrich; G9143), fixed between two plugs of quartz wool. The feed gas consisted of 495 ± 20 ppm NH_3, 2 vol.% H_2O, 10 vol.% O_2, and balance N_2. The feed gas flowed upwards through the catalyst bed with a total flow of 1000 NmL/min. The temperature was measured with a thermocouple placed inside the reactor at the catalyst bed outlet. Water was added to the gas mixture by bubbling a separate flow of N_2 through water at 40°C.

The concentrations of NH_3, NO, and NO_2 were measured using a continuous gas analyzer (Limas11-HW; ABB) and the concentration of water was determined using a humidity probe (HC2-IC102; Rotronic). After condensation of H_2O from the gas stream, a GC (Varian; CP-4900) measured the N_2O concentration, which was then converted to the concentration in the wet gas. The N_2 concentration was calculated from the N-balance, based on the measured concentrations of NH_3, NO, NO_2, and N_2O.

The catalyst activity was measured by heating from 150°C to 550°C at a rate of 5°C/min, holding at 550°C for 1 hour, and cooling to 150°C. The cooling was done at an initial rate of 5°C/min until the heat loss became controlling at around 450°C and the cooling rate then became slower. The heating and cooling procedure was repeated a second time for all catalysts.

3.3 Results

3.3.1 NH_3 Oxidation over Pt, Rh, and Pd supported on Al_2O_3

The activity measurements for 1 wt.% Pt, 5 wt.% Pt, 5 wt.% Pd, and 5 wt.% Rh supported on Al_2O_3 are presented in Figure 3.1 in terms of NH_3 conversion and yields of NO_x, N_2, and N_2O during the 1st cooling cycle. This procedure results in a representative comparison of activity measurements (see Figures B.1–B.4 of Appendix B.1 for more details).

Figure 3.1 a) compares the measured NH_3 conversion with temperature for the Pt, Rh, and Pd catalysts. The curves are similar in appearance and all show a steep transition between 0 and 100% conversion in the temperature range of 150–350°C. The temperatures of 50% conversion (T_{50}) are 198°C for 5wt.% Pt, 226°C for 1 wt.% Pt, 264°C for 5wt.% Rh, and 302°C for 5wt.% Pd. This illustrates that Pt is the most active, which is clearly emphasized by the fact that the 1 wt.% Pt catalyst also exhibits a significantly greater catalytic activity than the 5 wt.% Rh and 5 wt.% Pd catalysts.

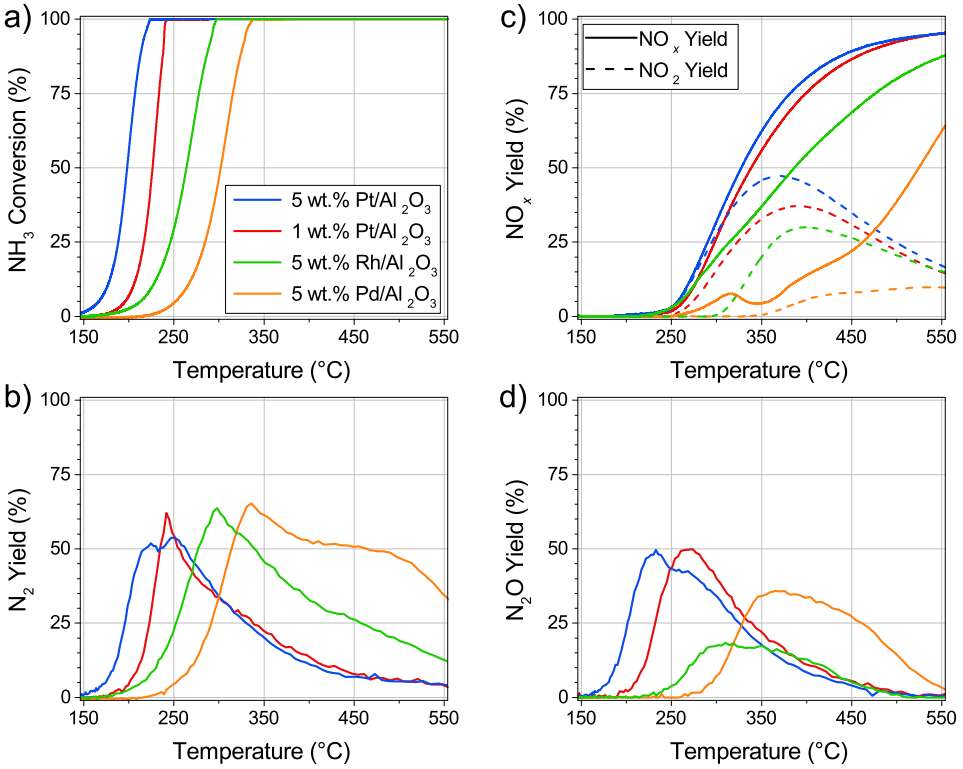

Figure 3.1: *Activity measurements from the 1st cooling cycle in terms of a) NH_3 conversion, b) N_2 yield, c) NO_x (solid) and NO_2 (dashed) yields, and d) N_2O yield for the different noble metal catalysts evaluated: 5 wt.% Pt/Al_2O_3, 1 wt.% Pt/Al_2O_3, 5 wt.% Rh/Al_2O_3, and 5 wt.% Pd/Al_2O_3. Operating conditions: 1000 NmL/min, 495 ± 20 ppm NH_3, 2 vol.% H_2O, 10 vol.% O_2, and balance N_2. Reactor loaded with 20 mg catalyst (150–300 µm) and 100 mg inert glass beads (212–300 µm).*

The oxidation of NH_3 with O_2 over the Pt, Rh, and Pd catalysts leads to the formation of N_2, N_2O, and NO_x. All catalysts show their highest selectivity towards N_2 and N_2O at lower temperatures, and are the most selective towards NO_x at higher temperatures. For Pt, NO_x formation starts around 250°C and becomes more dominant with increasing temperature, while the selectivity for N_2 and N_2O decreases towards 0% at high temperatures. The Pt catalyst is generally the most selective in the formation of NO_x, and also N_2O at temperatures below 350°C. The Pd catalyst shows the highest overall selectivity towards N_2, along with a modest NO_x formation relative to Pt and Rh. Pd is the most selective towards N_2O formation at temperatures above 350°C. For Rh, the selectivity for N_2O formation remains lower, compared to the other two metals. Furthermore, the selectivity towards NO_x and N_2 are intermediate relative to Pt and Pd. The difference in product selectivity of the different catalysts is further clarified by Figure B.5 in Appendix B.2.

3.3.2 Effect of the Pt Particle Size on NH_3 Oxidation

Figure 3.2 shows the a) NH_3 conversion, b) N_2 yield, c) NO_2 and NO_x yields, and d) N_2O yield with temperature during the 1st cooling cycle for the series of 1 wt.% Pt/Al_2O_3 catalysts with varying average Pt particle sizes. The inset in Figure 3.2a shows the T_{50} (temperature of 50% conversion) as a function of the Pt particle size. The 1 wt.% Pt/Al_2O_3 Sigma-Aldrich sample, with Pt particle size of 1.3 nm, is also included in Figure 3.2 as a reference catalyst. This procedure results in a representative comparison of activity measurement (see Figures B.6–B.11 of Appendix B.3 for more details).

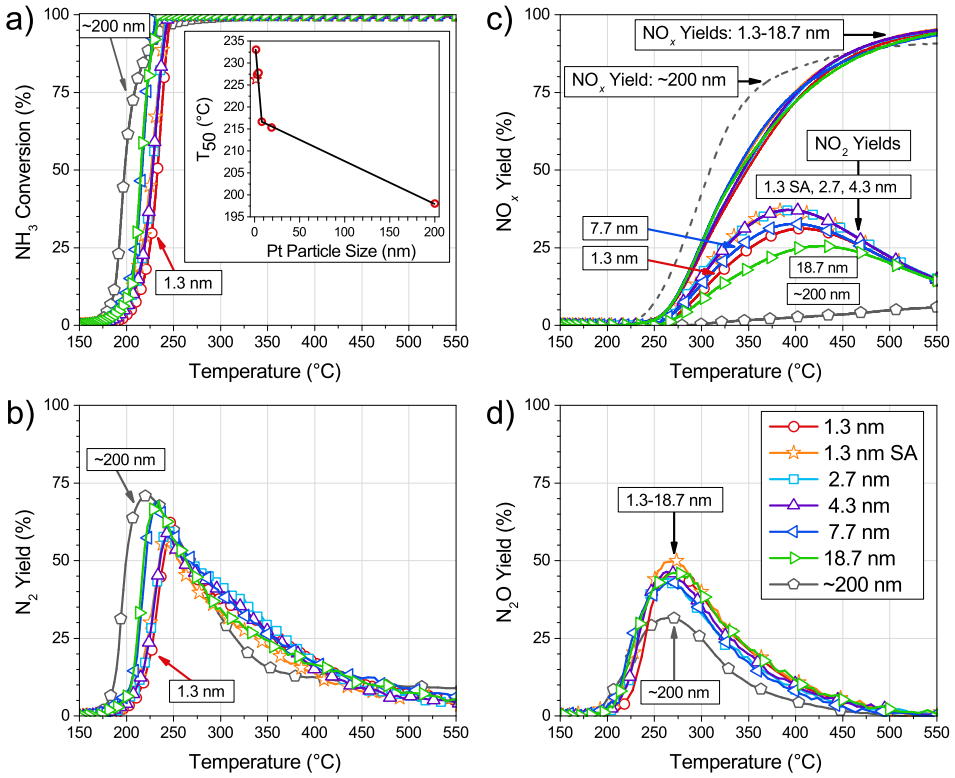

Figure 3.2: *Activity measurements from the 1st cooling cycle for the evaluated 1 wt.% Pt/Al_2O_3 catalysts with varying Pt particle sizes: a) NH_3 conversion with inset showing T_{50} as function of Pt particle size, b) N_2 yield, c) NO_x and NO_2 yields, and d) N_2O yield. The ⋆ symbols correspond to the 1 wt.% Pt/Al_2O_3 Sigma-Aldrich benchmark catalyst with Pt particle size of 1.3 nm. The black line in the inset of the NH_3 conversion is only meant to help guide the eye. Operating conditions: 1000 NmL/min, 495 ± 20 ppm NH_3, 2 vol.% H_2O, 10 vol.% O_2, and balance N_2. Reactor loaded with 20 mg catalyst (150–300 µm) and 100 mg inert glass beads (212–300 µm).*

From the NH_3 conversion curves shown in Figure 3.2a, all catalysts transition sharply between 0 and 100% NH_3 conversion across a temperature span of 50°C between 175–250°C. The curves for NH_3 conversion and the corresponding T_{50} show that the catalysts with large Pt particles (7.7, 18.7, and ∼ 200 nm) are the most active for NH_3 oxidation. Correspondingly, the T_{50} decreases with increasing

Pt particle size from 233°C for 1.3 nm to 198°C for ∼200 nm. This also shows the limited effect of the Pt particle size on the T_{50}, shifting it by only 35°C. In contrast to the Pt particle size effect observed in Chapter 2 for oxidation of CO, C_3H_6, and NO, it is unexpected that there is not an optimum in Pt particle size for NH_3 oxidation in the range below 20 nm, but rather that the largest Pt particles studied are the most active.

The effect of the Pt particle size on the selectivities of N_2, N_2O, and NO_x is rather limited. There is a tendency for larger Pt particles to achieve higher yields of N_2 and NO_x, and also a lower N_2O yield. However, there is a significant effect on the relative formation of NO and NO_2, as seen from Figure 3.2 c). This is further clarified in Figure 3.3 showing a) the development of the NO_2/NO_x ratio for the different catalysts in the temperature range of 200–550°C, and b) the maximum NO_2/NO_x ratio achieved as a function of the Pt particle size. From Figure 3.3a, Pt particles of 1.3–18.7 nm reach an overall ratio of NO_2/NO_x corresponding to ≥85% of maximum value between 250–300°C, which is also where NO_x is first formed in significant and measurable quantities. This ratio of NO_2/NO_x is sustained up until higher temperatures where the thermodynamic equilibrium for $NO + \frac{1}{2}\,O_2 \rightleftarrows NO_2$ causes a shift in the NO_x composition towards NO, in turn decreasing the formation of NO_2. The dependence on the Pt particle size is shown in Figure 3.3a and emphasized by Figure 3.3b, where a clear maximum in the NO_2/NO_x ratio is seen for catalysts with Pt particles in the range of 2–4 nm. This is quite similar to the particle size range with maximum oxidation activity for CO, HC, and NO observed in Chapter 2, page 21.

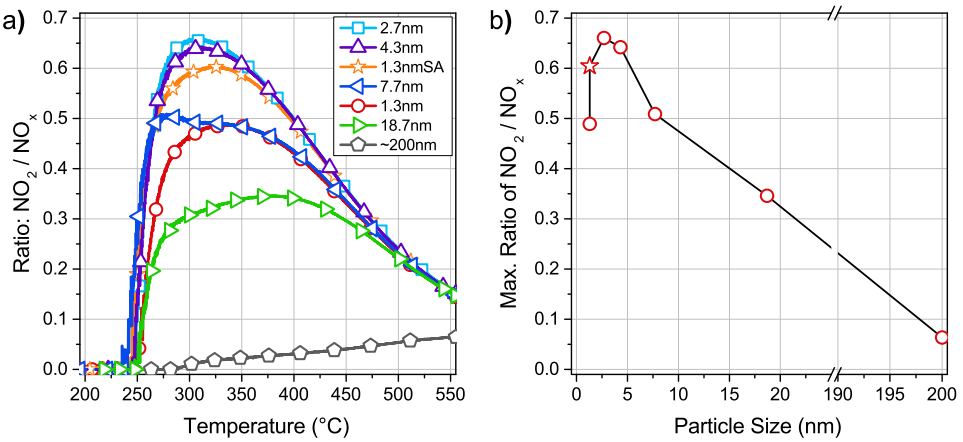

Figure 3.3: *a) The ratio of NO_2/NO_x during the catalytic oxidation of NH_3 for 1 wt.% Pt/Al_2O_3 with varying Pt particle size for the 1st cooling cycle. b) The maximum NO_2/NO_x ratio achieved during the catalytic oxidation of NH_3 during the 1st cooling cycle, as a function of the Pt particle size. The ⋆ symbol corresponds to the 1 wt.% Pt/Al_2O_3 Sigma-Aldrich sample.*

3.4 Discussion

The ideal AMOX catalyst to apply in the ASC should have good low temperature ($\leq$250°C) activity for NH_3 oxidation, allowing for full NH_3 conversion, and should also be highly selective towards the desired formation of N_2, minimizing the formation of undesired NO_x and N_2O. However, as was illustrated in Figure 3.1, the Pt, Rh, and Pd catalysts alone do not meet these requirements [7]. In general, the Rh and Pd catalysts exhibit better product selectivity than Pt for NH_3-SCO to N_2. The Rh catalyst is the least selective towards N_2O and the Pd catalyst is most selective towards N_2, while the Pt catalyst is most selective towards both NO_x and N_2O [14–21, 28]. However, the Pt catalyst demonstrates superior activity for low temperature NH_3 oxidation relative to Rh and Pd [14–21]. Regardless of the favorable product selectivity of both Pd and Rh, the necessary low temperature (175–400°C) oxidation activity of the ASC makes the Pt catalyst indispensable and the most popular choice as the AMOX catalyst [8, 13, 16]. The modern state-of-the-art ASC formulations combine a dedicated ammonia oxidation (AMOX) catalyst, used to provide high NH_3 oxidation activity, with an NH_3-SCR catalyst, which reduces NO_x formed to N_2 and decreases the formation of N_2O [7, 8, 12, 13, 16, 22]. Acknowledging that the Pt catalyst is the most commonly applied due to its high NH_3 oxidation activity, it is then relevant to consider the significance of the Pt particle size on the catalyst performance under conditions relevant for diesel exhaust aftertreatment, since it affects other oxidation reactions under similar conditions and it may affect the product selectivity of NH_3 oxidation [1, 8, 30].

The results presented in Figures 3.2 and 3.3 for catalysts with varying Pt particle size, evaluated under conditions relevant for diesel exhaust aftertreatment, show a weak dependence of the NH_3 oxidation activity and product selectivity on the Pt particle size in the 2–20 nm range. Very large Pt particles (~200 nm) show a higher activity, as indicated by the decrease in T_{50} with increasing Pt particle size. Also, the product selectivity is affected by the Pt particle size, with Pt particles of 2–4 nm being the most active in NO_2 formation, while very large Pt particles (~200 nm) form more NO_x (as NO) rather than N_2O above 225°C, which is an advantage since N_2O is hard to reduce to N_2 once formed. The high activity of the catalysts with large Pt particles is surprising considering the substantially lower quantity of available surface Pt atoms. Yet it is in agreement with previous studies of low temperature NH_3 oxidation, that catalysts consisting of large Pt particles, Pt wires, or Pt sponges provide a greater oxidation activity [30–34]. The effect is emphasized by a more rapid deactivation of catalysts with small Pt particles relative to large particles [30–34].

For studies with $p_{O_2}/p_{NH_3} = 0.1 - 5.5$, the Pt particle size is also reported to affect the product selectivity, with small Pt particles (2.7 nm) being more selective towards N_2 than N_2O, relative to large Pt particles (15.5 nm) [30]. In this study, a $p_{O_2}/p_{NH_3} = 200$ was used, and is likely the cause of the different trends in the effect of Pt particle size on selectivity. In general, the Pt particle size effect is suggested to be related to an influence on surface coverages and Pt oxide formation [30–34]. Adsorbates are expected to be strongly bound to edge and corner atoms, which are more abundant on small Pt particles, than to the terrace atoms predominant for large Pt particles [1, 35]. As a result, the small Pt particles will require a higher temperature than the large Pt particles to desorb inhibiting species, and

create surface vacancies for O_2 adsorption [35]. Similarly, oxygen adsorbed on small Pt particles is more strongly bound and less reactive than that adsorbed on large Pt particles, contributing to a higher oxidation activity on large Pt particles [30, 31, 36]. Additionally, Pt oxide formation begins once oxygen can adsorb to the Pt surface, with small Pt particles oxidizing more readily compared to large Pt particles [35]. Pt oxide is less active and therefore leads to catalyst deactivation, further contributing to the lower NH_3 oxidation activity exhibited by catalysts with small Pt particles [35]. The combination of these factors contributes to the lower NH_3 oxidation activity of catalysts with small Pt particles. With regards to product selectivity, the weakly bound oxygen of terrace Pt atoms is the source of increased NO oxidation activity of the catalysts samples with Pt particles of 2–4 nm, which is the Pt particle size range where terrace atoms are the most abundant [1] (Chapter 2). This is very likely also the cause of the greater NO_2/NO_x ratio achieved during NH_3 oxidation for the catalyst samples with Pt particles of 2.7 nm and 4.3 nm, shown in Figure 3.3. Additionally, the significant increase in gas phase NO for the ∼200 nm sample relative to all other Pt catalysts, including the 5 wt.% Pt catalyst, indicates a decrease in the adsorption strength of NO [28]. Since NO is a reactant in the formation of N_2O , the lower surface coverage of NO, resulting from a lower adsorption strength of NO, leads to a lower formation of N_2O [28, 37], as observed in Figure 3.2 for ∼200 nm sample. A more detailed discussion of the exact source and extent of the difference in catalytic activity and product selectivity is outside the scope of this work, and we focus the remainder of the discussion on the significance of varying the Pt particle size of the AMOX catalyst on the performance of the ASC.

A modern state-of-the-art ASC combines a dedicated AMOX catalyst with an NH_3-SCR catalyst, through either a layered and/or a mixed configuration [8, 12, 13, 22, 24, 25]. The AMOX catalyst, most popularly Pt-based, provides the initial oxidation of NH_3 in the ASC, to a combination of N_2, N_2O, NO, and NO_2. As only N_2 is desired, an SCR component is included that enables the reduction of NO_x formed with available NH_3 through the SCR reactions [8, 12, 13, 22, 24, 25]. The ASC performance is therefore expected to be dependent on the characteristics of both catalyst components, with the low temperature NH_3 oxidation activity determined by the AMOX catalyst and the combined selectivities of the AMOX and SCR catalyst determining the overall ASC product selectivity. In general, the rate of NO_x reduction to N_2 over Cu- and Fe-zeolites, and V_2O_5-based SCR catalysts is dependent on the NO_2/NO_x ratio of the gas [9, 38–43]. By varying the NO_2/NO_x, contributions from three different SCR reactions can be evoked: standard SCR (consumes only NO), slow SCR (consumes only NO_2), fast SCR (consumes equimolar amounts of NO and NO_2) [9, 38–43]. As designated, the fast SCR reaction is the fastest of the three and it occurs when both NO and NO_2 are present. It is selective towards N_2, but an appropriate SCR catalyst is necessary to avoid the simultaneous formation of N_2O from reactions between NH_3 and NO_2 over the catalyst [9, 38–43].

Based on the effect of the Pt particle size on the NO_2/NO_x ratio, we consider the case where an AMOX catalyst with Pt particles of 7.7 nm is combined with an SCR catalyst that is highly selective towards N_2 under fast and standard SCR conditions. The large Pt particles of 7.7 nm will provide an AMOX catalyst with a good NH_3 oxidation activity, that produces NO_x with a nearly constant composition

of NO_2/NO_x=0.5 (ideal for the fast SCR reaction) in the temperature range of 265–350°C, while the selectivity towards N_2 and N_2O is unaltered relative to the other Pt/Al_2O_3 catalysts (see Figures 3.2 and 3.3). Subsequently, the NO_x formed will interact with NH_3 over the SCR catalyst. Due to $NO_2/NO_x \approx 0.5$, the fast SCR reaction will be dominant, leading to an increased reduction of NO_x, relative to a situation where $NO_2/NO_x \neq 0.5$ and either the standard or slow SCR reaction is more dominant. However, it is important to note the limitations of this case. It is assumed that the desired NO_2/NO_x ratio is very quickly reached, so that the local NO_2/NO_x value corresponds to that measured at the outlet of the flow reactor experiments shown in Figures 3.2 and 3.3. If this is not the case, it may be necessary to use AMOX catalysts more active for NO_2 formation (2.7 nm and 4.3 nm) to attain the necessary local NO_2/NO_x ratio. Furthermore, the benefit of evoking the fast SCR reaction is primarily relevant if the SCR catalyst has a low activity for the standard SCR reaction and N_2O formation in the range of 250–350°C, commonly Fe-zeolites and V_2O_5-based catalysts rather than most Cu-zeolites [9, 38–43].

The first case considers ASC formulations that apply SCR catalysts where fast SCR conditions promote NO_x reduction selectively to N_2 between 250–350°C [9, 38, 40–43]. However, certain SCR catalysts, such as Cu-BEA, may exhibit a high standard SCR activity with a high N_2 selectivity at temperatures of 200–350°C, while having a high selectivity towards N_2O under fast and slow SCR conditions [10, 39]. If such a SCR catalyst is applied in the ASC, it is clearly necessary to limit the formation of NO_2 as much as possible, rather than strive for fast SCR conditions. For this reason, the second case considers the application of an AMOX catalyst with ∼200 nm Pt particles. As illustrated by Figure 3.2, the catalyst with ∼200 nm Pt particles has the best low temperature NH_3 oxidation activity relative to the other catalysts studied, while also maintaining a very similar N_2 selectivity. Additionally, the catalyst forms lower amounts of N_2O, although it is a trade-off for forming more NO_x, predominantly as NO. Considering that the formation of N_2O is practically irreversible in the ASC system, then N_2O is a final product and will not react further. Given the concerns with the formation and emission of N_2O, a strong greenhouse gas [24], it is actually an advantage to form NO rather than N_2O, since NO can be reduced to N_2. Furthermore, since the AMOX catalyst is predominantly forming NO (NO_2/NO_x=0), as illustrated by Figure 3.3, the subsequent formation of any N_2O will occur over the SCR catalyst and is limited by the N_2O selectivity of the SCR catalyst. In this manner, the Pt catalyst with ∼200 nm Pt particles could be used to improve the low temperature oxidation activity, lower the N_2O selectivity, and increase N_2 selectivity of the ASC.

3.5 Conclusion

The catalytic oxidation of NH_3 was investigated for a series of noble metal catalysts (1 wt.% Pt/Al_2O_3, 5 wt.% Pt/Al_2O_3, 5 wt.% Rh/Al_2O_3, and 5 wt.% Pd/Al_2O_3) and a series of 1 wt.% Pt/Al_2O_3 catalysts with varying Pt particles sizes (1.3–18.7 nm and ∼200 nm), under conditions relevant for diesel exhaust aftertreatment (500 ppm NH_3, 2 vol.% H_2O, 10 vol.% O_2, balance N_2 for 150–550°C).

Of the different noble metal catalysts, Pt is the most active for NH_3 oxidation with a T_{50} of 198–226°C compared to 264°C for Rh and 302°C for Pd. Furthermore,

the Pt catalysts are the most selective towards the formation of NO_x and N_2O. In contrast, the Rh catalyst is the least selective towards N_2O, while the Pd catalyst is most selective towards N_2 and formed the least NO_x.

Due to the NH_3 oxidation activity of the Pt catalyst, the effect of the Pt particle size on product selectivity and activity was investigated. From the activity measurements for catalytic NH_3 oxidation over 1 wt.% Pt/Al_2O_3 catalysts with Pt particle sizes of 1.3-18.7 nm and ∼200 nm, large Pt particles are the most active, as determined from the decrease in T_{50} from 233°C (1.3 nm) to 198°C (∼200 nm). Furthermore, large Pt particles of ∼200 nm lead to lower yields of N_2O and NO_2, but with an increase in total NO_x formation. The effect of the Pt particle size on the NO_2/NO_x ratio of formed NO_x corresponds well to the previously observed tendency for NO oxidation over 1 wt.% Pt/Al_2O_3 with Pt particles of 2–4 nm being the most active in NO_2 formation [1].

It is suggested that by controlling the Pt particle size it may be possible to tailor the NO_2/NO_x ratio from the AMOX catalyst to best suit the applied SCR catalyst. For a highly N_2 selective catalyst, a NO_2/NO_x=0.5 resulting from Pt particles of 2–8 nm would improve the rate of NO_x reduction of the SCR catalyst to N_2. Meanwhile, SCR catalysts active in N_2O formation from NO_2 would benefit from the decreased N_2O formation and very limited NO_2 formation from catalysts with Pt particles of ∼200 nm.

This study confirms the superior oxidation activity of Pt compared to Pd and Rh, also under conditions relevant for diesel exhaust aftertreatment. Furthermore, the Pt particle size affects both the NH_3 oxidation activity and product selectivity of the 1 wt.% Pt/Al_2O_3 catalysts, and may be beneficially used in the design of an ammonia slip catalysts.

3.6 References

[1] T.K. Hansen, M. Høj, B.B. Hansen, T.V.W. Janssens, and A.D. Jensen. The Effect of Pt Particle Size on the Oxidation of CO, C_3H_6, and NO over Pt/Al_2O_3 for Diesel Exhaust Aftertreatment. *Topics in Catalysis*, Accepted, 2017.

[2] Health and Environmental Effects. In *DieselNet Technology Guide*. Ecopoint Inc., 2012. Online. `https://dieselnet.com/tech/env_top.php` Accessed: February 28th, 2017.

[3] Health Effects of Gas Phase Components. In *DieselNet Technology Guide*. Ecopoint Inc., 1999. Online. `https://dieselnet.com/tech/health_gas.php` Accessed: March 1st, 2017.

[4] W.A. Majewski and H. Jääskeläinen. Environmental Effects of Emissions. In *DieselNet Technology Guide*. Ecopoint Inc., 2004. Online. `https://dieselnet.com/tech/env_effect.php` Accessed: March 1st, 2017.

[5] EU. Commision Regulation (EU) No 582/2011. *Official Journal of the European Union*, 25.6.(L 182):1–168, 2011.

[6] T.V.W. Janssens, H. Falsig, L.F. Lundegaard, P.N.R. Vennestrøm, S.B. Rasmussen, P.G. Moses, F. Giordanino, E. Borfecchia, K.A. Lomachenko, C. Lamberti, S. Bordiga, A. Godiksen, S. Mossin, and P. Beato. A Consistent Reaction

Scheme for the Selective Catalytic Reduction of Nitrogen Oxides with Ammonia. *ACS Catalysis Research*, 5:2832–2845, 2015.

[7] A. Walker. Future Challenges and Incoming Solutions in Emission Control for Heavy Duty Diesel Vehicles. *Topics in Catalysis*, 59:695–707, 2016.

[8] S. Shrestha, M.P. Harold, K. Kamasamudram, and A. Yezerets. Selective Oxidation of Ammonia on Mixed and Dual-layer Fe-ZSM-5 + Pt/Al_2O_3 Monolithic Catalysts. *Catalysis Today*, 231:105–115, 2014.

[9] P.S. Metkar, M.P. Harold, and V. Balakotaiah. Experimental and Kinetic Modeling Study of NH_3-SCR of NOx on Fe-ZSM-5, Cu-chabazite and Combined Fe- and Cu-zeolite Monolithic Catalysts. *Chemical Engineering Science*, 87:51–66, 2013.

[10] O. Mihai, C.R. Widyastuti, S. Andonova, K. Kamasamudram, J. Li, S.Y. Joshi, N.W. Currier, A. Yezerets, and L. Olsson. The Effect of Cu-loading on Different Reactions Involved in NH_3-SCR over Cu-BEA Catalysts. *Journal of Catalysis*, 311:170–181, 2014.

[11] M. Iwasaki. *Urea-SCR Technology for deNOx After Treatment of Diesel Exhausts*, chapter 8 Mechanistic Aspect of NO–NH_3–O_2 Reacting System. Springer Science+Business Media, 2014.

[12] S. Shrestha, M.P. Harold, K. Kamasamudram, A. Kumar, L. Olsson, and K. Leistner. Selective Oxidation of Ammonia to Nitrogen on Bi-functional Cu–SSZ-13 and Pt/Al_2O_3 Monolith Csatalyst. *Catalysis Today*, 267:130–144, 2016.

[13] S. Shrestha, M.P. Harold, K. Kamasamudram, and A. Yezerets. Ammonia Oxidation on Structured Composite Catalysts. *Topics in Catalysis*, 56:182–186, 2013.

[14] Y. Li and J.N. Armor. Selective NH_3 Oxidation to N_2 in a Wet Stream. *Applied Catalysis B: Environmental*, 13:131–139, 1997.

[15] L. Chmielarz, M. Jabłońska, A. Strumiński, Z. Piwowarska, A. Węgrzyn, S. Witkowski, and M. Michalik. Selective Catalytic Oxidation of Ammonia to Nitrogen over Mg-Al, Cu-Mg-Al and Fe-Mg-Al Mixed Metal Oxides Doped with Noble Metals. *Applied Catalysis B: Environmental*, 130-131:152–162, 2013.

[16] L. Chmielarz and M. Jabłońska. Advances in Selective Catalytic Oxidation of Ammonia to Dinitrogen: A Review. *RSC Advances*, 5:43408–43431, 2015.

[17] K. Sano, N. Sugishima, M. Ikeda, K. Yoshino, and J. Okamura. The New Technology for Selective Catalytic Oxidation of Ammonia to Nitrogen. *Studies in Surface Science and Catalysis*, 121:399–402, 1999.

[18] L. Gang, B.G. Anderson, J. van Grondelle, and R.A. van Santen. NH_3 Oxidation to Nitrogen and Water at Low Temperatures using Supported Transition Metal Catalysts. *Catalysis Today*, 61:179–185, 2000.

[19] N.I. Il'chenko. Catalytic Oxidation of Ammonia. *Russian Chemical Reviews*, 45(12):179–185, 1976.

[20] R.Q. Long and R.T. Yang. Noble Metal (Pt, Rh, Pd) Promoted Fe-ZSM-5 for Selective Catalytic Oxidation of Ammonia to N_2 at Low Temperatures. *Catalysis Letters*, 78(1-4):353–357, 2002.

[21] T. Pignet and L.D. Schmidt. Kinetics of NH_3 Oxidation on Pt, Rh, and Pd. *Journal of Catalysis*, 4:212–225, 1975.

[22] A. Scheuer, W. Hauptmann, A. Drochner, J. Gieshoff, H. Vogel, and M. Votsmeier. Dual Layer Automotive Ammonia Oxidation Catalysts: Experiments and Computer Simulation. *Applied Catalysis B: Environmental*, 111-112:445–455, 2012.

[23] I. Nova, M. Colombo, E. Tronconi, V. Schmeisser, B. Bandl-Konrad, and L. Zimmermann. Experimental and Modelling Study of a Dual-Layer NH_3 Slip Monolith Catalyst for Automotive SCR Aftertreatment Systems. *Topics in Catalysis*, 56:227–231, 2013.

[24] S. Shrestha, M.P. Harold, and K. Kamasamudram. Experimental and Modeling Study of Selective Ammonia Oxidation on Multi-functional Washcoated Monolith Catalysts. *Chemical Engineering Journal*, 278:24–35, 2015.

[25] A. Scheuer, A. Drochner, J. Gieshoff, H. Vogel, and M. Votsmeier. Runtime Efficient Simulation of Monolith Catalysts with a Dual-Layer Washcoat. *Catalysis Today*, 188:70–79, 2012.

[26] M. Colombo, I. Nova, E. Tronconi, V. Schmeißer, B. Bandl-Konrad, and L. R. Zimmermann. Experimental and Modeling Study of a Dual-Layer (SCR + PGM) NH_3 Slip Monolith Catalsyt (ASC) for Automotive SCR Aftertreatment Systems. Part 1. Kinetics for the PGM Component and Analysis of SCR/PGM Interactions. *Applied Catalysis B: Environmental*, 142-143:861–876, 2013.

[27] M. Colombo, I. Nova, E. Tronconi, V. Schmeißer, B. Bandl-Konrad, and L. R. Zimmermann. Experimental and Modeling Study of a Dual-Layer (SCR + PGM) NH_3 Slip Monolith Catalsyt (ASC) for Automotive SCR Aftertreatment Systems. Part 2. Validation of PGM Kinetics and Modeling of the Dual-layer ASC Monolith. *Applied Catalysis B: Environmental*, 142-143:337– 343, 2013.

[28] J. Pérez-Ramírez, E.V. Kondratenko, G. Novell-Leruth, and J.M. Ricart. Mechanism of Ammonia Oxidation over PGM (Pt, Pd, Rh) Wires by Temporal Analysis of Products and Density Functional Theory. *Journal of Catalysis*, 261:217–223, 2009.

[29] V. Singh. Catalytic Oxidation of Methane. Master's thesis, Friedrich-Alexander University of Erlangen-N uurnberg and Technical University of Denmark, 2016.

[30] J.J. Ostermaier, J.R. Katzer, and W.H. Manogue. Crystallite Size Effects in the Low-Temperature Oxidation of Ammonia Over Supported Platinum. *Journal of Catalysis*, 33:457–473, 1974.

[31] J.J. Ostermaier, J.R. Katzer, and W.H. Manogue. PlatinumCatalyst Deactivation in Low-Temperature Ammonia Oxidation Reactions I. Oxidation of Ammonia by Molecular Oxygen. *Journal of Catalysis*, 41:277–292, 1976.

[32] A.C.M. van den Broek. *Low Temperature Oxidation of Ammonia over Platinum and Iridium Catalysts*. PhD thesis, Technische Universiteit Eindhoven, 1998.

[33] D.P. Sobczyk, E.J.M. Hensen, A.M. de Jong, and R.A. van Santen. Low-temperature Ammonia Oxidation over Pt/γ-alumina: The Influence of the Alumina Support. *Topics in Catalysis*, 23(1–4):109–117, 2003.

[34] D.P. Sobczyk. *Positron Emission Profiling Study of Ammonia Oxidation on Platinum*. PhD thesis, Technische Universiteit Eindhoven, 2003.

[35] M. Casapu, A. Fischer, A.M. Gänzler, R. Popescu, M. Crone, D. Gerthsen, M. Türk, and J. Grunwaldt. Origin of the Normal and Inverse Hysteresis Behavior during CO Oxidation over Pt/Al_2O_3. *ACS Catalysis*, 7:343—355, 2017.

[36] B.M. Weiss and E. Iglesia. NO Oxidation Catalysis on Pt Clusters: Elementary Steps, Structural Requirements, and Synergistic Effects of NO_2 Adsorption Sites. *Journal of Physical Chemistry C*, 113(30):13331–13340, 2009.

[37] G. Novell-Leruth, J.M. Ricart, and J. Pérez-Ramírez. Pt(100)-Catalyzed Ammonia Oxidation Studied by DFT: Mechanism and Microkinetics. *Journal of Physical Chemistry C*, 112:13554–13562, 2008.

[38] W.A. Majewski. Selective Catalytic Reduction. In *DieselNet Technology Guide*. Ecopoint Inc., 2005. Online. `https://dieselnet.com/tech/cat_scr.php` Accessed: March 8th, 2017.

[39] O. Mihai, C.R. Widyastuti, A. Kumar, J. Li, S.Y. Joshi, K. Kamasamudram, N.W. Currier, A. Yezerets, and L. Olsson. The Effect of NO_2/NO_x Feed Ratio on the NH_3-SCR System Over Cu–Zeolites with Varying Copper Loading. *Catalysis Letters*, 144:70–80, 2014.

[40] I. Nova, C. Ciardelli, E. Tronconi, D. Chatterjee, and M. Weibel. NH_3-NO/NO_2 SCR for Diesel Exhausts After Treatment: Mechanism and Modelling of a Catalytic Converter. *Topics in Catalysis*, 42–43:43–46, 2007.

[41] A. Grossale, I. Nova, E. Tronconi, D. Chatterjee, and M. Weibel. NH_3-NO/NO_2 SCR for Diesel Exhausts Aftertreatment: Reactivity, Mechanism and Kinetic Modelling of Commercial Fe- and Cu-Promoted Zeolite Catalysts. *Topics in Catalysis*, 52:1837–1841, 2009.

[42] M. Iwasaki and H. Shinjoh. A Comparative Study of "Standard", "Fast" and "NO_2" SCR Reactions over Fe/zeolite Catalyst. *Applied Catalysis A: General*, 390:71–77, 2010.

[43] G. Madia, M. Koebel, M. Elsener, and A. Wokaun. Side Reactions in the Selective Catalytic Reduction of NO_x with Various NO_2 Fractions. *Industrial & Engineering Chemistry Reserach*, 41:4008–4015, 2002.

CHAPTER 4

Monolith Model for the Ammonia Slip Catalyst

An optimal automotive ammonia slip catalyst (ASC) combines the high activity of the ammonia oxidation (AMOX) catalyst with the high efficiency of selective catalytic reduction of NO_x with NH_3 over an SCR catalyst (NH_3-SCR), to ensure minimal NH_3 breakthrough and limited formation of NO_x and N_2O. In this chapter, a single channel 1D-1D steady state mathematical model of the dual layer ammonia slip catalyst is derived and validated, providing a tool to gain a better understanding of the ASC. The model includes film diffusion from the gas channel to the washcoat surface, and diffusion and reaction throughout the washcoat layer. The kinetic models applied were derived based on activity measurements for 1 wt.% Pt/TiO_2-SiO_2 (AMOX) and 3.5 wt.% Cu-BEA (SCR). The monolith model was validated against experimental data for NH_3 oxidation over monolithic ammonia slip catalysts with the single layer AMOX, single layer SCR, single mixed layer (AMOX+SCR), and dual layer (SCR/AMOX) ASC configurations. The model describes the NH_3 conversion for the different catalyst systems well, while also giving a good description of the product selectivities and yields of NO_x, N_2O, and N_2.

4.1 Introduction

Due to its harmful effects, emission control regulations strictly limit the release of NO_x from diesel engines [1–3]. To ensure low NO_x emissions, diesel exhaust aftertreatment systems contain a NO_x abatement unit, which employs a catalyst for the selective catalytic reduction of NO_x with NH_3 injected upstream of the catalyst (NH_3-SCR) [3]. An excess of ammonia is dosed in order to maximize NO_x reduction, leading to a slip of unreacted NH_3 from the SCR catalyst [4]. However, NH_3 is also a regulated pollutant, and an ammonia slip catalyst (ASC) is therefore placed immediately after the SCR catalyst with the purpose of limiting NH_3 slip through the selective catalytic oxidation of NH_3 to N_2 and H_2O (NH_3-SCO) [3].

Early versions of the ASC consisted solely of an ammonia oxidation (AMOX) catalyst (single layer AMOX; SL-AMOX) based on supported platinum group metals (PGM), due to their high oxidation activity [3, 5, 6]. The desired NH_3-SCO of ammonia to N_2 is given by reaction R 4.1:

$$4\,NH_3 + 3\,O_2 \rightarrow 2\,N_2 + 6\,H_2O \tag{R 4.1}$$

However, the PGM catalysts exhibit a poor selectivity towards N_2, with considerable N_2O formation (R 4.2) reaching a significant maximum between 225–300°C, and NO_x formation (R 4.3 and R 4.4) becoming increasingly dominant for temperatures above 250°C [3, 6–13].

$$4\,NH_3 + 4\,O_2 \rightarrow 2\,N_2O + 6\,H_2O \tag{R 4.2}$$

$$4\,NH_3 + 5\,O_2 \rightarrow 4\,NO + 6\,H_2O \tag{R 4.3}$$

$$NO + \frac{1}{2}\,O_2 \rightleftarrows NO_2 \tag{R 4.4}$$

This behavior is counterproductive for the diesel exhaust aftertreatment system, since NO_x and N_2O are formed from the NH_3 initially introduced to reduce NO_x. Furthermore, the formation of N_2O is problematic since it is a more potent greenhouse gas than CO_2 [3].

To improve the performance of the ASC, an SCR catalyst is introduced into the catalyst formulation, either mechanically mixed together with the AMOX catalyst (single mixed layer; SML) [8, 10–12, 14], or as a separate layer on top of the AMOX catalyst, resulting in a dual layer structure (dual layer; DL) [3, 6–12]. Recently, a combination of a mechanically mixed bottom layer with an SCR top layer has also been demonstrated (hybrid dual layer; HDL) [10]. The inclusion of the SCR catalyst introduces the SCR reactions (R 4.5–R 4.7) enabling unreacted NH_3 to reduce the NO_x formed through NH_3 oxidation over the AMOX catalyst. Depending on the SCR catalyst, NH_3 and NO_x may also react to form N_2O (R 4.8 and R 4.9) [15–17]. The result of including an SCR catalyst is an overall improved N_2 selectivity, and a correspondingly lower NO_x and N_2O selectivity [3, 6–12, 14].

$$4\,NH_3 + 4\,NO + O_2 \rightarrow 4\,N_2 + 6\,H_2O \tag{R 4.5}$$

$$4\,NH_3 + 3\,NO_2 \rightarrow \frac{7}{2}\,N_2 + 6\,H_2O \tag{R 4.6}$$

$$4\,NH_3 + 2\,NO + 2\,NO_2 \rightarrow 4\,N_2 + 6\,H_2O \tag{R 4.7}$$

$$4\,NH_3 + 4\,NO + 3\,O_2 \rightarrow 4\,N_2O + 6\,H_2O \quad \text{(R 4.8)}$$

$$4\,NH_3 + 4\,NO_2 \rightarrow 2\,N_2 + 2\,N_2O + 6\,H_2O \quad \text{(R 4.9)}$$

Figure 4.1 illustrates the different ASC configurations discussed and their working principles with regards to the initial oxidation of NH_3 to N_2, N_2O, and NO_x, and the subsequent NO_x reduction with NH_3 present over the SCR catalyst.

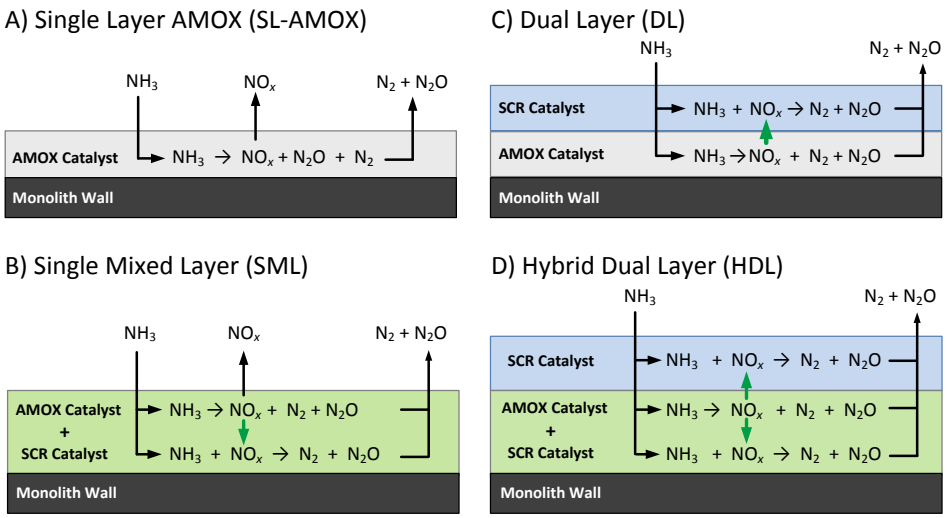

Figure 4.1: *Ammonia slip catalyst configurations: a) single layer AMOX (SL-AMOX), b) single mixed layer (SML), c) dual layer (DL), and d) hybrid dual layer (HDL) combining the SML and DL design. The green arrows emphasize the beneficial interactions of NO_x formed over the AMOX catalyst with the SCR reactions of the SCR catalyst, for the different ASC configurations. The black arrow indicates the release of NO_x from the AMOX catalyst to the gas phase.*

The ASC designs illustrated in Figure 4.1 have previously been studied using Pt/Al_2O_3 AMOX catalysts and Cu or Fe-zeolite SCR catalysts. Several experimental investigations and mathematical modeling studies have demonstrated a significantly improved N_2 selectivity of these ASC designs [5–7, 10–12, 14, 18, 19]. In the single layer AMOX and the SML, the AMOX catalyst is more directly accessible to the gas phase of the monolith channel, leading to higher NH_3 conversions. However, the greater accessibility also leads to a higher overall NO_x selectivity, since not all NO_x formed passes the SCR catalyst before transferring to the channel gas phase [10–12, 14]. In contrast, for the dual layer ASC designs with a SCR top layer, the NO_x formed over the AMOX catalyst diffuses through the SCR catalyst in order to reach the gas phase of the channel, which leads to a lower NO_x selectivity [5, 10–12, 14]. An additional benefit of the SCR top layer in the DL design is the better NH_3-SCR performance, in terms of N_2 selectivity and NO_x conversion, which is relevant in situations where the performance of the NH_3-SCR unit is insufficient and the ASC must act as an extension of the SCR unit [10, 12]. However, the SCR top layer impedes the accessibility of NH_3 to the AMOX catalyst because it acts as diffusion barrier, leading to lower NH_3 conversion [5, 10–12, 14]. With regard to N_2O selectivity, the SML design benefits from the close proximity of the AMOX

catalyst to the SCR catalyst, since the SCR catalyst is more readily accessible to the NO_x formed by the AMOX catalyst [8]. As a result, a greater fraction of NO is reduced to N_2 rather than reacting further over the AMOX catalyst to N_2O [10–12]. Overall, the inclusion of an SCR catalyst significantly improves N_2 selectivity of the ASC.

Further development of the ASC includes improvements of the individual catalyst formulations (AMOX and SCR) and improving how they compliment each other, as well as optimization of the monolithic catalyst design. The latter focuses on varying the catalyst loadings of the AMOX and SCR catalysts and controlling factors that influence the effective diffusion coefficients in the washcoat layers [5, 7, 10, 20]. Motivated by the potential to improve system understanding and reduce experimental effort, we further develop an isothermal steady-state mathematical model for a single channel of the monolithic ASC, based on previous work [21]. Kinetic models for a supported Pt-based AMOX catalyst and a Cu-BEA SCR catalyst, with high SCR and NH_3 oxidation activity, were derived based on activity measurements from fixed bed reactors. The kinetic model for the SCR catalyst includes a transition between low and high temperature kinetics, in order to describe the observed atypical behavior of the NO conversion in NH_3-SCR over Cu-zeolites [22–25]. The resulting single channel model was validated against experimental data for NH_3 oxidation over four monolithic catalysts: SL-AMOX, SL-SCR, SML, and DL. The model describes the NH_3 conversion for the different catalyst systems well, while also giving a good description of the product selectivities and yields of N_2, N_2O, NO_x.

4.2 Experimental

4.2.1 Catalyst Preparation

4.2.1.1 Powder Catalysts

The monolithic ASC samples studied in this work were prepared at Haldor Topsøe A/S and were based on the combination of a 1 wt.% Pt/TiO_2 AMOX catalyst stabilized with SiO_2 (referred to as 1 wt.% Pt/TiO_2-SiO_2) and a 3.5 wt.% Cu-BEA SCR catalyst. The 1 wt.% Pt/TiO_2-SiO_2 AMOX catalyst was prepared by impregnation of the support material with $Pt(NH_3)_4(HCO_3)_2$, followed by drying at 100°C and calcination at 550°C in air for 2 hours. The 3.5 wt.% Cu-BEA SCR catalyst was prepared by impregnation of the parent beta zeolite (Si/Al=20) with $Cu(NO_3)_2 \cdot 3\,H_2O$, followed by drying at 115°C and calcination in air at 550°C. The catalysts were tableted, crushed, and sieved to a fraction of either 106–150 µm or 150–300 µm prior to activity measurements using fixed bed reactors.

4.2.1.2 Monolith Catalysts

Four monolithic ammonia slip catalysts were prepared with four different configurations: single layer AMOX (SL-AMOX), single layer SCR (SL-SCR), single mixed layer (SML), and dual layer (DL). The catalysts were prepared by dip coating cordierite monolith substrates with square channels in slurries of 1 wt.% Pt/TiO_2-SiO_2 (AMOX catalyst) and/or 3.5 wt.% Cu-BEA (SCR catalyst). The aqueous slurries consisted of the respective catalysts and a colloidal silica binder. In the

case of the AMOX catalyst slurry for SL-AMOX and DL, Pt-free TiO_2-SiO_2 support material was added in order to dilute the Pt content from 1 wt.% to 0.25 wt.%. The Pt content was confirmed by inductively coupled plasma optical emission spectrometry (ICP-OES) for a calcined sample of the AMOX catalyst slurry to be 0.235 wt.% Pt. An aqueous NH_3 solution was used to regulate the pH of the washcoat slurry to 9–10. The slurries were milled to break agglomerates and obtain small catalyst particles with an average catalyst particle size of 3 µm for the AMOX catalyst and 18 µm for the SCR catalyst. For the SCR catalyst slurry applied to the SL-SCR and DL, an aqueous solution of organic stabilizer (xanthan gum) was added after milling. In order to control the catalyst loading applied by dip coating, the dry matter content was adjusted by adding demineralized water. Due to practical reasons, different batches of the 1 wt.% Pt/TiO_2-SiO_2 and 3.5 wt.% Cu-BEA were used for dip coating and fixed bed reactor experiments.

To avoid differences in the AMOX catalyst loading for the SL-AMOX and DL samples, a large monolith substrate (Ø 26.6 cm x L 15.2 cm) with 300 cells per square inch and 6 mil (152 µm) thick channel walls was initially coated with the AMOX washcoat slurry by dip coating. The excess slurry was removed by blowing a stream of air through the channels using an air knife. The coated monolith substrate was then dried overnight at room temperature, with a flow of air through the channels, followed by further drying overnight in an oven at 80°C. The dried AMOX catalyst coated monolith was cut into smaller samples (Ø 5 cm x L 3.7 cm). To prepare the DL sample, a small sample coated with AMOX catalyst was dip coated with SCR washcoat slurry. The single layer Cu-BEA SCR sample was prepared by dip coating a small (Ø 5 cm x L 3.7 cm) sample of uncoated cordierite monolith substrates of the same type used for the initial AMOX catalyst washcoating. The SML catalyst was prepared using a similar procedure, but using a slurry containing mixture of the AMOX and SCR catalysts. After dip coating and removal of excess slurry, the small monolithic catalyst samples were dried at room temperature with a flow of air through the channels for 30 minutes. Lastly, the monolithic catalyst samples were calcined at 550°C for 2 hours. An overview of the prepared catalysts is presented in Table 4.1.

Table 4.1: *Overview of the monolithic ammonia slip catalysts prepared by dip coating with slurries of 1 wt.% Pt/TiO_2-SiO_2 (AMOX) and/or 3.5 wt.% Cu-BEA zeolite (SCR). The values given in the shorthand notation indicate the loading (g/L) of each catalyst, in each layer.*

Sample	**AMOX Loading** ($\mathbf{g_{wc}/L_{monolith}}$)	**Pt Loading** ($\mathbf{g_{Pt}/L_{monolith}}$)	**SCR Loading** ($\mathbf{g_{wc}/L_{monolith}}$)	**Shorthand Notation**
SL-AMOX	26	0.06	0	$\overline{26\,\mathrm{AMOX}}$
SL-SCR	0	0	61	$\overline{61\,\mathrm{SCR}}$
SML	12	0.12	110	$\overline{12\,\mathrm{AMOX} + 110\,\mathrm{SCR}}$
DL	26	0.06	54	$\frac{54\,\mathrm{SCR}}{26\,\mathrm{AMOX}}$

4.2.2 Catalyst Evaluation

4.2.2.1 Fixed Bed Reactor

The catalytic activity of the AMOX and SCR catalysts were evaluated using two different fixed bed reactor setups. For the AMOX catalyst, the fixed bed reactor setup used a quartz U-tube reactor (D_i = 2 mm) loaded with 5 mg of the 1 wt.% Pt/TiO_2-SiO_2 catalyst (150–300 µm), fixed between two plugs of quartz wool. A thermocouple was placed at the position of the catalyst bed on the outside of the reactor. The feed gas consisted of 500 ppm NH_3, 5 vol.% H_2O, 10 vol.% O_2, and balance N_2, with a total flow of 400 NmL/min. A FTIR gas analyzer (Gasmet; CX4000) measured the concentrations of NH_3, NO, NO_2, N_2O, and H_2O in the outlet gas. The N_2 concentration was calculated from the N-balance. The catalyst was heated to 550°C at a rate of 20°C/min in the feed gas and held at these conditions for 1 hour. Afterwards, the catalyst was stepwise cooled to 200°C, with smaller steps taken for temperatures below 300°C. Steady-state measurements were made at each temperature for a duration of 20 minutes.

A second fixed bed reactor setup was used for the catalytic activity measurements of the 3.5 wt.% Cu-BEA SCR catalyst. A quartz U-tube reactor (D_i = 6 mm) was loaded with a mixture of 20 mg catalyst (106–150 µm) and 100 mg SiC (150–300 µm), fixed between two plugs of quartz wool. For measurements made below 225°C, a loading of 40 mg catalyst and 200 mg SiC was used instead to obtain sufficient activity. The gas flowed upwards through the catalyst bed and the temperature was measured with a thermocouple placed inside the reactor at the catalyst bed outlet. The base of the feed gas consisted of 5 vol.% H_2O, 10 vol.% O_2, and balance N_2, with a total flow of 1000 NmL/min. Water was added to the gas mixture by bubbling a separate flow of N_2 through water heated to 80°C. Concentrations of approximately 600 ppm NH_3 and 500 ppm NO_x were used to give an NH_3-to-NO_x ratio of 1.2. The NO_2/NO_x ratio was varied between 0, 0.5, or 1 to achieve standard, fast, or slow SCR conditions, respectively. Using feed gases where the only key reactant was NH_3, NO, or NO_2 allowed for the study of NH_3 oxidation, NO oxidation, or NO_2 decomposition, respectively. The concentrations of NH_3, NO, and NO_2 were measured using a continuous gas analyzer (Limas11-HW; ABB) and the concentration of H_2O was determined using a humidity probe (HC2-IC102; Rotronic). After the gas analyzer, H_2O was condensed from the gas and the concentration of N_2O in the resulting gas was measured using a micro-GC (Varian; CP-490), and corrected with regards to the concentration of water removed. The N_2 concentration was calculated from the N-balance. The catalyst was initially heated at 550°C in a standard SCR mixture for 1 hour and then cooled to 150°C in the same gas mixture. The catalyst was then heated to the temperatures of interest and the catalytic activity for the different reaction conditions were measured for a duration of 1 hour each, with feed gas measurements made both before and after. Studies with catalyst particles of 106–150 µm and 150–300 µm under standard and fast SCR conditions showed that the reactions were not diffusion limited.

4.2.2.2 Monolith Flow Reactor

The monolith catalysts prepared were tested for NH_3 oxidation in a flow reactor designed for testing of small monolith samples with a diameter of 5 cm. Prior to

loading the monolithic catalyst (Ø 5 cm x L 3.7 cm), a small hole was drilled in the middle of the outlet end of the monolith, in order to accommodate the thermocouple placed in the center of the sample. The monolith sample was then loaded into a steel reactor, with a mixing block placed directly upstream. The base of the feed gas was made by mixing flows of air, N_2, and H_2O. The gas flow was directed through a pre-heater which was used to heat the gas and thereby regulate the temperature of the reactor. Just before the mixing block, a concentrated NH_3 gas in N_2 was added to the feed gas. The resulting feed gas consisted of 200 ppm NH_3, 4 vol.% H_2O, 12 vol.% O_2, and balance N_2, with a total flow of 18,200 NL/hr. This gave a gas hourly space velocity (GHSV) of 250,000 hr^{-1}, based on the total gas flow and the total volume of the monolith catalyst sample. Shortly downstream of the catalyst, a FTIR gas analyzer (Gasmet; CX4000) was used to measure NH_3, NO, NO_2, N_2O, and H_2O. The reactor was initially heated to 170°C, and since the AMOX catalyst is not active for NH_3 oxidation at this temperature, the measurement made at these conditions was used as the feed gas measurement. Subsequently, steady-state measurements were made between 200–550°C.

4.3 Mathematical Modeling

4.3.1 Fixed Bed Reactor Model

The kinetic models of the AMOX and SCR catalysts were derived based on the activity measurements made (Section 4.2.2.1) and using a reactor model for the fixed bed reactor. The model was implemented in MATLAB, a commercial software, and the *lsqcurvefit* function was used to fit the kinetic parameters (A_j, $E_{A,j}$). The objective function was set to minimize the difference between simulated and experimental outlet concentrations of the reactants and products (i =NH_3, NO, NO_2, N_2O, and N_2), as given by equation 4.1:

$$\min_{A_j,\, E_{A,j}} = \sum_i \left(y(A_j,\, E_{A,j})_{\mathrm{sim},i} - y_{\mathrm{exp},i}\right)^2 \tag{4.1}$$

The model used to describe the fixed bed reactor considered steady-state, isothermal, and isobaric conditions. The equation for the fixed bed reactor material balance in terms of the concentration, C (mol/m^3), of reactant i for the gas phase is:

$$Q\frac{\mathrm{d}C_i}{\mathrm{d}W} = R_i' \tag{4.2}$$

For equation 4.2, Q (m^3/s) is the standard volumetric flow rate and the catalyst mass is given by W (kg_{cat}). R_i' (mol/(s·kg_{cat})) is the mass based catalytic rate of reaction for reactant i. The concentration of reactant i, C_i, was expressed using the partial pressure, p_i, via the ideal gas law ($C_i = p_i \cdot R \cdot T$). The material balance for the adsorbed phase is simplified by the steady-state conditions:

$$\Omega_i \frac{\mathrm{d}\theta_i}{\mathrm{d}t} \approx 0 \tag{4.3}$$

The adsorption capacity of the catalyst for reactant i is expressed by Ω_i (mol/kg_{cat}) and θ_i is the surface coverage of the catalyst with adsorbed reactant i. The catalytic mass based rate of reaction for each reactant i is expressed as:

$$R'_{\mathrm{cat},i} = \sum_{j=1}^{N_r} \nu_{i,j} \cdot r'_j(p_i, \theta_i, T) \tag{4.4}$$

In equation 4.4, $\nu_{i,j}$ is the stoichiometric coefficient for reactant i in reaction j, and r'_j (mol/(s·kg$_{cat}$)) is the rate of reaction j, which is further expressed using the respective gas phase concentrations (in partial pressures, p) and surface coverages of the reactants, and the reaction rate coefficient, k_j. The reaction rate coefficient is calculated from the Arrhenius expression:

$$k_j = A_j \exp\left(\frac{-E_{A,j}}{R \cdot T}\right) \tag{4.5}$$

In equation 4.5, A_j (mol/(s·kg$_{cat}$), mol/(s·kg$_{cat}$·bar), mol/(s·kg$_{cat}$·bar^2),mol/(s·kg$_{cat}$·bar$^{\frac{3}{2}}$) is the pre-exponential factor with units depending on the rate expression, $E_{A,j}$ (kJ/mol) is the activation energy, R (J/(mol·K)) is the gas constant, and T is the catalyst temperature.

4.3.2 Kinetic Model for the Ammonia Oxidation Catalyst (1 wt.% Pt/TiO$_2$-SiO$_2$)

A kinetic model for NH_3 oxidation catalyzed by the 1 wt.% Pt/TiO_2-SiO_2 was developed to describe the oxidation of NH_3 for the different ASC configurations. The kinetic model is summarized in Table 4.2 and includes the adsorption and desorption of NH_3 on the catalyst surface (AMOX.1), the oxidation of adsorbed NH_3 to N_2 (AMOX.2) and NO (AMOX.3), and the oxidation of NO to NO_2 (AMOX.5f). The oxidation of NO is a reversible reaction and is limited by the thermodynamic equilibrium, which pushes the equilibrium towards NO with increasing temperature, through the decomposition NO_2 (AMOX.5b) [11, 12, 15]. The equilibrium constant for this reaction was calculated using thermodynamic data [26] and ensured thermodynamic consistency. Furthermore, the formation of N_2O was accounted for by the reaction between NH_3 and NO (R 4.8) as described by previous experimental and modeling studies [5, 8, 12, 27]. The reaction conditions considered in this work include a significant excess of H_2O and O_2 compared to the key reactants and products (NH_3, NO, NO_2, and N_2O). Due to the high excess of H_2O and O_2, the concentrations of these species were constant and were not included in the kinetic model. The exception to this statement is the rate expression for NO oxidation and NO_2 decomposition (AMOX.5), where the O_2 concentration is included. The rate expressions used to describe the 1 wt.% Pt/TiO_2-SiO_2 AMOX catalyst are given in Table 4.2.

4.3.3 Kinetic Model for the Selective Catalytic Reduction Catalyst (3.5 wt.% Cu-BEA)

The kinetic model for the 3.5 wt.% Cu-BEA SCR catalyst is based on a kinetic model for Cu-CHA by Metkar et al. [15]. As summarized in Table 4.3, the model considers NH_3 adsorption and desorption on the catalyst (SCR.1). The adsorbed NH_3 reacts with O_2, NO, and NO_2 through the various oxidation and SCR reactions. The oxidation reactions are similar to those for the AMOX catalyst and include NH_3 oxidation (SCR.2), NO oxidation (SCR.3f), and NO_2 decomposition (SCR.3b). In contrast to the Pt-based AMOX catalyst, the NH_3 oxidation reaction on Cu-BEA primarily leads to the formation of N_2, with NO and N_2O being formed in rather insignificant quantities [10, 15, 16]. As a result, we only consider N_2 as the product of NH_3 oxidation. The oxidation of NO and the decomposition of NO_2 was

Table 4.2: *Kinetic model for the 1 wt.% Pt/TiO_2-SiO_2 AMOX catalyst.*

Reaction #	**Reaction**	**Rate Expression**	A_j	$E_{\mathrm{A},j}$
AMOX.1f	$\mathrm{NH_3} + * \rightarrow \mathrm{NH_3}*$	$k_{\mathrm{AMOX.1f}} \cdot p_{\mathrm{NH_3}} \cdot (1 - \theta_{\mathrm{NH_3}})$	1.2×10^3	0
AMOX.1b	$\mathrm{NH_3}* \rightarrow \mathrm{NH_3} + *$	$k_{\mathrm{AMOX.1b}} \cdot \theta_{\mathrm{NH_3}}$	1.3×10^9	91.0
AMOX.2	$4\,\mathrm{NH_3}* + 3\,\mathrm{O_2} \rightarrow 2\,\mathrm{N_2} + 6\,\mathrm{H_2O} + 4*$	$k_{\mathrm{AMOX.2f}} \cdot \theta_{\mathrm{NH_3}}$	2.0×10^{25}	258.8
AMOX.3	$4\,\mathrm{NH_3}* + 5\,\mathrm{O_2} \rightarrow 4\,\mathrm{NO} + 6\,\mathrm{H_2O} + 4*$	$k_{\mathrm{AMOX.3f}} \cdot \theta_{\mathrm{NH_3}}$	1.8×10^{29}	302.4
AMOX.4	$4\,\mathrm{NH_3}* + 4\,\mathrm{NO} + 5\,\mathrm{O_2} \rightarrow 4\,\mathrm{N_2O} + 6\,\mathrm{H_2O} + 4*$	$k_{\mathrm{AMOX.4f}} \cdot \theta_{\mathrm{NH_3}} \cdot p_{\mathrm{NO}}$	4.5×10^{22}	187.8
AMOX.5f	$\mathrm{NO} + \frac{1}{2}\,\mathrm{O_2} \rightarrow \mathrm{NO_2}$	$k_{\mathrm{AMOX.5f}} \cdot p_{\mathrm{NO}} \cdot p_{\mathrm{O_2}}^{\frac{1}{2}}$	1.2×10^4	28.7
AMOX.5b*	$\mathrm{NO_2} \rightarrow \mathrm{NO} + \frac{1}{2}\,\mathrm{O_2}$	$k_{\mathrm{AMOX.5b}} \cdot p_{\mathrm{NO_2}}$	—	—

* $k_{\mathrm{AMOX.5b}} = \frac{k_{\mathrm{AMOX.5f}}}{K_{\mathrm{eq}}}$, equilibrium constant, K_{eq}, calculated from thermodynamic data [26].
Units for $A_{\mathrm{AMOX.1b}}$, $A_{\mathrm{AMOX.2}}$, and $A_{\mathrm{AMOX.3}}$ are mol/(s·$\mathrm{kg_{cat}}$).
Units for $A_{\mathrm{AMOX.1f}}$, $A_{\mathrm{AMOX.4}}$, and $A_{\mathrm{AMOX.5b}}$ are mol/(s·$\mathrm{kg_{cat}}$·bar).
Units for $A_{\mathrm{AMOX.5f}}$ are mol/(s·$\mathrm{kg_{cat}}$·$\mathrm{bar}^{\frac{3}{2}}$) .

handled in the same manner as for the kinetic model of the AMOX catalyst, using thermodynamic data to ensure consistency with the thermodynamic equilibrium [26]. The SCR reactions are described in the model by the following reactions: standard (SCR.4), fast (SCR.8), and slow (SCR.6). Additionally, the Cu-BEA SCR catalyst is quite active in the formation of N_2O, and it has been attributed to the formation of an NH_4NO_3 intermediate from NH_3 and NO_2, and its subsequent decomposition [15, 16]:

$$2\,NH_3 + 2\,NO_2 \rightarrow [NH_4NO_3] + N_2 + H_2O \rightarrow N_2O + N_2 + 3\,H_2O \qquad \text{(R 4.10)}$$

The reaction between adsorbed NH_3 and NO_2 (SCR.7), based on reaction R 4.10, accounts for the formation of N_2O in the presence of NO_2 conditions, but not when only NO is present. As a result, we found it necessary to include a reaction between NH_3 and NO (SCR.5), similar to reaction R 4.8, in order to account for N_2O formation from a feed gas without NO_2. These two reactions account for the majority of N_2O formed during fast SCR conditions, but are not enough to account for all N_2O formed. As a result, it was necessary to include an extra N_2O contribution, due to an enhanced N_2O formation in the presence of both NO and NO_2 (SCR.9), similar to the improved rate of reaction during fast SCR conditions. By including the partial pressures of both NO and NO_2 in the rate expression, it is ensured that the reaction is only considered under fast SCR conditions, although it only consumes NO_2.

With regard to the standard SCR reaction, it has been reported in the literature [22–25] that the NO conversion versus temperature over Cu-zeolites is atypical. The NO conversion increases normally until about 225–250°C, at which point the conversion dips down to a local minimum, before increasing normally again at about 350°C [25]. This behavior corresponds to a gradual transition between a low temperature kinetic regime below 225°C and high temperature kinetic regime above 225°C. To account for this behavior in the kinetic model, two sets of kinetic parameters for the standard SCR and corresponding N_2O formation were included in the model; one set for each kinetic regime. To weigh the contribution of the low and high temperature kinetics, a fractional weighting given by x_{LT} and $x_{HT} = 1 - x_{LT}$ with values between 0 and 1 was applied. The balance and transfer between the kinetic regimes was modeled similar to an adsorption equilibrium reaction (SCR.10), with an equilibrium constant expressed using the following version of the Van 't Hoff equation:

$$K_{\mathrm{eq},\,x} = \exp\left(\frac{-\Delta H - T \cdot \Delta S}{R \cdot T}\right) \qquad (4.6)$$

The values for the change in reaction enthalpy, ΔH (J/mol), and entropy (J/(mol·K)), ΔS, were estimated by the parameter fitting. The fractions of x_{LT} and x_{HT} are determined from the equilibrium constant and the relationship between x_{LT} and x_{HT}:

$$x_{\mathrm{LT}} = \frac{1}{1 + K_{\mathrm{eq},x}} \qquad (4.7)$$

$$x_{\mathrm{HT}} = 1 - x_{\mathrm{LT}} \qquad (4.8)$$

Table 4.3 presents the reactions and rate expressions considered in the kinetic model for the 3.5 wt.% Cu-BEA SCR catalyst.

Table 4.3: *Kinetic model for the 3.5 wt.% Cu-BEA SCR catalyst.*

Reaction #	**Reaction**	**Rate Expression**	$\mathbf{A}_j$ [d]	$\mathbf{E}_{\mathrm{A},j}$ (kJ/mol)
SCR.1f[a]	$NH_3 + * \rightarrow NH_3*$	$k_{\mathrm{SCR.1f}} \cdot \frac{p_{NH_3}}{P_T} \cdot (1 - \theta_{NH_3})$	$6.68 \times 10^7 \cdot \rho_{\mathrm{SCR}}^{-1}$	0
SCR.1b[a]	$NH_3* \rightarrow NH_3 + *$	$k_{\mathrm{SCR.1b}} \cdot \theta_{NH_3}$	$4.00 \times 10^{15} \cdot \rho_{\mathrm{SCR}}^{-1}$	$145.9\,(1 - 0.97 \cdot \theta_{NH_3})$
SCR.2	$4\,NH_3* + 3\,O_2 \rightarrow 2\,N_2 + 6\,H_2O + 4*$	$k_{\mathrm{SCR.2}} \cdot \theta_{NH_3}$	9.94×10^{10}	162.87
SCR.3f[b]	$NO + \frac{1}{2}\,O_2 \rightarrow NO_2$	$k_{\mathrm{SCR.3f}} \cdot p_{NO} \cdot p_{O_2}^{\frac{1}{2}}$	1.28×10^3	31.06
SCR.3b[b]	$NO_2 \rightarrow NO + \frac{1}{2}\,O_2$	$k_{\mathrm{SCR.3b}} \cdot p_{NO_2}$	—	—
SCR.4	$4\,NH_3* + 4\,NO + O_2 \rightarrow 4\,N_2 + 6\,H_2O + 4*$	$k_{\mathrm{SCR.4,LT}} \cdot \theta_{NH_3} \cdot p_{NO} \cdot x_{LT} +$ $k_{\mathrm{SCR.4,HT}} \cdot \theta_{NH_3} \cdot p_{NO} \cdot x_{HT}$	LT: 1.56×10^{10} HT: 2.21×10^8	LT: 79.67 HT: 69.38
SCR.5	$4\,NH_3* + 4\,NO + 5\,O_2 \rightarrow 4\,N_2O + 6\,H_2O + 4*$	$k_{\mathrm{SCR.5}} \cdot \theta_{NH_3} p_{NO} x_{LT} +$ $k_{\mathrm{SCR.5}} \cdot \theta_{NH_3} \cdot p_{NO} x_{HT}$	LT: 6.14×10^6 HT: 1.70×10^4	LT: 56.22 HT: 39.88
SCR.6	$4\,NH_3* + 3\,NO_2 \rightarrow \frac{7}{2}\,N_2 + 6\,H_2O + 4*$	$k_{\mathrm{SCR.6}} \theta_{NH_3} \cdot p_{NO_2}$	1.83×10^{18}	157.17
SCR.7	$4\,NH_3* + 4\,NO_2 \rightarrow 2\,N_2 + 2\,N_2O + 6\,H_2O + 4*$	$k_{\mathrm{SCR.7}} \theta_{NH_3} \cdot p_{NO_2}$	6.08×10^{16}	140.74
SCR.8	$4\,NH_3* + 2\,NO + 2\,NO_2 \rightarrow 4\,N_2 + 6\,H_2O + 4*$	$k_{\mathrm{SCR.8}} \cdot \theta_{NH_3} \cdot p_{NO} \cdot p_{NO_2}$	8.17×10^{23}	162.21
SCR.9	$4\,NH_3* + 4\,NO_2 \rightarrow 2\,N_2 + 2\,N_2O + 6\,H_2O + 4*$	$k_{\mathrm{SCR.9}} \cdot \theta_{NH_3} \cdot p_{NO} \cdot p_{NO_2}$	2.65×10^{22}	149.25
SCR.10[c]	$x_{LT} \rightleftarrows x_{HT}$	$k_{\mathrm{SCR.10f}} \cdot x_{LT} - k_{\mathrm{SCR.10b}} \cdot x_{HT}$	—	—

[a] Kinetic parameters from reference [15]. Units of mol/(s·m^3_{cat}) , divided by ρ_{SCR} to convert to mass based value with units of mol/(s·kg_{cat}).
[b] $k_{\mathrm{SCR.3b}} = k_{\mathrm{SCR.3f}}/K_{\mathrm{eq}}$, equilibrium constant, K_{eq}, calculated from thermodynamic data.
[c] $k_{\mathrm{SCR.10f}}/k_{\mathrm{SCR.10b}} = K_{\mathrm{eq},x} = \exp\left(^{-\Delta H - T\Delta S}/_{RT}\right)$, $\Delta H = 1.04 \times 10^5$ J/mol and $\Delta S = 194.3$ J/(mol·K).
[d] Units for $A_{\mathrm{SCR.1b}}$ and $A_{\mathrm{SCR.2}}$ are mol/(s·kg_{cat}).
[d] Units for $A_{\mathrm{SCR.1f}}$, $A_{\mathrm{SCR.3b}}$, $A_{\mathrm{SCR.4}}$, $A_{\mathrm{SCR.5}}$, $A_{\mathrm{SCR.6}}$ and $A_{\mathrm{SCR.7}}$ are mol/(s·kg_{cat}·bar).
[d] Units for $A_{\mathrm{SCR.3f}}$ are mol/(s·kg_{cat}·$bar^{\frac{3}{2}}$).
[d] Units for $A_{\mathrm{SCR.8}}$ and $A_{\mathrm{SCR.9}}$ are mol/(s·kg_{cat}·bar^2).

4.3.4 Monolith Model for Dual Mixed Layer Ammonia Slip Catalyst

The ASC monolith reactor model was derived and implemented for a dual mixed layer (DML) configuration. The DML configuration consists of two catalyst layers, each containing a mixture of AMOX and SCR catalyst, as illustrated in Figure 4.2. Basing the framework of the ASC model on the DML configuration provides a flexible model that can simulate ten different ASC configurations, including single layer AMOX, single layer SCR, single mixed layer, and dual layer configurations.

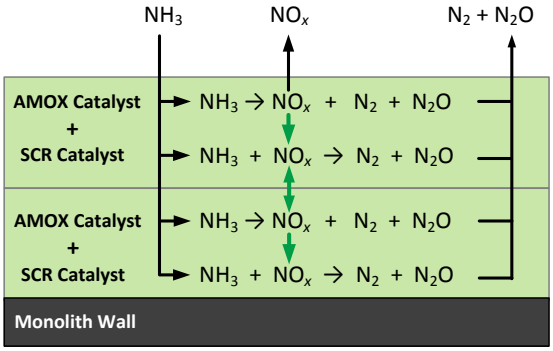

Figure 4.2: *Illustration of the dual mixed layer (DML) ammonia slip catalyst configuration, which the ASC monolith model was based on.*

The monolith reactor model was based on a single channel of a monolithic ASC catalyst. A tank-in-series modeling approach was taken and the model considered isothermal, isobaric, and steady state conditions. For each tank in the model, the convective gas flow into and out of the tank was considered, as well as the mass transfer across the gas film between the gas phase and the surface of the catalyst washcoat:

$$Q \cdot C_{\mathrm{g},i,k-1} - Q \cdot C_{\mathrm{g},i,k} = k_{\mathrm{mt},i} \cdot A_{\mathrm{S}} \left(C_{\mathrm{g},i,k} - C_{\mathrm{s},i,k}\right) \tag{4.9}$$

In equation 4.9 , the volumetric flow is given by Q (m^3/s) and is constant throughout the monolith channel. The external surface area of the catalyst washcoat per tank is A_{S} and is also constant throughout the monolith channel. The gas phase concentration ($\mathrm{mol}/\mathrm{m}^3$) of species i, entering tank number k, is given as $C_{\mathrm{g},i,k-1}$, while the concentration for the exiting gas flow is given as $C_{\mathrm{g},i,k}$. Similarly, the concentration ($\mathrm{mol}/\mathrm{m}^3$) of reactant i at the surface of the washcoat phase is $C_{\mathrm{s},i,k}$. The mass transfer coefficient of reactant i, $k_{\mathrm{mt},i}$ (m/s), was calculated using the bulk diffusion coefficient of species i, $D_{\mathrm{bulk},i}$ (m^2/s), the hydraulic diameter of the coated channel, d_{H} (m), and a position dependent Sherwood number, Sh:

$$k_{\mathrm{mt},i} = \frac{D_{\mathrm{bulk},i} \cdot Sh}{d_{\mathrm{H}}} \tag{4.10}$$

The bulk diffusion coefficients for NH_3, NO, NO_2, and N_2O were calculated using temperature dependent expressions readily available in literature for studies of similar catalyst systems [15], and are summarized in Table 4.4.

Table 4.4: *Expressions for the bulk diffusion coefficients with varying temperature [15].*

Species	**Diffusion Coefficient (m^2/s)**
NH_3	$1.215 \times 10^{-9} \cdot T^{1.7389}$
NO	$1.2365 \times 10^{-9} \cdot T^{1.7006}$
NO_2	$7.9236 \times 10^{-10} \cdot T^{1.7297}$
N_2O	$8.1452 \times 10^{-10} \cdot T^{1.7314}$

The position dependent Sherwood number was calculated using the following correlation [9, 28]:

$$Sh = Sh_\infty + 8.827\,(1000 \cdot z)^{-0.545} \exp\left(-48.2 \cdot z\right) \tag{4.11}$$

where Sh_∞ is the asymptotic Sherwood number (2.98 for square channels) and z is the dimensionless position in the channel. The dimensionless position, z, was calculated using equation 4.12, in which x (m) is the axial position in the channel and u_x (m/s) is the linear gas velocity:

$$z = \frac{x \cdot D_{\text{bulk},i}}{u_x \cdot d_{\text{H}}^2} \tag{4.12}$$

For each tank considered, the intrapore diffusion and reaction of NH_3, NO, NO_2, and N_2O throughout the catalyst washcoat phase was modeled:

$$D_{\text{eff},i} \frac{\mathrm{d}^2 C_{\text{wc},i}}{\mathrm{d}r^2} + \sum_{\text{cat}}^{\text{AMOX, SCR}} \left(\phi_{\text{cat}} \cdot \rho_{\text{cat}} \cdot R'_{\text{cat},i}\right) = 0 \tag{4.13}$$

The rate of reaction for reactant i, $R'_{\text{cat},i}$, is modeled using the kinetic models based on the fixed bed reactor data for the AMOX and SCR catalysts, and is converted to the volume based rate of reaction using the catalyst density, ρ_{cat} ($\text{kg}_{\text{cat}}/\text{m}^3$). The densities for the catalysts considered in this work are $\rho_{\text{AMOX}} = 1127\ \text{kg}_{\text{cat}}/\text{m}^3$ and $\rho_{\text{SCR}} = 954\ \text{kg}_{\text{cat}}/\text{m}^3$. The behavior of a mixed layer is modeled by the summation of the AMOX and SCR kinetics, with their independent contributions to the total rate of reaction determined from the volume fractions of each catalyst, ϕ_{cat} (cat=AMOX or SCR). For example, a volume fraction of $\phi_{\text{cat}} = 1$ will correspond to a pure single layer of the respective catalyst, while $\phi_{\text{cat}} = 0.5$ will correspond to a volume-based 1:1 mixture of the AMOX and SCR catalysts.

To calculate the concentration profiles through the washcoat layer at a given location in the monolith, we introduce the following boundary conditions for the washcoat layer. At the surface of the top washcoat layer (tl), the steady-state assumption entails that the mass transfer across the gas film is equal to the flux of mass into the washcoat phase, thereby avoiding an accumulation of mass in the system:

$$D_{\text{eff,tl},i} \left.\frac{\mathrm{d}C_{\text{wc},i}}{\mathrm{d}r}\right|_{\text{gas/tl}} = k_{\text{mt},i} \cdot A_{\text{S}} \left(C_{\text{g},i,k} - C_{\text{s},i,k}\right) \tag{4.14}$$

At the bottom of the washcoat phase, at the interface between the bottom layer (bl) and the non-porous monolith wall, the boundary condition is:

$$\left.\frac{\mathrm{d}C_{\text{wc},i}}{\mathrm{d}r}\right|_{\text{bl/wall}} = 0 \tag{4.15}$$

When modeling single layer catalysts, the bottom layer and the top layer are the same layer (bl=tl). For cases where there are two catalyst layers and the effective diffusivity of the top layer is different from that of the bottom layer, it is necessary to specify the boundary conditions at the interface between the catalyst layers. The first boundary condition (4.16) states that the amount of mass diffusing into the bottom layer from the top layer must be equal to the amount of mass diffusing into the top layer from the bottom layer.

$$D_{\text{eff,tl},i} \left.\frac{\mathrm{d}C_{\text{wc},i}}{\mathrm{d}r}\right|_{\text{tl/bl}} = D_{\text{eff,bl},i} \left.\frac{\mathrm{d}C_{\text{wc},i}}{\mathrm{d}r}\right|_{\text{bl/tl}} \tag{4.16}$$

The second boundary condition for the interface is an equation of continuity for the different species at the interface.

$$C_{\text{wc},i}|_{\text{tl/bl}} = C_{\text{wc},i}|_{\text{bl/tl}} \tag{4.17}$$

The effective diffusion coefficient in the catalyst washcoat phase, D_{eff}, is calculated using the mean transport pore model [29], which accounts for contributions from both bulk and Knudsen diffusion:

$$D_{\text{eff},i} = \frac{\epsilon}{\tau} \cdot \left(\frac{1}{D_{\text{bulk},i}} + \frac{1}{D_{\text{Knudsen},i}} \right)^{-1} \tag{4.18}$$

The values of the porosity, ϵ, and tortuosity, τ, are set to 0.4 and 3, respectively, which are realistic values. As previously mentioned, the bulk diffusion coefficients, $D_{\text{bulk},i}$, for NH_3, NO, NO_2, and N_2O were calculated using expressions readily available from previous studies of similar catalyst systems and are summarized in Table 4.4 [15]. The Knudsen diffusion coefficient, D_{Knudsen}, was calculated using equation 4.19, where $M_{\text{w},i}$ (kg/mol) is the molar mass of specie i, and $d_{\text{pore,wc}}$ (m) is the mean pore diameter for the respective catalyst washcoat layer (tl or bl):

$$D_{\text{Knudsen},i} = \frac{d_{\text{pore,wc}}}{3} \sqrt{\frac{8 \cdot R \cdot T}{M_{\text{w},i} \cdot \pi}} \tag{4.19}$$

The values for the average pore diameters, $d_{\text{pore,wc}}$, were the only unknown values for the ASC model and were estimated by fitting the model against the experimental data for the monolithic ASC catalysts.

The monolith model was implemented in MATLAB and solved using the *bvp4c* function used to solve boundary value problems. Initial simulations showed that by using 10 tanks or more, the difference in solutions resulting from a difference in number of tanks in series was negligible. Based on this, we chose to use 10 tanks for our simulations, and a frequency of 2 steps per µm washcoat to achieve a detailed mesh of the washcoat phase and a good resolution of the washcoat concentration profiles.

4.4 Results

4.4.1 Fit of the Kinetic Model for 1 wt.% Pt/TiO_2-SiO_2

The results of the activity measurements for NH_3 oxidation over the 1 wt.% Pt/TiO_2-SiO_2 AMOX catalyst is presented in Figure 4.3 together with the model fit. The

corresponding kinetic parameters of the model fit are presented in Table 4.2. The experimental data for NH_3 oxidation shows a steep decrease of the NH_3 concentration as the temperature is increased from 200°C to 250°C, reaching 50% conversion at 229°C and 100% at 250°C. The product selectivity is mostly towards N_2 between 200–250°C, with a maximum of 75% N_2 selectivity at 230°C. The selectivity towards N_2O formation steeply increases at temperatures above 220°C as the N_2 selectivity decreases, and a maximum of 49% N_2O selectivity at 270°C is observed. Above 250°C, the formation of NO becomes increasingly significant, while the product selectivity towards N_2 and N_2O decreases simultaneously. Furthermore, the formation of NO_2 is seen to increase from 275°C to a maximum of 100 ppm NO_2 at 450°C (20% NO_2 selectivity). The maximum in NO_2 is a result of the thermodynamic equilibrium for the $NO + {}^1/_2\,O_2 \rightleftarrows NO_2$ reaction, which causes the reaction to shift towards NO as the temperature is increased.

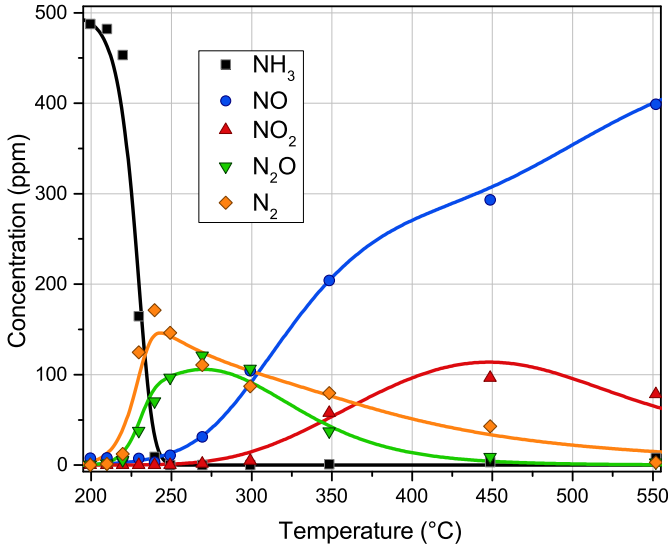

Figure 4.3: *Comparison of the NH_3 conversion and product yields, based on the experimental data (symbols) and the model (solid lines) with the fitted kinetic parameters, for the oxidation of NH_3 over the 1 wt.% Pt/TiO_2-SiO_2 catalyst. Values for N_2 were calculated from the N-balance. Operating conditions: 5 mg 1 wt.% Pt/TiO_2-SiO_2 AMOX catalyst sample, 500 ppm NH_3, 5 vol.% H_2O, 10 vol.% O_2, and balance N_2, with a total flow of 400 NmL/min.*

As shown in Figure 4.3, the oxidation of NH_3 over the 1 wt.% Pt/TiO_2-SiO_2 AMOX catalyst is very well described by the fixed bed reactor model using the kinetic model presented in Table 4.2. Between 250–350°C, the model predicts a slightly greater N_2 concentration of about 15 ppm and a N_2O concentration that is correspondingly 15 ppm lower. The kinetic parameters presented in Table 4.2 include extraordinarily high activation energies for reactions AMOX.2–AMOX.4, which are necessary for this kinetic model to describe the sharp transition from 0 to 100% conversion between 200–250°C seen in the experimental data.

4.4.2 Fit of the Kinetic Model for 3.5 wt.% Cu-BEA

The kinetic parameters determined from parameter fitting of the kinetic model for the SCR catalyst are presented in Table 4.3. The corresponding experimental data with model fits are presented in Figure 4.4 for A) NH_3 oxidation, B) NO oxidation, C) NO_2 decomposition, D) standard SCR (NO_2/NO_x=0), E) slow SCR (NO_2/NO_x=1), and F) fast SCR (NO_2/NO_x=0.5). For Figures 4.4 D, E, and F, the two points at 225°C are the result of overlap in measurements done with 40 mg catalyst for ≤225°C and 20 mg catalyst for ≥225°C (Section 4.2.2.1).

From Figure 4.4A, the 3.5 wt.% Cu-BEA catalyst is seen to become quite active and selective in the oxidation of NH_3 to N_2 starting from about 300°C, and reaching 80% conversion at 500°C with only 5 ppm N_2O and 22 ppm NO_x formed. The limited formation of these two species supports the decision not to include NH_3 oxidation to NO_x or N_2O in the SCR kinetic model. Figures 4.4B and 4.4C show the oxidation of NO and NO_2 decomposition over the Cu-BEA catalyst, respectively. Although the 3.5 wt.% Cu-BEA does catalyze these reactions, the activity is quite low relative to other catalysts, such as noble metals, e.g. Pt/Al_2O_3 [30].

The catalytic activity of the Cu-BEA catalyst for the standard SCR reaction is shown in Figure 4.4D, with the atypical behavior clearly noticeable in the measured NO concentrations and the N_2 concentration determined from the N-balance. Also interesting to note, is the bimodal behavior in the N_2O concentration profile. The N_2O concentration increases with temperature up until the maximum of 24 ppm N_2O at 250°C, at which point it decreases until a minimum of about 9 ppm N_2O between 325–400°C, before increasing again to 15 ppm N_2O at 500°C. Cu-BEA is a large pore zeolite which is generally known for forming large quantities of N_2O relative to small pore zeolites, such as Cu-CHA [15–17]. This is further emphasized by the activity measurements for slow SCR conditions shown in Figure 4.4E, where large quantities of N_2O are formed when NO_2 and NH_3 are present in the feed gas, relative to standard SCR conditions. Furthermore, slow SCR conditions provide greater NO_x and NH_3 conversions at all temperatures compared to the standard SCR conditions, already reaching full NO_x conversion at 250°C. This shows that slow SCR conditions do not necessarily result in slow reactions with a low conversion of NO_x. Overall, very large quantities of N_2O are formed under slow SCR conditions, with the maximum of 184 ppm N_2O reached at 250°C. The formation of such large quantities of N_2O and the high NO_x conversion suggest that N_2O formation is responsible for the high catalytic activity of the Cu-BEA catalyst under slow SCR conditions.

The fast SCR reaction is enabled by a mixture of NO and NO_2, and an equimolar ratio generally prompts the largest fast SCR contribution [15, 31–34]. The SCR activity measurement with an equimolar mixture of NO:NO_2 is shown in Figure 4.4F. The combination of NO and NO_2 provides an increase in low temperature conversion of NO_x to N_2, but also to N_2O. In fact, the N_2O selectivity is approximately 25% between 200–225°C with a corresponding maximum of about 100 ppm N_2O in this temperature range, followed by a decrease in N_2O selectivity above 225°C. Compared to slow SCR conditions, the formation of N_2O at ≥250°C during fast SCR conditions is approximately halved, for example from 184 ppm to 94 ppm N_2O at 250°C. This again suggests that N_2O formation from NO_2 is greatly contributing to the conversion NO_x. Overall, the N_2 yield is greatest for fast SCR conditions,

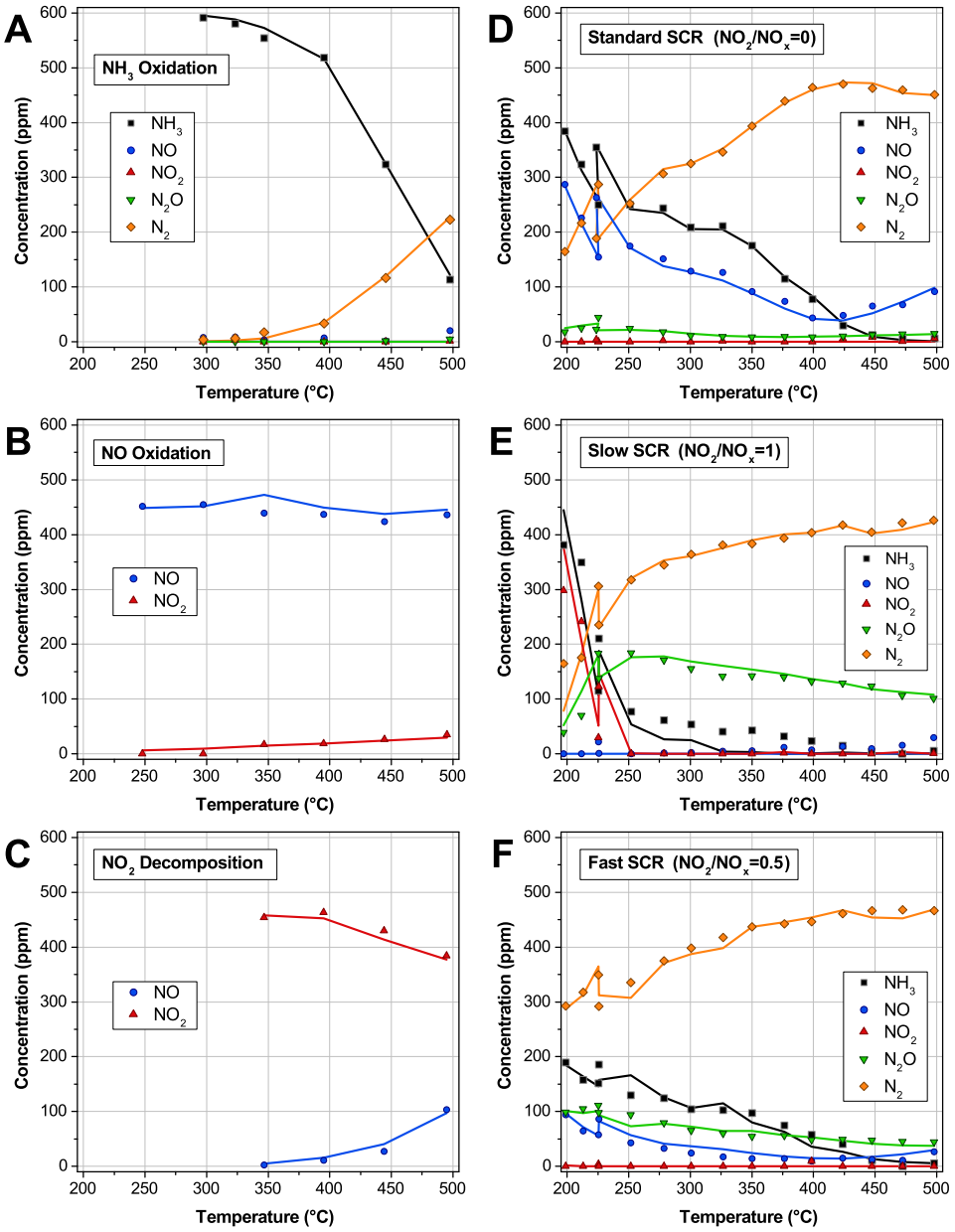

Figure 4.4: *Comparison of NH_3, NO, NO_2, N_2O, and N_2 outlet concentrations based on the experimental data (symbols) and the model fit for A) NH_3 oxidation (578 ppm NH_3), B) NO oxidation (470 ppm NO), C) NO_2 decomposition (463 ppm NO_2), D) standard SCR (563 ppm NH_3, 474 ppm NO), E) slow SCR (580 ppm NH_3, 497 ppm NO_2), and F) fast SCR (571 ppm NH_3, 236 ppm NO, 252 ppm NO_2). Values for N_2 were calculated from the N-balance. Operating conditions: 20 mg of 3.5 wt.% Cu-BEA SCR catalyst sample, 100 mg SiC, 5 vol.% H_2O, 10 vol.% O_2, and balance N_2, with a total flow of 1000 NmL/min. Activity measurements for $\leq 225°C$ were made with 40 mg catalyst and 200 mg SiC. This results in two points for 225° C (20 mg and 40 mg catalyst).*

showing the benefit of operating with NO in the presence of some NO_2.

The kinetic model for the Cu-BEA SCR catalyst includes the temperature dependent transition between two kinetic regimes of the standard SCR reactions (SCR.4 and SCR.5). The simulated NO_x conversion for the standard SCR operating conditions between 150–550°C is illustrated in Figure 4.5.

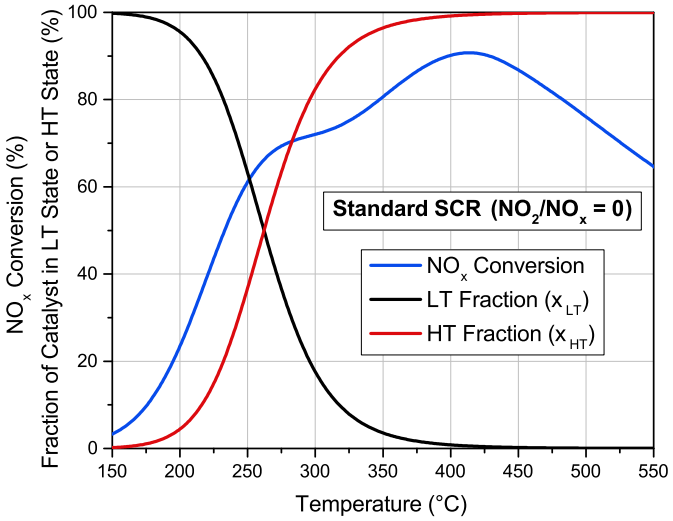

Figure 4.5: *Simulation of the NO_x conversion and the corresponding weighting of x_{LT} and x_{HT} under standard SCR conditions (NO_2/NO_x=0). Operating conditions: 20 mg of 3.5 wt.% Cu-BEA SCR catalyst sample, 600 ppm NH_3, 500 ppm NO, 5 vol.% H_2O, 10 vol.% O_2, and balance N_2, with a total flow of 1000 NmL/min.*

The contribution from each of the respective rate expressions is controlled by the fractions x_{LT} and x_{HT} as noted in Table 4.3. At temperatures below 220°C, the standard SCR kinetics are $\geq$ 90% controlled by the low temperature kinetics. Above 220°C, the contribution from the low temperature kinetics becomes continuously smaller with increasing temperature, reaching 50% at 260°C and 10% at 310°C. By including this transition between the kinetic regimes of the standard SCR reactions (SCR.4 and SCR.5) in the kinetic model, the simulation is able to accurately describe the atypical behavior of the Cu-BEA catalyst under standard SCR conditions.

4.4.3 Model Validation

Having established kinetic models for the performance of the Pt/TiO_2-SiO_2 component for the oxidation of ammonia, and of the Cu-BEA zeolite for the SCR reactions of NO_x and NH_3, the focus is now shifted to the combination of these components to model the performance of an ammonia slip catalyst. An ammonia slip catalyst generally consists of pure and/or mixed layers of AMOX and SCR catalysts. To validate the ASC model, four monolithic catalysts presented in Table 4.1 were prepared and tested for NH_3 oxidation and compared to corresponding simulations. Figure 4.6 presents the outlet concentrations of a) NH_3, b) N_2, c) NO_x, and d) N_2O

for the activity measurements of the monolithic catalysts (solid symbols), together with the simulations from the ASC monolith model (solid lines).

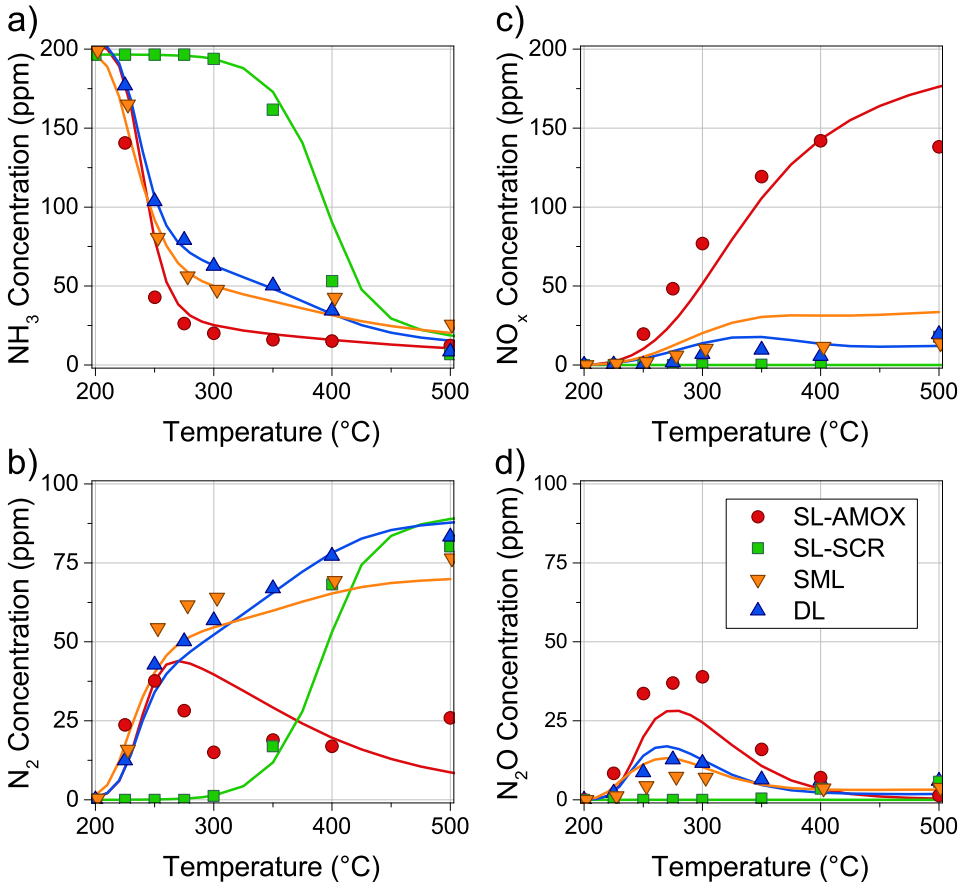

Figure 4.6: *NH_3 oxidation over the SL-AMOX, SL-SCR, SML, and DL ammonia slip catalysts. Solid symbols are the outlet concentrations measured during the activity measurements, while the solid lines are the simulated outlet concentrations using the monolith model. Values for N_2 were calculated from the N-balance. Operating conditions: 200 ppm NH_3, 3.3 vol.% H_2O, 12.3 vol.% O_2, and balance N_2, with a GHSV of 250,000 hr^{-1}.*

The effective diffusivities of the catalyst layers needed for the ASC model were unknown, and they were therefore fitted to the experimental data for the monolithic ammonia slip catalysts. This was done by varying was done by manually altering the average pore diameter of equation (4.19) of each catalyst layer, which corresponds to varying the effective diffusivity in equation (4.18). The resulting average pore diameters were 50 nm ($D_{\text{eff}} = 1.38 \times 10^{-6}$ m/s^2 at 200°C for NH_3) for each catalyst layer of the SL-AMOX, SL-SCR, and DL configurations, and 10 nm ($D_{\text{eff}} = 0.33 \times 10^{-6}$ m/s^2 at 200°C for NH_3) for the SML catalyst. The significantly lower effective diffusivity of the SML catalyst is reflective of the low NH_3 oxidation activity relative to the high Pt and SCR loading. From Figure 4.6, the mathematical model using the kinetic models based on fixed bed reactor data describes very well the NH_3 conversion of the different monolithic ASC configurations, showing

little difference between simulated and experimental values of NH_3. Furthermore, the model also provides a good, qualitative prediction of the product selectivities and yields of N_2, N_2O, NO_x, reflecting the biggest differences between ASC configurations consisting of a single catalyst component, two layered catalysts that are different, or a combination of two different catalyst components into a single layer. The most significant difference observed occurs for the single layer AMOX catalyst, where there is a significant difference in experimental and simulated concentrations of N_2 and N_2O in the range of 250–350°C. This matches well with the temperature region for which the fixed bed reactor model also predicts a higher N_2 concentration at the cost of a lower N_2O concentration. In general the monolithic model, using the kinetic models based on fixed bed reactor data, reflects the behavior of the different catalyst systems quite well, with the experimental data validating the mathematical model developed.

In general, the experimental data and the ASC model reflect the expected differences in performance, based on previous studies of ammonia slip catalysts [6, 10–12]. The Pt-based catalysts transition between low and high NH_3 conversion in the temperature range of 200–275°C, while the Cu-BEA catalyst first becomes significantly active for NH_3 oxidation above 300°C. The SL-AMOX catalyst is the most active, achieving the overall lowest NH_3 outlet concentrations. It is however also the least selective towards N_2, forming the most NO_x and N_2O, relative to the other catalysts. In contrast, the SL-SCR catalyst is the most N_2 selective at temperatures below 500°C, but also the least active. The SML and DL catalysts are combinations of the AMOX and SCR catalysts and their performance lies in between the SL-AMOX and SL-SCR catalysts. They have significantly greater N_2 selectivity than the SL-AMOX catalyst at all temperatures, and also show a greater oxidation activity than the SL-SCR catalyst at temperatures below 400°C. Although the SML catalyst has double the loading of both Pt and SCR catalyst compared to the DL catalyst, and different ASC configurations were used, there are only slight differences in their performance. The SML catalyst is slightly more active and N_2 selective at temperatures below 400°C, while the DL catalyst is slightly more active and selective towards N_2 at temperatures above 400°C. The N_2O formation is lower for SML, compared to the SL-AMOX and DL catalysts, and is likely due to the circumvention of N_2O formation in configurations where AMOX and SCR are mixed [8]. However, the catalysts studied in this work and others are not necessarily the optimal designs, and an optimization of the ASC should be done in order to compare the best case for each ASC configuration and draw sound conclusions. This is further discussed in Chapter 5.

4.5 Discussion

The ASC monolith model developed, and based on fixed bed reactor data, shows good agreement with the experimental data for the monolithic ammonia slip catalysts of different configurations. However, there are some differences between the simulated values and the experimental data which may arise from the underlying methods used to model the different aspects of the ASC model. Specifically, the mean transport model [29] is used to calculate the effective diffusivity based on an average pore diameter, the AMOX and SCR kinetic models that the determine the intrinsic activities for a set of operating conditions, and the differences between the

catalysts used in the development of the kinetic models and the monolithic catalysts used for model validation.

The effective diffusion coefficient in the washcoat was calculated based on the mean transport model (equation 4.18) [29], which accounts for resistances from both the bulk diffusion and Knudsen diffusion. The average pore diameters used were 15–50 nm with tortuosity and porosity set to 3 and 0.4, respectively. These values correspond to an effective diffusivity of NH_3 at 200°C of either 0.5×10^{-6} m^2/s or 1.4×10^{-6} m^2/s, respectively. In addition to the average pore diameter, the values are dependent on the gas species and temperature considered. Shrestha et al. [12] did not include Knudsen diffusion, and calculated the effective diffusivity by fitting the τ value of ϵ/τ, requiring unrealistic tortuosity values of 11–13. The ASC model also exhibited a significant gap to measured outlet NH_3 concentrations between 250–350°C. In comparison, a physically sound value of τ=3 could be used by using the mean transport model, along with average pore diameters in the range of 15–50 nm. Furthermore, the temperature dependence of the effective diffusivity is apparently adequately modeled using the mean transport model, showing a very good agreement between the simulated and measured NH_3 outlet concentrations. Compared to the mean transport model, the random pore model discerns between the average pore diameter and porosity of micropores and mesopores in the catalyst layer [29, 35]. In this manner, the complexity and flexibility of the model to calculate the effective diffusivity is increased. By applying the random pore model, it may be possible to increase the accuracy of the ASC model [29, 35].

The kinetic models of the AMOX and SCR catalysts determine the intrinsic activities for a set of given operating conditions, based on reactant concentrations and the temperature. They were based on the fixed bed reactor activity measurements, and the fitting of kinetic parameters resulted in very good fits. However, the kinetic models also likely contribute in part to the discrepancies in simulated and measured values.

The kinetic model for the AMOX catalyst contains rate coefficients with extreme activation energies between 187–303 kJ/mol, which are necessary to obtain the sharp transition between low and high activity observed. However, the extreme activation energies may provide a likewise extreme rate of reaction. The kinetic model therefore included the adsorption and desorption of NH_3, in order to limit the NH_3 oxidation at elevated temperature. This limitation is especially important when modeling the SML catalyst, where the AMOX and SCR catalyst compete for NH_3. If the AMOX catalyst is extremely active, the NH_3 will only be oxidized to NO_x and N_2O by the AMOX catalyst, while the reactions over the SCR catalyst between NO_x and NH_3 will be negligible. In contrast, limiting the activity of the AMOX catalyst with the adsorption and desorption of NH_3 leads to a lower rate of reaction that is more comparable to that of the SCR reactions, thereby allowing for a greater contribution from the SCR catalyst. The ASC model is therefore sensitive to uncertainty in the kinetic parameters for adsorption and desorption of NH_3 on the AMOX catalyst, mostly for the SML, since the SL-AMOX and DL configurations do not have a direct competition between the AMOX and SCR catalysts in the same washcoat layer. The accuracy of the ASC model might also be improved by using more detailed models of the AMOX catalyst [5, 12, 27].

The kinetic model for the SCR catalyst applied a transition between a low and high temperature regimes of kinetics to account for the bimodal behavior observed

in this work during standard SCR conditions for the 3.5 wt.% Cu-BEA catalyst, as well as for other Cu-zeolites [22–25]. The exact cause of the bimodal behavior is still unknown, but it is suggested to result from a low temperature route that peaks at 250°C and a high temperature route that becomes significantly active at temperatures above 350°C [25]. This has recently been shown to be determined by the state of the Cu active site. At temperatures below 250°C, isolated Cu sites cannot activate O_2 independently, and two mobile $[Cu^{I}(NH_3)_2]^+$ ions are needed, forming an $[Cu^{I}(NH_3)_2]^+$–O_2–$[Cu^{I}(NH_3)_2]^+$ intermediate. When the temperature increases, the Cu ions become immobilized on the zeolite framework, and the activation of O_2 now occurs on isolated Cu(I) sites, and has an increased reaction barrier [25]. The transition from a low temperature site to a high temperature site with different kinetics is in principle also what is described by the SCR kinetic model in this work. The value of x_{LT} reflects the quantity of low temperature sites in the SCR catalyst, while x_{HT} reflects high temperature sites, and in that manner also the contribution to the standard SCR activity from each type of site. The resulting kinetic model for the SCR catalyst accurately describes the network of reactions under a variety of conditions.

A final consideration of the source of discrepancies between the simulated and measured values, is the difference between the catalysts loaded into the fixed bed reactor and those present in the monolithic catalysts. Due to practical reasons, different batches of the AMOX and SCR catalysts were used for the fixed bed reactor activity measurements and the preparation of the monolithic catalysts. Although the different batches of catalysts were prepared of the same types and using the same methods, it may result in slight differences in catalytic activity. Furthermore, the catalyst slurries applied to the monolithic catalysts consists of the AMOX and SCR catalysts that are exposed to additional grinding, drying, calcination treatments, and mixing with water, binders, and other solvents. Despite these possible sources of uncertainty, the developed ASC monolith model provides a good simulation of the different ASC configurations tested.

In summary, a number of factors can contribute to differences in the simulated and measured values. Most importantly are the methods used to model the effective diffusivity of the monolithic catalysts, the kinetic models derived, and the differences in catalysts used for development of the kinetic model and for validation of the monolith model. In spite of these sources of uncertainty, the model provides a good prediction of NH_3 conversion and product selectivity.

4.6 Conclusion

An optimal automotive ammonia slip catalyst (ASC) combines the high activity of the ammonia oxidation (AMOX) catalyst with the efficiency of selective catalytic reduction of NO_x with NH_3 over an SCR catalyst (NH_3-SCR), to ensure minimal NH_3 breakthrough and limited formation of NO_x and N_2O. In this chapter, a single channel 1D-1D steady state mathematical model of the dual layer ammonia slip catalyst has been derived and validated. The model includes film diffusion from the gas channel to the washcoat surface, and the diffusion and reaction throughout the washcoat layers of one monolith channel. The kinetic models applied were derived based on activity measurements for 1 wt.% Pt/TiO_2-SiO_2 (AMOX) and

3.5 wt.% Cu-BEA (SCR). The kinetic model for the SCR catalyst accounted for the transition between low temperature and high temperature kinetics, reproducing the atypical behavior in the activity of Cu-zeolites during standard SCR conditions. The monolith model was validated against experimental data for NH_3 oxidation over monolith ammonia slip catalysts with different configurations, which were single layer AMOX, single layer SCR, single mixed layer (AMOX+SCR), and dual layer (SCR/AMOX). The model describes well the NH_3 conversion for the different catalyst systems investigated, while also giving a good agreement with the yields of NO_x, N_2O, and N_2.

4.7 References

[1] EU. Commision Regulation (EU) No 582/2011. *Official Journal of the European Union*, 25.6.(L 182):1–168, 2011.

[2] Environmental Protection Agency. Control of Air Pollution From New Motor Vehicles: Heavy-Duty Engine and Vehicle Standards and Highway Diesel Fuel Sulfur Control Requirements. *Federal Register*, 66(12):5001–5193, 2001.

[3] A. Walker. Future Challenges and Incoming Solutions in Emission Control for Heavy Duty Diesel Vehicles. *Topics in Catalysis*, 59:695–707, 2016.

[4] T.V.W. Janssens, H. Falsig, L.F. Lundegaard, P.N.R. Vennestrøm, S.B. Rasmussen, P.G. Moses, F. Giordanino, E. Borfecchia, K.A. Lomachenko, C. Lamberti, S. Bordiga, A. Godiksen, S. Mossin, and P. Beato. A Consistent Reaction Scheme for the Selective Catalytic Reduction of Nitrogen Oxides with Ammonia. *ACS Catalysis Research*, 5:2832–2845, 2015.

[5] A. Scheuer, W. Hauptmann, A. Drochner, J. Gieshoff, H. Vogel, and M. Votsmeier. Dual Layer Automotive Ammonia Oxidation Catalysts: Experiments and Computer Simulation. *Applied Catalysis B: Environmental*, 111-112:445–455, 2012.

[6] S. Shrestha, M.P. Harold, K. Kamasamudram, and A. Yezerets. Ammonia Oxidation on Structured Composite Catalysts. *Topics in Catalysis*, 56:182–186, 2013.

[7] M. Colombo, I. Nova, and E. Tronconi. A Simplified Approach to Modeling of Dual-layer Ammonia Slip Catalysts. *Chemical Engineering Science*, 75:75–83, 2012.

[8] M. Colombo, I. Nova, E. Tronconi, V. Schmeißer, B. Bandl-Konrad, and L. R. Zimmermann. Experimental and Modeling Study of a Dual-Layer (SCR + PGM) NH_3 Slip Monolith Catalsyt (ASC) for Automotive SCR Aftertreatment Systems. Part 1. Kinetics for the PGM Component and Analysis of SCR/PGM Interactions. *Applied Catalysis B: Environmental*, 142-143:861–876, 2013.

[9] A. Scheuer, A. Drochner, J. Gieshoff, H. Vogel, and M. Votsmeier. Runtime Efficient Simulation of Monolith Catalysts with a Dual-Layer Washcoat. *Catalysis Today*, 188:70–79, 2012.

[10] S. Shrestha, M.P. Harold, K. Kamasamudram, A. Kumar, L. Olsson, and K. Leistner. Selective Oxidation of Ammonia to Nitrogen on Bi-functional Cu–SSZ-13 and Pt/Al_2O_3 Monolith Csatalyst. *Catalysis Today*, 267:130–144, 2016.

[11] S. Shrestha, M.P. Harold, K. Kamasamudram, and A. Yezerets. Selective Oxidation of Ammonia on Mixed and Dual-layer Fe-ZSM-5 + Pt/Al_2O_3 Monolithic Catalysts. *Catalysis Today*, 231:105–115, 2014.

[12] S. Shrestha, M.P. Harold, and K. Kamasamudram. Experimental and Modeling Study of Selective Ammonia Oxidation on Multi-functional Washcoated Monolith Catalysts. *Chemical Engineering Journal*, 278:24–35, 2015.

[13] A. Scheuer, M. Votsmeier, A. Schuler, J. Gieshoff, A. Drochner, and H. Vogel. NH_3-Slip Catalysts: Experiments Versus Mechanistic Modelling. *Topics in Catalysis*, 52:1847–1851, 2009.

[14] M. Colombo, I. Nova, E. Tronconi, and G. Koltsakis. A Modeling Study of NH_3 Slip Catalysts: Analysis of the SCR/PGM Interactions. *Topics in Catalysis*, 56:177–181, 2013.

[15] P.S. Metkar, M.P. Harold, and V. Balakotaiah. Experimental and Kinetic Modeling Study of NH_3-SCR of NOx on Fe-ZSM-5, Cu-chabazite and Combined Fe- and Cu-zeolite Monolithic Catalysts. *Chemical Engineering Science*, 87:51–66, 2013.

[16] O. Mihai, C.R. Widyastuti, S. Andonova, K. Kamasamudram, J. Li, S.Y. Joshi, N.W. Currier, A. Yezerets, and L. Olsson. The Effect of Cu-loading on Different Reactions Involved in NH_3-SCR over Cu-BEA Catalysts. *Journal of Catalysis*, 311:170–181, 2014.

[17] P.N.R. Vennestrøm. *Selective Catalytic Reduction of Nitrogen Oxides with Ammonia over Microporous Zeolite Catalysts*. PhD thesis, Universitat Politècnica de València and Haldor Topsoe A/S, 2014.

[18] M. Colombo, I. Nova, E. Tronconi, V. Schmeißer, B. Bandl-Konrad, and L. R. Zimmermann. Experimental and Modeling Study of a Dual-Layer (SCR + PGM) NH_3 Slip Monolith Catalsyt (ASC) for Automotive SCR Aftertreatment Systems. Part 2. Validation of PGM Kinetics and Modeling of the Dual-layer ASC Monolith. *Applied Catalysis B: Environmental*, 142-143:337– 343, 2013.

[19] I. Nova, M. Colombo, E. Tronconi, V. Schmeisser, B. Bandl-Konrad, and L. Zimmermann. Experimental and Modelling Study of a Dual-Layer NH_3 Slip Monolith Catalyst for Automotive SCR Aftertreatment Systems. *Topics in Catalysis*, 56:227–231, 2013.

[20] M. Votsmeier, A. Scheuer, A. Drochner, H. Vogel, and J. Gieshoff. Simulation of Automotive NH_3 Oxidation Catalysts Based on Pre-computed Rate Data from Mechanistic Surface Kinetics. *Catalysis Today*, 151:271–277, 2010.

[21] T.K. Hansen. Modeling and preparation of dual layer ammonia oxidation catalyst. Master's thesis, Technical University of Denmark and Haldor Topsoe A/S, February, 2013.

[22] K. Kamasamudram, N. Currier, T. Szailer, and A. Yezerets. Side Reactions in the Selective Catalytic Reduction of NO_x with Various NO_2 Fractions. *SAE International Journal*, 3(2010-01-1182):664–672, 2010.

[23] F. Gao, E. Walter, M. Kollar, Y. Wang, J. Szanyi, and C. Peden. Understanding Ammonia Selective Catalytic Reduction Kinetics over Cu/SSZ-13 from Motion of the Cu Ions. *Journal of Catalysis*, 319:1–14, 2014.

[24] C. Paolucci, J.R. Di Iorio, F.H. Ribeiro, R. Gounder, and W.F. Schneider. Catalysis Science of NO_x Selective Catalytic Reduction With Ammonia Over Cu-SSZ-13 and Cu-SAPO-34. *Advances in Catalysis*, 59:1–107, 2016.

[25] F. Gao, D. Mei, Y. Wang, J. Szanyi, and C.H.F. Peden. Selective Catalytic Reduction over Cu/SSZ-13: Linking Homo- and Heterogeneous Catalysis. *Journal of the American Chemical Society*, 139:4935—4942, 2017.

[26] The National Institute of Standards and Technology (NIST). NIST Chemistry WebBook. Online. `http://webbook.nist.gov/chemistry/` Accessed: 2015.

[27] R. Kraehnert and M. Baerns. Kinetics of Ammonia Oxidation over Pt Foil Studied in a Micro-structured Quartz-reactor. *Chemical Engineering Journal*, 137:361–375, 2008.

[28] E. Tronconi and P. Forzatti. Adequacy of Lumped Parameter Models for SCR Reactors with Monolith Structure. *Aiche Journal*, 38:201–210, 1992.

[29] D. Karamitros and G. Koltsakis. *Urea-SCR Technology for deNOx After Treatment of Diesel Exhausts*, chapter 13 SCR Reactor Models for Flow-Through and Wall-Flow Converters. Springer Science+Business Media, 2014.

[30] T.K. Hansen, M. Høj, B.B. Hansen, T.V.W. Janssens, and A.D. Jensen. The Effect of Pt Particle Size on the Oxidation of CO, C_3H_6, and NO over Pt/Al_2O_3 for Diesel Exhaust Aftertreatment. *Topics in Catalysis*, Accepted, 2017.

[31] I. Nova, C. Ciardelli, E. Tronconi, D. Chatterjee, and M. Weibel. NH_3-NO/NO_2 SCR for Diesel Exhausts After Treatment: Mechanism and Modelling of a Catalytic Converter. *Topics in Catalysis*, 42–43:43–46, 2007.

[32] A. Grossale, I. Nova, E. Tronconi, D. Chatterjee, and M. Weibel. NH_3-NO/NO_2 SCR for Diesel Exhausts Aftertreatment: Reactivity, Mechanism and Kinetic Modelling of Commercial Fe- and Cu-Promoted Zeolite Catalysts. *Topics in Catalysis*, 52:1837–1841, 2009.

[33] M. Iwasaki and H. Shinjoh. A Comparative Study of "Standard", "Fast" and "NO_2" SCR Reactions over Fe/zeolite Catalyst. *Applied Catalysis A: General*, 390:71–77, 2010.

[34] G. Madia, M. Koebel, M. Elsener, and A. Wokaun. Side Reactions in the Selective Catalytic Reduction of NO_x with Various NO_2 Fractions. *Industrial & Engineering Chemistry Reserach*, 41:4008–4015, 2002.

[35] M. Dudák, V. Novák, P. Kočí, M. Marek, P. Blanco-García, and G. Jones. Prediction of Diffusivity and Conversion of n-Decane and CO in Coated Pt/Al_2O_3 Catalyst Depending on Porous Layer Morphology. *Applied Catalysis B: Environmental*, 150–151:446–458, 2014.

CHAPTER 5

Model Analysis of the Ammonia Slip Catalyst

The validated model for the ammonia slip catalyst (ASC) from Chapter 4 was used to analyze the sensitivity of the ASC performance to variations in selected parameters, in order to identify the key design parameters. For all ASC catalysts considered it is necessary to have an adequate Pt loading, since it determines the oxidation activity of the ASC from the Pt-based component. Beside the Pt loading, the key design parameters are the catalyst loading and effective diffusion coefficient, since these factors determine the layer thickness and transport of reactants through the catalyst layers. Furthermore, the SCR catalyst loading determines the SCR activity available for NO_x reduction, influencing product selectivity. A thin catalyst layer with a high SCR activity and effective diffusivity is therefore preferable since a high effectiveness factor is achieved. By varying the NO oxidation activity of the AMOX catalyst, e.g by varying the Pt particle size, it is possible to alter the NO_2/NO_x ratio of NO_x formed by the AMOX catalyst. A high NO_2/NO_x ratio evokes the fast SCR and slow SCR reactions and leads to an improved NO_x reduction and N_2 selectivity for the multi-functional catalysts, at the cost of an increased N_2O selectivity. Additionally, by disabling the N_2O formation kinetics of the AMOX or SCR catalyst, the AMOX catalyst was identified as the main source of N_2O formation. The multi-objective optimization of ten ASC configurations for NH_3 oxidation at 300°C was used to probe the sensitivity towards the catalyst architecture of the ASC. The resulting Pareto fronts indicate that the optimal catalyst systems are those involving at least one mixed layer of the AMOX and SCR catalysts, rather than pure layers of AMOX or top layers of SCR. This is mainly due to the ability of the mixed layers to circumvent N_2O formation with the more immediate reduction of NO_x with NH_3. Meanwhile, a pure SCR top layer acts as diffusion barrier that limits the NH_3 conversion, which can only be increased through a trade-off with NO_x emission.

5.1 Introduction

An optimal automotive ammonia slip catalyst (ASC) combines the high activity of the ammonia oxidation (AMOX) catalyst with the high efficiency of selective catalytic reduction of NO_x with NH_3 over an SCR catalyst (NH_3-SCR), to ensure minimal NH_3 breakthrough and limited formation of NO_x and N_2O [1–14]. Methods of combining the AMOX and SCR catalysts include mixing them into a single mixed layer (SML), layering the individual components to give a dual layer (DL) structure, or combining these two designs to form a hybrid dual layer (HDL) catalyst that has a dual layer structure where the bottom layer is a mixture and the top layer is a homogeneous layer of SCR catalyst [3–14].

Recent experimental studies comparing ASC configurations have demonstrated some of the advantages and disadvantages of the different configurations. The inclusion of an SCR catalyst, regardless of the ASC configuration, reduces NO_x emissions, since the SCR reactions are enabled in the ASC [3–14]. A dual layer structure with an SCR top layer provides an overall better NO_x selectivity during NH_3 oxidation, but also a decreased NH_3 conversion due the diffusion barrier effect of the SCR top layer [12–14]. The SCR top layer also provides a superior NH_3-SCR performance during periods where there are both NO_x and NH_3 slip from the SCR unit, in practice extending the length of the SCR unit [13, 14]. An advantage of the single mixed layer configuration is the increased accessibility to the AMOX catalyst, resulting in an increased NH_3 conversion. There are also indications that mixing the AMOX and SCR catalysts reduces N_2O yields [7, 9, 12–14]. However, the more readily accessible AMOX catalyst also increases the NO_x release to the gas phase, resulting in higher NO_x emissions [9, 12–14]. The hybrid dual layer ASC that results from combining the DL and SML designs displays a behavior in between those of the two above mentioned systems; good NH_3-SCR performance, decreased NH_3 conversion, low NO_x selectivity, and slightly lower N_2O formation [14].

The previous studies in literature consider a limited set of catalyst formulations, focusing primarily on the dual layer configuration with limited variations in Pt loading and the SCR loading, and comparing DL, SML, and HDL catalysts with the same catalyst loadings [3–14]. However, it is unlikely that the different ASC configurations share the same optimal design parameters, such as effective diffusivity, catalyst loadings, and intrinsic activities.

The literature only presents some investigations into the effect of the effective diffusivity, catalyst loadings, and intrinsic activities for the single layer AMOX and dual layer catalysts. These include a modeling study of the dual layer ASC configuration, which predicts that an increase in the effective diffusion coefficient of the SCR layer leads to an increase in the NH_3 conversion, but also an increase in NO_x selectivity [3]. Similarly, some experimental and modeling studies of the oxidation of CO and *n*-decane over Pt/Al_2O_3 with an inert Al_2O_3 top layer, show that increasing the effective diffusivity of the top layer leads to increased conversions [15, 16]. Additionally, the study of three top layers with different porosities emphasized the importance of Knudsen diffusion from compact layers with low porosity and small average pore diameter on the resulting effective diffusivity [15]. Cracks and cavities of the catalyst layer increase the effective diffusivity of the catalyst layer [17].

The amount of catalytic material on the monolith substrate (catalyst loading - g washcoat/L monolith) determines the thickness of the catalyst layers. An increase

in SCR loading of the DL catalyst has been shown to decrease NH_3 conversion, since the top layer becomes thicker, which increases the diffusion resistance to the AMOX catalyst [3, 13, 14]. Additionally, a higher SCR catalyst loading provides more SCR activity, resulting in a lower overall NO_x selectivity [3, 11, 14]. Similarly, a mathematical model study of a single layer AMOX, shows that a higher catalyst loading increases the NH_3 conversion significantly for temperatures below 225°C, indicating a kinetically limited regime [6]. Analysis of the concentration gradients of NH_3 (radially) in the washcoat layer and the effectiveness factor further emphasized the drop in effectiveness with increasing AMOX catalyst loading and layer thickness, suggesting that only the first 5–10 µm are effectively active [6]. A separate modeling study also shows a significant decrease in NH_3 conversion of the single layer AMOX, due to an increased dilution of the Pt catalyst with support material, emphasizing further the importance of mass transfer limitations for the AMOX catalyst layer [5]. Experimental studies focused on varying the Pt loading (g Pt/g washcoat) of single layer AMOX and dual layer catalysts, while maintaining a constant washcoat loading, show a decrease in NH_3 conversion with decreasing Pt loading, but also a slightly increased N_2 yield and decreased N_2O yield [12].

Furthermore, the trade-offs between NH_3 oxidation activity and formation of NO_x and N_2O emissions described makes the task of ASC design a multi-objective problem focused on minimizing emissions of all three components. For each ASC configuration there will likely be an individual set of optimal design specifications, consisting of catalyst loadings, intrinsic activities, and effective diffusivity. Additionally, the performance of an ASC design is dependent on the specified requirements, such as a high NH_3-SCR activity in the case of NH_3 and NO_x slip or high temperature performance. The combination of these considerations makes it difficult to conclude on the advantages and disadvantages of the different ASC configurations.

In this chapter, we apply the developed and validated ASC model from Chapter 4 to further analyze the sensitivity of the single layer AMOX, single mixed layer, and dual layer ASC systems to variations in selected design parameters. This is done to further improve our understanding of the ASC system and to reduce experimental efforts in catalyst design by identifying key design parameters. The investigated parameters include the intrinsic activity of the AMOX catalyst controlled by varying the Pt wt.% (assuming that they scale directly), the catalyst loadings of the AMOX and SCR catalysts, and the effective diffusivity of the catalyst layers, altered by varying the average pore diameter as calculated in equation (4.19). Variations in the NO oxidation activity of the AMOX catalyst were used to affect the local NO_2/NO_x ratio and determine the influence on the ASC performance. In practice, this may be obtained by varying the Pt particle size of the AMOX catalyst (Chapter 3). The contribution of the individual catalysts to N_2O emissions was studied by disabling all the reactions forming N_2O for either the AMOX or SCR catalyst and evaluating the effect on N_2O selectivity. The study of NO oxidation activity and N_2O formation helps provide further insight into the interactions between the AMOX and SCR catalysts in the ASC. Lastly, the performance of ten different ASC configurations for NH_3 oxidation was simulated and compared using Pareto fronts generated from multi-objective optimization. This is used to assess the sensitivity of the ASC to catalyst architecture and is also an example of how the design optimization of the ASC can be done.

5.2 Methodology

A single channel 1D-1D steady state mathematical model of an ammonia slip catalyst with a dual mixed layer design was derived and validated in Chapter 4. The model includes film diffusion from the gas channel to the washcoat surface, and the diffusion and reaction throughout the washcoat layers of one monolith channel. The kinetic models applied were derived based on activity measurements for 1 wt.% Pt/TiO_2-SiO_2 (AMOX) and 3.5 wt.% Cu-BEA (SCR). The kinetic model for the SCR catalyst accounted for the transition between low temperature kinetics and high temperature kinetics, reproducing the atypical activity behavior of Cu-zeolites during standard SCR conditions [18–21]. The monolith model was validated against experimental data for NH_3 oxidation over monolith ammonia slip catalysts of four different ASC configurations; single layer AMOX, single layer SCR, single mixed layer (AMOX+SCR), and dual layer ($^{SCR}/_{AMOX}$). Please see Chapter 4 (page 63) for more details on the ASC model.

The model considers a dual mixed layer design where both catalyst layers consist of a mixture of AMOX and SCR catalyst. By setting either the AMOX or SCR catalyst loading to 0 g/L in a given layer, the respective catalyst can be excluded. As a result, a series of ten ASC configurations can be simulated:

1) *Single Layer AMOX (SL-AMOX)* – A single pure layer of AMOX catalyst.

2) *Single Layer SCR (SL-SCR)* – A single pure layer of SCR catalyst.

3) *Dual Layer (DL)* – A dual layer design with a pure layer of SCR catalyst on top of a pure layer of AMOX catalyst.

4) *Inverse Dual Layer (IDL)* – An inverse dual layer design with an AMOX catalyst on top of an SCR catalyst.

5) *Hybrid Dual Layer with SCR Top Layer (HDL-S)* – A hybrid dual layer catalyst consisting of a pure SCR top layer on a mixed bottom layer.

6) *Inverse Hybrid Dual Layer with SCR Bottom Layer (IHDL-S)* – An inverse hybrid dual layer catalyst consisting of a mixed top layer with a pure SCR bottom layer.

7) *Hybrid Dual Layer with AMOX Top Layer (HDL-A)*– A hybrid dual layer catalyst consisting of a top layer of pure AMOX on a mixed bottom layer.

8) *Inverse Hybrid Dual Layer with AMOX Bottom Layer (IHDL-A)* – An inverse hybrid dual layer catalyst with a mixed top layer on a bottom layer of pure AMOX.

9) *Single Mixed Layer (SML)* – A single mixed layer of AMOX and SCR catalyst.

10) *Dual Mixed Layer (DML)* – A dual layer design with two mixed layers of AMOX and SCR catalyst.

These ten configurations are illustrated in Figure 5.1.

For the SL-AMOX, SML, and DL configurations, the sensitivity of the ASC system to variations in the intrinsic activity of the AMOX catalyst, the catalyst

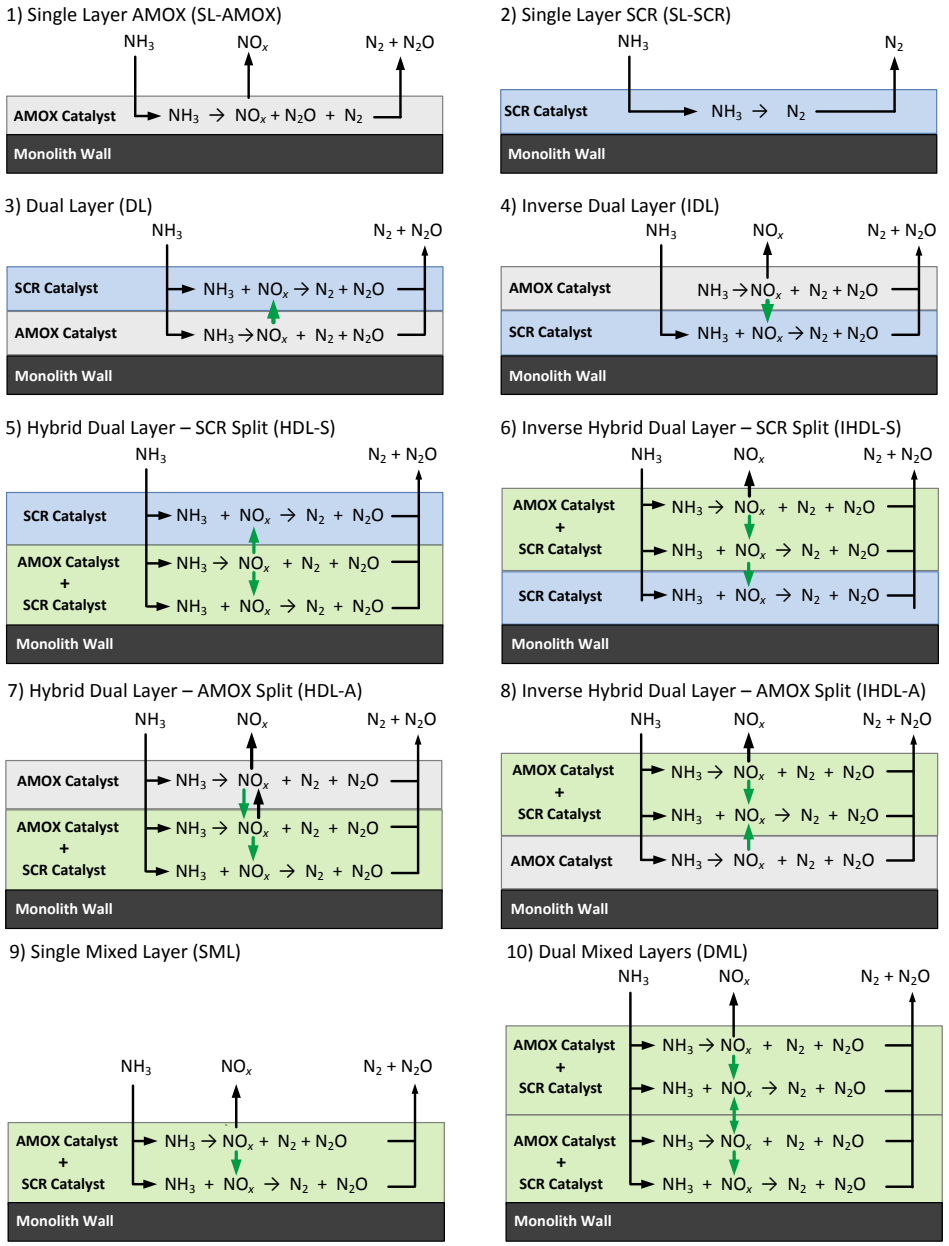

Figure 5.1: *The ten possible ammonia slip catalyst configurations that can be simulated using the dual mixed layer model. 1) single layer AMOX (SL-AMOX), 2) single layer SCR (SL-SCR), 3) dual layer (DL), 4) inverse dual layer (IDL), 5) hybrid dual layer with top layer of SCR (HDL-S), 6) inverse hybrid dual layer with bottom layer of SCR (IHDL-S), 7) hybrid dual layer with top layer of AMOX (HDL-A), 8) inverse hybrid dual layer with bottom layer of AMOX (IHDL-A), 9) single mixed layer (SML), and 10) dual mixed layer (DML).*

loadings, and the effective diffusivity of the bottom and top washcoat layers, NO oxidation activity, and ability of the AMOX or SCR catalysts to form N_2O were studied independently. A reference catalyst system for each of the three configurations is used to assist in evaluating the effect of parameter changes. The reference catalyst systems are presented in Table 5.1.

Table 5.1: *Overview of the reference catalyst systems for SL-AMOX, SML, and DL used for studying the effect of variations in design parameters. The pore diameter of both layers was set to 50 nm and the Pt wt.% of the AMOX loading is 0.235 wt.% Pt/g_{AMOX}.*

Configuration	Abbrev.	Bottom Layer		Top Layer		Architecture
		AMOX	SCR	AMOX	SCR	
Single Layer	SL-AMOX	26	–	–	–	$\overline{26\,\mathrm{AMOX}}$
AMOX Single Layer	SML	26	54	–	–	$\overline{26\,\mathrm{AMOX} + 54\,\mathrm{SCR}}$
Mixed Dual Layer	DL	26	–	–	54	$\frac{54\,\mathrm{SCR}}{26\,\mathrm{AMOX}}$

The intrinsic activity of the AMOX catalyst was varied using the Pt wt.%, which in the model corresponds to multiplying the rate coefficients by a set factor. For example, the kinetic model is based on a 1 wt.% Pt AMOX catalyst, but the rate coefficients of the AMOX catalyst in the validated monolithic ASC model are multiplied by 0.235 to regulate the oxidation activity. This assumes that the oxidation activity scales linearly with the Pt wt.%. In this manner, the intrinsic activity of the AMOX catalyst is varied between 4–426% (0.01–1 wt.% Pt) relative to the reference catalyst system (0.235 wt.% Pt). Since the AMOX loading is kept constant at 26 g/L, the total Pt loading varies between 0.0026–0.26 g_{Pt}/L. The Pt loading is calculated by multiplying the AMOX loading with the Pt wt.%.

The catalyst loadings are simply varied by specifying a loading within 1–120 g/L for the AMOX catalyst and 1–200 g/L for the SCR catalyst. Other than catalytic activity, the catalyst loading also affects layer thickness and surface area since the model calculates these parameters based on the catalyst loadings, catalyst density, and available geometric surface area of the monolith substrate with square channels. Furthermore, the Pt loading will vary since the Pt wt.%, corresponding to $g_{Pt}/g_{AMOX} \times 100$, is kept constant at 0.235 wt.% Pt, leading to variations in Pt loading of 0.00235–0.28 g_{Pt}/L. Note that this range of Pt loading for variations in AMOX loading is comparable to that for variations in intrinsic activity (Pt wt.%).

The effective diffusivity of reactants through the catalyst layers was calculated using the mean transport model (equation 4.18; page 76), which uses the average pore diameter of the catalyst to describe the change in effective diffusivity with temperature. By varying the average pore diameter of the catalyst layer and keeping the porosity ($\epsilon = 0.4$) and tortuosity ($\tau = 3$) constant, the effective diffusivity is varied between 0.33×10^{-6}–5.99×10^{-6} m^2/s (d_p=10–1000 nm) for NH_3 at 200°C relative to 1.38×10^{-6} m^2/s for the reference catalyst system with d_{pore}=50 nm. The effective diffusivity of the other reactants varies in a similar manner.

To evaluate the potential and significance of controlling the local NO_2/NO_x ratio of NO_x from the AMOX catalyst, which is known to affect the SCR reactions between NH_3 and NO_x [22–28], the $k_{\text{NO ox.}}$ of the AMOX kinetic model for SL-AMOX, SML, and DL catalysts ($k_{\text{AMOX.5f}}$ in Table 4.2, page 71) was multiplied by factors of 0–32, thereby either decreasing (<1) or increasing (>1) the oxidation of NO to NO_2. In practice, the NO_2/NO_x ratio can be altered by controlling the Pt particle size, as was presented in Chapter 3. Similarly, the contributions of the AMOX and SCR catalysts to the formation N_2O was evaluated by disabling all the reactions leading to N_2O formation for the respective catalyst (AMOX.4 in Table 4.2 on page 71 or SCR.5+SCR.7+SCR.9 in Table 4.3 on page 73) and comparing the simulations. Since N_2O is a final product in the kinetic models for the AMOX catalyst (Table 4.2, page 71) and the SCR catalyst (Table 4.3, page 73), the contributions of each catalyst could be evaluated using this method.

The effect of variations in the design parameters on the ASC performance was evaluated by comparing NH_3 conversion and selectivity towards the different products. Conversion and selectivity were calculated as follows:

$$\text{NH}_3 \text{ Conversion: } X_{\text{NH}_3} = \frac{[\text{NH}_3]_{\text{in}} - [\text{NH}_3]_{\text{out}}}{[\text{NH}_3]_{\text{in}}} \tag{5.1}$$

$$\text{N}_2 \text{ Selectivity: } S_{\text{N}_2} = \frac{2 \cdot [\text{N}_2]_{\text{out}}}{[\text{NH}_3]_{\text{in}} - [\text{NH}_3]_{\text{out}}} \tag{5.2}$$

$$\text{N}_2\text{O Selectivity: } S_{\text{N}_2\text{O}} = \frac{2 \cdot [\text{N}_2\text{O}]_{out}}{[\text{NH}_3]_{in} - [\text{NH}_3]_{out}} \tag{5.3}$$

$$\text{NO}_x \text{ Selectivity: } S_{\text{NO}_x} = \frac{[\text{NO}_x]_{\text{out}}}{[\text{NH}_3]_{\text{in}} - [\text{NH}_3]_{\text{out}}} \tag{5.4}$$

The design of an ASC is a multi-objective optimization problem since the goal is to minimize emissions of NH_3, NO_x, and N_2O, as well as the cost, size, and weight of the ASC. For simplicity, we focus on minimizing emissions and disregard the other design objectives, as well as consider and equal N-based weighting for NH_3, NO_x, and N_2O slip. An optimal set of values for the design parameters therefore results in the lowest total emissions of NH_3, NO_x, and N_2O. Due to the trade-off that occurs between NH_3 conversion and the emissions of NO_x and N_2O for the ASC, there exist many possible combinations of NH_3, NO_x, and N_2O that provide the lowest total emissions, all with their respective set of parameter values. This is common for multi-objective problems and the set of optimal solutions forms a front reflecting the trade-off, known as a Pareto front. This concept is illustrated for the ASC in Figure 5.2, where the sum of NO_x and N_2O slip is plotted against NH_3 slip. The ideal solution occurs for 0 NH_3 slip, 0 NO_x+N_2O slip, corresponding to 100% N_2 yield (origin in green region). The optimal solutions are those closest to the ideal solution and they form the Pareto front (solid green circles connected by solid black lines). The remaining solutions are non-optimal (red crosses).

The multi-objective optimization was performed for each of the ten different ASC configurations presented in Figure 5.1 by optimizing a bound set of parameters: intrinsic activity of AMOX catalyst (χ_{Pt}=0.01–6.11 wt.% Pt), AMOX catalyst loading (ψ_{AMOX}=1–60 g/L), SCR catalyst loading (ψ_{SCR}=1–200 g/L), and effective diffusivity of catalyst layers ($d_{\text{pore, wc}}$=40–200 nm). The system was constrained to a

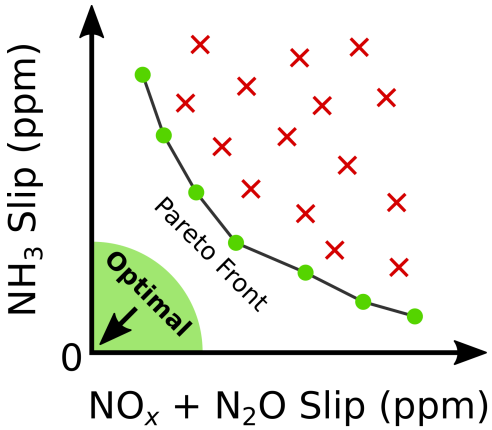

Figure 5.2: *Example of the Pareto front obtained through multi-objective optimization for the ASC system. Ideal solution: origin in green region of graph. Optimal solutions: solid green circles. Non-optimal solutions: red crosses.*

maximum Pt loading of 6.11 g_{Pt}/L corresponding to the Pt loadings of the reference catalysts systems in Table 5.1. The system was also constrained to maximum total load of 200 g/L SCR. These ranges and constraints were chosen to limit the system to reasonable values for Pt loading, intrinsic activity, AMOX and SCR catalyst loadings, and effective diffusivity.

The overall objective of the ASC optimization was the minimization of NH_3, NO_x, and N_2O emissions. It should be noted that the optimization is affected by the weighting, and that for simplicity, an equal weighting based on the N atoms was applied to each emission. The resulting objective function for the multi-objective optimization problem was:

$$\min_{\psi_{\mathrm{AMOX}},\, \psi_{\mathrm{SCR}},\, d_{\mathrm{pore,bl}},\, d_{\mathrm{pore,tl}}\, \chi_{\mathrm{Pt}}} [\mathrm{NH_3}]_{\mathrm{out}} + [\mathrm{NO}_x]_{\mathrm{out}} + 2 \times [\mathrm{N_2O}]_{\mathrm{out}} \tag{5.5}$$

The optimization was completed using MATLAB's *gamultiobj* function, which employs the genetic algorithm (GA) for multi-objective optimization [29–31]. The GA applies concepts of natural selection from biological evolution, to iteratively optimize a set of parameters for a given optimization problem [29]. The algorithm flowchart is illustrated in Figure 5.3. The genetic algorithm begins by creating an initial population, either randomly generated under the constraints and boundaries applied, or generated based on a user defined population. To assist the simulation in converging to the optimal solutions, the possible combinations of the limits of the parameter ranges were initially supplied as part of the initial population and mixed with randomly generated individuals. The population size was set to consist of 50 individuals multiplied by the number of parameters being varied, $50 \times n_{\mathrm{param.}}$, to account for the increase in possible solutions with the increase in parameters for the more complex configurations considered.

The fitness of the individuals in the first generation is evaluated using the fitness function, similar to the objective function given by equation 5.5. The fitness values are used to compare and rank the individuals, and generally the most fit individuals are selected as parents for the next generation. However, some less fit individuals

may also be selected to diversify the population. The resulting set of parents then produce the children that form the next generation. The parents can produce three types of children: 1) elite children, which are replicates of the most fit parents, 2) mutation children, which are created by introducing random changes to a single parent, and 3) crossover children, which are created by combining the vectors of a pair of parents [31]. The new generation, consisting of the generated children, replaces the current generation and the individuals are evaluated in a similar fashion as the initial population. Through the successive iterations (generations), the population evolves toward a set of optimal solutions. This loop of the algorithm is repeated until a stopping criteria is met, such as when a maximum number of generations is reached or when the relative change in the fitness function value decreases below a set tolerance [31]. In this study a maximum number of 10 generations was used as the stopping criteria. The Pareto fronts resulting from final set of optimal solutions were used to evaluate the sensitivity of the ASC performance to the possible ASC configurations.

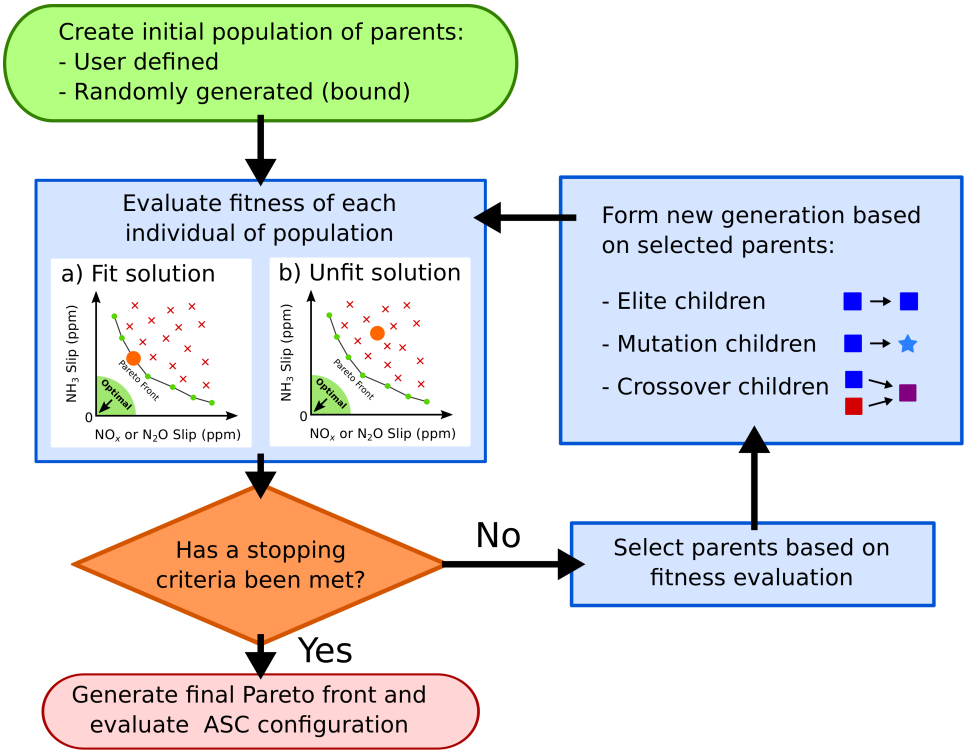

Figure 5.3: *Flowchart for the genetic algorithm used to optimize the multi-objective ammonia slip catalyst design.*

5.3 Results

Figures 5.4–5.10 present a series of simulations for the SL-AMOX, SML, and DL catalyst configurations that illustrate and compare the predicted effect of varying

the following design parameters: the intrinsic activity of the AMOX component (Pt wt.%), the AMOX catalyst loading, the SCR catalyst loading, the effective diffusivity of the catalyst layers, the NO oxidation activity of the AMOX catalyst ($k_{\text{NO ox.}}$), and the significance of hindering N_2O formation over the AMOX or SCR catalyst ($k_{\text{N2O form.}}$). The figures are structured similarly, showing the NH_3 conversion, N_2, NO_x, and N_2O selectivity in a single column for the configuration indicated above the respective column. In general, the figures present the lower extreme of the parameter range as a gray solid line and the upper extreme as a solid black line. The reference catalyst systems are given as a solid red line and correspond to the catalyst system specified in Table 5.1. Simulations for design parameters in between these points are indicated by dashed red lines.

As was presented in Chapters 3 (page 47) and 4 (page 63), the Pt-based ammonia slip catalysts exhibit a sharp transition between low and high activity between 200–300°C. The SL-AMOX catalyst exhibits its highest N_2 selectivity at temperatures below 300°C, which decreases with increasing temperature, as the selectivity for N_2O and NO_x increases. N_2O formation is most significant between 200–350°C, while NO_x becomes dominant at temperatures above 300°C. The SML and DL catalysts exhibit a comparable oxidation activity, but with a greatly increased N_2 selectivity relative to SL-AMOX. These overall trends are also present for the following series of simulated SL-AMOX, SML, and DL catalysts.

5.3.1 Varying the Intrinsic Activity of the Ammonia Oxidation Catalyst

Figure 5.4 presents simulations for the cases where the intrinsic activity of the AMOX catalyst was varied by changing the Pt loading of the AMOX catalyst (g_{Pt}/g_{AMOX}) (Pt wt.%/g_{AMOX}) between 0.01–1 wt.% for the SL-AMOX, SML, and DL catalysts. For all three ASC configurations, the variations in intrinsic activity affect the oxidation activity similarly. A low intrinsic activity leads to a low NH_3 conversion, as illustrated by simulations for 0.01 wt.% Pt. Increasing the intrinsic activity by increasing the Pt wt.% leads to a very significant increase in NH_3 conversion, with the effect being most significant at the lower end of the parameter range. An increase from 0.5 to 1 wt.% Pt has a very limited effect on ASC performance compared to 0.05 to 0.1 wt.%, suggesting that the rate of NH_3 consumption is kinetically controlled until a sufficient Pt loading is applied. For both SML and DL, the effect is less prominent at temperatures above 300°C due to the onset of NH_3 oxidation activity for the Cu-BEA SCR catalyst included in the SML and DL catalysts. This onset of NH_3 oxidation is clearly seen for the SML and DL catalyst with 0.01 wt.% Pt and for the NH_3 oxidation over the SL-SCR catalyst shown in Figure B.12 of Appendix B.4.

The simulations also predict that variations in intrinsic activity of the AMOX catalyst affect product selectivity. The N_2O formation is significantly affected for all three configurations. The lowest N_2O selectivity is observed for the lowest intrinsic activity achieved with 0.01 wt.% Pt (7.5–10%), and increases significantly to a maximum value observed for 1 wt.% Pt g/L (29–36%). This trend in N_2O selectivity is related to the correspondingly higher selectivity towards NO_x and N_2 exhibited by lower Pt wt.% for all three configurations, especially below 300°C. This is due to the combination of a low oxidation of NH_3 to NO and the dependence of N_2O

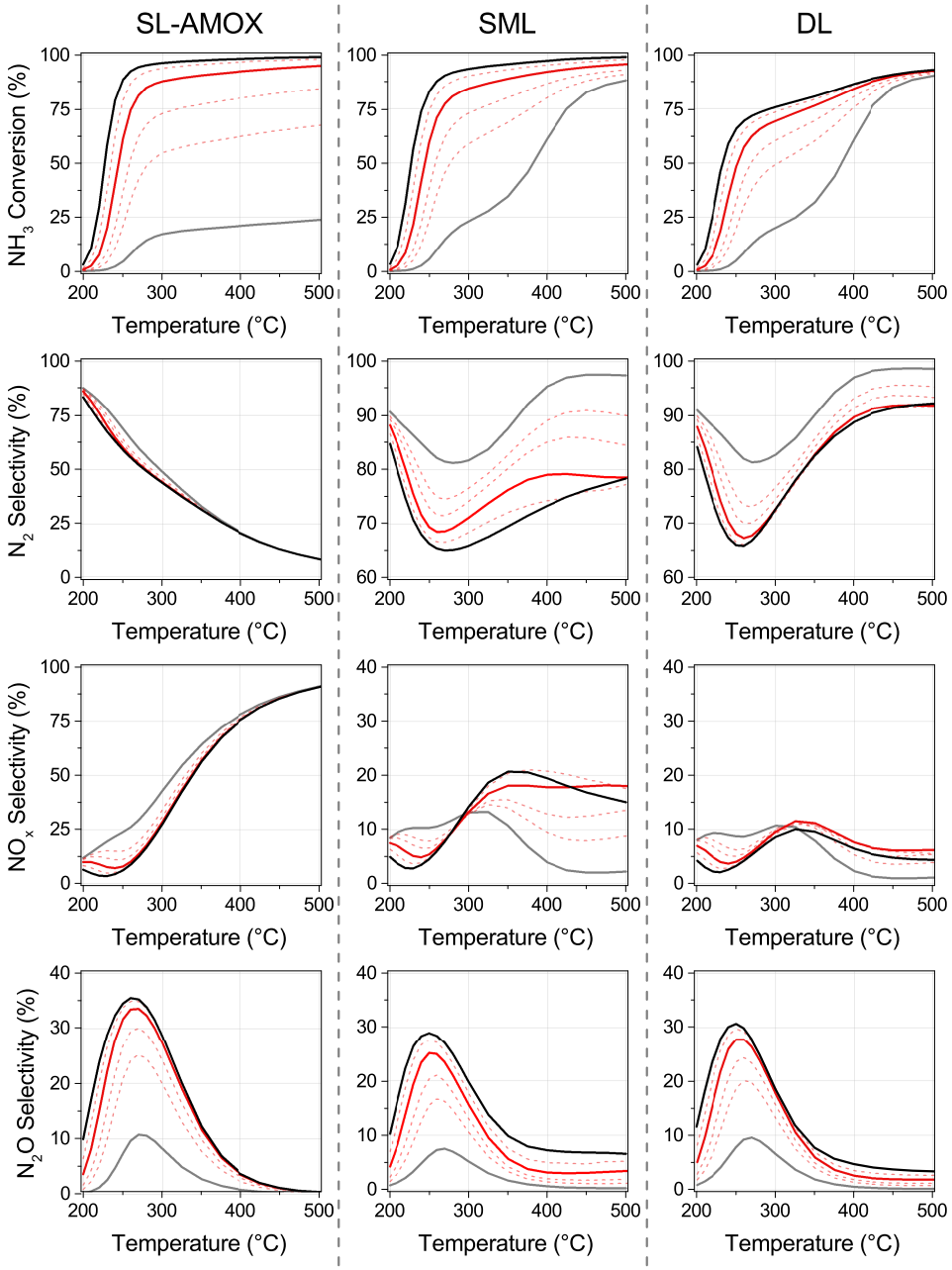

Figure 5.4: *Simulation of SL-AMOX, SML, and DL with varying intrinsic activity of the AMOX catalyst. Variations in intrinsic activity are represented by changes in Pt wt.% of AMOX catalyst between 0.01–1 wt.% Pt:* χ_{Pt}*= 0.01 (solid gray line), 0.05, 0.1, 0.235 (solid red line), 0.5, and 1 (solid black line). Base catalyst parameters:* ψ_{AMOX}*=26 g/L AMOX,* $d_{pore,\ bl}$*=50 nm,* ψ_{SCR}*=54 g/L, and* $d_{pore,\ SCR}$*=50 nm. Operating conditions: 200 ppm* NH_3*, 3.3 vol.%* H_2O*, 12.3 vol.%* O_2*, balance* N_2*, with GHSV 250,000* hr^{-1}*.*

formation on the presence of both NH_3 and NO over the AMOX catalyst expressed by reaction R 5.1:

$$4\,NH_3 + 4\,NO + 3\,O_2 \rightarrow 4\,N_2O + 6\,H_2O \qquad (R\,5.1)$$

The low formation of NO limits the rate of N_2O formation, leaving NO unreacted and shifting the product selectivity towards NO_x, while also decreasing competition for oxidation of NH_3 to N_2, thereby slightly increasing N_2 selectivity at temperatures below 350°C.

For the SML and DL catalysts, the inclusion of the SCR catalyst enables the SCR reactions and greatly decreases the NO_x selectivity, in turn greatly increasing N_2 selectivity. This effect is most prominent for the DL catalyst which has a maximum NO_x selectivity of 12% compared to 20% for SML. By increasing the intrinsic activity of the AMOX catalyst the dominance of the AMOX reactions relative to the SCR reactions is increased, resulting in a higher contribution from the AMOX catalyst at a given point in the washcoat layer. This means that a higher intrinsic activity increases the likelihood of NH_3 oxidation over the AMOX catalyst relative to the possible reduction reactions between NH_3 and NO_x over the SCR catalyst. The simulations reflect this through the decreasing N_2 selectivity and increasing NO_x selectivity for the SML catalyst.

5.3.2 Varying the Loading of the Ammonia Oxidation Catalyst

Figure 5.5 presents the NH_3 conversion and product selectivity for the series of simulations considering the variations in AMOX catalyst loading between 1–120 g/L for the SL-AMOX, SML, and DL catalysts. For all three ASC configurations, the AMOX loading affects the oxidation activity similarly. At temperatures below 250°C, the AMOX loading clearly impacts the NH_3 oxidation activity, with higher loadings leading to greater NH_3 conversion for the entire span of 1–120 g/L AMOX catalyst, indicating a kinetic controlled regime. The effect is also very noticeable for SL-AMOX at temperatures above 250°C. For SL-AMOX with AMOX loadings between 26–120 g/L, the effect decreases at higher temperatures where the process becomes limited by mass transfer across the gas film. For both SML and DL, the effect is less prominent at temperatures above 300°C due to the onset of NH_3 oxidation activity for the Cu-BEA SCR catalyst included in the SML and DL catalysts.

The product selectivity towards N_2, NO_x, and N_2O is also affected by variations in the AMOX loading. In general, the low loadings of AMOX catalyst lead to a higher N_2 selectivity and NO_x selectivity below 350°C, and a correspondingly lower N_2O selectivity. An increase in AMOX loading results in a general increase in N_2O and NO_x selectivity. The reasoning for these observations is again based on a combination of the dependence on both NH_3 and NO to form N_2O and the respective NH_3 conversion achieved.

The simulations with varying AMOX catalyst loading give results very similar to those for variations in intrinsic activity of the AMOX catalyst, with an increase in AMOX loading having the same general effects on NH_3 conversion and product selectivity as described for an increase in AMOX intrinsic activity. A significant difference between the results is related to the differences in system sensitivity to changes in the AMOX loading and intrinsic activity at the upper extreme of the

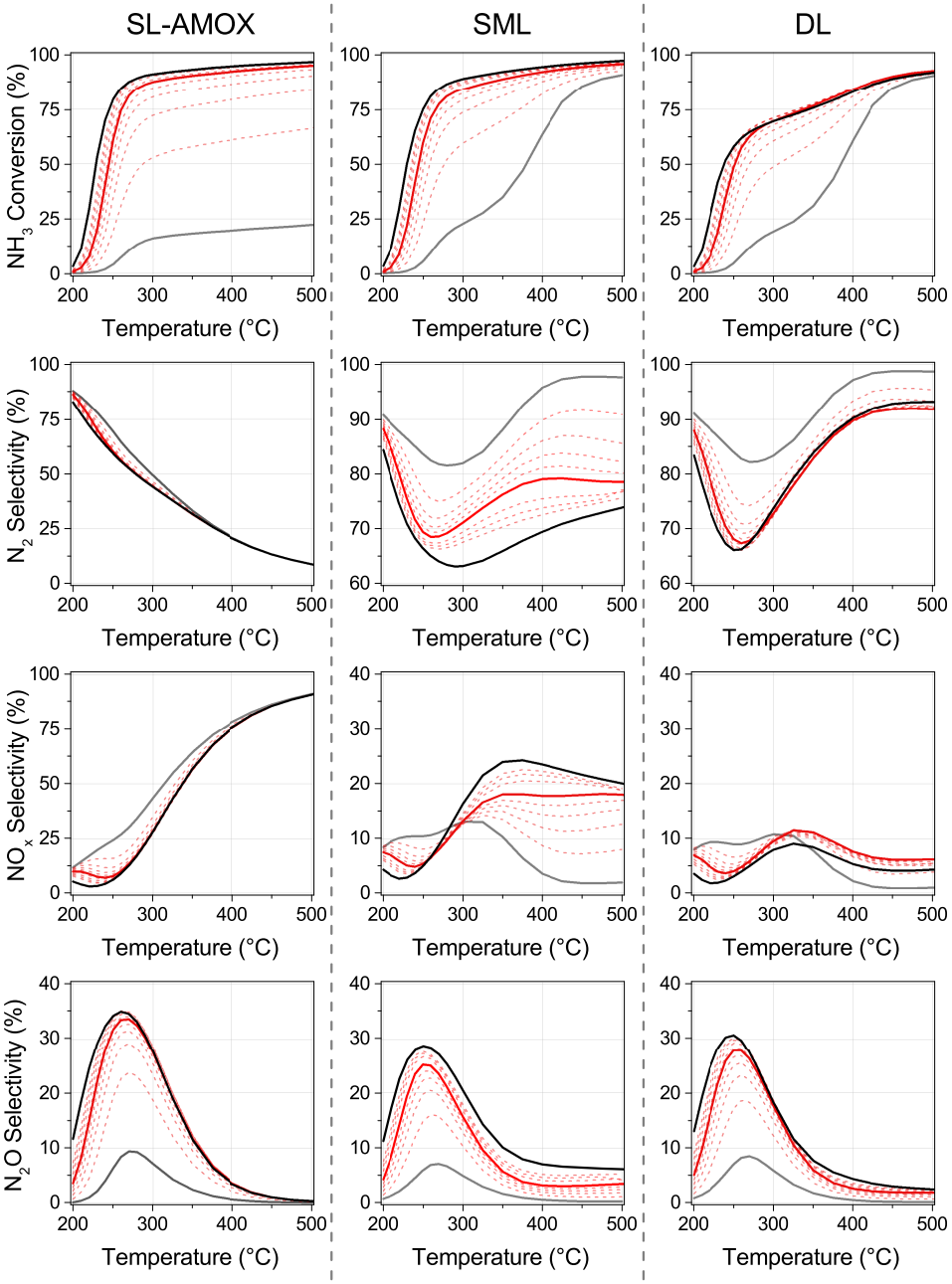

Figure 5.5: *Simulations of SL-AMOX, SML, and DL configurations with varying AMOX loading (g/L): ψ_{AMOX}=1 (solid gray line), 5, 10, 15, 26 (solid red line), and 120 (solid black line). Base catalyst parameters: χ_{Pt}=0.235 Pt wt.%/g_{AMOX}, $d_{\text{pore, bl}}$=50 nm, ψ_{SCR}=54 g/L, and $d_{\text{pore, SCR}}$=50 nm. Operating conditions: 200 ppm NH_3, 3.3 vol.% H_2O, 12.3 vol.% O_2, balance N_2, with GHSV 250,000 hr^{-1}.*

parameter range, relative to the reference catalyst systems. The effect of changing the parameter from the value of the reference system to the upper extreme is clearly largest when considering intrinsic activity of the AMOX catalyst compared to changes in the AMOX loading, although the Pt loading is slightly larger for the resulting AMOX catalyst system with 120 g/L AMOX (0.28>0.26). This suggests that there is a change in the resistances from intrapore diffusion and/or external mass transfer when the AMOX catalyst loading is varied. For example, an increase in AMOX loading leads to a thicker catalyst layer that results in an increased diffusion resistance. Similarly, a thicker catalyst loading decreases the available geometric surface area of the coated channel and decreases the residence time in the monolith sample. In contrast, the constant thickness of the AMOX layer, resulting from a constant AMOX loading of 26 g/L with variations in the intrinsic activity (Pt wt.%), means that the diffusion limitation on reactants throughout the entirety of the AMOX layer is also kept constant. It then follows that the greatest activity for a given Pt loading is achieved by applying the thinnest catalyst layer possible with the correspondingly higher Pt wt.%, thereby providing a higher effectiveness factor.

5.3.3 Varying the Loading of the Selective Catalytic Reduction Catalyst

The SCR catalyst loadings of the SML and DL catalysts were varied between 1–200 g/L and the resulting simulations are shown in Figure 5.6. The SCR loading clearly affects the catalyst performance, having a significant impact on NH_3 conversion and product selectivity. The overall effects of varying the SCR loading are the same for both the single mixed layer and dual layer catalysts. The catalysts with low SCR loadings are the catalysts that achieve the greatest NH_3 conversion. However, these catalysts also have the highest selectivity towards NO_x and N_2O, corresponding to the lowest N_2 selectivity. The NO_x and N_2O selectivity are then decreased when the SCR loading is increased, although this also leads to a decrease in NH_3 conversion due to the decrease in AMOX accessibility.

By comparing the simulations for the SML and DL catalysts, three key differences are seen. Firstly, the NH_3 conversion of the SML is much less sensitive to variations in the SCR loading than the DL catalyst. Again, this is related to how the accessibility to the AMOX catalyst is affected. An addition of the SCR catalyst to the DL configuration increases the thickness of the SCR top layer, which acts as a diffusion barrier. In contrast, the SCR catalyst added to the SML configuration dilutes the AMOX catalyst component, also decreasing the AMOX accessibility, but not to the same extent as for the DL catalyst.

Secondly, the overall N_2 selectivity is highest for the DL configuration and obtained for high loadings of SCR catalyst. Again, this is at the cost of NH_3 conversion since the thicker SCR layer is also a thicker diffusion barrier. Similarly, the overall NO_x selectivity is lowest for the DL catalyst.

Thirdly, the SML catalyst is capable of achieving lower N_2O selectivities than the DL catalyst. By diluting the AMOX catalyst with the SCR catalyst, the SCR reactions between NH_3 and NO limit the reactions between NH_3 and NO over the AMOX catalyst, leading to significantly lower N_2O selectivity over the SML

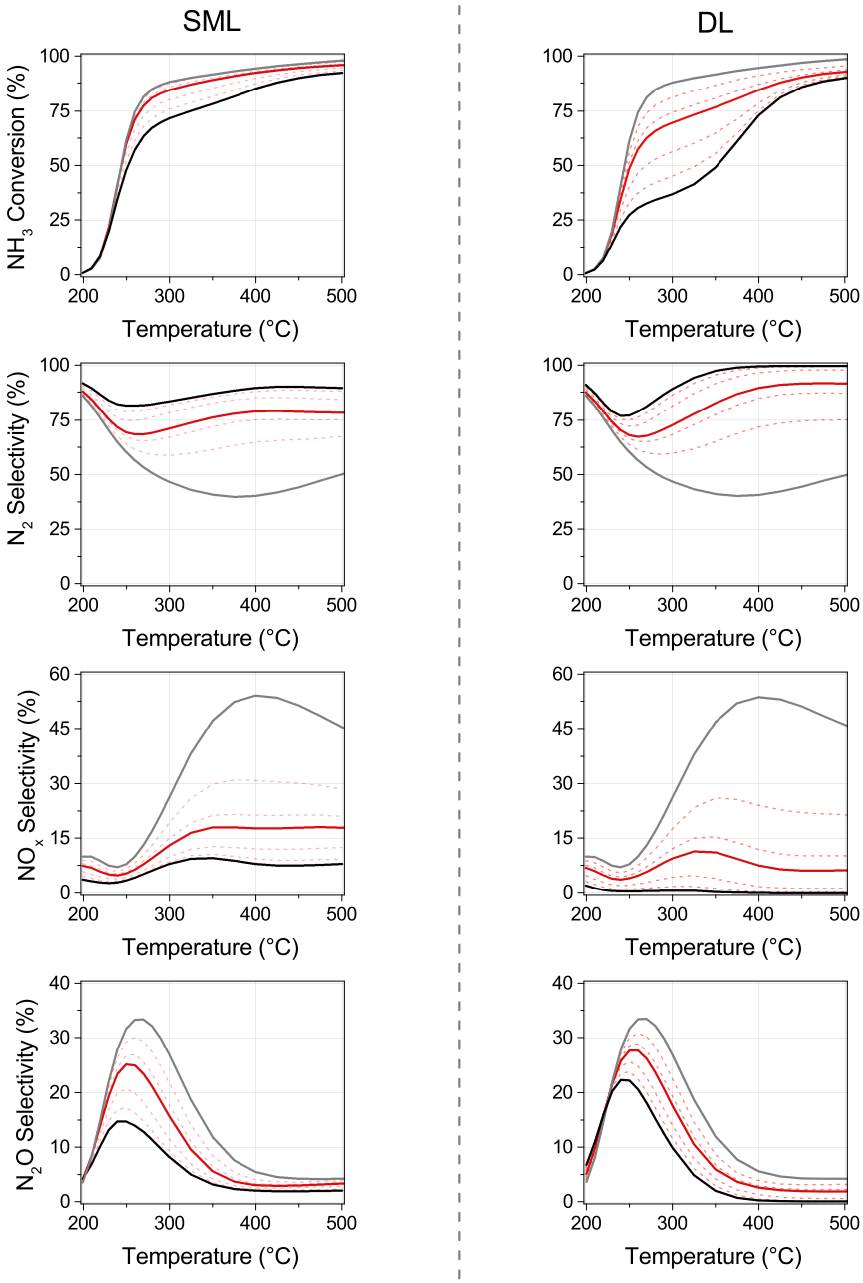

Figure 5.6: *Simulation of SML and DL with varying ψ_{SCR} between 1–200 g/L: ψ_{SCR}= 1 (solid gray line), 20, 40, 54 (solid red line), 100, 150, and 200 (solid black line). Base catalyst parameters: ψ_{AMOX}=26 g/L AMOX, χ_{Pt}= 0.235 wt.% Pt, $d_{\mathrm{pore,\,bl}}$=50 nm, and $d_{\mathrm{pore,\,tl}}$=50 nm. Operating conditions: 200 ppm NH_3, 3.3 vol.% H_2O, 12.3 vol.% O_2, balance N_2, with GHSV 250,000 hr^{-1}.*

configuration with a maximum of 15% for 200 g/L SCR, compared to 22% for the DL catalyst.

5.3.4 Varying the Effective Diffusivity of the Catalyst Layers

The effective diffusivity was varied for the catalyst layers of the SL-AMOX, SML, and DL configurations by varying the average pore diameter of the catalyst layers between 10–1000 nm corresponding to a variation in the effective diffusion coefficient from 0.33×10^{-6} m^2/s to 5.99×10^{-6} m^2/s. Figure 5.7 shows the resulting simulations. For the DL configuration, the effective diffusivity of the two layers were set to be the same by applying the same average pore diameter. In general, an increase in the effective diffusivity leads to an increase in NH_3 conversion, with the effect being the most significant for changes in the low end of the parameter range. For example, the SL-AMOX catalyst is barely affected by the change from 50 nm (1.38×10^{-6} m/s^2) to 1000 nm (5.99×10^{-6} m^2/s), but significantly affected by the increase from 10 (0.33×10^{-6} m^2/s) to 50 nm (1.38×10^{-6} m/s^2). Of the three configurations considered, the NH_3 conversion of the DL configuration is the most sensitive to changes in the effective diffusivity. This is again related to the diffusion barrier effect of the SCR top layer. With regard to product selectivity, the SL-AMOX and SML catalyst are not affected significantly. In contrast, the NO_x selectivity of the DL catalyst is increased when the effective diffusivity is increased, which is related to the increased accessibility of the AMOX catalyst to the gas phase and a faster diffusion of NO_x out to the channel, thereby limiting the reaction with NH_3 in the SCR layer. The N_2 selectivity is correspondingly decreased.

For Figure 5.7 the effective diffusivity of the bottom and top layers were set to be equal and showed that the DL configuration is affected the most by variations in effective diffusivity. This is further investigated in Figure 5.8 by comparing the simulations where the bottom and top layer have the same effective diffusivity with cases where only the effective diffusivity of one of the layers is varied. In this manner, the contribution from changes in the effective diffusivity of the two layers can be better identified. Figure 5.8 shows that the effective diffusivity of the top layer is the most controlling for the performance of the DL catalyst based on the similarity between the simulations for equal diffusivity in both layers (left column) with those where the diffusivity of only the top layer is varied (right column). A low diffusivity of the top layer results in a much lower NH_3 conversion, but also a greater N_2 selectivity. This is similar to the balance between NH_3 conversion and N_2 selectivity that is seen when the SCR loading is varied.

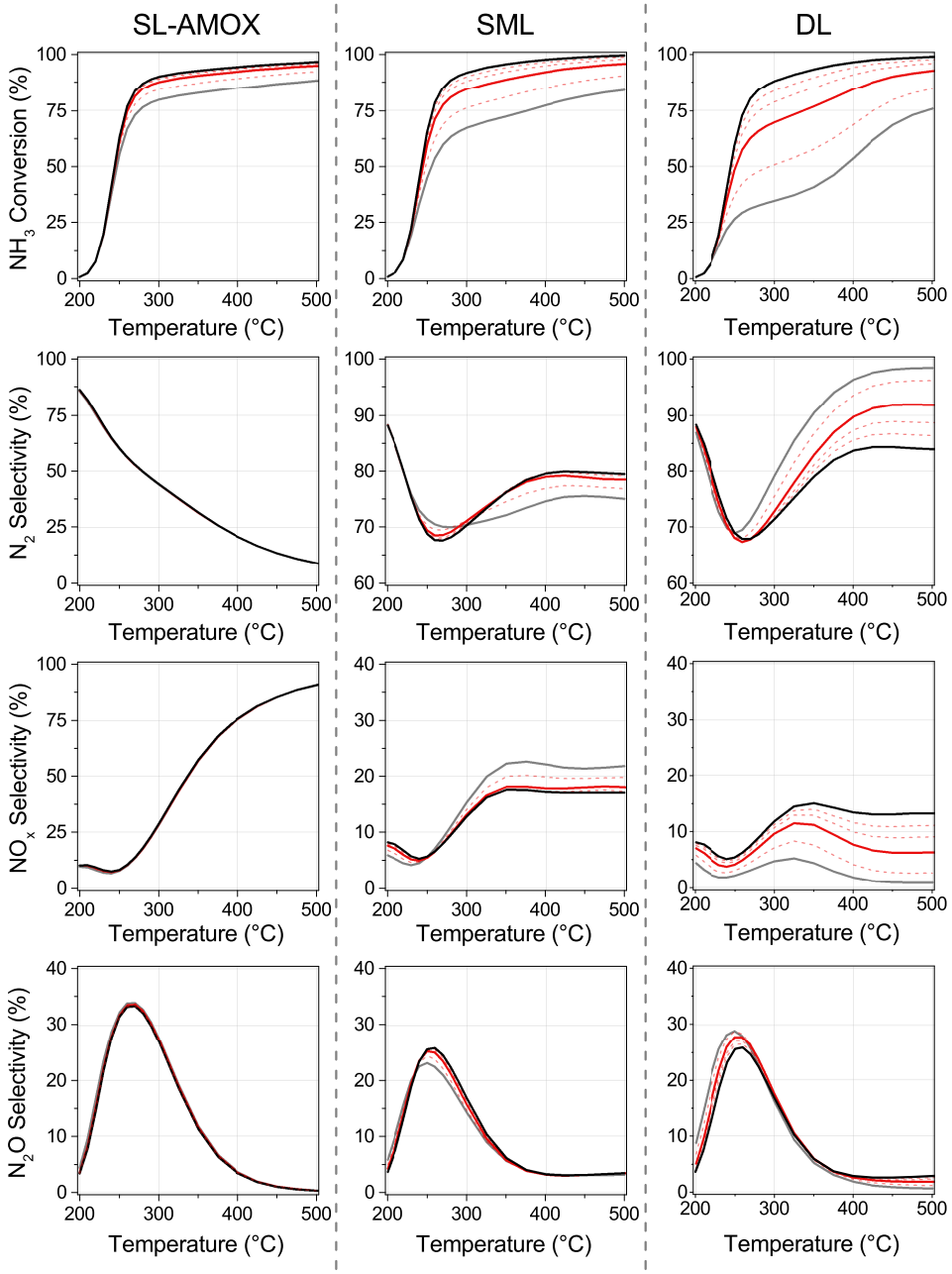

Figure 5.7: *SL-AMOX, SML, and DL ASC configurations with varying effective diffusivity. The effective diffusivity of the bottom and top layers is to the be the same:* $d_{\text{pore bl}}$=$d_{\text{pore tl}}$=*10 (solid gray line), 20, 50 (solid red line), 100, 200, and 1000 (solid black line). Base catalyst parameters:* ψ_{AMOX}=*26 g/L AMOX,* χ_{Pt}= *0.235 wt.% Pt, and* ψ_{SCR}=*54 g/L SCR. Operating conditions: 200 ppm* NH_3*, 3.3 vol.%* H_2O*, 12.3 vol.%* O_2*, balance* N_2*, with GHSV 250,000* hr^{-1}.

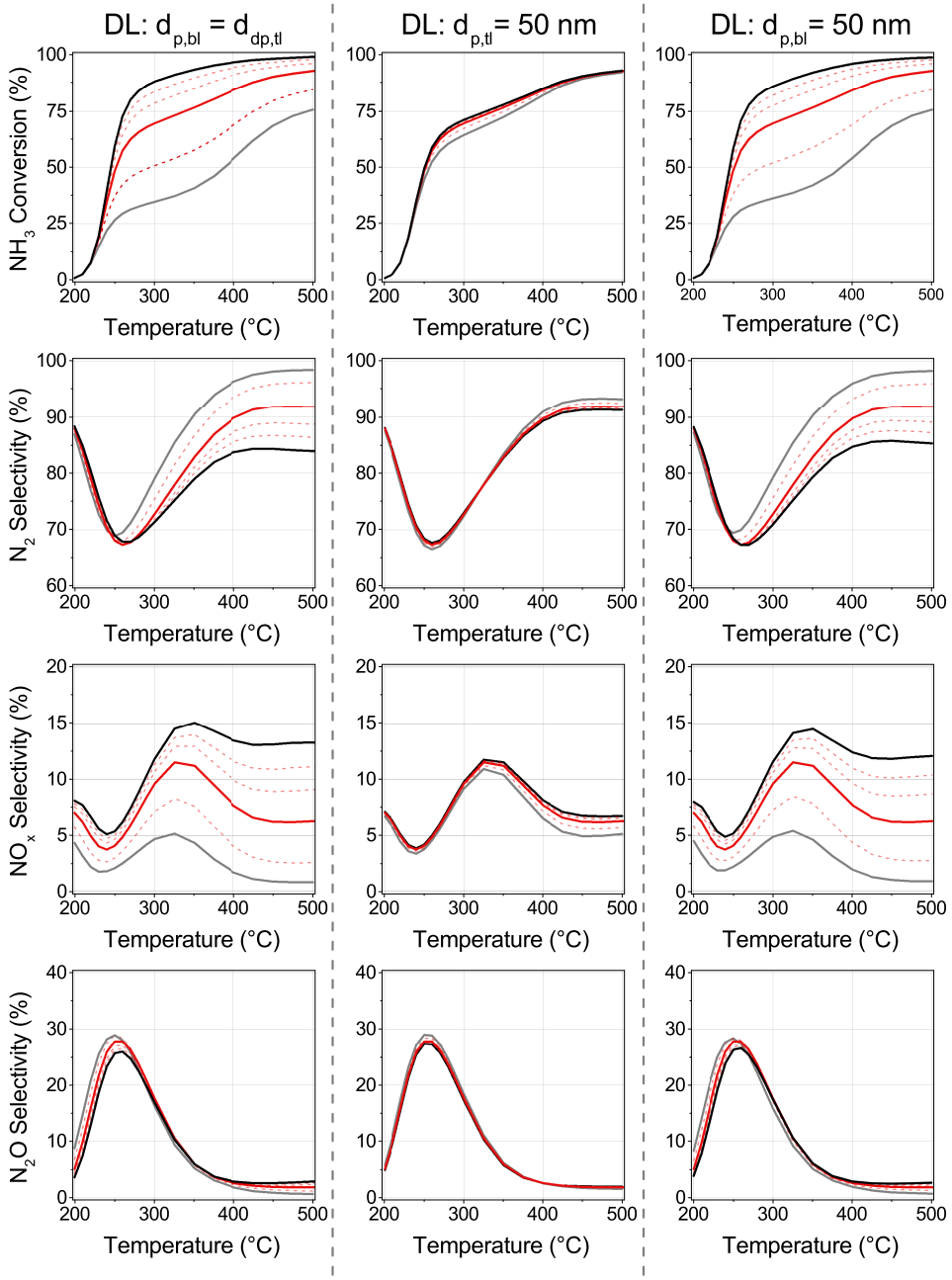

Figure 5.8: *Simulations of the DL catalyst with variations in the effective diffusivity for the bottom layer and top layer. Left column:* $d_{\text{pore bl}}$=$d_{\text{pore tl}}$*, middle column:* $d_{\text{pore bl}}$ *is varied while* $d_{\text{pore tl}}$=*50 nm, and right column:* $d_{\text{pore bl}}$=*50 nm while* $d_{\text{pore tl}}$ *is varied. Values for varied* d_{pore}*: 10 (solid gray line), 20, 50 (solid red line), 100, 200, and 1000 nm (solid black line). Base catalyst parameters:* ψ_{AMOX}=*26 g/L,* χ_{Pt}=*0.235 wt.% Pt, and* ψ_{SCR}=*54 g/L. Operating conditions: 200 ppm* NH_3*, 3.3 vol.%* H_2O*, 12.3 vol.%* O_2*, balance* N_2*, with GHSV 250,000* hr^{-1}.

This page is intentionally left blank. Please turn to next page.

5.3.5 Varying the NO Oxidation Activity of the Ammonia Oxidation Catalyst

The significance of the NO_2/NO_x ratio of NO_x formed during NH_3 oxidation was investigated by simulating cases where the rate coefficient for NO oxidation over the AMOX catalyst was multiplied by factors of 0, 1, 3.3, 8, 16, and 32. This was done for the SL-AMOX, SML, and DL configurations, and the results are shown in Figure 5.9. It is seen from the simulations for all three systems that the change in $k_{\text{NO ox.}}$ has a negligible effect on the conversion of NH_3. Furthermore, the SL-AMOX simulations show that there is no influence of $k_{\text{NO ox.}}$ on the N_2 selectivity. However, there is some effect on the N_2O selectivity, since a higher oxidation of NO to NO_2 decreases the rate of N_2O formation from NH_3 and NO. This is reflected by a small increase in NO_x selectivity for increased NO oxidation activity. Overall, the variations in $k_{\text{NO ox.}}$ have a focused effect on the ratio of NO_2/NO_x from the AMOX catalyst, allowing us to investigate its significance for SML and DL. The simulations of the SML and DL systems show the same general trends; an increase in $k_{\text{NO ox.}}$ increases the NO_2/NO_x ratio and leads to a beneficial effect on NO_x and N_2 selectivity, but also leads to an increase in N_2O selectivity. The change in product selectivity arises due to the higher NO_2/NO_x ratios evoking the fast and slow SCR reactions. Especially the fast SCR reaction causes an increase in NO_x reduction. However, the fast and slow SCR reactions over the Cu-BEA catalyst have a higher selectivity towards N_2O relative to the standard SCR reaction, and an increase in $k_{\text{NO ox.}}$ therefore leads to an increase in N_2O selectivity.

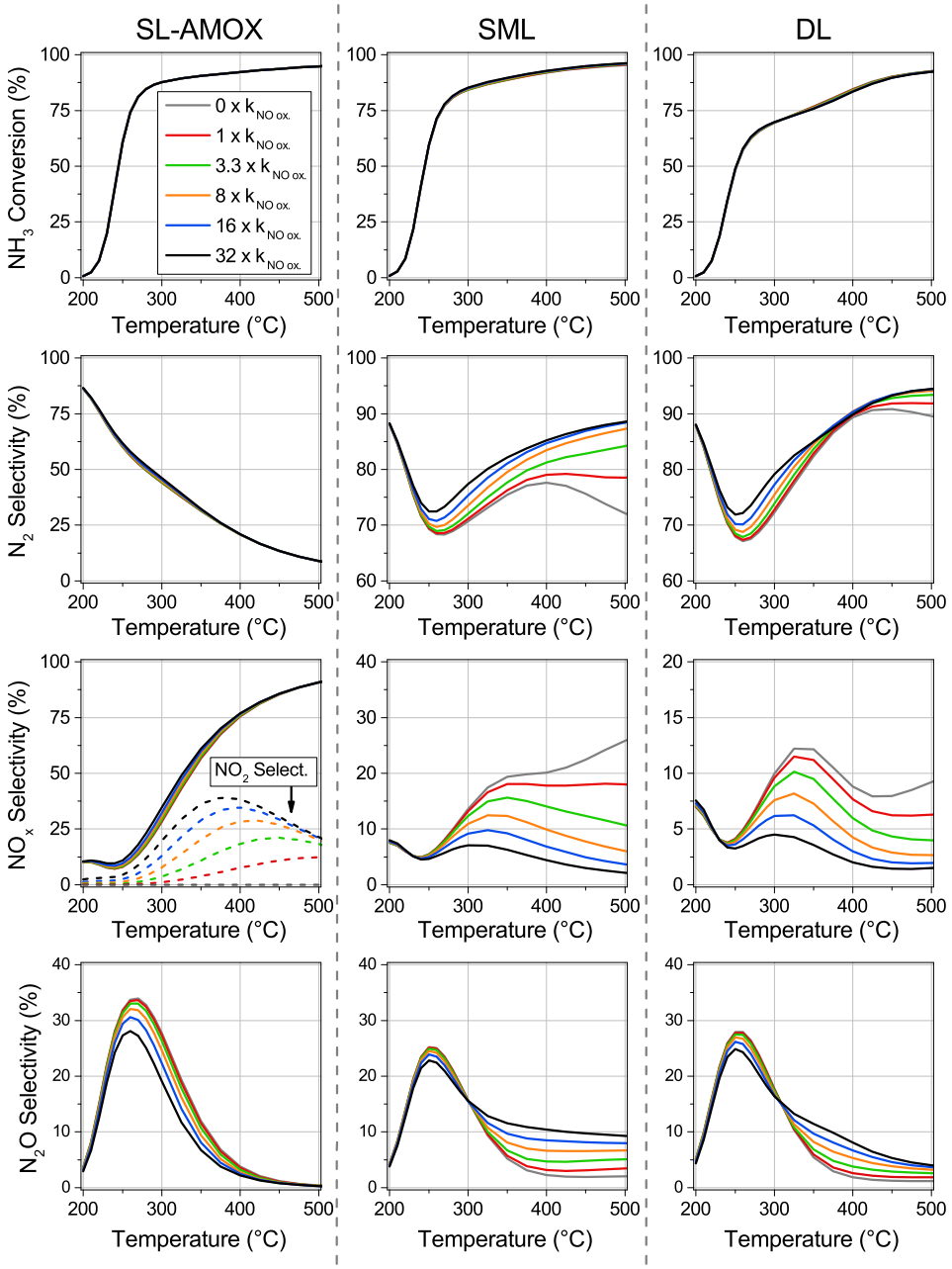

Figure 5.9: *Simulation of SL-AMOX, SML, and DL catalysts with varying NO oxidation activity, k_{NO_x} = 0×, 1×, 3.3×, 8×, 16×, and 32×. Base catalyst parameters: ψ_{AMOX}=26 g/L, χ_{Pt}=0.235 wt.% Pt, and $d_{pore,\ bl}$=50 nm, $d_{pore,\ tl}$=50 nm, and ψ_{SCR}=54 g/L. Operating conditions: 200 ppm NH_3, 3.3 vol.% H_2O, 12.3 vol.% O_2, balance N_2, with GHSV 250,000 hr^{-1}.*

5.3.6 Disabling N_2O Formation of the Individual Catalysts

The Pt-based AMOX catalyst and the Cu-BEA SCR catalyst both have a significant selectivity towards the formation of N_2O. In order to probe the contribution from each catalyst to N_2O formation over the ASC, simulations were run where the reactions leading to N_2O were disabled for either the AMOX or SCR catalyst, for the SML and DL configurations. These simulations are shown in Figure 5.10, along with the respective reference systems. From Figure 5.10, it is seen that the changes in $k_{N_2O,\,AMOX}$ and $k_{N_2O,\,SCR}$ have a negligible effect on NH_3 conversion, and only have a significant impact on the product selectivity. Focusing on the N_2O selectivity, it is seen that for both catalyst systems, that disabling the N_2O formation from the AMOX catalyst removes the large peak in N_2O selectivity occurring between 200-300°C, which corresponds to the majority of N_2O formed, while the N_2O selectivity at >400°C is unchanged. Overall, disabling N_2O formation from the AMOX catalyst results in a N_2O selectivity of less than 5% for the entire temperature range for the catalysts considered. In contrast, disabling N_2O formation over the Cu-BEA catalyst has little effect in the range of 200–350°C, but instead decreases the N_2O selectivity at temperatures above 350°C. For both catalyst systems, the disabling of N_2O formation leads to an corresponding increase in both N_2 and NO_x selectivities. Based on the presented simulations, it is clear that the AMOX catalyst is responsible for most of the N_2O formed below 350°C, which accounts for the majority of N_2O formed over the ASC. Meanwhile, the SCR catalyst is responsible for most of the N_2O formed above 350°C, and a small portion of that formed below 350°C. ASC catalysts with lower N_2O yield should thus focus on minimizing N_2O formation from the AMOX catalyst.

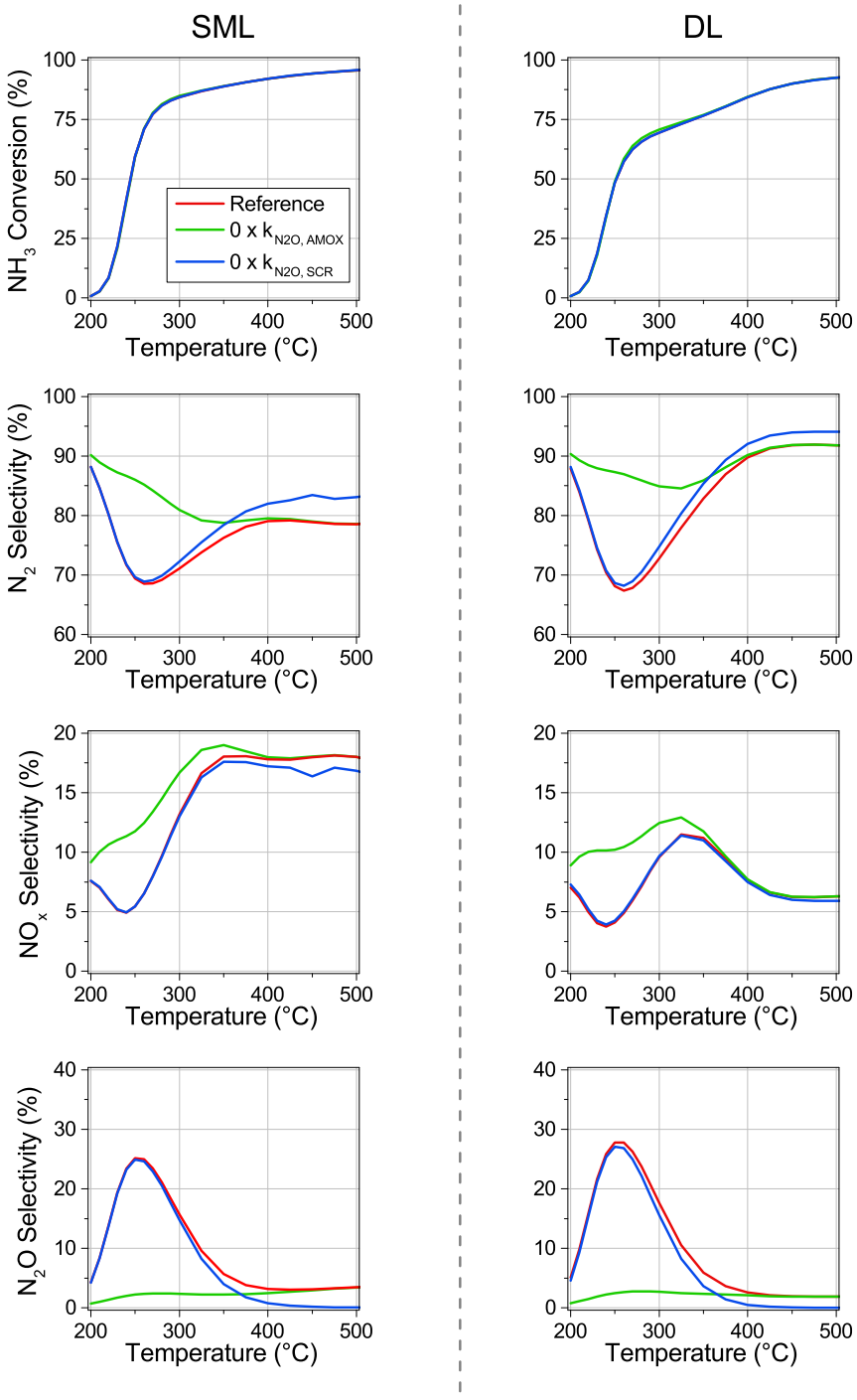

Figure 5.10: *Simulations of the SML and DL catalysts with the N_2O formation reactions of either the AMOX catalyst ($k_{N_2O,AMOX}$) or SCR catalyst ($k_{N_2O,SCR}$) disabled. Base catalyst parameters: ψ_{AMOX}=26 g/L, χ_{Pt}=0.235 wt.% Pt, and $d_{pore,\ bl}$=50 nm, $d_{pore,\ tl}$=50 nm, and ψ_{SCR}=54 g/L. Operating conditions: 200 ppm NH_3, 3.3 vol.% H_2O, 12.3 vol.% O_2, balance N_2, with GHSV 250,000 hr^{-1}.*

5.3.7 Varying the Ammonia Slip Catalyst Configuration

To further improve the understanding of the ASC system, the sensitivity of the system performance to the catalyst configuration was studied. For this purpose, the ten possible ASC configurations for the dual mixed layer model presented in Figure 5.1 were optimized using multi-objective optimization at a typical operating temperature of 300°C and the same operating conditions as for the other simulations. The Pareto fronts generated from the multi-objective optimization by varying the design parameters (catalyst loadings, intrinsic activity of AMOX catalyst, and effective diffusivity) are presented in Figure 5.11 in terms of A) NO_x slip, B) N_2O slip, C) combined NO_x and N_2O slip, and D) N_2 slip, all as function of the NH_3 slip.

The Pareto front of Figure 5.11 A) reflect the ability of the different ASC configurations to oxidize NH_3 without forming NO_x. The majority of catalysts are overlaying, since they all effectively have a mixed top layer. In contrast, the SL-AMOX catalyst produces the most NO_x when oxidizing NH_3, which is the known issue with this catalyst design [1–14]. The IDL consists of a top layer of AMOX catalyst, and it is therefore also quite active in NO_x formation, although the SCR bottom layer greatly improves its NO_x selectivity. Similarly, the HDL-A also has an AMOX top layer, leading to a more significant NO_x slip. However, since this configuration has the option of mixing the majority of the AMOX catalyst together with the SCR catalyst in the bottom layer, the effect is more limited than the IDL configuration. Lastly, the DL catalyst also has a significant NO_x slip since the trade-off for a higher NH_3 conversion, by increasing accessibility to the AMOX catalyst, is an increase in NO_x slip due to a more accessible gas phase to any NO_x formed. However, the DL and HDL-S catalysts have a top layer of SCR catalyst which allows them to achieve the lowest NO_x slip at the cost of NH_3 conversion.

Figure 5.11 B) shows the Pareto front represents the trade-off seen for NH_3 conversion and N_2O formation for the different configurations. The highest N_2O slip is seen for the SL-AMOX, DL, and IDL catalysts. These catalyst configurations contain a single pure layer of AMOX catalyst, which leads to a high N_2O formation. Unexpectedly, the N_2O slip from the HDL-A is one of the lowest even though the catalyst includes a pure top layer of AMOX catalyst. This is likely possible due to a combination of a moderate intrinsic activity and a high effective diffusivity limiting the reaction between NH_3 and NO to N_2O over the AMOX catalyst. Meanwhile, all catalysts with mixed layers of AMOX and SCR catalyst achieve a low N_2O slip.

In Figure 5.11 C), the NO_x slip and N_2O slip are combined and plotted as a function of NH_3 slip, and their total sum corresponds to the objective function used for optimization. In general, the previous observations from Figure 5.11 A) and B) still apply; the catalysts that are most selective in oxidizing NH_3 to NO_x and N_2O are the SL-AMOX, IDL, and DL. While the mixed layer catalysts are overlaying, and the least selective towards NO_x and N_2O (most selective to N_2). This is also exemplified by Figure 5.11 D) which shows the N_2 slip for the different configurations. The dashed gray line represents the N_2 selectivity of an ideal ASC, for which NH_3 is only oxidized to N_2. The N_2 slip is an expression of the N_2 yield, combining NH_3 conversion and N_2 selectivity. The maximum seen in most of the curves corresponds to the most optimal solutions, which are those that achieve the

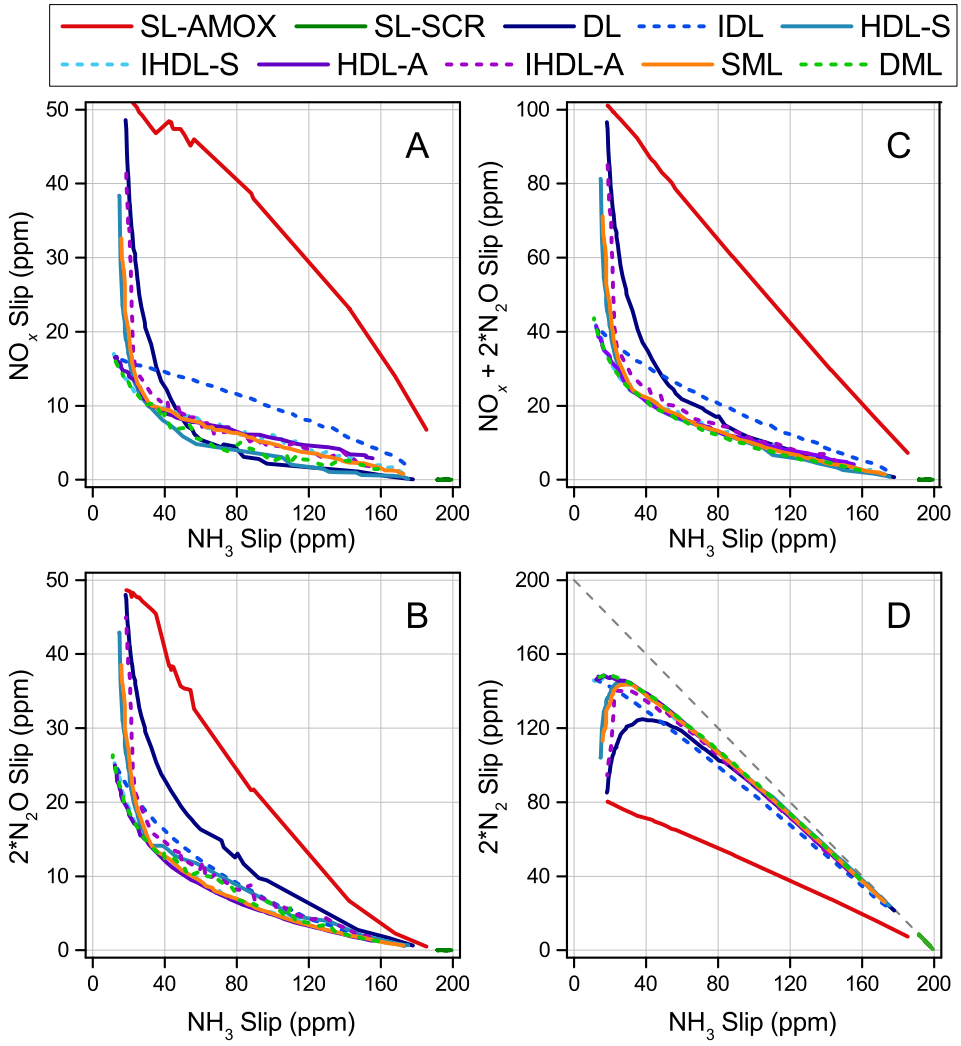

Figure 5.11: *Pareto fronts generated for the ten ammonia slip catalyst configurations investigated. Operating conditions: 300° C, 200 ppm NH_3, 3.3 vol.% H_2O, 12.3 vol.% O_2, balance N_2, with GHSV 250,000 hr^{-1}.*

highest selective oxidation of NH_3 to N_2. Similarly to the Pareto fronts for NO_x and N_2O slip, the SL-AMOX is the least selective towards N_2, followed by the IDL and DL configurations, due again to the pure AMOX catalyst layers. In contrast, the most effective catalysts for oxidizing NH_3 to N_2 are those that contain mixed layers. By combining the AMOX and SCR components, the NH_3 oxidation activity is balanced with the NO_x reduction leading to a significant improvement in the selective oxidation of NH_3 to N_2. Multi-objective optimization was also done for systems for which the effective diffusivity and/or catalyst loadings were varied, and the same trends were seen.

5.4 Discussion

The sensitivity analysis and results from multi-objective optimization of the ten different ASC configurations presented in this chapter contribute to the system understanding of the ASC. In general, the performance of the ASC is highly dependent on the Pt loading (g_{Pt}/L), since an absence of Pt results in a lack of NH_3 oxidation activity. This is more clear at temperatures below 300°C where the rate of NH_3 oxidation is limited by the reaction kinetics. However, if the oxidation activity is sufficiently high, the rate of NH_3 oxidation becomes more controlled by internal or external mass transfer limitations. At this point, the catalyst loading (layer thickness) and effective diffusivity of the catalyst layers become significant. The thickness of the catalyst layer is affected by variations in catalyst loading, influencing how readily reactants can diffuse throughout the catalyst phase. As a consequence, it is more beneficial to apply a low loading of an AMOX catalyst with a high Pt loading, thereby keeping diffusion limitations to a minimum. Diffusion limitations are an especially important design parameter for the DL catalyst, since the SCR top layer is acting as a diffusion barrier for NH_3 to the AMOX catalyst, while also providing the necessary SCR activity. Assuming a sufficient Pt loading, the catalyst loading and effective diffusivity of the SCR top layer are therefore the key design parameters for the DL configuration. For the SML catalyst, the key design parameter is the SCR catalyst loading since it used to balance the NH_3 oxidation activity with the SCR activity, in effect determining product selectivity of the ASC. The effective diffusivity is still significant in ensuring a high effectiveness factor, but is less critical than the SCR loading for the SML.

The significance of the NO oxidation activity of the AMOX catalyst was motivated by the results of Chapter 3 that showed an effect of the Pt particle size on the NO_2/NO_x ratio of NO_x formed during NH_3 oxidation. It was therefore suggested in the subsequent discussion that the Pt particle size could be used to control the local NO_2/NO_x ratio in the ASC washcoat phase, and lead to the fast SCR reaction and help reduce NO_x emissions. This theory is supported by the simulations performed in this chapter, where the $k_{NO\,ox.}$ was multiplied by factors of 0–32 to vary the NO_2/NO_x ratio. The simulations however also support the consideration that a higher NO_2/NO_x ratio leads to a higher N_2O selectivity due to increased N_2O formation over Cu-BEA. This suggests that it is in fact possible to decrease NO_x slip from the ASC by generating NO_x with a higher NO_2/NO_x ratio, but also that an appropriate SCR catalyst with a low N_2O selectivity must be used in order to avoid an increased N_2O slip.

Due to the potential future regulations on N_2O slip it was relevant to consider the contribution of the AMOX and SCR catalysts to N_2O formation in order to identify their contributions. The simulations clearly showed that the majority of N_2O formation is dependent on the activity of the AMOX catalyst, and that the N_2O selectivity below 350°C becomes drastically reduced by disabling N_2O formation over the AMOX catalyst, even though the Cu-BEA SCR catalyst is potentially highly active in N_2O formation [32, 33]. Furthermore, the simulations indicate that the Cu-BEA SCR catalyst is responsible for N_2O formation at temperatures above 350°C. In this manner, the contributions of the AMOX and SCR catalyst towards N_2O formation are unraveled, and identify the reaction of NH_3 and NO over the AMOX catalyst as the main source.

The multi-objective optimization of the ten ASC configurations optimized the general design parameters studied in the sensitivity analysis (intrinsic activity, catalyst loading, and effective diffusivity), and was effectively a sensitivity analysis concerning how the ASC is affected by changes in the catalyst configuration. Based on the optimal solutions it became clear that for NH_3 oxidation it is the catalyst configurations with mixed layers that perform best. This is suggested to be due to a combination of a more readily accessible AMOX catalyst providing a high NH_3 conversion with an significantly increased N_2 selectivity due to a more readily available SCR catalyst that effectively circumvents the formation of N_2O through a more immediate reduction of NO compared to catalyst configurations where pure layers of AMOX are present. It should be emphasized that this sensitivity analysis was focused solely on the selective oxidation of NH_3 to N_2 for a single temperature of 300°C, and that the outcome of this investigation is dependent on the conditions considered together with any system specifications and relative weighting placed on the objective functions. For example, an SCR top layer may prove to be more advantageous if NO_x is present in the feed with NH_3 or at higher temperatures where the SCR catalyst is active for selective oxidation of NH_3. Furthermore, the NH_3 conversion was weighted equally with NO_x and N_2O selectivity, but if a higher or lower weight is specified for N_2 selectivity, then other configurations will be more beneficial. The sensitivity of the ASC to system specifications and operating conditions makes it necessary to develop the ASC to achieve high performance for a broad range of different operating conditions.

5.5 Conclusion

The validated model for the ammonia slip catalyst from Chapter 4 was used to perform a sensitivity analysis in order to probe the influence of the different design parameters and identify the key design parameters of the ASC. The importance of the intrinsic activity of the AMOX catalyst (Pt wt.%), the loadings of the AMOX and SCR catalysts (g/L), the effective diffusivity of the catalyst layers (average pore diameter), NO oxidation activity ($k_{\mathrm{NO\,ox.}}$), and N_2O formation over each catalyst were studied for the single layer AMOX catalyst, single mixed layer catalyst, and the dual layer catalyst by varying each parameter independently and simulating the oxidation of NH_3. A multi-objective optimization of ten ASC configurations was used to investigate the sensitivity of the ASC towards catalyst architecture.

In all cases, the Pt loading, determined by the combination of loading and Pt wt.% of the AMOX catalyst, was a key design parameter since it determines the

activity of the Pt-based oxidation component. However, once an upper limit of 6.11–26 g/L is reached, the effect dwindles and the system is no longer kinetically controlled, and instead becomes limited by intrapore diffusion and external mass transfer. The catalyst loading and effective diffusivity are therefore also key design parameters, as these factors determine the layer thickness and diffusion of reactants throughout the catalyst phase. Furthermore, the SCR catalyst loading determines the SCR activity available for NO_x reduction. A thin catalyst layer with a high SCR activity and effective diffusivity is therefore preferential since diffusion resistance is minimized and a high effectiveness factor is achieved. The NO oxidation activity of the AMOX catalyst was shown to influence the NO_2/NO_x ratio of NO_x formed by the AMOX catalyst. It was then possible to increase N_2 selectivity for the DL and SML catalysts by increasing the NO_2/NO_x ratio and evoking the fast SCR reaction to further reduce NO_x selectivity at the cost of also increasing N_2O selectivity. Additionally, the AMOX catalyst was identified as the main source of N_2O formation, indicating a necessary development of the AMOX catalyst to reduce N_2O emissions.

The sensitivity of the ASC to catalyst configuration was investigated by using the model to perform a multi-objective optimization of ten possible configurations for NH_3 oxidation at 300°C. From the resulting Pareto fronts, it is clear that the most effective catalyst designs are those that contain a mixed layer (AMOX+SCR). The mixed layer generally provides a high NH_3 oxidation activity due to the accessibility of NH_3 to the AMOX catalyst, while the tight contact with the SCR catalyst provides a more immediate reduction of NO_x with NH_3, which also circumvents the formation of N_2O. In contrast, the catalyst configurations with pure layers of AMOX catalyst generally produce the most N_2O. Furthermore, the SCR top layer of the dual layer configuration acts as diffusion barrier, which can only increase NH_3 conversion with simultaneous increase in NO_x, leading to a significantly higher NO_x selectivity at high NH_3 conversion compared to configurations with the mixed layer.

5.6 References

[1] A. Walker. Future Challenges and Incoming Solutions in Emission Control for Heavy Duty Diesel Vehicles. *Topics in Catalysis*, 59:695–707, 2016.

[2] A. Scheuer, M. Votsmeier, A. Schuler, J. Gieshoff, A. Drochner, and H. Vogel. NH_3-Slip Catalysts: Experiments Versus Mechanistic Modelling. *Topics in Catalysis*, 52:1847–1851, 2009.

[3] A. Scheuer, W. Hauptmann, A. Drochner, J. Gieshoff, H. Vogel, and M. Votsmeier. Dual Layer Automotive Ammonia Oxidation Catalysts: Experiments and Computer Simulation. *Applied Catalysis B: Environmental*, 111-112:445–455, 2012.

[4] A. Scheuer, A. Drochner, J. Gieshoff, H. Vogel, and M. Votsmeier. Runtime Efficient Simulation of Monolith Catalysts with a Dual-Layer Washcoat. *Catalysis Today*, 188:70–79, 2012.

[5] M. Votsmeier, A. Scheuer, A. Drochner, H. Vogel, and J. Gieshoff. Simulation of Automotive NH_3 Oxidation Catalysts Based on Pre-computed Rate Data from Mechanistic Surface Kinetics. *Catalysis Today*, 151:271–277, 2010.

[6] M. Colombo, I. Nova, and E. Tronconi. A Simplified Approach to Modeling of Dual-layer Ammonia Slip Catalysts. *Chemical Engineering Science*, 75:75–83, 2012.

[7] M. Colombo, I. Nova, E. Tronconi, V. Schmeißer, B. Bandl-Konrad, and L. R. Zimmermann. Experimental and Modeling Study of a Dual-Layer (SCR + PGM) NH_3 Slip Monolith Catalsyt (ASC) for Automotive SCR Aftertreatment Systems. Part 1. Kinetics for the PGM Component and Analysis of SCR/PGM Interactions. *Applied Catalysis B: Environmental*, 142-143:861–876, 2013.

[8] M. Colombo, I. Nova, E. Tronconi, V. Schmeißer, B. Bandl-Konrad, and L. R. Zimmermann. Experimental and Modeling Study of a Dual-Layer (SCR + PGM) NH_3 Slip Monolith Catalsyt (ASC) for Automotive SCR Aftertreatment Systems. Part 2. Validation of PGM Kinetics and Modeling of the Dual-layer ASC Monolith. *Applied Catalysis B: Environmental*, 142-143:337– 343, 2013.

[9] M. Colombo, I. Nova, E. Tronconi, and G. Koltsakis. A Modeling Study of NH_3 Slip Catalysts: Analysis of the SCR/PGM Interactions. *Topics in Catalysis*, 56:177–181, 2013.

[10] I. Nova, M. Colombo, E. Tronconi, V. Schmeisser, B. Bandl-Konrad, and L. Zimmermann. Experimental and Modelling Study of a Dual-Layer NH_3 Slip Monolith Catalyst for Automotive SCR Aftertreatment Systems. *Topics in Catalysis*, 56:227–231, 2013.

[11] S. Shrestha, M.P. Harold, K. Kamasamudram, and A. Yezerets. Ammonia Oxidation on Structured Composite Catalysts. *Topics in Catalysis*, 56:182–186, 2013.

[12] S. Shrestha, M.P. Harold, K. Kamasamudram, and A. Yezerets. Selective Oxidation of Ammonia on Mixed and Dual-layer Fe-ZSM-5 + Pt/Al_2O_3 Monolithic Catalysts. *Catalysis Today*, 231:105–115, 2014.

[13] S. Shrestha, M.P. Harold, and K. Kamasamudram. Experimental and Modeling Study of Selective Ammonia Oxidation on Multi-functional Washcoated Monolith Catalysts. *Chemical Engineering Journal*, 278:24–35, 2015.

[14] S. Shrestha, M.P. Harold, K. Kamasamudram, A. Kumar, L. Olsson, and K. Leistner. Selective Oxidation of Ammonia to Nitrogen on Bi-functional Cu–SSZ-13 and Pt/Al_2O_3 Monolith Csatalyst. *Catalysis Today*, 267:130–144, 2016.

[15] M. Dudák, V. Novák, P. Kočí, M. Marek, P. Blanco-García, and G. Jones. Prediction of Diffusivity and Conversion of *n*-Decane and CO in Coated Pt/Al_2O_3 Catalyst Depending on Porous Layer Morphology. *Applied Catalysis B: Environmental*, 150–151:446–458, 2014.

[16] M. Václavík, M. Dudák, V. Novák, R. Medlín, F. Štěpánek, M. Marek, and P. Kočí. Yeast Cells as Macropore Bio-templates Enhancing Transport Properties and Conversions in Coated Catalyst Layers for Exhaust Gas Oxidation. *Chemical Engineering Science*, 116:342–349, 2014.

[17] V. Novák, P. Kočí, T. Gregor, J Choi, F. Štěpánek, and M. Marek. Effect of Cavities and Cracks on Diffusivity in Coated Catalyst Layer. *Catalysis Today*, 216:142–149, 2013.

[18] K. Kamasamudram, N. Currier, T. Szailer, and A. Yezerets. Side Reactions in the Selective Catalytic Reduction of NO_x with Various NO_2 Fractions. *SAE International Journal*, 3(2010-01-1182):664–672, 2010.

[19] F. Gao, E. Walter, M. Kollar, Y. Wang, J. Szanyi, and C. Peden. Understanding Ammonia Selective Catalytic Reduction Kinetics over Cu/SSZ-13 from Motion of the Cu Ions. *Journal of Catalysis*, 319:1–14, 2014.

[20] C. Paolucci, J.R. Di Iorio, F.H. Ribeiro, R. Gounder, and W.F. Schneider. Catalysis Science of NO_x Selective Catalytic Reduction With Ammonia Over Cu-SSZ-13 and Cu-SAPO-34. *Advances in Catalysis*, 59:1–107, 2016.

[21] F. Gao, D. Mei, Y. Wang, J. Szanyi, and C.H.F. Peden. Selective Catalytic Reduction over Cu/SSZ-13: Linking Homo- and Heterogeneous Catalysis. *Journal of the American Chemical Society*, 139:4935–4942, 2017.

[22] P.S. Metkar, M.P. Harold, and V. Balakotaiah. Experimental and Kinetic Modeling Study of NH_3-SCR of NOx on Fe-ZSM-5, Cu-chabazite and Combined Fe- and Cu-zeolite Monolithic Catalysts. *Chemical Engineering Science*, 87:51–66, 2013.

[23] W.A. Majewski. Selective Catalytic Reduction. In *DieselNet Technology Guide*. Ecopoint Inc., 2005. Online. `https://dieselnet.com/tech/cat_scr.php` Accessed: March 8$^{\text{th}}$, 2017.

[24] O. Mihai, C.R. Widyastuti, A. Kumar, J. Li, S.Y. Joshi, K. Kamasamudram, N.W. Currier, A. Yezerets, and L. Olsson. The Effect of NO_2/NO_x Feed Ratio on the NH_3-SCR System Over Cu–Zeolites with Varying Copper Loading. *Catalysis Letters*, 144:70–80, 2014.

[25] I. Nova, C. Ciardelli, E. Tronconi, D. Chatterjee, and M. Weibel. NH_3-NO/NO_2 SCR for Diesel Exhausts After Treatment: Mechanism and Modelling of a Catalytic Converter. *Topics in Catalysis*, 42–43:43–46, 2007.

[26] A. Grossale, I. Nova, E. Tronconi, D. Chatterjee, and M. Weibel. NH_3-NO/NO_2 SCR for Diesel Exhausts Aftertreatment: Reactivity, Mechanism and Kinetic Modelling of Commercial Fe- and Cu-Promoted Zeolite Catalysts. *Topics in Catalysis*, 52:1837–1841, 2009.

[27] M. Iwasaki and H. Shinjoh. A Comparative Study of "Standard", "Fast" and "NO_2" SCR Reactions over Fe/zeolite Catalyst. *Applied Catalysis A: General*, 390:71–77, 2010.

[28] G. Madia, M. Koebel, M. Elsener, and A. Wokaun. Side Reactions in the Selective Catalytic Reduction of NO_x with Various NO_2 Fractions. *Industrial & Engineering Chemistry Reserach*, 41:4008–4015, 2002.

[29] MathWorks. What Is the Genetic Algorithm? Online. `se.mathworks.com/help/gads/what-is-the-genetic-algorithm.html` Accessed: April 26th, 2017.

[30] MathWorks. Genetic Algorithm Terminology. Online. `se.mathworks.com/help/gads/some-genetic-algorithm-terminology.htmls` Accessed: April 26th, 2017.

[31] MathWorks. How the Genetic Algorithm Works. Online. `se.mathworks.com/help/gads/how-the-genetic-algorithm-works.html` Accessed: April 26th, 2017.

[32] O. Mihai, C.R. Widyastuti, S. Andonova, K. Kamasamudram, J. Li, S.Y. Joshi, N.W. Currier, A. Yezerets, and L. Olsson. The Effect of Cu-loading on Different Reactions Involved in NH_3-SCR over Cu-BEA Catalysts. *Journal of Catalysis*, 311:170–181, 2014.

[33] P.N.R. Vennestrøm. *Selective Catalytic Reduction of Nitrogen Oxides with Ammonia over Microporous Zeolite Catalysts*. PhD thesis, Universitat Politècnica de València and Haldor Topsoe A/S, 2014.

CHAPTER 6

Further Work

The understanding of the diesel oxidation catalyst and the ammonia slip catalyst have been further developed through the research conducted in this Ph.D. thesis. However, additional important topics and research questions exist.

Through the work with the DOC, the importance of the Pt particle size for the oxidation of CO, propene, and NO was shown. The effect was investigated individually for each oxidation reaction considered, and as such, is not necessarily representative of the conditions in a real diesel exhaust aftertreatment system, where all three components and more are present at once. It is therefore of interest in further work to consider the series of 1 wt.% Pt/Al_2O_3 catalysts with different Pt particle sizes for the oxidation reactions in a mixture of CO, hydrocarbons, and NO. Even better would be the preparation and test of small or full scale monolith catalysts with varying Pt particle sizes. An important aspect to consider under real exhaust conditions is the competitive inhibition by different reactants, which potentially could dampen or enhance the Pt particle size effect [1]. Additionally, the presence of both NO and hydrocarbons may result in the formation of significant quantities of N_2O, which again may be influenced by the Pt particle size [1, 2]. Furthermore, Pt particles between 2–4 nm are likely to sinter under diesel exhaust conditions, and a method of stabilizing the catalyst is necessary to achieve the needed catalyst durability. These concerns validate the continued development and investigation of the Pt particle size effect for the diesel oxidation catalyst.

The modern state-of-the-art ammonia slip catalyst combines the Pt-based AMOX catalyst with an SCR catalyst. The ASC performance is in part determined by the individual properties of the AMOX catalyst and the SCR catalyst, but also by how they are combined. As a result, the development of the individual components and the combined system (AMOX and SCR) is necessary. With regards to the development of the AMOX catalyst, the significance of the Pt particle size was investigated, and showed that it has an effect on both catalyst activity and product selectivity during NH_3 oxidation. Specifically the influence on the NO_2/NO_x ratio and N_2O selectivity is of interest. By controlling the Pt particle size to give a local ratio of NO_2/NO_x=0.5, it is potentially possible to evoke the fast SCR reaction in the ASC, and further reduce NO_x emissions. This could be verified through activity measurements using a fixed bed reactor and/or monolith reactors, where the Pt/Al_2O_3 catalysts with different Pt particle sizes are mixed with a selected SCR catalyst (Cu-BEA, Fe-BEA, V_2O_5-based, etc.). The observed increase in NH_3 oxidation activity for Pt particles of ∼200 nm is unexpected since the availability of all types of surface atoms is significantly lowered for this particle size. A closer investigation of this, including the determination of reaction orders for NH_3 and O_2 over catalysts with different Pt particles sizes may be very informative in understanding this behavior. Furthermore, NH_3 oxidation over Pt, Rh, and Pd showed a clear superiority of Pt for oxidation activity, while Rh exhibited a very low N_2O selectivity. Given

the particle size effect observed for Pt and the preferred product selectivity of Rh, it is relevant to investigate if the activity of a Rh based catalyst can be increased while retaining its product selectivity. This could possibly be done by controlling the particle size of Rh or by combining Rh with Pt, for example by impregnation of Rh with Pt. These considerations may improve ASC performance and justify the continued development of the ammonia oxidation component.

The mathematical model derived for the ASC system was validated against experimental data for small monolith samples and provided a good description of the ASC system. The sensitivity analysis was performed for NH_3 oxidation at 300°C and helped gain system understanding and identify key design parameters. However, the usefulness of the analysis could be increased by broadening the operating conditions to consider other relevant situations, such as when a feed gas contains both NO_x and NH_3 or when the ASC operates at a higher temperature. Further modifications to the model that may increase its applicability could include the implementation of the random pore model to improve flexibility in describing the effective diffusivity with temperature, the introduction of a third layer to increase the number of possible configurations, or modifying the model to consider a transient system, which it inherently is in the real application. Given the ability of the model to employ kinetic models based on fixed bed reactor data and satisfactorily describe the ASC performance, the library of kinetic models could readily be expanded to include other AMOX (Rh, Pd, bimetallic, etc.) or SCR catalysts (Fe-ZSM-5, Cu-CHA,V_2O_5/WO_3-TiO_2, etc.). By expanding the library with new catalysts of interest, the model could be used to provide an initial investigation of new formulations, prior to extensive preparation campaigns. These benefits of using mathematical modeling in catalyst development support the continued development of the ASC model and its application in system analysis and catalyst design.

6.1 References

[1] M. Al-Harbi, R. Hayes, M. Votsmeier, and W.S. Epling. Competitive NO, CO and Hydrocarbon Oxidation Reactions Over a Diesel Oxidation Catalyst. *The Canadian Journal Of Chemical Engineering*, 90:1527–1538, 2012.

[2] R. Burch and D. Ottery. Selective Catalytic Reduction of NO_x by Hydrocarbons on Pt/Al_2O_3 Catalysts at Low Temperatures Without the Formation of N_2O. *Applied Catalysis B: Environmental*, 9:L19–L24, 1996.

Nomenclature

Abbreviations and Acronyms

NH_3-SCO	Selective Catalytic Oxidation of NH_3
NH_3-SCR	Selective Catalytic Reduction with NH_3
AMOX	Ammonia Oxidation
ASC	Ammonia Slip Catalyst
BDC	Bottom-Dead-Center
cDPF	Catalyzed Diesel Particulate Filter
cpsi	Cells per square inch
DFT	Density Functional Theory
DL	Dual Layer
DML	Dual Mixed Layer
DOC	Diesel Oxidation Catalyst
DPF	Diesel Particulate Filter
EEA	European Environment Agency
EGR	Exhaust Gas Recirculation
ELR	European Load Response Engine Test
EPA	Environmental Protection Agency
ESC/ETC	European Stationary/Transient Cycle
FBR	Fixed Bed Reactor
GHG	Greenhouse Gas
HC	Hydrocarbons
HDD	Heavy-Duty Diesel
HDL	Hybrid Dual Layer
HDL-A	Hybrid Dual Layer with AMOX top layer
HDL-S	Hybrid Dual Layer with SCR top layer
ICP-OES	Inductively Coupled Plasma Optical Emissions Spectrometry
IDL	Inverse Dual Layer
IHDL-A	Inverse Hybrid Dual Layer with AMOX bottom layer
IHDL-S	Inverse Hybrid Dual Layer with SCR bottom layer

MM	Mechanical Mixing
NEI	National Emission Inventory
NMVOC	Non-Methane Volatile Organic Compounds
PM	Particulate Matter
PN	Particle Number
SA	Sigma-Aldrich
SCO	Selective Catalytic Oxidation
SCR	Selective Catalytic Reduction
SEM	Scanning Electron Microscopy
SL-AMOX	Single Layer AMOX
SL-SCR	Single Layer SCR
SML	Single Mixed Layer
SOF	Soluble Organic Fraction
TCD	Thermal Conductivity Detector
TDC	Top-Dead-Center
TEM	Transmission Electron Microscopy
TOF	Turnover Frequency
TPD	Temperature Programmed Desorption
VOC	Volatile Organic Compounds
WHSC/WHTC	World Harmonized Stationary/Transient Cycle
WI	Wet Impregnation

Arabic Letters

p_{O_2}/p_{NH_3}	Ratio of oxygen partial presure to ammonia partial pressure [ ]
$A_{Pt,S}$	Pt surface area $\left[\text{Å}^2_{Pt}/g_{Pt}\right]$
$A_{Pt,X}$	Cross-sectional area of one Pt atom $\left[8.0\text{Å}^2_{Pt}/\text{Pt atom}\right]$
A_j	Pre-exponential factor for reaction j [mol/(s·kg$_{cat}$), mol/(s·kg$_{cat}$·bar), mol/(s·kg$_{cat}$·bar^2), mol/(s·kg$_{cat}$·bar$^{\frac{3}{2}}$)]
A_S	External surface area of the catalyst washcoat per tank $\left[m^2\right]$
C_i	Concentration of chemical compound $\left[mol/m^3\right]$
$C_{g,i,k}$	Concentration of chemical compound in gas phase of monolith channel $\left[mol/m^3\right]$
$C_{s,i,k}$	Concentration of chemical compound on surface of washcoat phase of monolith catalyst $\left[mol/m^3\right]$

$C_{\mathrm{wc},i,k}$	Concentration of chemical compound in washcoat phase of monolith channel $\left[\mathrm{mol/m^3}\right]$
d_{H}	Hydraulic diameter of the coated channel [m]
$D_{\mathrm{bulk},i}$	Bulk diffusion coefficient of compound i $\left[\mathrm{m^2/s}\right]$
$D_{\mathrm{eff},i}$	Effective diffusion coefficient of compound i $\left[\mathrm{m^2/s}\right]$
$D_{\mathrm{Knudsen},i}$	Knudsen diffusion coefficient of compound i $\left[\mathrm{m^2/s}\right]$
$d_{\mathrm{pore,\ wc}}$	Average pore diameter of washcoat layer, where wc = bl or tl [m]
D_{Pt}	Disperision of Pt [%]
d_{Pt}	Average diameter of Pt particles [nm]
$E_{\mathrm{A},j}$	Activation energy for reaction j [kJ/mol]
$K_{\mathrm{eq,x}}$	Equilibrium constant for $x_{\mathrm{LT}} \leftrightarrows x_{\mathrm{HT}}$ of SCR kinetic model [ ]
K_{eq}	Equilibrium constant for $\mathrm{NO} + \frac{1}{2}\,\mathrm{O_2} \leftrightarrows \mathrm{NO_2}$ [ ]
k_j	Reaction rate coefficient [mol/(s·kg$_{\mathrm{cat}}$), mol/(s·kg$_{\mathrm{cat}}$·bar), mol/(s·kg$_{\mathrm{cat}}$·bar^2), mol/(s·kg$_{\mathrm{cat}}$·bar$^{\frac{3}{2}}$)]
$k_{\mathrm{mt},i}$	Mass transfer coefficient of chemical compound from gas phase to washcoat phase of monolith catalyst $\left[\mathrm{mol/m^3}\right]$
$M_{\mathrm{W},i}$	Molar mass of compound i [kg/mol]
N_r	Number of reactions [ ]
$N_{\mathrm{CO\ ads}}$	CO adsorption capacity [mmol $\mathrm{CO_{ads}/g_{Pt}}$]
$N_{\mathrm{Pt,\ S}}$	Number of surface Pt atoms $\left[\mathrm{Pt_S atoms/g_{Pt}}\right]$
N_{Pt}	Total number of Pt atoms $\left[\mathrm{Ptatoms/g_{Pt}}\right]$
p_i	Partial pressure [bar]
Q	Standard volumetric flow rate $\left[\mathrm{m^3/s}\right]$
R	Gas constant = 8.314 [J/(mol · K)]
r	Radial position in monolith washcoat [m]
r'	Mass based rate of reaction [mol/(s · g$_{\mathrm{Pt}}$)]
R'$_{\mathrm{cat},i}$	Mass based catalytic rate of reaction [mol/(s · kg$_{\mathrm{cat}}$)]
$S_{\mathrm{N_2O}}$	$\mathrm{N_2O}$ selectivity [%]
$S_{\mathrm{N_2}}$	$\mathrm{N_2}$ selectivity [%]
S_{NOx}	NO_x selectivity [%]
Sh	Sherwood number [ ]
$Sh\infty$	Asymptotic Sherwood number = 2.98 for square channels [ ]
T	Temperature [K]
t	Time [s]
T_{20}	Temperature of 20% conversion of key reactant [°C]
T_{50}	Temperature of 50% conversion of key reactant [°C]

u_x	Linear gas velocity [m/s]
V_{Pt}	Pt volume $\left[\mathrm{\AA}^3_{\mathrm{Pt}}/\mathrm{g}_{\mathrm{Pt}}\right]$
W	Standard volumetric flow rate [$\mathrm{kg}_{\mathrm{cat}}$]
x	Axial position in monolith channel [m]
x_{HT}	Fractional weighting of high temperature SCR kinetics [ ]
x_{LT}	Fractional weighting of low temperature SCR kinetics [ ]
$X_{\mathrm{NH_3}}$	NH_3 conversion [%]
$y_{\mathrm{exp},i}$	Outlet concentration measured at reactor outlet [ppm]
$y_{\mathrm{sim},i}$	Outlet concentration calculated by model simlulation [ppm]
z	Dimensionless axial position in monolith channel [ ]
P_{T}	Total pressure [bar]
D_i	Inner diameter [mm]
TOF	Turnover frequency [$\mathrm{mol}/(\mathrm{s}\cdot\mathrm{mmol\ Pt_S})$]

Greek Letters

χ_{Pt}	Pt wt.% of AMOX catalyst in monolithic ASC [wt.%]
ΔH	Change in reaction enthalpy [J/mol]
ΔS	Change in reaction entropy [$\mathrm{J}/(\mathrm{mol}\cdot\mathrm{K})$]
ϵ	Porosity of catalyst layer, set to 0.4 [ ]
ν_i	Stoichiometric coefficient for reactant i in reaction j [ ]
Ω_i	Adsorption capacity of the catalyst for reactant $\left[\mathrm{mol}/\mathrm{kg}_{\mathrm{cat}}\right]$
ϕ_{cat}	Volume fraction of specified catalyst in catalyst layer [ ]
ψ_{cat}	Catalyst loading in monolith catalyst [g/L]
ρ_{cat}	Catalyst density $\left[\mathrm{kg}_{\mathrm{cat}}/\mathrm{m}^3\right]$
ρ_{Pt}	Pt density $\left[2.145\cdot10^{-23}\mathrm{g}^3_{\mathrm{Pt}/\mathrm{\AA}}\mathrm{Pt}\right]$
τ	Tortuosity of catalyst layer, set to 3 [ ]
θ_i	surface coverage of the catalyst with adsorbed reactant [ ]

Subscripts and Superscripts

bl	Bottom layer
cat	Catalyst: AMOX or SCR
tl	Top layer
i	Chemical compound i
j	Reaction j
k	Tank number k

APPENDIX A

Diesel Oxidation Catalyst

A.1 CO, C_3H_6, and NO Oxidation over Pt/Al_2O_3 with Varying Pt Particle Size

Figures A.1 and A.2 show the activity measurements for CO and C_3H_6 oxidation over the 1 wt.% Pt/Al_2O_3 catalysts with varying Pt particle size for the a) 1st heating cycle, b) 1st cooling cycle, c) 2nd heating cycle, and d) 2nd cooling cycle. The activity measurements during the 1st heating cycle behave significantly different compared to the subsequent cooling and heating phases. This suggests that the catalysts undergo a change during the heating cycle shown in Figure A.1a and Figure A.2a, and that the catalysts reach a stable state after the initial heating to 550°C, indicated by the subsequently similar CO conversion curves.

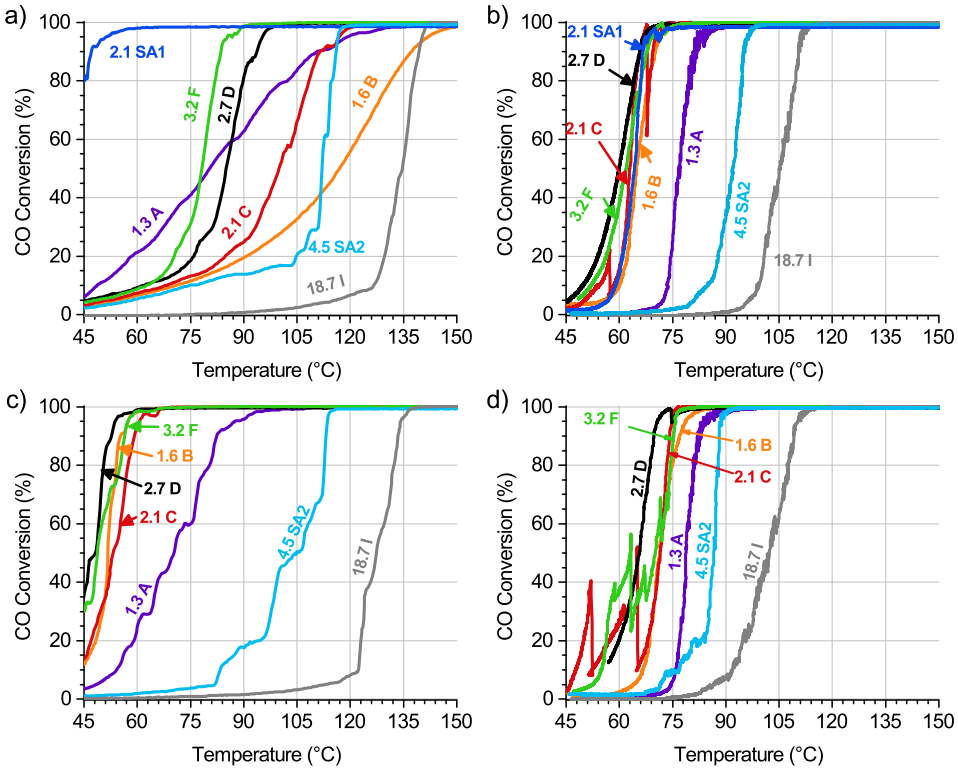

Figure A.1: *CO oxidation conversion curves over 1 wt.% Pt/Al_2O_3 for the a) 1st heating cycle, b) 1st cooling cycle, c) 2nd heating cycle, and d) 2nd cooling cycle. Operating conditions: 10 mg catalyst (150-300 µm), 50 mg inert glass beads (212-300 µm), 310 NmL/min gas flow, SV = 0.021 mol/(gcat·s), 240 ppm CO, 2.8 vol.% H_2O, 9.7 vol.% O_2, and balance N_2.*

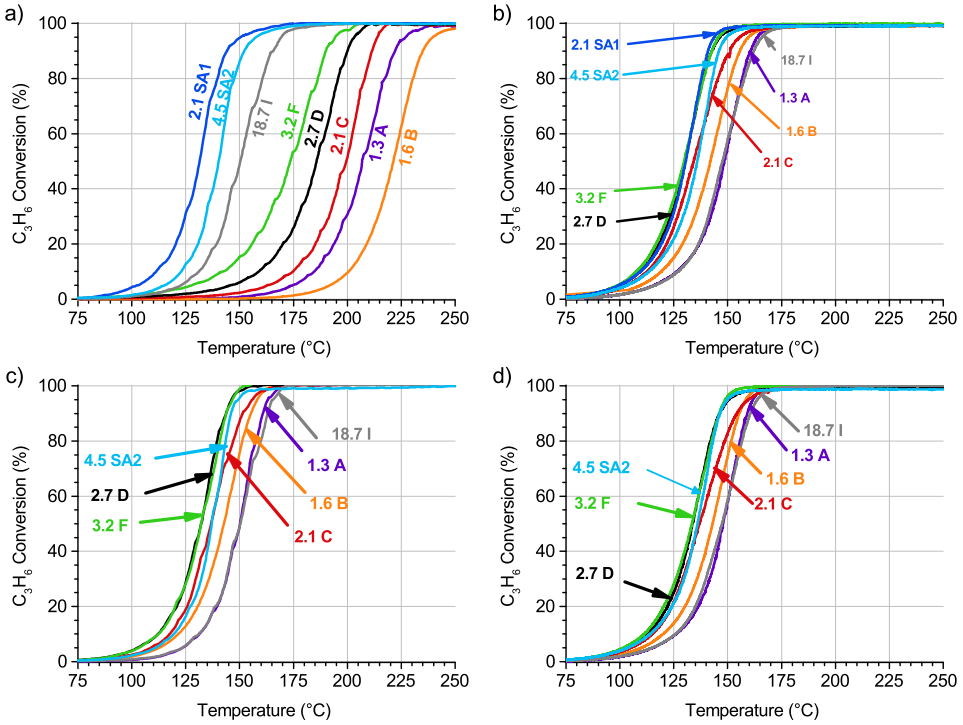

Figure A.2: *C_3H_6 oxidation conversion curves over 1 wt.% Pt/Al_2O_3 for the a) 1st heating cycle, b) 1st cooling cycle, c) 2nd heating cycle, and d) 2nd cooling cycle. Operating conditions: 10 mg catalyst (150-300 µm), 50 mg inert glass beads (212-300 µm), 310 NmL/min gas flow, SV = 0.021 mol/(gcat·s), 145 ppm C_3H_6, 2.8 vol.% H_2O, 9.7 vol.% O_2, and balance N_2.*

Figure A.3 shows the NO oxidation activity measurements for the a) 1st heating cycle and the b) 1st cooling cycle. Similarly to CO and C_3H_6 oxidation, the 1st heating curve for NO oxidation is significantly different than the subsequent cooling curve, indicating again a change in the catalyst.

For NO oxidation, we decided to exhibit two different catalyst samples to repeated heating and cooling cycles in order to verify the stability of the catalysts tested. Figure A.4 shows repeated heating and cooling cycles for 1 wt.% Pt/Al_2O_3 catalysts with an average Pt particle diameter of a) 1.3 nm (tested with four heating and cooling cycles) and b) 2.7 nm (tested with three heating and cooling cycles). The catalysts were prepared using the methods described in Section 2.2.1, with 1.3 nm Pt particles prepared using the same procedure as for sample A, while the sample with 2.7 nm Pt particles used the same procedure as for sample C, but with a calcination temperature of 750°C and a duration of 12 hours. Figure A.4 shows again the significant change in catalytic activity from the 1st heating cycle to the subsequent cooling and heating cycles, for both samples. The subsequent cooling and heating cycles show a stable catalytic activity, with only limited changes occurring between the cooling cycles. Based on this we chose to limit the NO oxidation activity measurements to one heating and cooling cycle and used the activity measurement during the 1st cooling curve to compare catalytic activity of samples.

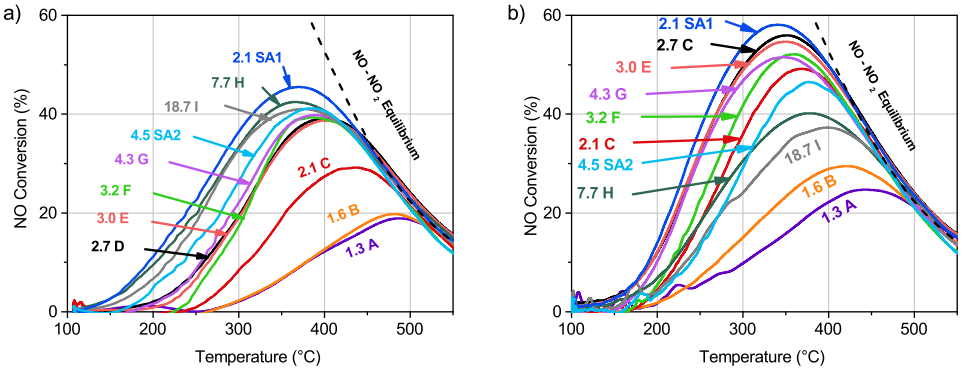

Figure A.3: *NO oxidation conversion over 1 wt.% Pt/Al_2O_3 with for a) 1st heating cycle and b) 1st cooling cycle. Operating conditions: 20 mg catalyst (150-300 µm), 100 mg inert glass beads (212-300 µm), 1030 NmL/min gas flow, SV = 0.035 mol/(gcat·s), 485 ppm NO, 7.8 vol.% H_2O, 9.7 vol.% O_2, and balance N_2.*

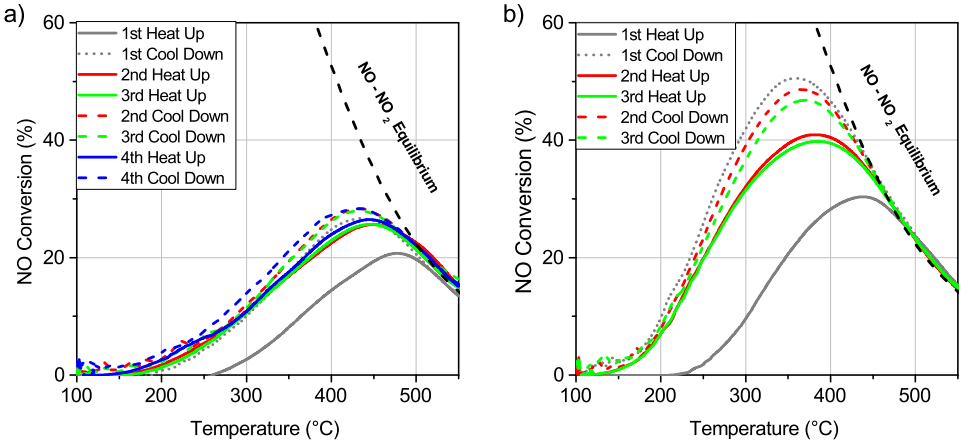

Figure A.4: *NO oxidation conversions over 1 wt.% Pt/Al_2O_3 for several heating and cooling cycles with average Pt particle diameters of a) 1.3 nm and b) 2.7 nm. Operating conditions: 20 mg catalyst (150-300 µm), 100 mg inert glass beads (212-300 µm), 1030 NmL/min gas flow, SV = 0.035 mol/(gcat·s), 485 ppm NO, 7.8 vol.% H_2O, 9.7 vol.% O_2, and balance N_2.*

APPENDIX B

Ammonia Slip Catalyst

B.1 Ammonia Oxidation over Pt, Rh, and Pd Supported on Al_2O_3

Figures B.1–B.4 present the activity measurements for NH_3 oxidation over the 5 wt.% Pt/Al_2O_3, 1 wt.% Pt/Al_2O_3, 5 wt.% Rh/Al_2O_3, and 5 wt.% Pd/Al_2O_3 catalysts 1st and 2nd heating and cooling cycles. The activity measurements during the 1st heating cycle are significantly different from the subsequent cooling and heating cycles. This suggests that the catalysts undergo a change during the 1st heating cycle, and that the catalysts reach a stable state after the initial heating to 550°C, indicated by the similarity of the subsequent measurements.

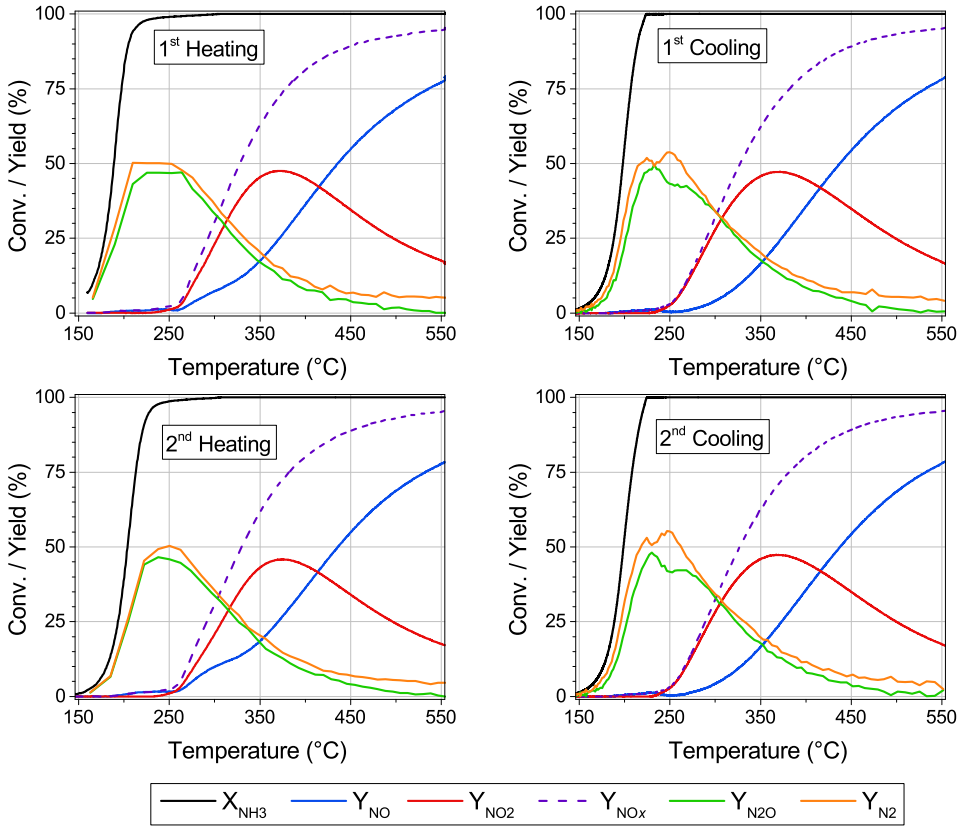

Figure B.1: *NH_3 oxidation over 5 wt.% Pt/Al_2O_3 for consecutive heating and cooling cycles. Operating conditions: 20 mg catalyst (150-300 µm), 100 mg inert glass beads (212-300 µm), 1000 NmL/min gas flow, 500 ppm NH_3, 2 vol.% H_2O, 10 vol.% O_2, and balance N_2.*

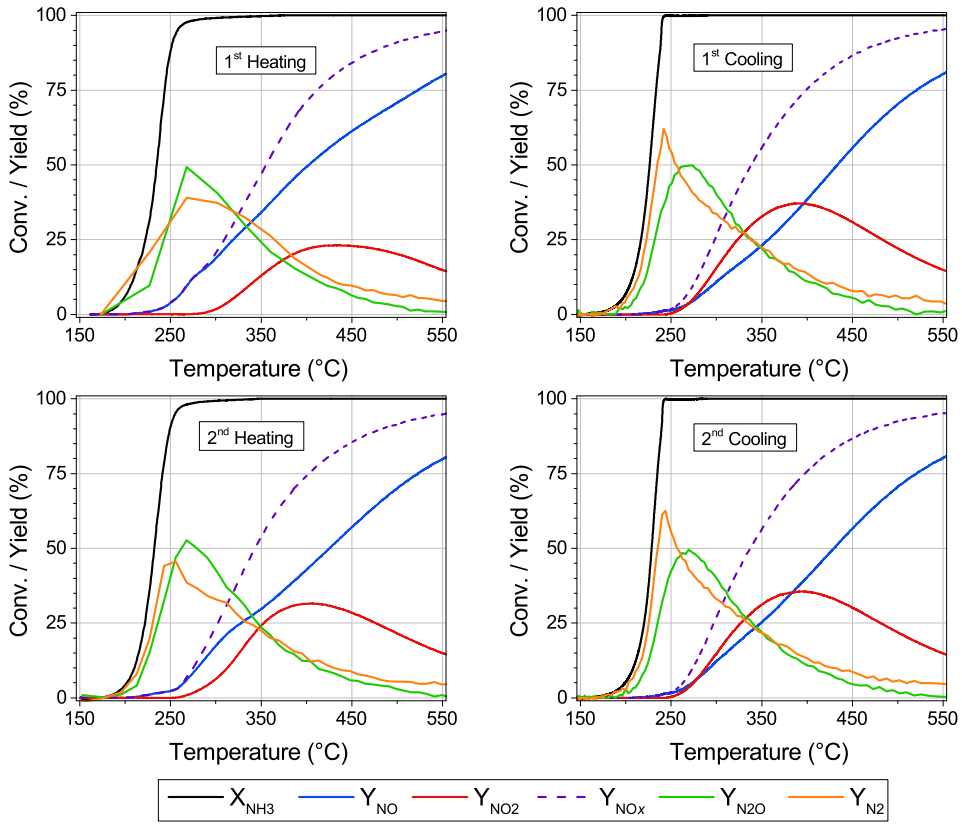

Figure B.2: *NH_3 oxidation over 1 wt.% Pt/Al_2O_3 for consecutive heating and cooling cycles. Operating conditions: 20 mg catalyst (150-300 µm), 100 mg inert glass beads (212-300 µm), 1000 NmL/min gas flow, 500 ppm NH_3, 2 vol.% H_2O, 10 vol.% O_2, and balance N_2.*

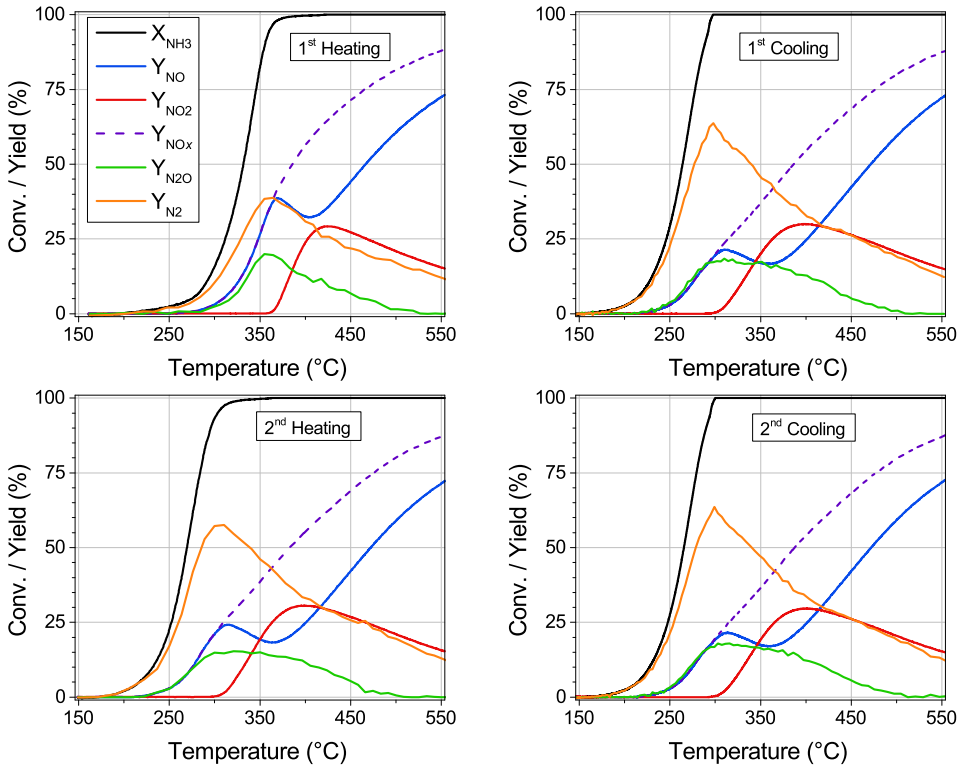

Figure B.3: *NH_3 oxidation over 5 wt.% Rh/Al_2O_3 for consecutive heating and cooling cycles. Operating conditions: 20 mg catalyst (150-300 µm), 100 mg inert glass beads (212-300 µm), 1000 NmL/min gas flow, 500 ppm NH_3, 2 vol.% H_2O, 10 vol.% O_2, and balance N_2.*

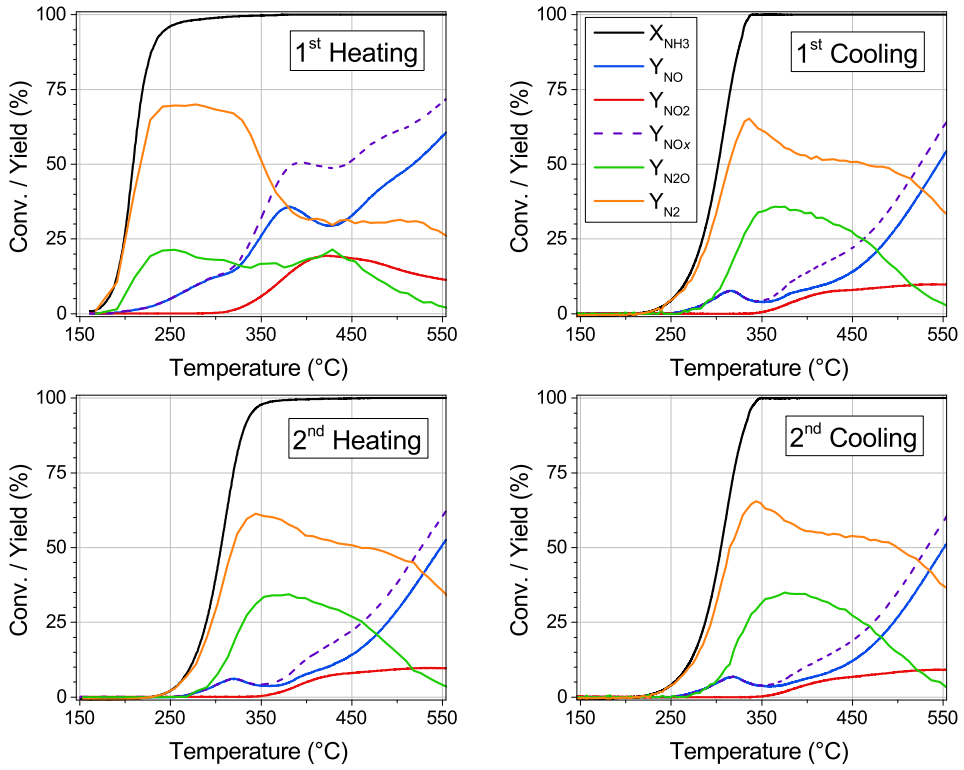

Figure B.4: *NH_3 oxidation over 5 wt.% Pd/Al_2O_3 for consecutive heating and cooling cycles. Operating conditions: 20 mg catalyst (150-300 µm), 100 mg inert glass beads (212-300 µm), 1000 NmL/min gas flow, 500 ppm NH_3, 2 vol.% H_2O, 10 vol.% O_2, and balance N_2.*

B.2 Selectivity during NH_3 Oxidation over Pt, Rh, and Pd Supported on Al_2O_3

Figure B.5 presents the a) NH_3 conversion, b) N_2 selectivity, c) NO_x selectivity, and d) N_2O selectivity during the 1st cooling cycle of the activity measurements for the 5 wt.% Pt/Al_2O_3, 1 wt.% Pt/Al_2O_3, 5 wt.% Rh/Al_2O_3, and 5 wt.% Pd/Al_2O_3 catalysts evaluated for NH_3 oxidation. The N_2 selectivity is clearly greatest for Pd, followed by Rh, and then the two Pt catalysts. Meanwhile, Rh is clearly the least selective towards N_2O, while Pt is the most selective at temperatures below 325°C, and Pd is the most selective at temperatures above 325°C. Pt is overall the most selective towards NO_x.

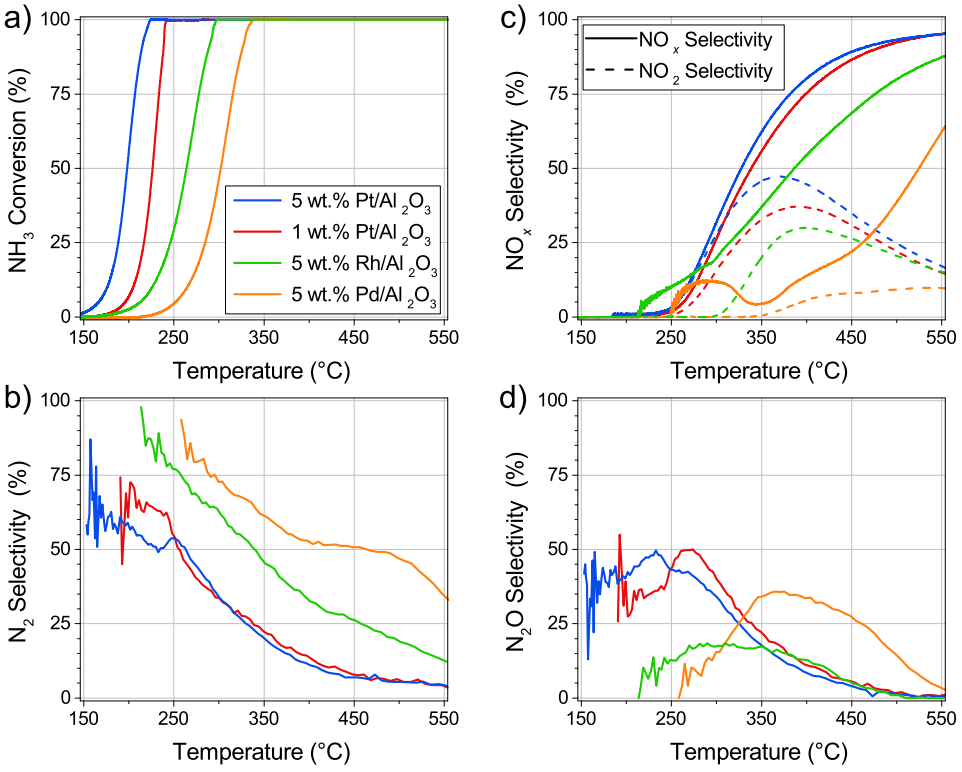

Figure B.5: *Selectivity of a) NH_3 conversion, b) N_2 selectivity, c) NO_x selectivity, and d) N_2O selectivity during NH_3 oxidation over 1 wt.% Pt/Al_2O_3, 5 wt.% Pt/Al_2O_3, 5 wt.% Rh/Al_2O_3, and 5 wt.% Pd/Al_2O_3 for the 1st cooling cycles. Operating conditions: 20 mg catalyst (150-300 µm), 100 mg inert glass beads (212-300 µm), 1000 NmL/min gas flow, 495 ppm NH_3, 2 vol.% H_2O, 10 vol.% O_2, and balance N_2.*

B.3 Ammonia Oxidation over Pt/Al_2O_3 with Varying Pt Particle Size

Figures B.6–B.11 present the activity measurements for NH_3 oxidation over the 1 wt.% Pt/Al_2O_3 catalysts with varying Pt particle sizes, during the 1st and 2nd, heating and cooling cycles. The activity measurements during the 1st heating cycle are significantly different from the subsequent cooling and heating cycles. This suggests that the catalysts undergo a change during the 1st heating cycle, and that the catalysts reach a stable state after the initial heating to 550°C, indicated by the similarity of the subsequent measurements.

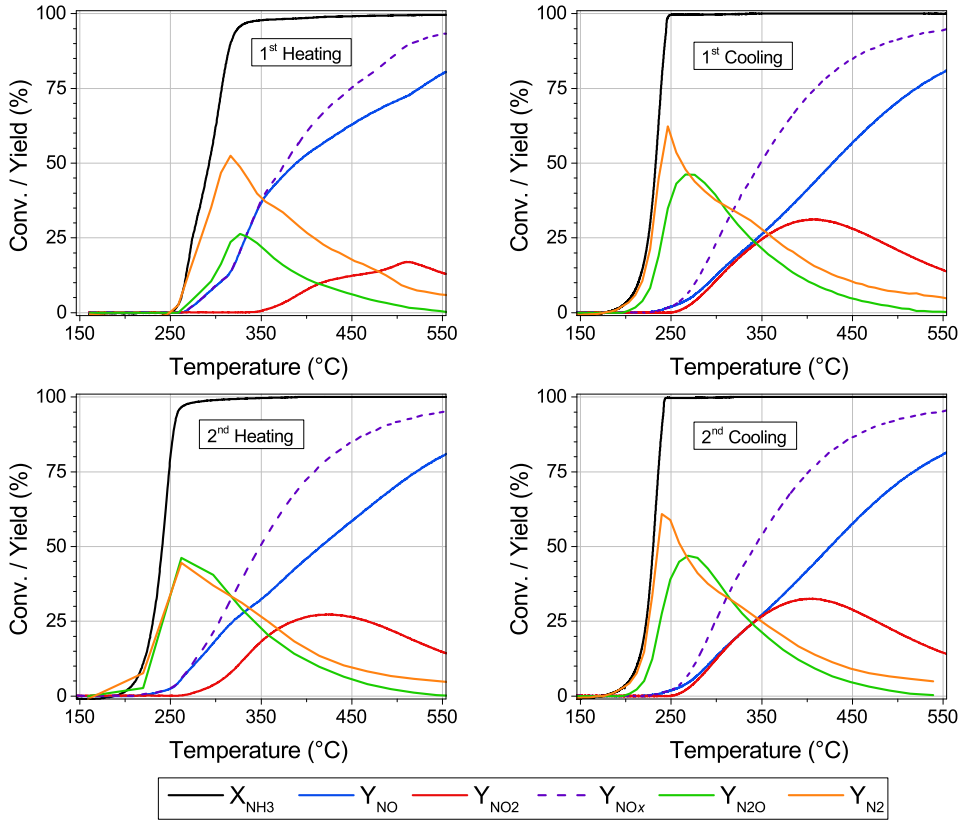

Figure B.6: *NH_3 oxidation over 1 wt.% Pt/Al_2O_3 with an average Pt particle size of 1.3 nm for two consecutive heating and cooling cycles. Operating conditions: 20 mg catalyst (150-300 µm), 100 mg inert glass beads (212-300 µm), 1000 NmL/min gas flow, 500 ppm NH_3, 2 vol.% H_2O, 10 vol.% O_2, and balance N_2.*

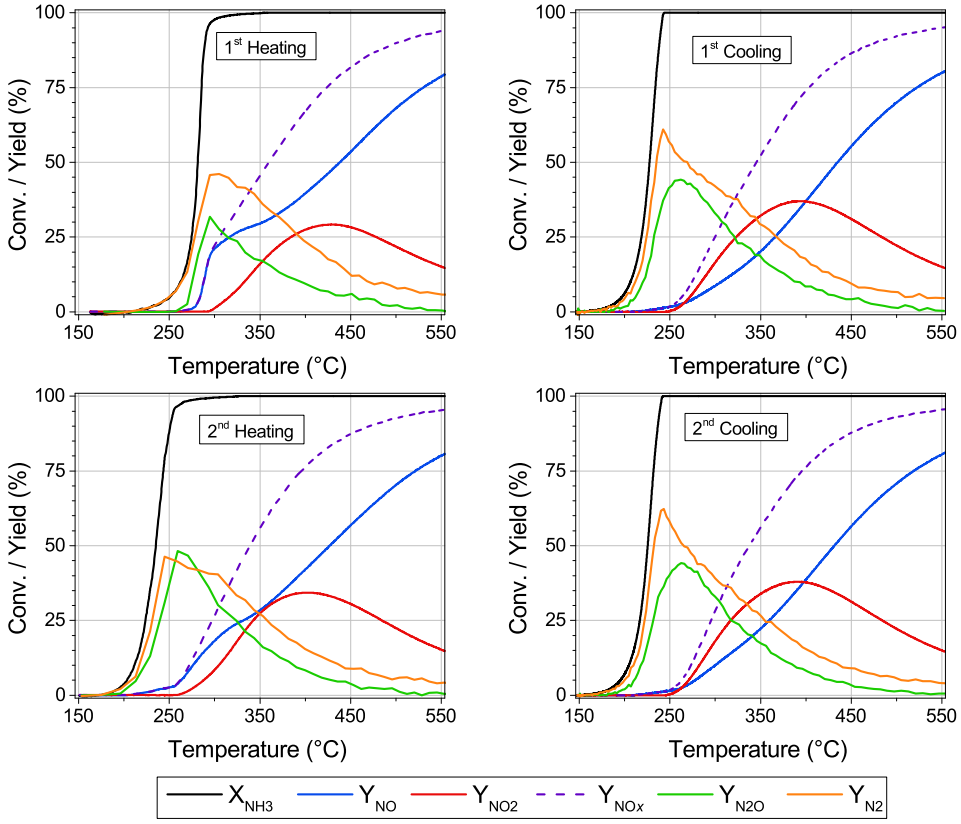

Figure B.7: *NH_3 oxidation over 1 wt.% Pt/Al_2O_3 with an average Pt particle size of 2.7 nm for two consecutive heating and cooling cycles. Operating conditions: 20 mg catalyst (150-300 µm), 100 mg inert glass beads (212-300 µm), 1000 NmL/min gas flow, 500 ppm NH_3, 2 vol.% H_2O, 10 vol.% O_2, and balance N_2.*

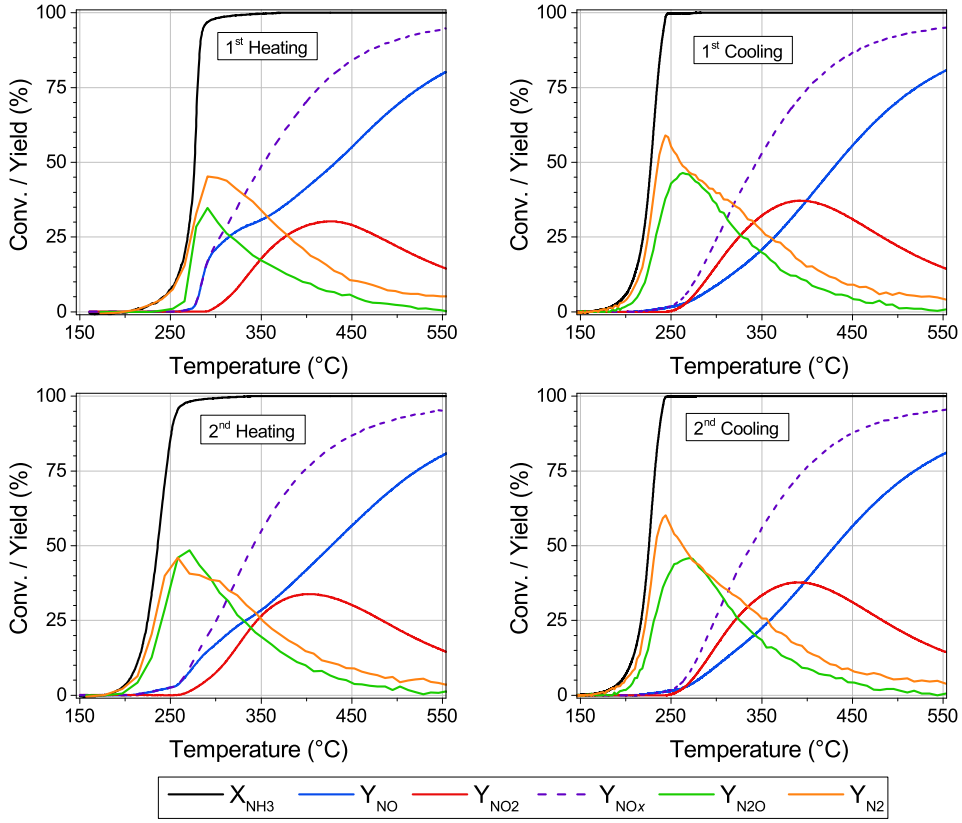

Figure B.8: *NH_3 oxidation over 1 wt.% Pt/Al_2O_3 with an average Pt particle size of 4.3 nm for two consecutive heating and cooling cycles. Operating conditions: 20 mg catalyst (150-300 µm), 100 mg inert glass beads (212-300 µm), 1000 NmL/min gas flow, 500 ppm NH_3, 2 vol.% H_2O, 10 vol.% O_2, and balance N_2.*

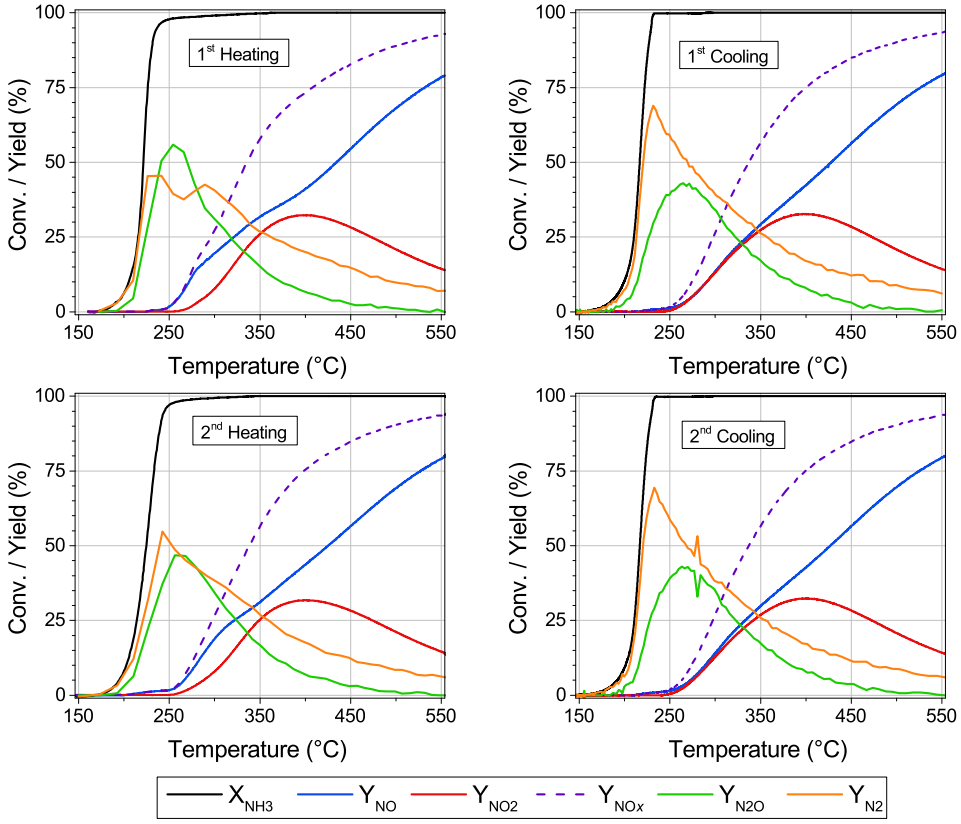

Figure B.9: *NH_3 oxidation over 1 wt.% Pt/Al_2O_3 with an average Pt particle size of 7.7 nm for two consecutive heating and cooling cycles. Operating conditions: 20 mg catalyst (150-300 µm), 100 mg inert glass beads (212-300 µm), 1000 NmL/min gas flow, 500 ppm NH_3, 2 vol.% H_2O, 10 vol.% O_2, and balance N_2.*

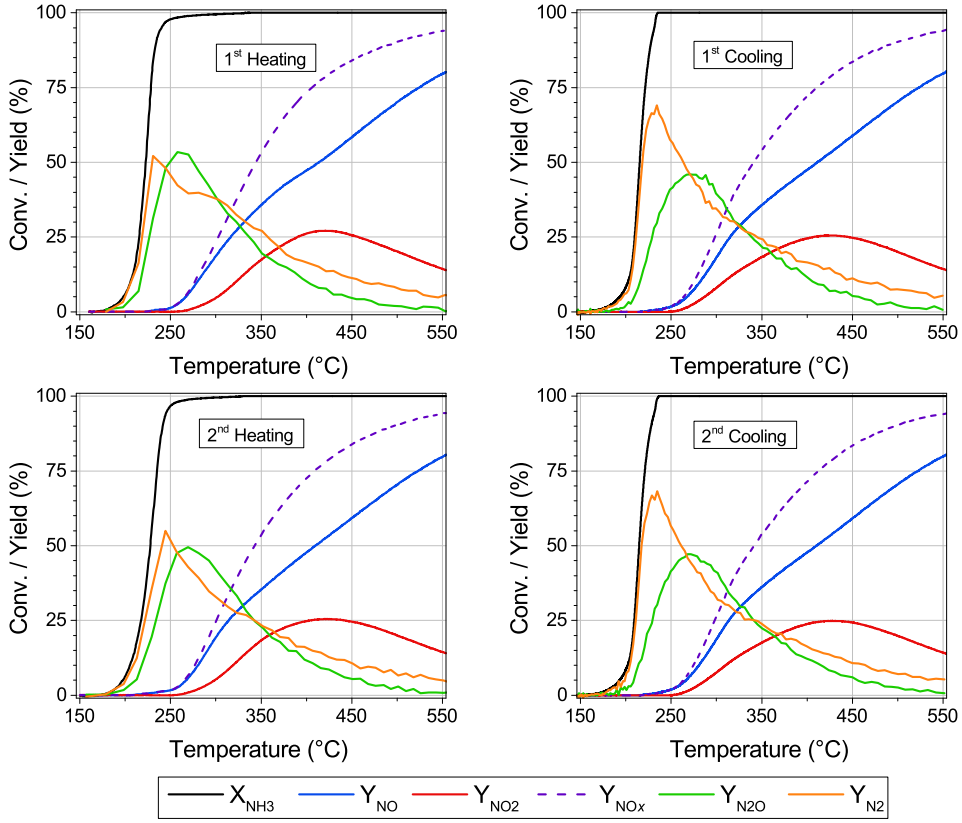

Figure B.10: *NH_3 oxidation over 1 wt.% Pt/Al_2O_3 with an average Pt particle size of 18.7 nm for two consecutive heating and cooling cycles. Operating conditions: 20 mg catalyst (150-300 µm), 100 mg inert glass beads (212-300 µm), 1000 NmL/min gas flow, 500 ppm NH_3, 2 vol.% H_2O, 10 vol.% O_2, and balance N_2.*

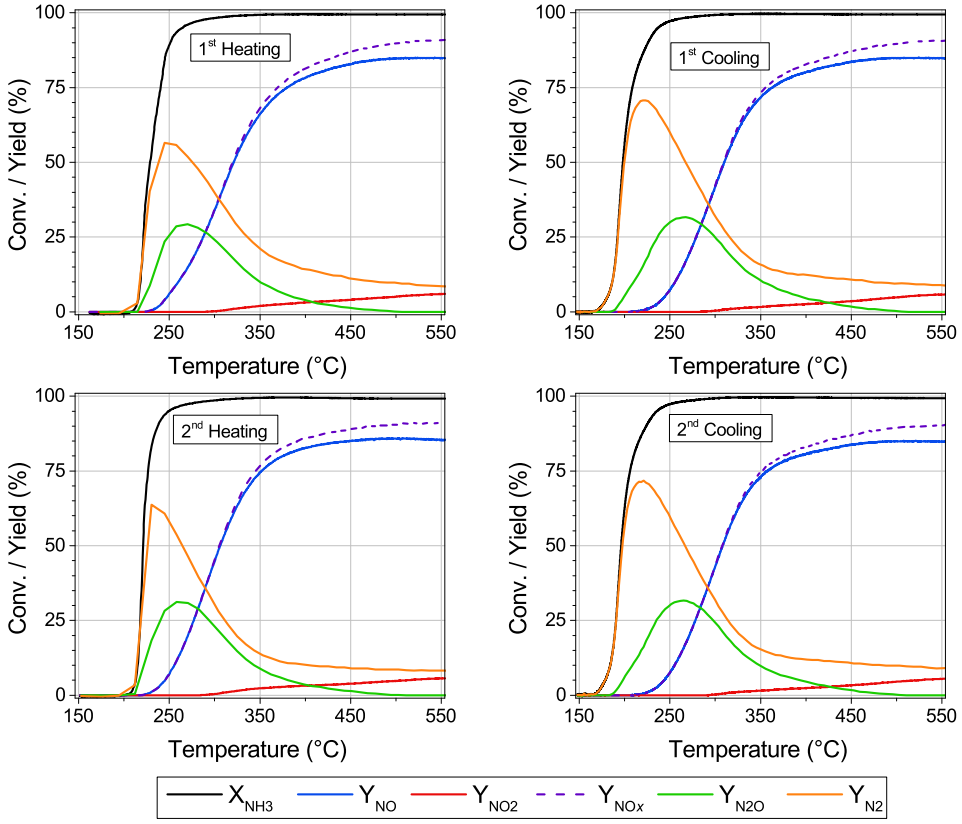

Figure B.11: *NH_3 oxidation over 1 wt.% Pt/Al_2O_3 with an average Pt particle size of ∼200 for two consecutive heating and cooling cycles. Operating conditions: 20 mg catalyst (150-300 µm), 100 mg inert glass beads (212-300 µm), 1000 NmL/min gas flow, 500 ppm NH_3, 2 vol.% H_2O, 10 vol.% O_2, and balance N_2.*

B.4 Supplementary Simulation for Ammonia Slip Catalyst

Figure B.12 presents the experimental data and simulation for oxidation of NH_3 over the single layer SCR catalyst with 61 g/L. The oxidation of NH_3 begins just below 300°C and increases quickly with temperature. The product selectivity towards N_2 is dominating, although low levels of NO_x and N_2O are also measured.

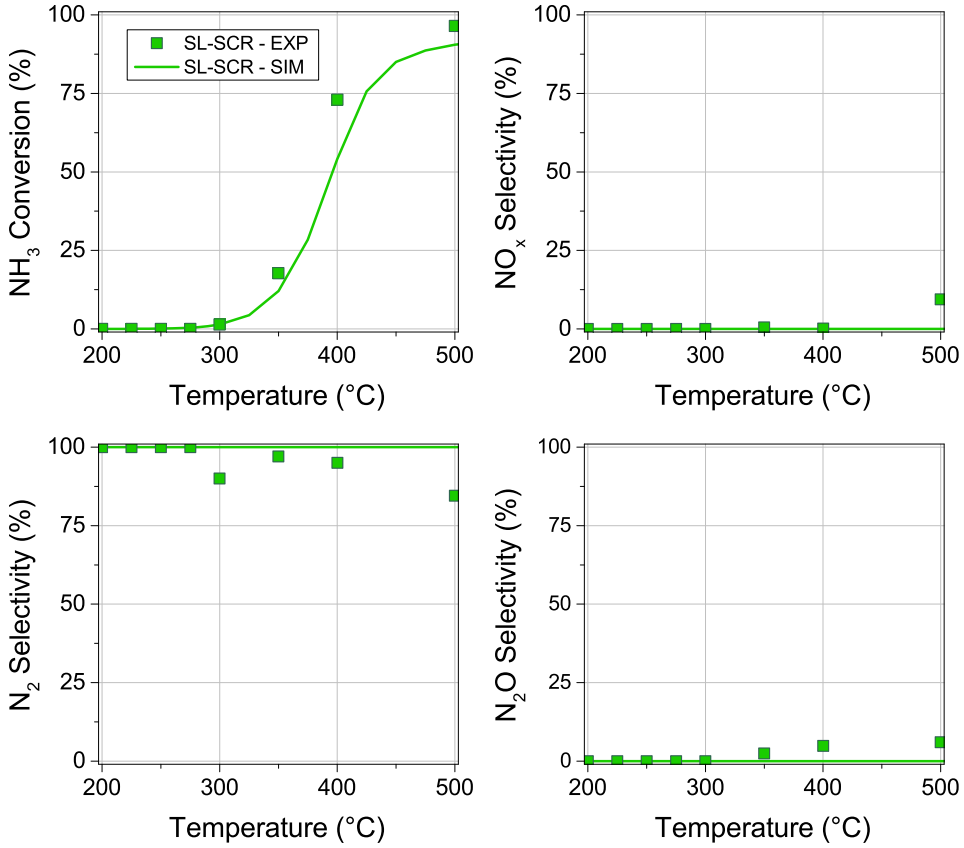

Figure B.12: *NH_3 oxidation over the single layer SCR (SL-SCR) monolith catalyst simulated using the monolith model for the ammonia slip catalyst. Base catalyst parameters: ψ_{SCR}=61 g/L and $d_{pore,\ bl}$=50 nm. Operating conditions: 200 ppm NH_3, 3.3 vol.% H_2O, 12.3 vol.% O_2, balance N_2, with GHSV 250,000 hr^{-1}.*